HAL
open science

Thermal illusion based on metamaterials and metasurfaces: conduction and radiation

Ahmed Alwakil

▶ To cite this version:

Ahmed Alwakil. Thermal illusion based on metamaterials and metasurfaces: conduction and radiation. Optics / Photonic. Aix-Marseille Université, 2018. English. NNT : . tel-02472870

HAL Id: tel-02472870
https://hal.science/tel-02472870v1

Submitted on 10 Feb 2020

HAL is a multi-disciplinary open access archive for the deposit and dissemination of scientific research documents, whether they are published or not. The documents may come from teaching and research institutions in France or abroad, or from public or private research centers.

L'archive ouverte pluridisciplinaire **HAL**, est destinée au dépôt et à la diffusion de documents scientifiques de niveau recherche, publiés ou non, émanant des établissements d'enseignement et de recherche français ou étrangers, des laboratoires publics ou privés.

AIX-MARSEILLE UNIVERSITÉ

Ecole Doctorale : Physique et Sciences de la Matière (ED352)

Agence Nationale de la Recherche

Institut Fresnel UMR 7249 CNRS/AMU/ECM

Thèse présentée pour obtenir le grade universitaire de docteur en sciences

Discipline : Optique, Photonique et Traitement d'Images

Ahmed ALWAKIL

Illusions thermiques basées sur les métamatériaux et lesmétasurfaces : conduction et rayonnement

Soutenue le 27/06/2018 devant le jury composé de :

Martin WEGENER	Institute of Applied Physics - Karlsruhe Institute of Technology	Rapporteur
André DE LUSTRAC	Université Paris Saclay, C2N	Rapporteur
Stefano MACI	Dipartimento di Ingegneria dell'Informazione e Scienze Matematiche, Université de Siene	Examinateur
Karl JOULAIN	Ecole Nationale Supérieure d'Ingénieurs de Poitiers (ENSI Poitiers), Institut Pprime	Examinateur
Franck ENGUEHARD	Laboratoire EM2C, Centrale Supelec	Examinateur
Philippe ADAM	Direction Générale de l'Armement	Examinateur
Myriam ZERRAD	Institut Fresnel, Aix Marseille Université	Co-Directeur de thèse
Claude AMRA	Institut Fresnel, CNRS	Directeur de thèse

Résumé de la thèse Les techniques de camouflage, mimétisme ou invisibilité ont récemment connu une forte émergence, qui se poursuit aujourd'hui avec l'apparition des méta-surfaces. C'est dans ce contexte que ce travail de doctorat a été réalisé, notamment avec un premier objectif d'étendre ces outils et concepts aux problèmes inverses du domaine de la diffusion de la chaleur. La suite du travail a concerné le rayonnement thermique, les méta-surfaces, les transformations de champ, et enfin le mimétisme d'objets en mouvement. Après avoir étendu les techniques de mimétisme au domaine de la conduction, nous avons résolu le problème inverse associé, qui consiste à camoufler des objets imposés en forme ou conductivité. Ce premier travail a permis de mettre en évidence les classes de transformation qui laissent invariantes les paramètres physiques, conférant ainsi plus de pragmatisme au domaine du mimétisme. Nous avons ensuite considéré le cas du rayonnement thermique, et démontré pour la première fois que les illusions par rayonnement étaient envisageables, en appui sur l'invariance du théorème de fluctuation/dissipation. Dans une deuxième étape, nous avons mis au point une nouvelle méthode pour calculer le rayonnement thermique par des objets de forme arbitraire, mettant en jeu des méta-surfaces inhomogènes, anisotropes, chirales et non locales. Nous montrons également comment tirer profit des méta-surfaces pour remplacer les capes volumiques tout en conservant la fonction de camouflage. Cette technique est particulièrement prometteuse pour les applications, même si elle reste intrinsèquement liée à l'éclairement. Des techniques similaires sont développées pour que soit facilitée l'utilisation de transformations discontinues de l'espace.

Summary of the Thesis in English Mimetism, camouflage or invisibility have motivated numerous efforts in the last decade, which are now extended with metasurfaces. This Ph.D. work fits this international context and was first focused on inverse problems in heat conduction before we address thermal radiation and metasurfaces, field transformation, and the mimetism of moving objects. After we generalize the mimetism techniques to heat diffusion, we solved the associated inverse problem which consists in the camouflage of given objects, that is, objects with shape or conductivity that are beforehand chosen. The results allowed us to emphasize the class of transformations which hold the physical parameters, hence giving more pragmatism to the field of mimetism. Then we addressed the case of thermal radiation and proved for the first time that mimetism effects could also be controlled in this field, on the basis of the fluctuation/dissipation theorem. In a second step, we built an original technique able to predict the thermal radiation from objects of arbitrary shapes. This technique involves inhomogeneous, anisotropic, chiral and nonlocal metasurfaces. We also show how to take more benefits of metasurfaces in order to replace the bulk mimetism cloaks. We believe this technique to give again more push forward to the field, though the mimetism efficiency now relies on the illumination conditions. Similar techniques are further developed to allow a practical use of discontinuous space transformations. Eventually, field transformation is introduced to complete all these results.

Résumé de thèse vulgarisé pour le grand public Les illusions électromagnétiques et l'invisibilité ont souvent été romancées par les auteurs de science-fiction, et largement étudiées pour des applications du domaine de la furtivité ou du camouflage. Pour la Défense, il s'agit en général de rendre difficilement détectables la présence d'avions ou de chars, voire de soldats, eu égard aux systèmes de détection adverses. Les techniques utilisées peuvent s'inspirer de celles que l'on trouve déjà dans la nature, dites bio-inspirées, comme celles des insectes dont la peau change de couleur pour s'adapter à l'environnement local et minimiser ainsi le contraste en imagerie... Ce travail de doctorat s'inscrit dans ce contexte en donnant une place majeure à l'étude des illusions par conduction et rayonnement thermique, en incluant le mimétisme d'objets en mouvement.

Thesis Summary for Public Audience Electromagnetic illusions had been either a topic of science fiction authors or stealth technologists and engineers. For stealth technology, engineers design planes and tanks structures to making them hard to be detected by radars and thermal detectors. Similarly, camouflage coats had been designed to help soldiers are hard to be seen, these camouflage techniques already use the same techniques used by animals and insects where they change the color of their skin to match the surrounding environment to minimize the contrast making them undetectable by the other animal species. During this Ph.D. research work, the main focus is to propose a new technique to achieve both scattering and thermal radiation illusion.

To Heba and Diaa.

TABLE OF CONTENTS

DEDICATION 1

LIST OF FIGURES 6

LIST OF APPENDICES 21

LIST OF ABBREVIATIONS 22

PREFACE 23

LIST OF PUBLICATIONS 33

CHAPTER

I. Introduction 1

1.1 Motivation 1
1.2 Invisibility and Illusion Cloaking 3
1.2.1 Transformation optics cloaks using metamaterials . 4
1.2.2 Scattering cancellation using mantle meta-surfaces . 9
1.3 Thermal Energy Transfer 21
1.3.1 Heat conduction 21
1.3.2 Thermal radiation 23
1.3.3 Thermal radiation from meta-surfaces 30
1.3.4 Near field thermal radiation computation 32
1.4 Duality Transformation 33

II. Controlling Temperature Signature using Transformation Optics 41

2.1 Introduction 41
2.2 Inverse Transformation 43
2.3 Inverse Transformation at the Static regime 47
2.4 Cloak Design Procedure 61
2.5 Numerical Simulation 64

2.6 Conclusion 71

III. Transformation Fluctuation Electrodynamics: Application of Transformation Optics upon Thermal Radiation Illusion . . 73

3.1 Introduction 73
3.2 Transformation optics and Fluctuation Electrodynamics . . . 74
3.3 Transformation Fluctuation Electrodynamics 76
3.4 Two Dimensional E/H-polarization Thermal Radiation 78
3.5 Two Dimensional E/H-Polarization Camouflages 84
3.6 Limitations and Conclusions 89

IV. Cloaking and Scattering Camouflage using Transformation Optics based Mantle Meta-surfaces 92

4.1 Introduction 92
4.2 Meta-surface models: GSTC versus Impedance Matrix 95
4.2.1 Impedance matrix representation 95
4.2.2 GSTC 99
4.3 Equivalence between Scattering Cancellation and Discontinuous T.O 107
4.3.1 1D discontinuous space transformation 107
4.3.2 2D polar/cylindrical discontinuous space transformation 118
4.3.3 Compression of non cylindrical shell into an inhomogeneous and spatial dispersive MS: 136
4.4 Conclusion 156

V. Circuit Model for Thermal Radiation from Arbitrary Thermal Emitter at Constant Temperature 158

5.1 Introduction 158
5.2 TR Pattern for Arbitrary Thermal Emitter 163
5.3 Equivalent Surface Admittance 166
5.3.1 Surface impedance/admittance: Quick Review . . . 167
5.3.2 Equivalent surface admittance for arbitrary shaped emitter 170
5.3.3 Admittance matrix representation 174
5.3.4 Reciprocal surfaces 174
5.4 GSTC description of an Equivalent Surface 179
5.5 TR from Circularly Symmetric Object 181
5.5.1 Equivalence between surface admittance and GSTC descriptions: 182
5.5.2 Numerical example 188

5.6 TR from arbitrary thermal emitter characterized by a Surface Impedance . . . 193
5.6.1 Nyquist thermal sources . . . 195
5.6.2 TR from Nyquist sources . . . 196
5.7 Numerical Calculation . . . 199
5.8 Conclusions and Limitations . . . 202

VI. Fluctuation Electrodynamics in Reciprocal Chiral Media using Field Transformation and Discontinuous Field Transformation based Mantle Cloaks . . . 204

6.1 Introduction . . . 204
6.2 Field Transformation . . . 206
6.2.1 Decomposition into longitudinal and transverse components . . . 207
6.2.2 Transforming between virtual and physical spaces . 210
6.3 Transformation Fluctuation Electrodynamics . . . 212
6.3.1 Covariance of FE under FT transformation . . . 212
6.3.2 FE in the physical space . . . 214
6.3.3 Thermal illusion using FT based cloaks . . . 218
6.4 Discontinuous Field Transformation . . . 220
6.4.1 GSTC model for a discontinuous FT based mantle cloak . . . 221
6.4.2 Circuit model for the discontinuous FT mantle cloak 228
6.5 Conclusion . . . 232

VII. Conclusions and Future Work . . . 234

APPENDICES . . . 238
A.1 Introduction . . . 239
A.2 Helmholtz Equation in Isotropic and Homogeneous Media . . 241
A.3 Thermal Radiation from Planar Slabs . . . 243
A.3.1 Telegraphic equation . . . 246
A.3.2 TR using Z-matrix . . . 250
A.3.3 Masloviski's model . . . 253
A.4 Thermal Radiation from Cylindrical Shells . . . 256
A.4.1 Radial transmission line . . . 258
A.4.2 TR from cylindrical shell using circuit model . . . 259
A.5 Thermal Radiation from Semi-Infinite Planar or Cylindrical Emitters with Constant Temperature . . . 261
B.1 Informal introduction . . . 266
B.1.1 Covariant vs contravariant components of a vector . 266
B.1.2 Geometric algebra objects . . . 268
B.2 Tensor calculus convention . . . 271

B.3 Space Transformation 272
B.3.1 Tensors of first order 274
B.3.2 Tensors of second order 276
B.4 Coordinate Transformation of Maxwell's and Fourier's law of Heat Conduction 278
B.4.1 Maxwell's Equations 278
B.4.2 Space Transformation of Fourier's law of heat conduction 280
C.1 Generalized Kirchoff's laws for arbitrary Thermal Emitters . 282
C.2 Proof for the circuit model using Landauer Formalism 285
E.1 Fluctuation Dissipation Theorem 296
E.2 Fluctuation Electrodynamics correlations: Simplified derivation 298

BIBLIOGRAPHY 301

LIST OF FIGURES

Figure

1.1 Schematic for the thermal illusion problem addressed in this thesis. 1

1.2 Illustration of the main concept in electromagnetic invisibility cloaking using meta-materials. A point is expanded and the space is deformed such that the geodesics of propagating field is avoiding the cloaked region. Fig.s are adapted from [120]. 5

1.3 Left: The physical space after the space transformation of Eq.(1.4). Right: the realization of the cloak that is located at $a < \rho' < b$. Figures is adapted from [105] 8

1.4 TO based invisibility cloak had been applied to diffusion as heat or electric conduction. For electric conduction, the conductance of the media can vary in space such that electric current flow around a cloaked region. Left: virtual space. Right: physical space. Fig.s are adapted from [104]. 9

1.5 (a) Mantle cloaks for different geometric configurations: planar , cylindrical and spherical shaped mantle cloaks.(b) Experimental setup of a mantle cloak surrounding a dielectric rod. Figure is adapted from [111]. 10

1.6 Schematic for planar frequency selective surface (FSS) with (a) inductive surface impedance (b) capacitive surface impedance. Adapted from [116]. 11

1.7 Schematic for the typical procedure for scattering illusion using TO approach. First the cylindrical object B (with media ϵ_B and μ_B and radius ρ_B) is transformed to cylindrical object A (with media ϵ_A and μ_A and radius ρ_A), while the vacuum space located at $\rho_B < \rho < \rho_{ex}$ is transformed into cloak $\rho_A < \rho' < \rho_{ex}$. The outer region $\rho > \rho_{ex}$ (typically vacuum) is unity transformed into $\rho' > \rho_{ex}$, so that the electromagnetic field and media parameters are the same for both spaces. 13

1.8 Schematic for the scattering cancellation technique using Mantle cloaks. The object A with permittivity ϵ_A and permeability μ_A (typically non magnetic $\mu_A = \mu_0$) coated with a MS/Mantle cloak such that the scattered field for an incident field is the same as the scattering of another object B with permittivity ϵ_B and permeability μ_B(vacuum in case of invisibility cloaking) under the same incident field. The problem is typically treated as a matching problem between incident cylindrical wave of order n and terminating. In this case, the surface impedance of the MS is the terminating load. Transmission line models are used to model the propagation of cylindrical waves (see appendix A). E_z and H_ϕ are the electric and magnetic fields of E-polarization. . . . 14

1.9 Sketch of the working principle of scattering cancellation technique adapted for illusion purposes using mantle meta-surfaces. Fig. is adapted from ref.[118]. 17

1.10 Schematic for discontinuous transformation optics. Top: virtual space. Middle: physical space under continuous space transformation with the cylindrical shell of the virtual space is compressed into a zero thickness shell(blue ring). Bottom: physical space under discontinuous space transformation where a metasurface is replacing the blue shell (a scissor to symbolize the space discontinuity). 21

1.11 All figures are adapted from [108]. (a) schematic of the space transformation where a horizontal line is expanded into the hidden region. (b) Schematic of the experimental setup including the invisibility cloak, thermal detector and thermal emitting object to be cloaked (the mouse shaped toy). (c) Comparison of the thermal images read by the thermal detector. 29

1.12 (a) A thermal emitter is located $r < a$ exchanging radiative heat with its surroundings located at $r > b$ and an equivalent circuit representing such heat exchange. Figure is adapted from [79].(b) stack of magneto dielectric planar multilayer and the equivalent four-pole network of layer i at thermal equilibrium at temperature $T = T_i$. Figure is adapted from [78]. (c) Thermal noise from N-port network can be used to compute thermal radiation an arbitrary object or a metasurface using their own surface impedance or admittance as it will be shown in chapter V. Figure is adapted from [40]. 32

1.13 Schematic showing the differnec between transformation optics and field transformation. Fig. is adapted from [71] 35

1.14 Schematic for the Duality transformation of Eq.(1.26). 36

2.1 left: Departure (virtual) space where the object to be mimicked $\partial\omega$ resides. b) Arrival (physical) space where the object to be mimic $\partial\Omega$ and the coat (cloak) reside. The function of the cloak is to mimic, in the domain $\bar{E}$, the flux of another predefined object ω given on the left side (departure space). H and L are space transformations from the departure space to the arrival space. 44

2.2 Schematic of the transformations mentioned in Eq.s (2.47and2.48) for an objectω (with blue frontiers) that can be mimicked when the same Ω object (with red frontier) is cloaked. (Left Figure):Only radial transformation with $\mu < 1$. (Middle Figure): Only rotational transformation. (Right Figure): Combination of both radial and rotational transformations. The two conductivities are chosen beforehand (with κ_{rr} to be proportional to κ_ω), which forces the nature of the transformation. The external frontier of the cloak is circular and plotted in black. 54

2.3 Departure (or virtual) space- Three different shapes of the starting object $\partial\omega$ to mimic (from the left to the right): an ellipse, a flower and a butterfly. The color scales are for the conductivity. 59

2.4 Cloak matrix conductivities to mimic the ellipse of Fig.2.3, with parameters $\mu = 1$ (left figure) and $\mu = 3$ (right figure). 60

2.5 Case of the flower, with $\mu = 1$ (left figure) and $\mu = 3$ (right figure). 60

2.6 Case of the butterfly, with $\mu = 1$ (left figure) and $\mu = 3$ (right figure). 60

2.7 Case where $\partial\omega$ is an ellipse. Heat flow patterns are calculated with the conductivity matrices of Fig. 2.4. The top figure is for the scattering pattern of ω , and the bottom figures are for Ω surrounded by its cloak, with $\mu = 1$ (left figure) and $\mu = 3$ (right figure). All patterns are identical beyond the circular cloak ∂E. 64

2.8 Case where $\partial\omega$ is a flower. Heat flow patterns are calculated with the conductivity matrices of 2.5. The top figure is for the scattering pattern of ω , and the bottom figures are for Ω surrounded by its cloak, with $\mu = 1$ (left figure) and $\mu = 3$ (right figure). All patterns are identical beyond the circular cloak ∂E. 65

2.9 Case where $\partial\omega$ is a butterfly. Heat flow patterns are calculated with the conductivity matrices of Fig.2.6. The top figure is for the scattering pattern of ω , and the bottom figures are for Ω surrounded by its cloak, with $\mu = 1$ (left figure) and $\mu = 3$ (right figure). All patterns are identical beyond the circular cloak ∂E. 65

2.10 Flux pattern calculated for the horizontal ellipse of Fig.2.7 after 90° rotation (right figure) completed by reduction (left figure). All fluxes are identical beyond the circular cloak. 66

2.11 Flux pattern calculated for the flower of Fig.2.8 after 90° rotation (left figure) completed by reduction (right figure). All fluxes are identical beyond the circular cloak. 66

2.12 Flux pattern calculated for the butterfly of 2.9 after 90° rotation (left figure) completed by reduction (right figure). All fluxes are identical beyond the circular cloak. 66

2.13 Conductivity matrix of the flower in the case of 90° rotation with no scaling. 67

2.14 Legend analogous to Fig.2.7 , but for the dynamic regime. 69

2.15 Legend analogous to Fig.2.8, but for the dynamic regime. 69

2.16 Legend analogous to Fig.2.9, but for the dynamic regime. 70

2.17 Legend analogous to Fig.2.10, but for the dynamic regime. The left figure is for rotation, and the right figure is for rotation and scaling. 70

2.18 Legend analogous to Fig.2.11, but for the dynamic regime. The left figure is for rotation, and the right figure is for rotation and scaling. 70

3.1 schematic of the TR illusion example discussed in section (3.5). The middle figure is for the E/H physical space (departure space) with a homogeneous anisotropic lossy circular object with radiusr_0 [$\varepsilon_{obj}^{mn} = \delta^{mn}(3+i0.02)$ and $\mu_{obj}^{mn} = \delta^{mn}(1+i0.02\delta^{mz})$] coated with an inhomogeneous anisotropic circular coat with radius r_{ex}. The left figure is for the E-polarization virtual space with inhomogeneous anisotropic horizontal elliptical shaped object with semi-axes a and b embedded in a homogeneous medium. The right figure is similar but for a vertical ellipse and for H-polarization. The region outside r_{ex} is unity transformed for both polarizations. The areas of all spaces between the dotted external cylinder and the virtual or physical objects, are lossless and do not contribute to the thermal radiation. For numerical calculations, L was set to be 11.1λ with matched boundary conditions at the square frames. 85

3.2 Numerical calculation of normalized time averaged radiated poynting vector (log scale) at the virtual and physical spaces of E- and H-polarization as depicted in Fig.3.1, (a) H-polarization physical (left) and virtual (right) (b) E-polarization physical (left) and virtual (right). Colored surfaces, red arrows and white contours indicate the modulus (log scale), direction and isolines of the poynting vector respectively. The left figures consider the circular radiating cylinder given in the middle part of Fig. 3.2. These left figures give the TR pattern of the cylinder coated to mimic the TR patterns of vertical (Fig. 3.2(a)) and horizontal (Fig. 3.2(b)) ellipses for E-and H- polarizations. The right figures consider the vertical and horizontal coated ellipses of 3.1. These right figures give the TR pattern of the ellipses for each polarization and these patterns must be compared to those of the left figures. Normalization constants are: for H-polarization, $< S >_0 = 5.7 \times 10^{-33} \frac{W}{m^2}$, while for E-polarization, $< S >_0 \; 10^{-28} \frac{W}{m^2}$. We notice that the emitted power has the same distribution outside the transformation regions for both polarizations at the physical and virtual spaces. 87

4.1 Representation of Z-matrix in the Fourier space for a homogeneous (planar or cylindrical) MS. 96

4.2 Series connected impedance Z_s causing an electric field discontinuity while the magnetic field is continuous. 104

4.3 Parallel connected Admittance Y_p causing a magnetic field discontinuity while the electric field is continuous. 105

4.4 T-Network with arbitrary impedances $\{Z_{s,1}, Z_{s,2}, \frac{1}{Y_p}\}$ causing simultaneous electric and magnetic discontinuities. 105

4.5 Schematic showing the equivalence between a discontinuous 1D space with lumped TO based MS, where a region in the 1D transmission line with length Δy is compressed to be a point or a lumped network of the MS. Up: Continuous 1D virtual space. Middle: Intermediate space. Bottom: The physical space including the metasurface. . . . 108

4.6 Schematic for the discontinuous transformation of Eq.(4.27) where two regions of the virtual space y are transformed differently, while the region of length Δy is compressed into a point $y' = 0$ in the physical space. In this graph the transformation is plotted for $y' = (y - \Delta y)^2$ for $y \geq \Delta y$ and $\Delta y = 5$. 109

4.7 Z-matrix relating the electric and magnetic fields of the terminals of a transmission line of length Δy. 110

4.8 Numerical simulation setup for examining the concept of compressing a region of space into a lumped meta surface. A plane wave is incident from the right into a parallel plate wave guide with PMC walls (to guarantee planar wave front). In the virtual space, the wave-guide has three sections and it is terminated by a matched boundary condition. It is required to compress the middle section (between planes A and B) into a lumped meta-surface in the physical space. Up: Virtual space. Bottom: Physical space. 112

4.9 Up: Virtual space Electric field and its phase plots. Middle: Intermediate Electric field and its phase plots (the space is still the same as the virtual space but with replacing the $A - B$ space region with its equivalent circuit for a normal incident plane wave). Down:Physical space-(including the MS) Electric field and its phase plots. 114

4.10 Two consecutive connected dual networks are equivalent to a short circuit. 115

4.11 Schematic for the discontinuous transformation of Eq.(4.33) where two regions of the virtual space y are transformed differently and the point $y = 0$ is expanded into the region $0 \leq y' \leq \Delta y$ in the physical space. In this graph the transformation is plotted for $y' = y + \Delta y$ for $y \geq 0$ and $\Delta y = 5$. 115

4.12 Numerical simulation Setup for examining the concept of 1D Expansion or replacing a plane/point by two dual media or a space region and dual meta-surface. A plane wave is incident from the right into a parallel plate wave guide with PMC walls (to guarantee planar wave front). The wave-guide has four sections and it is terminated by a matched boundary condition. It is required to compress the third section (between planes C and B) to a meta-surface.Up: Virtual space. Middle: Intermediate space. Bottom: Physical space. 117

4.13 Up: Plot of the amplitude and phase of the Electric field propagating in an intermediate space including two dual media of the same thickness. Middle: Plot of the amplitude and phase of the Electric field propagating in the same intermediate space but with replacing the media with negative permittivity and permeability space region with its equivalent circuit for a normal incident plane wave). Down: Plot of the amplitude and phase of the Electric field propagating in the physical space including the MS. 118

4.14 Schematic of the discontinuous radial transformation where the cylindrical shell located at $\rho_1 < \rho < \rho_2$ ($\Delta\rho = \rho_2 - \rho_1$) in the virtual space is compressed into a cylindrical MS at $\rho' = \rho_2$ in the physical space. Note that A is transformed into A' and B is unity transformed into B' ($B = B'$). 120

4.15 A simulation setup : left: Virtual space. Right: Physical space. A Surface electric current $J_s = e^{in\phi}$ is flowing on the surface of a cylindrical perfect magnetic conductor with radius ρ_0. The emitted radiation is of the same order n. The space is transformed such that the annulus shell $\rho_1 < \rho < \rho_2$ is compressed into a cylindrical boundary $\rho' = \rho_2$. 124

4.16 Plot of the radiated electric field E_z from electric surface current $J_s = e^{in\phi}$ with $n = 1$. Left: full virtual space, Middle: discontinuous virtual space, Right:physical space. 125

4.17 Plot of the radiated electric field E_z from electric surface current $J_s = e^{in\phi}$ with $n = 2$. Left: full virtual space, Middle: discontinuous virtual space, Right: physical space. 125

4.18 Plot of the radiated electric field E_z from electric surface current $J_s = e^{in\phi}$ with $n = 10$. left: full virtual space, middle: discontinuous virtual space, right:physical space. 126

4.19 Simulation setup (2) : left: Virtual space. Right: Physical space. A plane wave is propagating in y direction in a PMC parallel plate wave guide. The space is transformed according to Eq.(4.47) such that the annulus ring $\rho_1 < \rho < \rho_2$ is compressed into a MS located at $\rho' = \rho_2$ in the physical space. The MS is designed to be spatial dispersive (non local) with respect to ϕ (see Fig.(4.15)). 127

4.20 Simulation results of the simulation setup shown in Fig.(4.19). Figs.(a-e) show the electric field distribution in the physical space for $N = \{0, 5, 10, 15, 20\}$. Fig.(f) is the virtual space with a propagating plane wave. 128

4.21 Comparison between the electric field E_z distribution. (a) Non-local MS with $N = 50$. (b) Homogeneous virtual space. 128

4.22 Comparison of the performance of the local and spatial Metasurfaces when compared with the virtual space for different wave lengths $\{1mm, 10\mu m$ and$10\mu m$ $\}$and $\Delta\rho = \rho_2 - \rho_1$. left: Local MS. Middle: Virtual space. Right: Non local MS. 130

4.23 Schematic of the discontinuous radial space transformation shown in Eq.(4.46) where the cylindrical boundary $\rho < \rho_2$ in the virtual space is expanded into the cylindrical shell $\rho_1 < \rho' < \rho_2$ cascaded with a dual cylindrical Meta-surface at in the physical space 131

4.24 A simulation setup : left: Virtual space. Right: Physical space. A Surface electric current $J_s = e^{in\phi}$ is flowing on the surface of a cylindrical perfect magnetic conductor with radius ρ_0. The emitted radiation is of the same order n. The space is transformed such that the cylindrical boundary $\rho = \rho_2$ is replaced by an annulus shell $\rho_1 < \rho' < \rho_2$ and consequent dual MS located at $\rho' = \rho_2$ in the physical space. 132

4.25 Plot of the radiated electric field E_z from electric surface current $J_s = e^{in\phi}$ with $n = 0$. left: full virtual space, right:physical space. . . 133

4.26 Plot of the radiated electric field E_z from electric surface current $J_s = e^{in\phi}$ with $n = 2$. left: full virtual space, right:physical space. . . 134

4.27 Plot of the radiated electric field E_z from electric surface current $J_s = e^{in\phi}$ with $n = 10$. left: full virtual space, right:physical space. . 134

4.28 Simulation setup (2) : left: Virtual space. Right: Physical space. A plane wave is propagating in y direction in a PMC parallel plate wave guide. The space is transformed according to Eq.(4.45) such that the cylindrical region $\rho \leq \rho_2$ in the virtual space is compressed into the cylindrical region $\rho' \leq \rho_1$ while the region $\rho \geq \rho_2$ is unity transformed into $\rho' \geq \rho_2$. The boundary $\rho = \rho_2$ is expanded into a cylindrical shell (chosen to be vacuum) surrounded by a cylindrical dual MS located $\rho' = \rho_2$. The MS is designed to be spatial dispersive (non local) and homogenous. 135

4.29 Comparison of the performance of the local and spatial Metasurfaces when compared with the virtual space for wave length $100\mu m$. left: Local MS. Middle: Virtual space. Right: Non local MS. 136

4.30 Comparison of the performance of the local and spatial Metasurfaces when compared with the virtual space for wave length $10\mu m$. left: Local MS. Middle: Virtual space. Right: Non local MS. 136

4.31 Schematic of the discontinuous radial transformation where the blue coloured shell located at $\sigma(\phi) < \rho < \rho_s$ in the virtual space in Fig.(a) is compressed into the red coloured cylindrical shaped MS located at $\rho' = \rho_s$ in the physical space in Fig.(b). Note that A is transformed into A' and B is unity transformed into B' ($B = B'$). 138

4.32 Schematic of a simulation setup: left: Virtual space filled with vacuum. Right: Physical space. In the vacuum filled virtual space, an incident cylindrical wave of order n is reflected so the distribution of the electric field $\tilde{E}_z[n] = A_n J_n(k\rho)e^{in\phi}$ where J_n is Bessel function of 1st type and order n. The virtual space is transformed into the physical space through Eq.(4.59)such that the non-cylindrical shell $\sigma(\phi) < \rho < \rho_s$ is compressed into a MS located at $\rho' = \rho_s$ in the physical space. Note the electric field E_z is transformed as a scalar quantity and is expected to be unity transformed for the regions $\rho' > \rho_s$ and $\rho' > \rho_s$. 145

4.33 Plot of the electric field E_z with $n = 0$. (a) full virtual space, (b) physical space. The electric field at $\rho = \rho' > \rho_s$ is a standing cylindrical wave of order $n = 0$ with the following form $E_z = A_0 J_0(k\rho)e^{i\phi}$ where A_0 is a constant. 146

4.34 Plot of the electric fields E_z of virtual space for $\rho < \sigma(\phi)$ and E'_z of physical space for $\rho' < \rho_s$ with $n = 0$. (a) virtual space, (b) physical space. It is clear the $E_z(\rho) = E'_z(\rho')$. 146

4.35 Plot of the electric field E_z with $n = 1$. (a) full virtual space, (b) physical space. The electric field at $\rho = \rho' > \rho_s$ is a standing cylindrical wave of order $n = 1$ with the following form $E_z = A_1 J_1(k\rho)e^{i\phi}$ where A_1 is a constant. 147

4.36 Plot of the electric field E_z with $n = 10$. (a) full virtual space, (b) physical space.The electric field at $\rho = \rho' > \rho_s$ is a standing cylindrical wave of order $n = 10$ with the following form $E_z = A_{10} J_{10}(k\rho)e^{i10\phi}$ where A_{10} is a constant. 148

4.37 Simulation setup (2) : left: Virtual space. Right: Physical space. A plane wave is propagating in y direction in a PMC parallel plate wave guide. The space is transformed according to Eq.(4.59) such that the non-cylindrical ring $\sigma(\phi) < \rho < \rho_s$ is compressed into a MS located at $\rho' = \rho_s$ in the physical space. The MS is designed to be spatial dispersive (non local) and in-homogenous with respect to ϕ (see Fig.(4.15)). 148

4.38 with non-local and in-homogeneous MS with $N = 50$ cylindrical orders. simulation is done at wavelength $\lambda = 100\mu m$. 149

4.39 Schematic of the discontinuous radial space transformation of Eq.(4.60), where the cylindrical boundary $\rho < \rho_s$ in the virtual space of Fig.(a) is expanded into a blue coloured non-cylindrical shell $\sigma(\phi) < \rho' < \rho_s$ cascaded with a red coloured dual cylindrical Meta-surface at in the physical space of Fig.(b). Note that the cylindrical region A in the virtual is transformed into A' of the outer surface $\sigma(\phi)$ in the physical space, while the outer region is unity transformed $B' = B$. 150

4.40 Plot of the electric field E_z with $n = 0$. (a) full virtual space, (b) physical space. The electric field at $\rho = \rho' > \rho_s$ is a standing cylindrical wave of order $n = 0$ with the following form $E_z = A_0 J_0(k\rho)e^{i\phi}$ where A_0 is a constant. 152

4.41 Plot of the electric fields E_z of virtual space for $\rho < \rho_s$ and E'_z of physical space for $\rho' < \sigma(\phi)$ with $n = 0$. (a) virtual space, (b) physical space. It is clear the $E_z(\rho) = E'_z(\rho')$. 153

4.42 Simulation setup (2) : left: Virtual space. Right: Physical space. A plane wave is propagating in y direction in a PMC parallel plate wave guide. The space is transformed according to Eq.(4.60) such that the cylindrical boundary $\rho = \rho_s$in the virtual space is expanded into the non-cylindrical shell $\sigma(\phi) \leq \rho' \leq \rho_s$ cascaded with the dual MS, while the region $\rho \geq \rho_s$ is unity transformed into $\rho' \geq \rho_s$. The dual MS is designed to be both spatial dispersive (non local) and in-homogenous. 154

4.43 Comparison of the performance of the local and spatial dispersive dual Metasurfaces for wave length $1mm$. (a) Local MS. (b) Non local MS. 155

4.44 Comparison of the performance of the local and spatial dispersive dual Metasurfaces for wave length $100\mu m$. (a) Local MS. (b) Non local MS. 155

5.1 Schematic of discontinuous space transformation where a mantle cloak is designed to coat an isolated cloaked region so as to thermally radiate and scatter the electromagnetic field as another target object. (a) Target object. (b) After application of discontinuous TO (chapter(3)). (c) An isolated cloaked region is introduced. A target thermal emitter (red) and surrounding vacuum (white) are compressed into an equivalent surface (red) for E-polarization case. The origin is expanded into a finite cylindrical region occupied with perfect magnetic conductor media. Finally a cavity can be introduced inside the the PMC which can include an arbitrary object to be cloaked. . . . 159

5.2 Illustration of the effect of translation symmetry upon the surface impedance representation of semi-infinite scatterer. (a) Tangential wave number k_x is conserved under Fresnel's reflection from planar slab and the reflection from such planar surface can be modelled as reflection of an incident plane wave from a surface impedance which is homogeneous but spatial frequency dispersive. (b) The scattering of an incident plane wave by a non-planar profile can be modelled as the reflection by a $N-$ port network quantified by the surface admittance which will be spatial frequency dispersive and in-homogeneous. . . . 168

5.3 Illustration of the effect of circular symmetry upon the surface impedance representation of a bounded scatterer. (a) cylindrical order n is conserved when an incident cylindrical wave is scattered by a circular symmetric scatterer and the scatterer is represented by a surface impedance which is homogeneous but spatial frequency dispersive $\tilde{Y}_s[n]$. (b) The scattering of an incident cylindrical wave by a non-circular shaped profile can be modelled as the reflection from a $N-$port network quantified by the surface admittance which will be spatial frequency dispersive and in-homogeneous $\tilde{\tilde{Y}}_s[n, n-m]$. Note that the quantities $\tilde{Y}_s[n]$ and $\tilde{\tilde{Y}}_s[n, n-m]$ are defined in section(5.3.2). . 169

5.4 The 2D Fourier transform of the surface admittance is represented as an admittance matrix such that at each port of order n.. 175

5.5 Schematic for the proof of Eq.(5.18). Two reciprocal situations are considered. Case(A): a point current sources is located on the surface at point a with polar coordinates (ρ_s, ϕ_a). Case(B): a point current sources is located on the surface at point b with polar coordinates (ρ_s, ϕ_b). For both cases, The reactions $< a, b >$ and $< b, a >$ are calculated. If the surface is Lorentz reciprocal then the reaction is reciprocal or $< a, b >=< b, a >$. 178

5.6 Two equivalent circuit models for thermally radiated n^{th} order cylindrical wave from lossy homogeneous equivalent surface, (a) Thevinin representation (b) Norton representation. The thermal noise sources are represented as voltage (current) sources connected in series (parallel) to the losses represented as series impedance (parallel admittance) at Thevenin (Norton) equivalent circuits respectively. 183

5.7 Thermal discrete dipole approximation (TDDA) simulation setup: the thermal emitter is meshed and the thermal electric current density is discretized and thermal radiated Poynting vector is calculated according to the procedure used in appendix D. Note that for the E polarization, since permeability is real, and the permittivity is complex, only a thermal electric current exist. 189

5.8 Equivalent thermal surface current (semi-analytical) simulation setup. The thermal electric current density is replaced by an equivalent surface thermal electric current flowing on the surface of the thermal emitter. Note that only the permittivity is complex, then only thermal electric surface current exist. 190

5.9 Left: schematic of the circuit model of the thermal radiation for cylindrical order n. The radiated Power per unit angle is calculated from the circuit as following: $\mathrm{Re}\{< \mathbb{P}_{nn} >_\omega\} = 4 \times \frac{1}{2} < \tilde{V}^+[n]\tilde{I}^{+*}[n] >$. Right: circuit model simulation setup with the equivalent surface admittance of the thermal emitter is used to calculate the thermal radiated poynting vector. 192

5.10 Plot of the thermal radiated Poynting vector multiplied by $2\pi\rho_s$ due to the following simulation setups: (a)The thermal discrete dipole approximation (TDDA) of Fig.(5.7) (b) Equivalent thermal surface current (semi-analytical Calculation) of Fig.(5.8) (c)Theoretical calculation of Fig.(5.9) using Eq.(5.58). 192

5.11 The circuit configuration as Fig.(5.4) but with the associated thermal sources represented as Nyquist voltage sources $\tilde{e}_n$. 195

5.12 Schematic for the numerical example used to validate the proposed circuit model. The thermal emitter consists of a cylindrical dielectric with permittivity $\epsilon = 3 - i0.02$ with an elliptic shaped PMC (infinite permeability). Due to the broken circular symmetry, thermally radiated power is expected to have a pattern which is not circularly symmetric. 200

5.13 Thermal discrete dipole approximation (TDDA) simulation setup . 200

5.14 Plot of the real power radiated $2\pi\,\mathrm{Re}\{< \mathbb{P}(\rho_s, \phi) >_\omega\}$ computed at $\rho = \rho_s$. Blue line is for The thermal discrete dipole approximation (TDDA) of Fig.(5.13), while the red line is for the theoretical calculation of the poynting vector is calculated using Eq.(5.76). 201

5.15 Plot of the normalized thermal radiated Poynting vector to due to the following simulation setups: (a) The thermal discrete dipole approximation (TDDA) of Fig.(5.13). (b) Theoretical calculation. The poynting vector is calculated using Eq.(5.76). 202

6.1 schematic of the TR illusion. 218

6.2 Thermally radiated poynting vector in both physical and virtual spaces. (a) Physical space. (b) virtual space. Simulation is done at $\lambda = 5\mu m$, $\rho_{ex} = 60\mu m$ and $\rho_0 = 30\mu m$ 220

6.3 Schematic of invisibility cloaking using metasurface based on discontinuous FT. (a) Virtual space of vacuum. (b) Physical space including discontinuous FT based metasurfaces. Simulation is done with the following parameters: $\rho_s = 50\mu m$, wavelength is $100\mu m$, $\epsilon_d = \epsilon_0$, $\mu_d = \mu_0$ and $A = 2$ 225

6.4 Schematic of scattering illusion cloaking using metasurface based on discontinuous FT. (a) Virtual space of vacuum. (b) Physical space including discontinuous FT based metasurfaces. Simulation is done with the following parameters: $\rho_s = 50\mu m$, wavelength is $100\mu m$,$\epsilon_d = 10\epsilon_0$, $\mu_d = 2\mu_0$, $A = 2$ 226

6.5 Comparison of invisibility cloaking using continuous FT based cloaks and discontinuous FT based metasurfaces. A plane wave is incident from the left side.(a) Virtual space of vacuum. (b) Physical space including continuous FT based cloak. (c) Physical space including discontinuous FT based metasurfaces. Simulation is done with the following parameters: $\rho_0 = 30\mu m$, $\rho_{ex} = 60\mu m$ and wavelength is $100\mu m$. 227

6.6 Plot of the magneto-electric coupling coefficient k_{zx} of the cloak due to continuous FT transformation. 227

6.7 Schematic for thermal emitters in both spaces without metasurfaces and their equivalent surface impedance representation. (a)Virtual thermal emitter. (b) Physical space thermal emitter. 229

6.8 A Metasurface based on discontinuous FT can be modelled as a lossless electric transformer with turns ratio $A : 1$. The imput impedance of the metasurface with the emitter in the physical space has the same surface impedance as the emitter in the virtual space. 230

6.9 Circuit models of the thermal radiation the physical and virtual spaces. (a) Physical space circuitry where the thermal emitter is represented by surface impedance $Z_s'[n]$ and thermal noise is represented by voltage source $V_s'[n]$ connected with the transformer that represent the cloaking metasurface. (b)Virtual space circuitry where the thermal emitter is represented by surface impedance $Z_s[n]$ and thermal noise is represented by voltage source $V_s[n]$. 232

A.1 In this appendix, thermal radiation from (a)stack of planar slabs aligned along x-axis and (b) cascaded cylindrical shells. 240

A.2 Distributed parameter model of a transmission line. 247

A.3 T-Network representation for the $Z-$matrix of a planar slab. 251

A.4 Two equivalent T-networks with the impedances are associated with Nyquist noise sources represented as voltage (current) sources connected in series (parallel) to the losses represented as series impedance (parallel admittance) respectively. (a) The parallel branch is associated with $\tilde{V}_p$ (b) The parallel branch is associated with $\tilde{I}_p$. 252

A.5 The equivalent circuit model as proposed by Masloviski et al. A planar slab is represented as a network which is quantified by Z-matrix. The sources of the thermal noise are represented by the voltage sources $\tilde{e}_1$ and $\tilde{e}_2$ which spectral correlations are depicted in Eq.s (A.43). 255

A.6 Schematic shows the steps for deriving the spectral correlations of Eq.s (A.43) from the T-Network shown in Fig.(A.4) 256

A.7 Schematic of the T-circuit model for a thermally radiated mode(q) from a semi-infinite planar emitter located at $x \leq x_S$ or a cylindrical emitter located at $0 \leq \rho \leq \rho_S$. Terminal 1 is an open circuit. Then the equivalent circuit model is reduced to a surface impedance $\tilde{Z}_S(q) = \tilde{Z}_{22}$ with the Nyquist voltage connected in series. 263

A.8 Schematic of the circuit model for thermal radiation of the mode ($\bar{q}$) into vacuum from either a semi-infinite planar emitter located at $x < 0$ or from a cylindrical emitter located at $\rho < \rho_s$. The equivalent impedance of the mode from emitter side is $\tilde{Z}(q) = \tilde{R}(q) + j\tilde{X}(q)$ and the input impedance from the vacuum side is $\tilde{Z}_0(q)$. This circuit model is applied to both E and H polarizations using the appropriate corresponding impedance 264

B.1 A position vector $\bar{r}$ has its components described in: (a) Cartesian coordinates. (b)(u, v) coordinate system using contravariant components. (c) (u, v) coordinate system using covariant components. . . 267

C.1 schematic of the scattering matrix matrix $\underline{\underline{S}}$ 283

LIST OF APPENDICES

Appendix

A. Circuit Model for Thermal Radiation 239

B. Transformation Optics Theory 265

C. Kirchoff's Reciprocity and Circuit Model's Proof 282

D. Thermal Radiation Calculation using TDDA 290

E. Fluctuation dissipation theorem 296

LIST OF ABBREVIATIONS

- TR: Thermal radiation.
- MS: Meta-surface.
- TO: Transformation Optics.
- FE: Fluctuation electrodynamics.
- FDT: Fluctuation Dissipation Theorem.
- DT: Duality transformation.
- FT: Field transformation
- GSTC: Generalized Sheet Transverse Conditions.
- 1D: One dimensional.
- 2D: Two dimensional.
- 3D: Three dimensional.
- TE_z: Transverse Electric to z-axis.
- TM_z: Transverse Electric to z-axis.
- PMC: Perfect Magnetic Conductor.
- PEC: Perfect Electric Conductor.
- TL: Transmission Line

PREFACE

Electromagnetic illusions had been either a topic of science fiction authors or stealth technologists and engineers. For stealth technology, engineers design planes and tanks structures to minimize the scattering and thermal radiation signatures making them hard to be detected and located by counter forces. Similarly, camouflage coats had been designed to make soldiers hard to be spotted, these camouflage techniques already use the same methodologies used by animals and insects where they manipulate the colour of their skin to match the surrounding environment to minimize the contrast making them undetectable by other competitive species. However such state of art hasn't been formally investigated by physicists until the year 2000, when the start of the invisibility and illusion science emerged, starting with the seminal theoretical work of sir. J.Pendry and independently U. Leonhardt. Both showed the possibility of invisibility using transformation optics theory as the appropriate theoretical tool to address electromagnetic scattering and consequently invisibility and illusions. Transformation optics is a collection of mathematical tools that are based on both differential geometry and tensor calculus that can be applied to nearly any physical problem associated with well defined space. Its main idea is that media act as effective geometries for the propagating fields. Since then, tremendous amount of theoretical and experimental research investigated different possibilities of making an object invisible for detection. Such research work was accelerated by the parallel vast development in meta-materials and nano-photonics technologies in both design, fabrication and testing. For each domain of physics, theorists could formulate theoretical

framework to describe scattering and found the necessary conditions to achieve both invisibility and scattering illusion where an object is invisible or is detected as another object of different shape and properties. Experimental research work followed to implement such theoretical techniques. The combination of both theoretical and experiment work led to the emergence of a new branch of science named as the science of invisibility. Similar to electromagnetic scattering, thermal radiation from an object exposes the object to be detected. Actually little attention had been focused on implementing techniques to achieve thermal radiation illusion, where an object is unseen or detected as another object by thermal detectors. Accordingly, the aim of this thesis is to fill such gap in the literature by investigating thermal radiation illusion problem and propose techniques to achieve such aim.

During this Ph.D. thesis, the main focus is to borrow the well established techniques in the realm of electromagnetic invisibility and scattering illusions to be applied analogously upon thermal radiation illusion problem. The primary goal is to provide a working design procedures to design cloaks in order to achieve scattering and thermal radiation camouflage. In parallel to the already existing techniques for designing scattering illusion cloaks where the coated object has the same scattering signature as another target object, we propose both electromagnetic scattering and thermal illusion cloaks such that the coated object both thermally radiates and scatters an arbitrary incident electromagnetic field in the same way as the target so that an arbitrary electromagnetic detector cannot differentiate between both objects. Actually, from a physical point of view, electromagnetic scattering and thermal radiation are closely related physical phenomena, however, in the same time, they are driven by different mechanisms. Electromagnetic scattering originates from a discontinuity between the wave impedance of the surrounding media and that of the scatterer as "seen" by the incident field. Electromagnetic scattered field from a specific scat-

terer is typically related to the incident field by a scattering matrix or operator. On the other hand, thermal radiation is an implicit property of a thermal emitter which is independent of the surrounding environment. Actually thermal radiation is the electromagnetic radiation due to thermally fluctuating electric and magnetic current densities embedded in the bulk of the thermal emitter. These thermal sources are related to the losses of the thermal emitter through Kirchoff's reciprocity which equates the absorptivity of an object to its emissivity at thermal equilibrium. Both the absorptivity and the emissivity are closely related to the scattering matrix of the object. Fluctuation electrodynamics is the electromagnetic theoretical framework that allows the computation of the thermal radiation due to such thermal sources. Thermal radiation has two main measurable quantities, the thermal radiated power and the radiation pattern which is the distribution of the thermally radiated power in space. Both quantities at specific wavelength depend on its absolute temperature, the constitutive material and the outer surface shape of the thermal emitter. Then, in order to achieve thermal radiation illusion, a designer must take into account both the temperature and the distributions of the losses of the object to be cloaked. In this research work, different techniques, including transformation optics are involved in order to achieve thermal radiation illusion of thermal emitters under thermal equilibrium while keeping fluctuation electrodynamics as the theoretical framework.

Transformation optics theory provides exact solutions for the scattering illusion and invisibility problems. The main theme is that the object to be cloaked can be space transformed to the target object. However the physical parameters of the objects to be cloaked or to mimicked are constrained by the space transformation. This constraint reduces the field of practical applications so one do not really choose what to be hidden or camouflaged. In practice, one would be interested in working with predefined objects of given constitutive parameters, and these objects would be over-

coated to mimic other predefined objects beyond the cloak. Such an inverse engineering problem introduces constraints that restrict the range of space transformations, thereby classifying the set of objects that can be mimicked with another one which is beforehand chosen and must be over-coated. In order to analyze the implications of such conditions, we study the inter-relation between shapes and media of the object pre- and post-transformation with in the heat conduction physics in both transient and steady state regimes. The same conclusions can be drawn to electromagnetic propagation in two dimensional space due to the similarity between the governing equations of both physics. On the other hand concerning electromagnetic field upon applying space transformation, it is possible to decouple the interdependence between the shape and media utilizing further transformation. Duality transformation allows transformation between different objects with the same shapes but with different media. Duality transformation is a transformation in the field space which is spanned by the electric and magnetic fields. The main theme of duality transformations, is that field polarizations (i.e: E and H-polarizations) can be coupled and new polarizations can be emerged in the physical space. As a consequence a virtual space of dielectric media can be transformed into a physical space including chiral (also called bi-anisotropic) media which could be nonreciprocal as well. Duality transformation provides extra degrees of freedom that can relax the constraints imposed by transformation optics. We propose the usage of duality transformation to design coats to achieve thermal illusion.

Another concern about the cloaks based on transformation optics is that they are bulky, highly inhomogeneous and anisotropic. On the other hand, scattering cancellation, which is an alternative cloaking technique, proposes replacing the bulky cloaks by sub wavelength thick surfaces named mantle metasurfaces or mantle cloaks. The electromagnetic properties of such metasurfaces can be quantified using two equiva-

lent descriptions, generalized sheet transverse condition (GSTC) and the impedance matrix network representation. In both descriptions a metasurface is represented as a linear operator which connects the electric and magnetic fields at its sides. The main theme of scattering cancellation is to design the surface impedance of the metasurface such that the cloaked object, in combination with the cloaking mantle metasurface, have the same surface impedance as the target object. Scattering cancellation is a technique which independent of transformation optics and doesn't include space transformations. However, we explore such concept and it will be shown that a meta-surface is a discontinuity (a jump) in the electromagnetic space (also commonly named virtual space). In other words, a zero thickness meta-surface with arbitrary susceptibility tensors, located in a physical space is equivalent to a discontinuity in the corresponding virtual space. The discontinuity can either occur in the spatial electromagnetic space which is described in the context of space transformation, or it can occur in the fields' polarization space which is described in the context of duality transformation. Actually based on the former point of view, we propose a new technique to design mantle cloaks based on both transformation optics and duality transformation such that these cloaks can replace both the transformation optics classical cloaks and the scattering cancellation based cloaks.

As a summary, this thesis is arranged as following:

Chapter I provides some background information on the field electromagnetic invisibility and scattering illusion. The basic physics of thermal radiation is summarized focusing on fluctuation electrodynamics theorem. Further, this chapter provides an overview on the state of art concerning different topics of research: scattering illusion, invisibility cloaking, near field thermal radiation and metasurfaces.

Chapter II focuses on applying transformation optics theory upon heat conduction. The framework is Fourier's laws of heat conduction. The aim is to study the interrelation between the shapes and media upon space transformation, focusing on objects which are composed of isotropic and homogeneous media. The main parameters to control are the thermal conductivity and heat capacitance. This chapter is outlined as following: first, the inverse transformation scheme is explained and the constraints on the thermal parameters of the objects to mimic and cloak. Then, we show how to design the illusion coat, in both static and dynamic regimes. In the static case only the frontiers and thermal conductivity are the effective parameters, while in the case of dynamic regime, the same conditions on the thermal conductivity have to be satisfied beside extra conditions on heat capacity. Numerical simulations are reported and they are in accordance with the theory presented in this chapter.

Chapter III explores the application of transformation optics theory upon fluctuation electrodynamics. The purpose is to show that thermal radiation illusion can be achieved using cloaks designed by transformation optics theory. In this chapter, we show that fluctuation electrodynamics is covariant under space transformations depicted by transformation optics theory, so that the same fluctuation dissipation theorem is recovered in the physical space after space transformation. By applying transformation optics, thermal current sources are transformed in the same manner as coherent sources according to source transformation, and these transformed sources are then compared to those which are proportional to dissipative losses in the physical space according to fluctuation dissipation theorem. Hence, both ways of transforming the thermal currents are shown to be consistent and the only constraint is the validity of fluctuation dissipation theorem in both spaces. Thermal illusion is explored using the proposed theory by considering designing a cloak for an object so the thermal radiation of the composite object is the same as thermal signature of another object.

Such example is chosen to be performed in two-dimensional (2D) space where the electromagnetic radiation is the combination of transverse electric (E-polarization) and transverse magnetic (H-polarization) polarizations. Numerical calculations are done with thermal discrete dipole approximation (TDDA) and results in accordance with the proposed theory.

In chapter IV, we propose a novel procedure to design meta-surfaces that can replace the cloaks designed by either transformation optics or scattering cancellation techniques. Actually, the proposed procedure combines both transformation optics and scattering cancellation techniques. First the correspondence between the impedance matrix elements and the susceptibility surface tensors is formulated for planar and circular (cylindrical) shaped metasurfaces. Later, we show the equivalence between a thin meta-surface separating two regions and a discontinuous space transformation that yields at the boundary between two space regions which were transformed differently. It will be shown that the former point of view can be applied to scattering camouflage where a transformation optics based mantle cloak is designed to replace the classic typical bulky transformation optics cloak of chapter III. Two types of discontinuous space transformations are explored, one where a region of the electromagnetic space is compressed into a lumped metasurface. The second type of space discontinuity is that two regions are transformed differently, with the boundary is extended to be non zero volume region. Such volume can be filled by two dual media or a media with a consequent dual metasurface. For both types of space discontinuities, the corresponding metasurfaces are represented by an equivalent circuit model which is based on the modal transmission line model for planar slabs and cylindrical shells explained in appendix (A). Results of numerical simulations are shown to be consistent with the theoretical models shown in this chapter.

In chapter V, we consider the case where an arbitrary shaped thermal emitter is compressed into a meta-surface characterized by its surface impedance or admittance. It will be shown that both the compressed metasurface and the original thermal emitter has the same thermal radiation signature. First thermal radiation from arbitrary shaped thermal emitter is analyzed in terms of cylindrical waves. The role of the cross terms of cylindrical waves of different orders in the calculation of the radiated power is highlighted. Then the notion of surface impedance (admittance) is revised focusing on the general case where the surface impedance (admittance) is non-local and in-homogeneous. It will be shown that an arbitrary surface admittance can be represented as an admittance matrix representing a network coupling different cylindrical orders. Also, in order to compute the thermal radiation signature from an arbitrary shaped thermal emitter whose equivalent surface impedance (admittance) is, in general, in-homogeneous and spatial cylindrical order dispersive, we propose a circuit model such that the metasurface is represented as a linear electrical network with the thermal radiation is the generated thermal noise which is computed according to Nyquist's theorem of noise in electrical resistors. Finally, numerical calculation according to the proposed model is compared with the numerical calculations due to thermal discrete dipole approximation (TDDA).

In Chapter VI, we investigate a further extension of the techniques proposed in chapters III and IV. First, it is shown that fluctuation electrodynamics is covariant under duality transformation. In this chapter we investigate thermal radiation from chiral media at local thermal equilibrium, by applying duality transformations upon fluctuation electrodynamics theory. It will be shown that the spectral correlations of the thermal electric and magnetic currents are found in terms of the imaginary parts of the complex permittivity and permeability and also the cross correlations between the electric and magnetic currents are found in terms of the coupling coefficients

(magneto-electric and electro-magnetic). It will be shown that two thermal emitters related by duality transformation can have the same thermal radiation signature if the cloak is designed in accordance to the duality transformation. Similarly to transformation optics, the cloak is highly inhomogeneous and anisotropic, accordingly a metasurface a chiral metasurface can replace the cloak. Such metasurface is shown to be a result of a discontinuity in duality transformations. In a similar manner to chapter IV, two regions of space are duality transformed differently and a chiral metasurface is computed according to the discontinuity. Finally, numerical calculation according to the proposed models is compared with the numerical calculations due to thermal discrete dipole approximation (TDDA).

Appendix A focuses on providing the necessary background for the circuit models utilized in chapters IV and V. Also the circuit model of Masloviski to compute thermal radiation is revised. First a modal transmission line model which models 1D electromagnetic propagation. Then thermal noise is introduced to the modal transmission line through Nyquist's theorem. The same model is shown to be equivalent to computing thermal radiation from fluctuating current sources utilizing fluctuation electrodynamics theory. The correspondence between the two models are highlighted. Thermal radiation from planar slabs and cylindrical shells were considered. Finally, thermal radiation from semi-infinite planar emitter and from cylindrical emitter (that includes the origin) is studied. It will be shown that the surface impedance in both cases includes all the necessary information required to calculate for the thermal radiation. Appendix (B) summarizes the tensor calculus background needed for transformation optics theory in 2D space, while appendix (C), the implication of Kirchoff's reciprocity upon thermal radiation from arbitrary shapes thermal emitters are highlighted. Appendix (D), TDDA procedure for thermal radiation calculations is summarized. Appendix (E) provides simplified derivations for fluctuation electrody-

namics and statement of Nyquist's theorem.

In Chapter VII, we summarize the main contributions and limitations of the research work provided by this thesis. Also, future extensions and possible realizations of thermal illusion are discussed.

LIST OF PUBLICATIONS

1. **Alwakil A.**, Zerrad, M., Bellieud, M. and Amra, C. (2017). Inverse heat mimicking of given objects. Scientific Reports, 7.
2. **Alwakil A.**, Zerrad M., Bellieud M., Veynante D., Enguehard F., Rolland N., Volz S. and Amra C., Transformational fluctuation electrodynamics: application to thermal radiation illusion. Optics express. 2017; 25 (15).
3. **Alwakil A.**, Zerrad, M. and Amra, C., Electromagnetic Scattering and Thermal Radiation Illusion using Transformation Optics based Mantle Cloaks (Submission before end of defense).
4. **Alwakil A.**,Zerrad, M. and Amra, C., Circuit Model for Thermal Radiation from Arbitrary Shaped Thermal Emitters (Submission before end of defense).
5. **Alwakil A.**,Zerrad, M. and Amra, C.,Calculating Near Field Thermal Radiation from Bi-anisotropic Emitters using Duality Transformations (Submission before end of defense).

CHAPTER I

Introduction

1.1 Motivation

The work presented in this thesis is focused on proposing theoretical solutions for the following three problems:

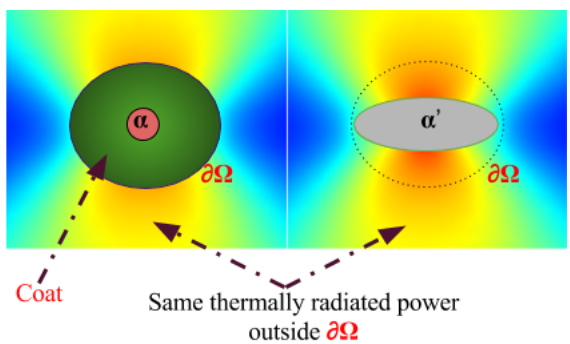

Figure 1.1: Schematic for the thermal illusion problem addressed in this thesis.

1. As shown in Fig.(1.1), given two thermal emitters (α and α') with different constitutive parameters (permittivity, permeability and electromagnetic and magneto-electric coefficients, generally complex), both in general at thermal thermal equilibrium at different temperature distributions (T' and T), with different thermal conductivity tensors and heat capacitances and with different outer surface shapes. It is required to design a cloak such that the thermal radiation signature of the object with the cloak is the same as thermal signature of

the target object both computed outside a predetermined surface $\partial\Omega$ as shown in Fig.(1.1). Also it is assumed that the temperature distribution is the result of steady state heat conduction while heat convection is ignored. In chapter II, we apply transformation optics upon heat conduction while ignoring thermal radiation. We derive the necessary conditions upon the thermal conductivities of the cloaked object and the target object so that the temperature distribution outside $\partial\Omega$ is the same. Then similarly, in chapter III, based on transformation optics and focusing on thermal radiation, we derive the necessary conditions upon the constitutive parameters of both objects to be satisfied in close connection with their outer shapes. This theoretical work is done with in the framework of fluctuation electrodynamics theory. The transformation optics cloaks, proposed in chapters II and III are bulky, anisotropic and in-homogeneous. Accordingly we propose the usage of zero thickness mantle cloaks that can replace the TO based cloaks. In chapter IV, discontinuous transformation optics are discussed and mantle cloaks are modelled as a discontinuity in the space transformation. The mantle cloak proposed is a generalization of lumped components in electrical network theory.

2. Given an isolated cavity with perfectly electromagnetically isolating walls (perfect electric or perfect magnetic conductor). The cavity is isolated such that no electromagnetic radiation enter or gets out of such cavity. The cavity is required to be coated by a zero thickness cloak (i.e a meta-surface). It is required to compute for the meta-surface's surface impedance (admittance) or equivalently susceptibility tensor, such that the thermal radiation signature of such meta-surface resembles the thermal signature of another target object. The isolated cavity serves as hidden region when an arbitrary object can be located in. In such case, the meta-surface is the same as the equivalent surface of the target thermal emitter. In chapter V, a circuit network model is proposed to

calculate the thermal radiation signature, having the surface impedance or admittance of the thermal emitter or the coating meta-surface. It will be shown that the thermal radiation pattern is closely related to the in-homogeneity of the surface impedance (admittance) while the total thermally radiated power is closely related to the non-locality or the spatial dispersion of the metasurface. The circuit model proposed in chapter V is an extension for the circuit model proposed by S. Maslovski et al [79], [80] and [78] which is summarized in appendix A.

3. The solutions proposed for the former two problems assume that the cloaked and target objects can be transformed into each other using transformation optics. Transformation optics imposes conditions on the media of both the objects than can be cloaked. In order to widen the range of the media to be cloaked, Field transformation [71] needs to be applied. In a similar manner to transformation optics, field transformation results in bulky and anisotropic cloaks. In chapter VI, It will be shown that a chiral metasurface can be used to account for discontinuous field transformation.

In what follows, we briefly summarize the necessary background about the state of art concerning the topics discussed in this thesis.

1.2 Invisibility and Illusion Cloaking

Since the year 2000, tremendous amount of theoretical and experimental research investigated different possibilities of making an object invisible for detection. Such research work was accelerated by the parallel vast development in meta-materials and nano-photonics technologies in both design and fabrication. The start of the invisibility and illusion science can be traced to the seminal work of J.Pendry [97] and independently U. leonhardt [62]. Both made use of the space transformation as

a tool to achieve invisibility. Since then a huge amount of research had been done and different technique had been proposed. In what follows we focus on the relevant invisibility and cloaking techniques which transformation optics and scattering cancellation cloaking using mantle cloaks. The reader is referred to the following review papers [32] and [22] for different invisibility cloaking techniques.

1.2.1 Transformation optics cloaks using metamaterials

The usage of space transformation in physics can be traced to the space-time transformations performed in special and general relativity theories [64], where transformations are done in the 4-dimensional space space-time. On the other hand, transformation Optics (TO) is the theory of the space transformations performed in the 3-dimensional space with time is a parameter as in the Newtonian's physical picture. Although the mathematical basis is the same, however much more interest in TO was raised among classical physicist and engineers mainly because of the possibility to practically realize the ideas proposed by TO, which was driven by the technological advances in metamaterials [14]. Historically, after the major advances in photonic crystals [51] technology in 1990s, the research focus was shifted to the so called metamaterials. Metamaterials are averaged or homogenized media composed of sub-wavelength unit cells so as to provide special electromagnetic properties that are not available in natural materials such as negative permittivity and/or permeability. Such exotic nature of the metamaterials can be tailored to satisfy the demanding designs provided by TO. The reader is advised to refer to [63] for detailed explanation for TO theory and to the following review papers for the exciting literature for the developed TO based devices [82], [56] and [74].

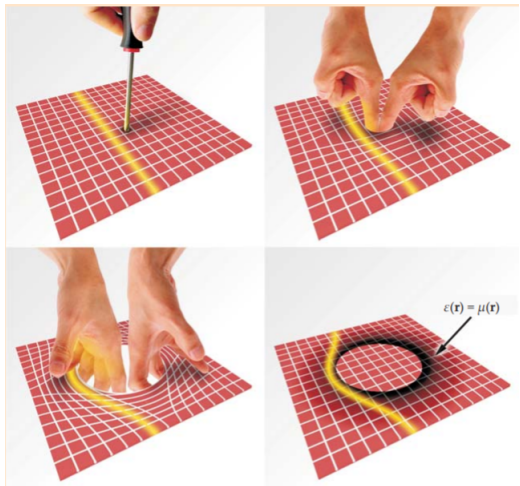

Figure 1.2: Illustration of the main concept in electromagnetic invisibility cloaking using meta-materials. A point is expanded and the space is deformed such that the geodesics of propagating field is avoiding the cloaked region. Fig.s are adapted from [120].

The mathematical background necessary for TO theory is summarized in appendix B. The main idea of TO is that the physics is covariant under space transformation. One way to understand such statement that the physics are independent of the space coordinates used to describe it. What is meant by physics is the governing equations, i.e: Maxwell equations for electromagnetism; so they have the same form before and after the space transformation. Also, it is known from geometric optics that light when propagate in a media, it follows the paths with least optical phase [31]. In other words, their trajectory are the geodesics of such "optical" space. It is important to recognize that we always refer to "optical" space which is the space as "seen" by electromagnetic waves as the space and this should be understood implicitly unless we state otherwise. In a homogeneous media or equivalently a flat space, a geodesics is a straight line. In a curved space the geodesics is not a straight line, however it is a curve. For instance it is a circular curve when the space is the outer surface of an impenetrable sphere. Indeed, in order to calculate for the geodesics of a space, one must know how to measure the distance between to points in a curved space. In order to do so one need to know a priori the metric tensor of such space. Quantitatively, the

distance between two 'nearby' points in a curved space can be written as following:

$$ds = \sqrt{\sum_{i,j=1}^{N} g_{ij} dx^i dx^j} \tag{1.1}$$

where dx^i are the differential distance in the increase direction of the coordinate system used. i and j are indices and N is the number of dimensions of the space. g_{ij} is the metric tensor. It is interesting that in case of a flat space, one can retrieve Pythagoras's relation as following:

$$ds = \sqrt{\sum_{i,j=1}^{N} \delta_{ij} dx^i dx^j} = \sqrt{(dx^1)^2 + (dx^2)^2 + (dx^3)^2} \tag{1.2}$$

where for a flat space the metric tensor is just an identity tensor $g_{ij} = \delta_{ij}$ with δ is Kronecker delta symbol. The core idea of TO is the equivalence between the metric tensor which quantify the "curviness" of the optical space at one side and the in-homogeneity and anisotropicity of such media on the other side. Such correspondence is obvious when dealing with Maxwell equation in coordinate free form as following:

$$\frac{\epsilon^{ij}}{\epsilon_0} = \frac{\mu^{ij}}{\mu_0} = \sqrt{g} g^{ij} \tag{1.3}$$

where ϵ^{ij} and μ^{ij} are the permittivity and permeability tensors, g is the determinant of the metric tensor g_{ij}. The notation is explained in appendix (B). The latter equation simply says that an electromagnetic field don't "see" the difference between a curved space with the metric tensor g_{ij} filled with vacuum (of permittivity ϵ_0 and permeability μ_0) and a flat space filled with in-homogeneous and anisotropic media of permittivity ϵ^{ij} and permeability μ^{ij}. In summary, media act as effective geometries for electromagnetic fields.

Based on the latter equivalence between the media and space space geometry, electromagnetic invisibility was made possible. A simple illustration for a space transformation used to achieve electromagnetic invisibility is shown in Fig.(1.2). The main theme is to consider a point in a flat "optical" space where the geodesics are straight line, by expanding such point, a new deformed space is resulted. The new space contains a "hole" or a hidden region as the geodesics in the new space are curved and none pass into such hole. In order to understand such space transformation, let's consider another space transformation that can be written as following:

$$\rho' = \begin{cases} \frac{a}{\varepsilon}\,\rho \quad \text{for } \rho < \varepsilon \\ \\ \frac{b-a}{b-\varepsilon}\,\rho + \frac{a-\varepsilon}{b-\varepsilon}\,b \quad \text{for } \varepsilon \leq r \leq b \qquad \varepsilon < a \\ \\ \rho^{'} \quad \text{for } \rho \geq b \end{cases} \tag{1.4}$$

$$\phi = \phi^{'}$$

$$z = z^{'}$$

here the unprimed and primed quantities are the polar coordinates of the virtual (pre-transformation) and the physical space (the post-transformation) spaces respectively. The transformation of Eq.(1.4) expands the region $\rho < \varepsilon$ into $\rho' < a$, while compressing the region $\varepsilon \leq r \leq b$ into $a \leq r \leq b$. By taking the limit $\varepsilon \longrightarrow 0$, the transformation becomes as following

$$\rho' = \begin{cases} \frac{b-a}{b}\,\rho + a \quad \text{for } 0 \leq r \leq b \\ \\ \rho^{'} \quad \text{for } \rho \geq b \end{cases} \tag{1.5}$$

$$\phi = \phi^{'}$$

$$z = z^{'}$$

In this new transformation, it is the origin that is expanded into a cylinder of radius a, while the region $r \leq b$ is compressed into $a \leq r \leq b$. In the physical space, the region $\rho' < a$ is the cloaked region while the region $a \leq r \leq b$ is the cloak the surround the cloaked region. The cloak due to the former space transformation is typically called Pendry's cloak. The geometry of the physical space and the physical realization are shown in Fig.(1.3). Pendry's cloak was fabricated using split ring resonators [110] and experimentally verified in microwave regime [105].

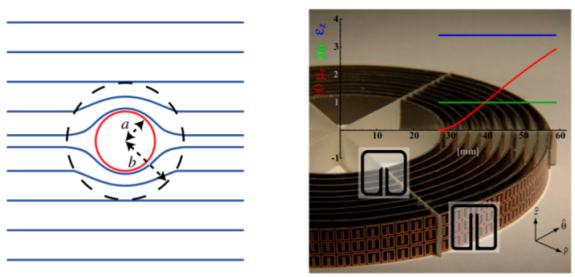

Figure 1.3: Left: The physical space after the space transformation of Eq.(1.4). Right: the realization of the cloak that is located at $a < \rho' < b$. Figures is adapted from [105]

Invisibility cloaking using TO theory is not limited to electromagnetic, virtually, it can be applied to any physics with a well defined space topology. An illustrative example is shown in Fig.(1.4) where electrical resistors can distort the flowing of electric currents such that the cloaked hole region is invisible for the flowing electric currents [104]. Actually, TO theory was explored and experimentally verified in other domains of physics, for instance, among others, heat conduction [36] and [104]. TO theory is not limited to invisibility but also applied to scattering illusion. A space transformation to design a cloak to coat an object such that the scattering signature of the object with the cloak is the same as the scattering signature of another object.

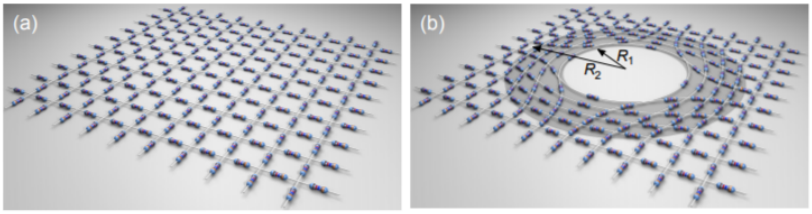

Figure 1.4: TO based invisibility cloak had been applied to diffusion as heat or electric conduction. For electric conduction, the conductance of the media can vary in space such that electric current flow around a cloaked region. Left: virtual space. Right: physical space. Fig.s are adapted from [104].

1.2.2 Scattering cancellation using mantle meta-surfaces

Despite the success of metamaterials to realize TO based cloaks, the performance of such cloaks is low such that they are impractical for real life usages. The main draw backs is the media dispersion, the cloaking can be almost perfect but just at one frequency. Another draw back is that the TO based cloaks are bulky, highly anisotropic and in-homogeneous. Such drawback motivated the research on the usage of meta-surfaces to replace the TO based cloaks. A meta-surface is a sub-wavelength layer (ideally zero thickness) with its surface properties are controlled by the homogenized behaviour of surface allocated sub-wavelength unit cells. In what follows we summarize the state of art concerning the usage of meta-surface (also called mantle cloaks) in invisibility and illusion purposes. The technique of using mantle metasurfaces in order to achieve invisibility and electromagnetic illusion, is often called scattering cancellation technique. The reader is referred to the following review papers [32] and [22] for detailed literature surveys concerning scattering cancellation technique.

Invisibility cloaking using scattering-cancellation-technique is classified into such plasmonic and mantle cloaking. The main theme is to design a cloak that scatters the incident field such that a destructive interference occurs between the scattering due to

the cloaked object and the scattered field due to the cloak itself. Plasmonic cloaks are mainly bulky cloaks with negative permittivity to coat positive permittivity dielectric object so that the total induced electric polarization, of the cloak and the cloaked object togather due to an incident field, is cancelled so the scattered field is minimized. On the other hand, mantle cloaks are optically thin conformal metasurface which is defined such that the surface impedance of the cloak with the coated object, is the same as the surface impedance incident field.

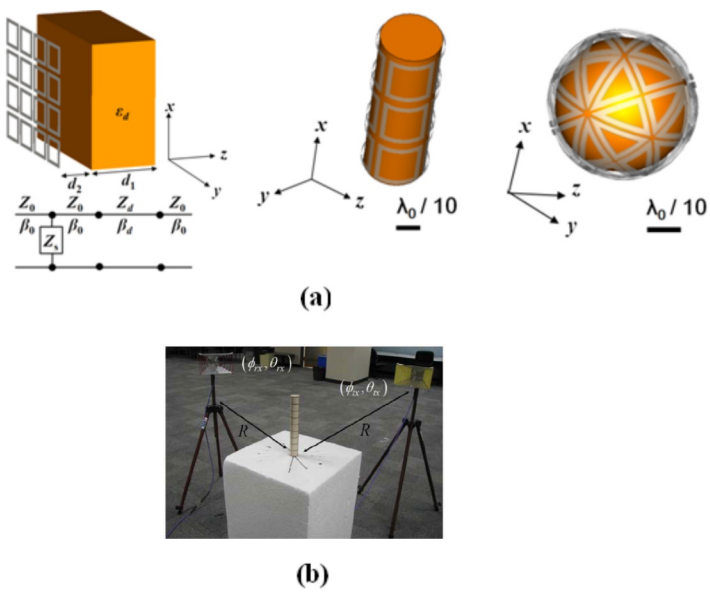

Figure 1.5: (a) Mantle cloaks for different geometric configurations: planar , cylindrical and spherical shaped mantle cloaks.(b) Experimental setup of a mantle cloak surrounding a dielectric rod. Figure is adapted from [111].

Cloaking using mantle meta-surfaces was first proposed by A.Alu for spherical and cylindrical objects in [4] and [5] respectively. The state of art of designing such meta-surfaces heavily depends on the what is known in the RF and microwave scientific literature as the Frequency selective structures (FSS) [85]. FSS are surfaces with designed surface impedance that can be implemented by patterning the surface with dielectric and metallic medias. FSS can be considered as a three-dimensional generalization of electric filters and its surface shape is patterned so as to match the

desired the frequency responses as shown in Fig.(1.6).Mantle cloaks are the same as FSS but used for invisibility and illusion cloaking.

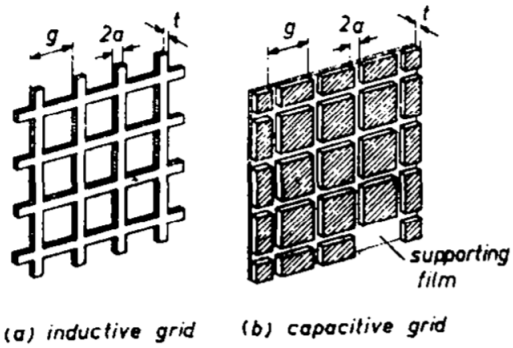

Figure 1.6: Schematic for planar frequency selective surface (FSS) with (a) inductive surface impedance (b) capacitive surface impedance. Adapted from [116].

In what follows, the standard design procedure is summarized.

The design procedure of such mantle invisibility cloaks is more appropriate for objects with sizes much smaller than the wavelength. Since the incident field is a linear sum of spherical in 3D or cylindrical waves in 2D, then in the case of optically small objects, only the lowest spherical or cylindrical orders are dominant and exist in the vicinity of the object[95]. In such case, Mantle cloaks can be approximated by being local and homogeneous. Actually a local metasurface may not be an optimal design, especially when not only the lowest order is the dominant. An interesting design strategy was reported in [73] where a local Ms was used to cancel the scattering due to the first three orders, however the frequency of operation (3 GHZ) was chosen such that the matching surface impedance of the Ms required for these order are close in value. From circuit theory perspective a meta-surface can be viewed as an electrical network of lumped elements introducing a discontinuity or a jump in the electromagnetic fields along its sides. For objects with size comparable to the wavelength, due to the capacitive nature of reactive fields around dielectric objects, inductive meta-surfaces are usually required to cancel the scattered fields, this is why an inductive surface impedance is typically required and it is usually implemented

in RF frequency range using a simple conducting helical sheath due the inductive nature of a simple wire [21]. Mantle cloaks are modelled as a shunt load connected to a transmission line (wave guide) carrying the incident and the scattered plane, cylindrical or spherical waves [17] which is valid for planar slabs, infinite cylindrical and spherical objects respectively [19] as shown in Fig.(1.5). Analytical expression for the required surface impedance to cloak a perfectly conducting infinite cylinder for arbitrary orders was provided in [60].

In what follows, we briefly summarize the scattering cancellation technique and the context where transformation optics based mantle cloaks proposed in chapter IV emerged. When considering the TO cloaking approach, one interesting case is that when a circular symmetric object A centered at the origin with permittivity ϵ_A, permeability $\mu_A = \mu_0$ and radius A is ρ_A, is linearly radially transformed into object B also centered at the origin with permittivity ϵ_B, permeability $\mu_B = \mu_0$ and radius ρ_B. The transformation is:

$$\begin{aligned} \rho' &= \frac{\rho_A}{\rho_B}\rho \\ \phi' &= \phi \end{aligned} \tag{1.6}$$

and the materials physical parameters are transformed as:

$$\begin{aligned} \epsilon_B &= \frac{\epsilon_A}{(\rho_A \,/\, \rho_B)} \\ \mu_A &= \mu_B = \mu_0 \end{aligned} \tag{1.7}$$

Hence one can simply transform between two different dielectric cylinders using a simple radial transformation, and the result is the same scattered field outside the region $\rho \geq \rho_{ex}$. However this TO approach requires a bulky in-homogeneous and anisotropic cloak to ensure the continuity of the physical space with the outer unity

transformed space region $\rho = \rho' = \rho_{ex}$ as shown in Fig.(1.7). On the other hand, a mantle meta-surface can be treated as a matching network and scattering cancellation technique can be viewed as an impedance matching [59] problem as shown below.

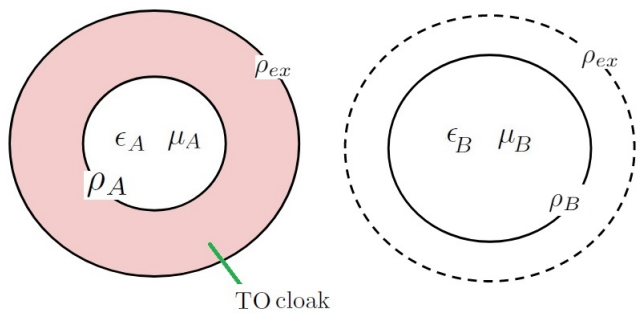

Figure 1.7: Schematic for the typical procedure for scattering illusion using TO approach. First the cylindrical object B (with media ϵ_B and μ_B and radius ρ_B) is transformed to cylindrical object A (with media ϵ_A and μ_A and radius ρ_A), while the vacuum space located at $\rho_B < \rho < \rho_{ex}$ is transformed into cloak $\rho_A < \rho' < \rho_{ex}$. The outer region $\rho > \rho_{ex}$ (typically vacuum) is unity transformed into $\rho' > \rho_{ex}$, so that the electromagnetic field and media parameters are the same for both spaces.

In 2-D space (see Fig.(1.8)), consider a homogeneous, isotropic and bounded circularly symmetric scattering object A . It is desired to cloak the object A with a meta-surface (MS) of surface impedance Z_s such that the scattered field is identical to that of another circularly symmetric object B with homogeneous media (ϵ_B, μ_B) and same outer shape as object A. For an incident cylindrical wave from vacuum with order n, the input impedance of the circularly symmetric object A is $Z_A[n] = -j\eta_A \frac{J_n(k_A\rho_s)}{\dot{J}_n(k_A\rho_s)}$ and the input impedance for B at order n is $Z_B[n] = -j\eta_B \frac{J_n(k_B\rho_s)}{\dot{J}_n(k_B\rho_s)}$ with J_n is ordinary bessel function of first type, $\dot{J}_n(k\rho) = \frac{d}{d(k\rho)} J_n(k\rho)$, $k_A = \omega\sqrt{\epsilon_A\mu_0}$ and $k_B = \omega\ \sqrt{\epsilon_B\mu_0}$. Then, accordingly the necessary surface impedance will be:

$$Z_s[n] = \frac{Z_A[n]Z_B[n]}{Z_A[n] - Z_B[n]} \tag{1.8}$$

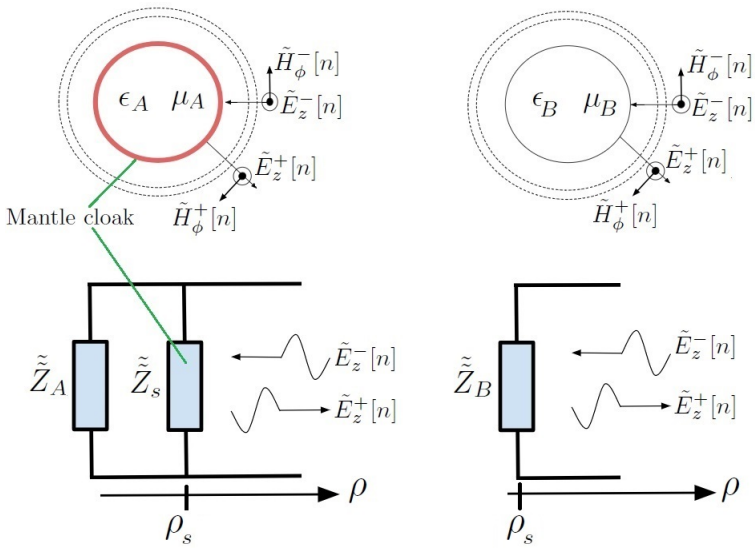

Figure 1.8: Schematic for the scattering cancellation technique using Mantle cloaks. The object A with permittivity ϵ_A and permeability μ_A (typically non magnetic $\mu_A = \mu_0$) coated with a MS/Mantle cloak such that the scattered field for an incident field is the same as the scattering of another object B with permittivity ϵ_B and permeability μ_B(vacuum in case of invisibility cloaking) under the same incident field. The problem is typically treated as a matching problem between incident cylindrical wave of order n and terminating. In this case, the surface impedance of the MS is the terminating load. Transmission line models are used to model the propagation of cylindrical waves (see appendix A). E_z and H_ϕ are the electric and magnetic fields of E-polarization.

It is clear that the required metasurface to achieve illusion depends on the order n , i.e cylindrical order dispersive or non-local metasurface. Although the shunt connected load as a representation for a mantle metasurface seems natural from circuit theory perspective, it is more clear to derive the former relation from first principles as following: Considering the object A depicted in Fig. (1.8) coated by the metasurface at $\rho = \rho_s$ then for E-polarization, the fields on both sides of the metasurface can be

expressed in terms of cylindrical waves (see appendix A) as follows:

$$E_z(\rho,\phi) = \begin{cases} \sum_n \alpha_n J_n(k\rho) e^{in\phi} & \text{for } \rho < \rho_s \\ \\ \sum_n \left[\beta_n H_n^{(2)}(k_0\rho) + \gamma_n H_n^{(1)}(k_0\rho)\right] e^{in\phi} & \text{for } \rho > \rho_s \end{cases}$$

$$H_\phi(\rho,\phi) = \begin{cases} j\frac{1}{\eta} \sum_n \alpha_n \dot{J}_n(k\rho) e^{in\phi} & \text{for } \rho < \rho_s \\ \\ j\frac{1}{\eta_0} \sum_n \left[\beta_n \dot{H}_n^{(2)}(k_0\rho) + \gamma_n \dot{H}_n^{(1)}(k_0\rho)\right] e^{in\phi} & \text{for } \rho > \rho_s \end{cases} \tag{1.9}$$

where $J_n(k\rho)$ is Bessel function of order n representing cylindrical standing wave, $H_n^{(1)}(k\rho)$ and $H_n^{(2)}(k\rho)$ are Hankel functions of 1st and 2nd types representing in and out going cylindrical waves respectively. α_n, β_n and γ_n are the amplitudes of such cylindrical waves. Then applying the boundary conditions at $\rho = \rho_s$, where:

$$\begin{aligned} E_z(\rho = \rho_s^-) &= E_z(\rho = \rho_s^+) = E_z(\rho = \rho_s) \\ E_z(\rho = \rho_s) &= Z_s \left(H_\phi(\rho = \rho_s^-) - H_\phi(\rho = \rho_s^+)\right) \end{aligned} \tag{1.10}$$

Then by applying mode matching, where field components on the same cylindrical order equates due to cylindrical symmetry, we get a system of two equations in two unknowns as following

$$\begin{bmatrix} J_n(k\rho_s) & H_n^{(2)}(k_0\rho_s) \\ j\frac{1}{\eta}\dot{J}_n(k\rho_s) - \frac{1}{Z_s}J_n(k\rho_s) & j\frac{1}{\eta_0}\dot{H}_n^{(2)}(k_0\rho_s) \end{bmatrix} \begin{bmatrix} t_n \\ r_n \end{bmatrix} = - \begin{bmatrix} H_n^{(1)}(k_0\rho_s) \\ j\frac{1}{\eta_0}\dot{H}_n^{(1)}(k_0\rho_s) \end{bmatrix} \tag{1.11}$$

where $t_n = \frac{\alpha_n}{\gamma_n}$ and $r_n = \frac{\beta_n}{\gamma_n}$ are the transmitting and scattering coefficient. Then

solving for r_n by using Cramer's method of linear algebra, then defining:

$$\begin{aligned} P &= \begin{vmatrix} J_n(k\rho_s) & H_n^{(2)}(k_0\rho_s) \\ j\frac{1}{\eta}\dot{J}_n(k\rho_s) - \frac{1}{Z_s}J_n(k\rho_s) & j\frac{1}{\eta_0}\dot{H}_n^{(2)}(k_0\rho_s) \end{vmatrix} \\ &= \left(\frac{1}{\eta_0}\dot{H}_n^{(2)}(k_0\rho_s)J_n(k\rho_s) - \frac{1}{\eta}H_n^{(2)}(k_0\rho_s)\dot{J}_n(k\rho_s)\right) - \frac{1}{Z_s}J_n(k\rho_s)H_n^{(2)}(k_0\rho_s) \end{aligned} \tag{1.12}$$

and defining

$$\begin{aligned} Q &= \begin{vmatrix} J_n(k\rho_s) & H_n^{(1)}(k_0\rho_s) \\ j\frac{1}{\eta}\dot{J}_n(k\rho_s) - \frac{1}{Z_s}J_n(k\rho_s) & j\frac{1}{\eta_0}\dot{H}_n^{(1)}(k_0\rho_s) \end{vmatrix} \\ &= \left(\frac{1}{\eta_0}\dot{H}_n^{(1)}(k_0\rho_s)J_n(k\rho_s) - \frac{1}{\eta}H_n^{(1)}(k_0\rho_s)\dot{J}_n(k\rho_s)\right) - \frac{1}{Z_s}J_n(k\rho_s)H_n^{(1)}(k_0\rho_s) \end{aligned} \tag{1.13}$$

then the reflection coefficient

$$r_n = -\frac{Q}{p} = \frac{Z_B - Z_n^+}{Z_B - Z_n^-} \tag{1.14}$$

where $Z_n^+ = -j\eta_0\frac{H_n^{(2)}(k_0\rho)}{H_n^{(2)}(k_0\rho)}$ and $Z_n^- = -j\eta_0\frac{H_n^{(1)}(k_0\rho)}{H_n^{(1)}(k_0\rho)}$ are the wave impedance of out and in-going cylindrical waves of order n respectively and $\frac{1}{Z_B} = \frac{1}{Z_s} + \frac{1}{Z_A}$ from which one retrieve the shunt connection relation of Eq.(1.8).

The scattering cancellation procedure shown above requires the prior knowledge of the impedance of the object A for order n, and this is why only objects with circular symmetry are those that are typically cloaked using scattering cancellation technique. Also, Z_s is cylindrical order dispersive (non-local) and typically it is not feasible to fabricate such spatial dispersive MS. Scattering cancellation approach is typically restricted to optically/electrically small objects where only the lowest order $n = 0$ is the dominant, so the physical fabricated MS is a local one $Z_s[n] = Z_s[0]$ for all n. It is extremely advantageous to combine both approaches such that the thin

mantle cloak replaces the bulk TO cloak. Also, to our best knowledge, there is no generic approach to design Mantle cloaks in the case where the cloaked object is not circularly symmetric.

A mantle cloak can also be anisotropic and it was reported in [84] in order to cloak a cylindrical dielectric object against an oblique incident plane wave where E- and H-polarizations are coupled. It is important to stress that we only consider scattering thermal radiation problems in 2D spaces where E- and H- polarizations are uncoupled unless otherwise is stated.

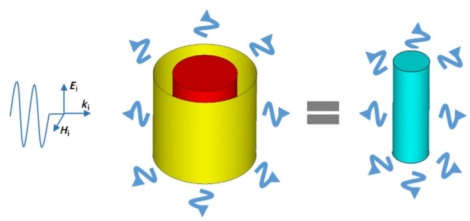

Figure 1.9: Sketch of the working principle of scattering cancellation technique adapted for illusion purposes using mantle meta-surfaces. Fig. is adapted from ref.[118].

Scattering cancellation technique had been extended beyond invisibility cloaking to achieve scattering illusion as shown in Fig.(1.9). In [118], analytical expressions for a local surface impedance was driven in terms of the permittivity of the coated and targeted cylinders. However the analysis in [118] was restricted to optically (electrically) small objects where the lowest order $n = 0$ dominant. The surface impedance driven was imaginary (lossless metasurface) and designed to mimic the scattering cross section of the target object due to the lowest order cylindrical wave. In other words, both the cloaked and the target objects are restricted to be optically small spherical objects whose scattering response is dominated by that of an electric dipole, i.e. objects for which the electrostatic approximation is sufficient to describe their response [30]. As a summary scattering cancellation is restricted to optically small

cylindrical or spherical symmetry and in chapter IV we propose a technique combining TO and scattering cancellation to overcome the inherent limitations in both of them.

Now, we briefly mention the recent relevant advances with respect to mantle cloak realizations. In [94] at Rf frequency band, FSS arrays were realized using 2D printed patches and slotted structures and they has been used to tailor a local surface reactance of cylindrical mantle cloaks [95], while tunability was introduced by using varactors (voltage controlled capacitors) as in [72]. On the other hand, graphene had proved to be attractive for mantle cloak realization as it is known to be highly spatial dispersive, anisotropic, and also offers real time tunability as an applied voltage can tune the chemical potential of the layer which eventually tunes the surface electromagnetic properties of graphene. Graphene Monolayers were utilized in [18] targeting cloaking at THZ regime and also graphene based FSS were proposed in [23].
Actually, the advances in theory and technology meta-surface is so rapid, however most metasurfaces classified either as plasmonic or dielectric. Plasmonic MS.s are composed of sub-wavelength metallic (plasmonic) unit cells exhibiting plasmonic resonances, while the dielectric ones are composed of high refractive index dielectric resonators electric and magnetic dipole responses based on Mie resonances [119]. For either type, a metasurface's electromagnetic properties can be quantified through its susceptibility tensors which determine its electromagnetic response using the so called generalized sheet transverse conditions (GSTC) [47], [57] and[2] as following:

$$
\begin{aligned}
\hat{e}_n(\bar{r}_s) \times \Delta\bar{H}_{\parallel}(\bar{r}_s,t) &= \frac{\partial}{\partial t}\bar{P}_{\parallel}(\bar{r}_s,t) - \hat{e}_n(\bar{r}_s,t) \times \nabla_{\parallel} M_{\perp}(\bar{r}_s,t) \\
\Delta\bar{E}_{\parallel}(\bar{r}_s,t) \times \hat{e}_n(\bar{r}_s) &= \frac{\partial}{\partial t}\bar{M}_{\perp}(\bar{r}_s,t) - \nabla_{\parallel}\left(\frac{P_{\parallel}}{\epsilon_0}\right) \times \hat{e}_n(\bar{r}_s) \\
\hat{e}_n(\bar{r}_s) \cdot \Delta D_{\parallel}(\bar{r}_s,t) &= -\nabla_{\parallel} \cdot P_{\parallel}(\bar{r}_s,t) \\
\hat{e}_n(\bar{r}_s) \cdot \Delta B_{\parallel}(\bar{r}_s,t) &= -\mu_0 \nabla_{\parallel} \cdot M_{\parallel}(\bar{r}_s,t) \\
&\text{Where:} \\
\bar{E}(\bar{r}_s) &= \bar{E}_{\parallel}(\bar{r}_s) + \hat{e}_n(\bar{r}_s) E_{\perp}(\bar{r}_s) \\
\bar{H}(\bar{r}_s) &= \bar{H}_{\parallel}(\bar{r}_s) + \hat{e}_n(\bar{r}_s) H_{\perp}(\bar{r}_s) \\
\bar{P}(\bar{r}_s) &= \bar{P}_{\parallel}(\bar{r}_s) + \hat{e}_n(\bar{r}_s) P_{\perp}(\bar{r}_s) \\
\bar{M}(\bar{r}_s) &= \bar{M}_{\parallel}(\bar{r}_s) + \hat{e}_n(\bar{r}_s) M_{\perp}(\bar{r}_s)
\end{aligned}
\tag{1.15}
$$

Where P and M are the Meta-surface's electric polarization and magnetic magnetization vectors respectively, Δ is the difference operator for the jump of the fields value on both sides 1 and 2 of the M.S, ($\parallel$ and $\perp$) are parallel and normal to the metasurface; $\hat{e}_n(\bar{r}_s)$ is the local normal unit vector to the metasurface at $\bar{r}_s$ which is the position vector for points on the metasurface. It is clear that GSTC conditions are an integral form of Maxwell's equations on both sides of the M.S discontinuity. The constitutive relations that relates the electric and magnetic polarizabilities to the electric and magnetic fields is determined based on the exact nature of the constitutive unit cells (atoms) that constitutes the M.S. Different special cases can be retrieved by choosing a combination of the following set of properties [(Non)Locality, (In)Homogenity,(Bi and/or An) Isotropicity, Active/Passive].

Design of Mantle cloaks based on GSTC was proposed in [50] which was used to suppress the cylindrical scattered orders $n = 0, 1$ simultaneously due to the extra degree freedom of the radial component of the magnetic susceptibility. Mantle cloak

was experimentally demonstrated for long cylinder with sub-wavelength diameter $D = 0.3\lambda$ [112] and in [111] at GHz regime for E-polarization.

The Mantle cloak has been expanded to carpet cloaking as in [29] which also called skin cloak [88] due to its conformal physical shape. The general theme of this cloaking technique is called local phase compensation, where the metasurface manipulates the reflection phase along the edge of the bump such that the scattering from the bump is the same as the scattering due to flat surface. Such carpets were experimentally verified in THz [121], GHz [125]- [45] and at visible frequency band in [88]. In [46] the carpet is designed to be tunable so the object to be cloaked can mimic different shapes not necessarily flat surface. However nearly all of the previous designs are constrained to be mimicking empty space.

All the previously mentioned designs are valid for a single frequency as an inductive surface impedance was used to anti-resonate with the capacitive load of the dielectric object to be cloaked, however the cloaking effect is required to be achieved in a finite bandwidth a negative capacitive impedance is required (non foster element). Such meta-surface was reported in [20] using negative impedance converters which are active lumped circuits which typically include nonlinear element as transistors or Operational Amplifiers [1].

In chapter IV, mantle cloaks based on discontinuous TO are proposed. The main idea is that two regions of space are transformed differently and a metasurface is placed to compensate for the discontinuity jump. In Fig.(1.10), an invisibility cloaking using mantle cloaks based on discontinuous TO, such that a cylindrical shell of space is compressed into a zeo thickness region and a metasurface can be placed to provide the same "distance" in the electromagnetic space or equivalently the same optical phase as the original region. In chapter IV, other types of space discontinuities are discussed.

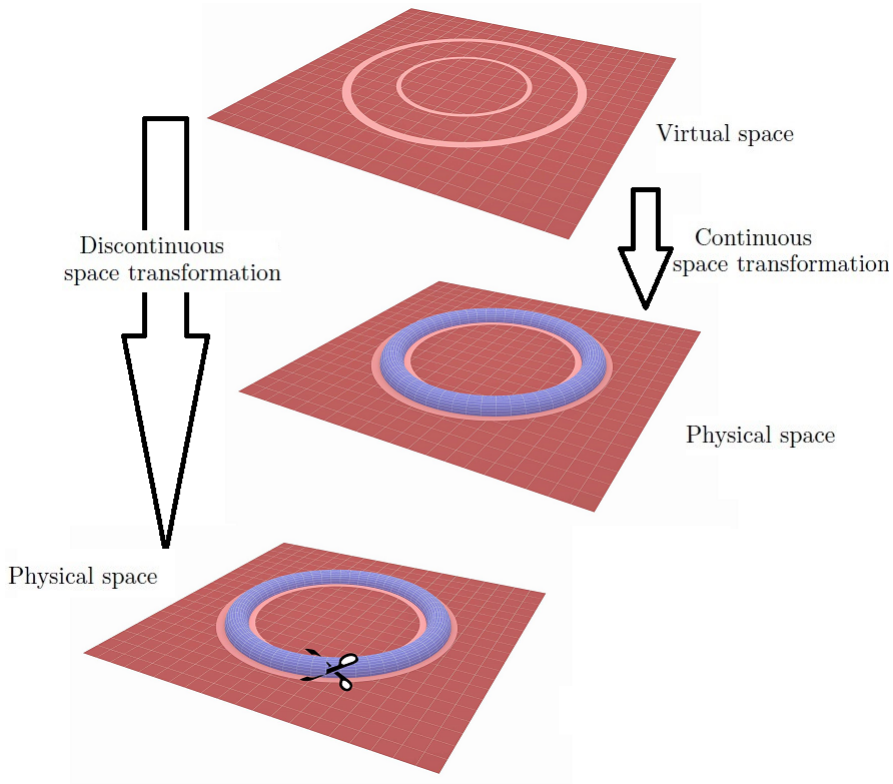

Figure 1.10: Schematic for discontinuous transformation optics. Top: virtual space. Middle: physical space under continuous space transformation with the cylindrical shell of the virtual space is compressed into a zero thickness shell(blue ring). Bottom: physical space under discontinuous space transformation where a metasurface is replacing the blue shell (a scissor to symbolize the space discontinuity).

1.3 Thermal Energy Transfer

In this section we summarize the basic processes of thermal energy transport. Thermal transport is typically classified into Heat conduction, heat convection and thermal radiation. Heat convection is excluded from the foregoing summary as it is not treated in this thesis.

1.3.1 Heat conduction

Heat conduction can be defined as the thermal energy flow through solid state matter. From microscopic point of view, thermal energy is transported through the

propagation of phonons and electrons which are regarded as the thermal energy carriers [77]. A phonon is a quanta of the sound wave which propagates along the media and causes the vibration of the crystal lattice that constitutes the media. The propagation of the phonons and electrons are typically computed through density function theory utilizing some of their quantum mechanical properties [41]. It is interesting to mention that in the case when heating a thin film of polar media, for instance silicon carbide (SiC), heat transport is dominated by surface phonon-polaritons which is a hybrid mode coupling electromagnetic surface waves and phonons and despite its quantum nature, they can be treated classically by Maxwell's in the same way surface plasmons are treated [91]. In all cases, the quantum nature of heat conduction is beyond the scope of this Ph.D. thesis and it will not be presented any further.

On the other hand, from macroscopic point of heat conduction can be viewed as the flow of heat 'rays' or flux which are controlled by the temperature gradient as following:

$$\bar{q} = -\kappa \nabla T \tag{1.16}$$

where $\bar{q}$ is the heat flux, κ is the thermal conductivity and T is the temperature field. The heat flux are subjected to energy conservation such that:

$$\nabla \cdot \bar{q} = -C\frac{\partial T}{\partial t} + Q \tag{1.17}$$

where Q is thermal flux source($Q > 0$) or sinks ($Q < 0$) and C is the heat capacity. When combining the diffusion of heat flux with the energy conversation, one can get the Fourier's law of heat conduction as following:

$$\nabla \cdot \kappa \nabla T = C\frac{\partial T}{\partial t} - Q \tag{1.18}$$

1.3.2 Thermal radiation

Thermal radiation is a universal property for all objects with temperatures above 0K. The thermal radiation is the electromagnetic radiation due to the vibrations of the constitutive free and bounded charges embedded in the atoms and molecules constitutes the media of the thermal emitter. One main foundation of the physics of thermal radiation is Kirchoff's reciprocity [34], which state that at thermal equilibrium, the amount of energy absorbed by an object at temperature T equates the amount of thermal energy emitted by the same object. Based on Kirchoff's reciprocity, the black body as a perfect emitter and absorber what defined and it serves as a reference for all thermal emitter. A black body is defined as an object that absorbs all the incident field with no reflection. The spectral properties of the thermal radiation from the black body was provided by Planck. Wein's law relates the temperature of the black body to the wavelength of maximum intensity of thermal radiation, where

$$\lambda_T = \frac{b}{T} \quad b = 2900\mu m.K \tag{1.19}$$

λ_T is called the thermal wavelength. λ_T serves as a boundary between the far field zone where the thermal radiation only include only propagating field and the near field zone where the thermal radiation includes both propagating and evanescent near field components. Another factor that determines the physics of the thermal radiation is the skin depth of a thermal emitter. If the thermal emitter is strongly lossy at a specific wavelength, then an incident field will be absorbed by the volume near the surface, then by reciprocity, it is the same volume that dominates the thermal radiation. Also, the whole volume of a thermal emitter contributes to the thermal radiation when the object's size is smaller than the skin depth and conversely the region determined by the skin depth dominates the thermal radiation if the object's size is bigger than the skin depth.

In the far field zone or equivalently when the thermal emitter dimensions are much larger than the thermal wavelength λ_T, thermal radiation is viewed as rays. The total far field heat flux (power per unit surface area of the emitter) emitted by a thermal emitter at temperature T is computed as following:

$$q = \sigma \varepsilon T^4 \tag{1.20}$$

where σ is Stephan Boltzmann's constant and ε is the thermal emitter's emissivity which is always than 1 as the case of the black body is retrieved when $\varepsilon = 1$. In the case of multiple emitters, and when the sizes of the emitters and the inter distances are larger than λ_T, heat transfer is computed using radiative transfer theory [44]. Although radiative transfer theory is successful in every day problems, it fails dramatically in the near field zone due to the existence of the near field. Also, radiative transfer theory shows incompatibility with Maxwell's equation. In the near field zone or when the thermal emitter dimensions are smaller or in order of the emitted wavelength, the wave nature of the emitted thermal radiation becomes more evident and the ray picture is no more valid. In such case, Thermal radiation is computed using Maxwell's equations accompanied by Fluctuation electrodynamics theory that governs the fluctuations of the thermal sources inside the thermal emitter. Fluctuation Electrodynamics was first developed by Rytov [103], who introduced the fluctuation dissipation theory [13] into the realm of thermal radiation.

As it was discussed above, we are interested in thermal radiation camouflage and illusion and in chapter III we present an illusion scheme based on transformation optics theory. Although the objects to camouflages are optically large objects, However we adopt FE theory of thermal radiation in the theoretical work presented in this

thesis for the following reasons:

1. FE is compatible with Maxwell's equations and consequently compatible with transformation optics theory.

2. FE theory is exact and can be applied in any length to thermal wavelength ratio scale.

In what follows, FE theory is summarized.

1.3.2.1 Thermal radiation using fluctuation electrodynamics

FE is the application of Fluctuation dissipation theory (FDT) upon electromagnetic fluctuation problem. The theoretical basis of FDT is summarized in appendix . According to FDT, given a system that is characterized by a transfer function that relates linearly between an input and an output, then the spectral correlations or the "ac power" of such thermal fluctuations induced at the output of such linear system are related linearly to the losses inherent in such system. Then according to FE, given a lossy linear medium with complex permittivity and permeability tensors in thermodynamic equilibrium with temperature T, the thermal energy of such medium is associated with the fluctuating thermal electric and magnetic currents, which are the sources of the electromagnetic source of the thermal radiation. These thermal currents are driven by stochastic process with spectral correlations are proportional to both of the imaginary part of the permittivity and permeability tensors which represent the losses of such medium as follows,

$$\begin{aligned}\left\langle \bar{J}(\underline{r}_1,\omega_1)\otimes\bar{J}^*(\underline{r}_2,\omega_2)\right\rangle_\omega &= 4\frac{\omega_1}{\pi}\Theta(\omega_1,T(\underline{r}))Im\{\underline{\underline{\epsilon}}(\underline{r}_1,\omega_1)\}\delta(\underline{r}_1-\underline{r}_2)\delta(\omega_1-\omega_2)\\ \left\langle \bar{K}(\underline{r}_1,\omega_1)\otimes\bar{K}^*(\underline{r}_2,\omega_2)\right\rangle_\omega &= 4\frac{\omega_1}{\pi}\Theta(\omega_1,T(\underline{r}_1))Im\{\underline{\underline{\mu}}(\underline{r}_1,\omega_1)\}\delta(\underline{r}_1-\underline{r}_2)\delta(\omega_1-\omega_2)\end{aligned} \tag{1.21}$$

where $\bar{J}$ and $\bar{K}$ are the thermal electric and magnetic current densities,$\otimes$ is tensor product, $<>_\omega$ represent spectral correlation and ensemble average, $\Theta(\omega, T(\underline{r}))$ corresponds to the mean energy of a single quantum oscillator with angular frequency ω, $\bar{r}_1$ and $\bar{r}_2$ are two different position vectors in the thermal emitter, δ indicates Dirac delta function, $\underline{\underline{\epsilon}}$ and $\underline{\underline{\mu}}$ are the complex permittivity and permeability tensors of the thermal emitter and the star (*) indicates the complex conjugation operator. It is important to mention that the theory is restricted to thermal emitters at local thermodynamic equilibrium. Also, thermal sources are modelled as thermal fluctuating current densities with no fluctuating electric or magnetic charges due to the fact that charged interfaces does not alter significantly the thermal radiation [43].

Due to the linearity of Maxwells equations, a linear relation is considered between the electric and magnetic fields at position $\underline{r}$ and the thermally fluctuation electric and magnetic sources at position $\underline{r}'$ as following:

$$\begin{aligned} \bar{H}(\underline{r}) &= \int \left(\underline{\underline{G}}^{HH}(\underline{r}, \underline{r}')\bar{K}(\underline{r}_1) + \underline{\underline{G}}^{HE}(\underline{r}, \underline{r}')\bar{J}(\underline{r}')\right) d^2\underline{r}' \\ \bar{E}(\underline{r}) &= \int \left(\underline{\underline{G}}^{EH}(\underline{r}, \underline{r}')\bar{K}(\underline{r}') + \underline{\underline{G}}^{EE}(\underline{r}, \underline{r}')\bar{J}(\underline{r}')\right) d^2\underline{r}' \end{aligned} \tag{1.22}$$

where $\underline{\underline{G}}^{HH}$, $\underline{\underline{G}}^{HE}$, $\underline{\underline{G}}^{EH}$ and $\underline{\underline{G}}^{EE}$ are the magnetic and electric fields Green functions due to the magnetic and electric current densities respectively. The the ensemble averaged time average thermally radiated Poynting vector is calculated as following:

$$\langle S \rangle = 4 \times \frac{1}{2} Re\{\langle \underline{E} \times \underline{H}^* \rangle\} \tag{1.23}$$

1.3.2.2 Thermal radiation invisibility cloaking

Every object with a specific shape and emissivity has its own thermal radiation signature. Such signature allows the object to be detected and recognized which can be an undesirable situation. The spectral transmittance windows of the atmosphere

are at 3 to $5\mu m$ and 8 to $12\mu m$. Fortunately, thermal radiation of emitters at biologically relevant temperatures (-40 till 100 degree) peaks in the infrared wavelength range of 8 to $12\mu m$ [108]. Thermal invisibility is an attractive topic for stealth technology where engineers design planes and tanks structures to minimize the radar cross section [76] and thermal radiation signatures [48] making them hard to be detected and located by counter forces. similarly, camouflage coats had been designed to help soldiers are hard to be seen, these camouflage techniques already use the same techniques used by animals and insects where they change the colour of their skin to match the surrounding environment to minimize the contrast making them undetectable by the other animal species. The main theme of the thermal invisibility coating is to reduce the emissivity of an emitter in order to be undetectable by thermal detectors. In general, thermal invisibility depends on two main factors [48]:

1. **Temperature and emissivity similarity**: Since the radiance of the thermal emission is the quantity to be detected, the thermal emitter has to have similar radiance as its own background. This can be achieved that the apparent temperature and emissivity of the target is close to the temperature of the background.

2. **Spatial similarity**: The temperature distribution over the target is similar to the temperature distribution of the background.

In summary to be successfully camouflaged, a target should display both temperature and emissivity similarity and spatial similarity to its background [107]. Alot of techniques had been proposed to achieve thermal radiation invisibility, This can be achieved by covering the emitter with low-emissivity paints [122], [6], [38] where such thermal layers are fabricated to keep the thermal emission close to that of the background, thanks to the control of their infrared reflectance. However such techniques have to face the challenge of time temperature increase due to such isolation [100],

hence limiting their usage to relatively short time. On the other hand, Controlling TR can be done by controlling the temperature of the outer surface of the target, such technique has been active cloaking. Recent military stealth technology employs the concept of active cloaking where Peltier panels and thermal cameras are to be fixed on the surface of the cloaked object in order to detect the background temperature, and the Peltier panels are programmed to continually got heated or cooled accordingly [123]. Such technique can be employed for both thermal invisibility and illusion, however, the validity of the performance of such coating is strongly dependent on the contrast with background environment of the coated emitter. Another possible technology to control emissivity's dependence of the temperature is using negative differential thermal emittance which was reported for VO2 thin film deposited on saphire such that the thermal emissivity of decreases with increasing temperature > 10 degrees [54].

On the other hand, the application of TO theory upon thermal radiation for invisibility purposes was first reported in [108]. In this work, similarly to Pendry's cloak, a line is expanded into a finite region and the surroundings are transformed into a cloak such the background thermal radiation is guided around the cloaked object as shown in Fig.(1.11). Although this cloak is successfully fabricated and tested experimentally, such design suffers from few draw backs. First, the cloaking region acts as a cavity such that the thermal radiation of the cloaked thermal is not allowed to propagate towards the the thermal sensor. Second, if the cloak is extended to three dimensional case, the cloaked object will be totally isolated and its thermal radiation is trapped inside causing its temperature to increase till the peak wavelength becomes outside of the design's bandwidth. Another research [66] has been recently reported where a structured surface with an emissivity matches that of the background coats an opaque object. When the object and cloak are both coated with transformation thermotics (stedy state heat conduction) based cloak, an external IR detector cannot

detect the the cloaked object. Although this work has been verified numerically and experimentally, it suffers from a main constraint that the emissivity of the background has to be known apriori and such design cannot be used in the case of dynamically changing environment.

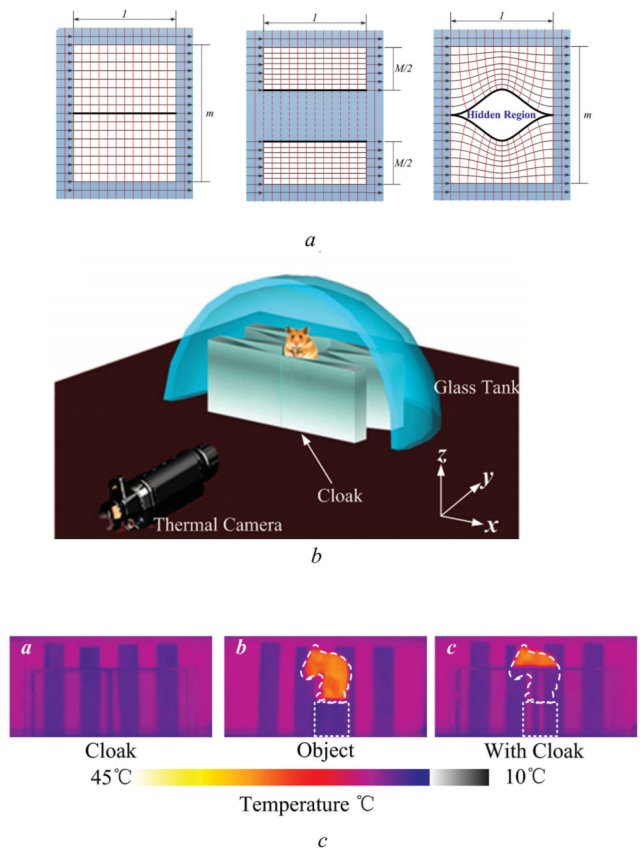

Figure 1.11: All figures are adapted from [108]. (a) schematic of the space transformation where a horizontal line is expanded into the hidden region. (b) Schematic of the experimental setup including the invisibility cloak, thermal detector and thermal emitting object to be cloaked (the mouse shaped toy). (c) Comparison of the thermal images read by the thermal detector.

In chapter III, we apply transformation optics theory to the thermal radiation problem to develop an electromagnetic illusion by controlling the thermal radiation signature of a given object. Starting from the fluctuation dissipation theorem where

thermally fluctuating sources are related to the radiative losses, we demonstrate that it is possible for objects residing in two spaces, virtual and physical, to have the same thermal radiation signature if the complex permittivities and permeabilities satisfy the standard space transformations. We show that the fluctuation electrodynamics physics is covariant under transformation or in other words FE has the same form under transformation.

1.3.3 Thermal radiation from meta-surfaces

Fluctuation electrodynamics theory is the extension of Nyquist noise theorem [90] of thermal noise in electrical conductors which was later formally reformulated by Callen and Welton [13] as Fluctuation dissipation theorem (FDT). Actually lot of physical phenomena are explained by FDT, among others, thermal radiation [102], thermal noise in electrical circuits [115]. Actually both phenomena are electromagnetic fluctuations with their physical origins are the same but occur at different wave length ranges. It is interesting to note that one can even use the same models to compute and control such behavior for example, electrical engineers design low noise electrical circuit components while physicists design photonic crystals with photonic band gaps to prohibits thermal radiation with the frequency range of the band-gap [75],[24] or just to tailor the emission properties [28] and [86]. Such similarity between the two phenomena propose that both can be analyzed by the same theoretical tools. Thermal noise in electrical systems is typically analyzed using electrical network theory, while thermal radiation is calculated by fluctuation electrodynamics by solving Maxwell's equation. Actually distributed and lumped circuit models are known to be used electromagnetic problems, for example, spectral transverse equivalent network is used to compute electromagnetic radiation from dipoles embedded in multilayer dielectric or modal transmission line model is used to compute for electromagnetic diffraction from multilayer diffraction gratings [96]. Other circuit models had been

used to model mutual coupling between cavities, proximity antennas and even electromagnetic propagation. Actually, it was S. Masloviski et al who proposed treating thermal radiation as thermal noise [78], [109] and using the former circuit models in both lumped forms to compute thermal radiation from arbitrary planar magneto-dielectric slabs [78] and for spherical shaped thermal emitters in [80]. A distributed circuit model for thermal noise from one dimensional transmission lines was proposed in [113]. In [79], without computations, Masloviski et al showed in analytically that the thermally radiated time averaged Poynting vector from arbitrary thermal emitter can computed in terms of the surface impedance in a similar manner the thermal noise power from the lumped N-port network was investigated in [115] and [40]. The main focus of the research work [80],[79], [109] and [78] is to maximize the thermal energy transfer between a thermal reservoir and energy collecting heat sink.

On the other hand, we are concerned with thermal radiation illusion. In chapter V, we propose using using lossy mantle metasurface in order to achieve thermal radiation illusion. Mantle metasurface were successful to achieve invisibility and scattering illusion using scattering cancellation technique. In a similar manner, scattering cancellation technique can be extended such that mantle meta-surfaces are used to achieve thermal radiation illusion. The electromagnetic properties of metasurface is typically quantified by its own surface impedance. Also, as it will be shown in chapter IV, meta-surfaces are the higher dimensional generalization of the lumped components of the one dimensional circuit network. Accordingly the former circuit models can be used to compute thermal radiation from a mantle meta-surface. Actually in chapter V, we will show that the surface impedance is the sole factor to control thermal radiation signature. In other words, in order to duplicate a thermal radiation pattern or signature it is enough to design the surface impedance.

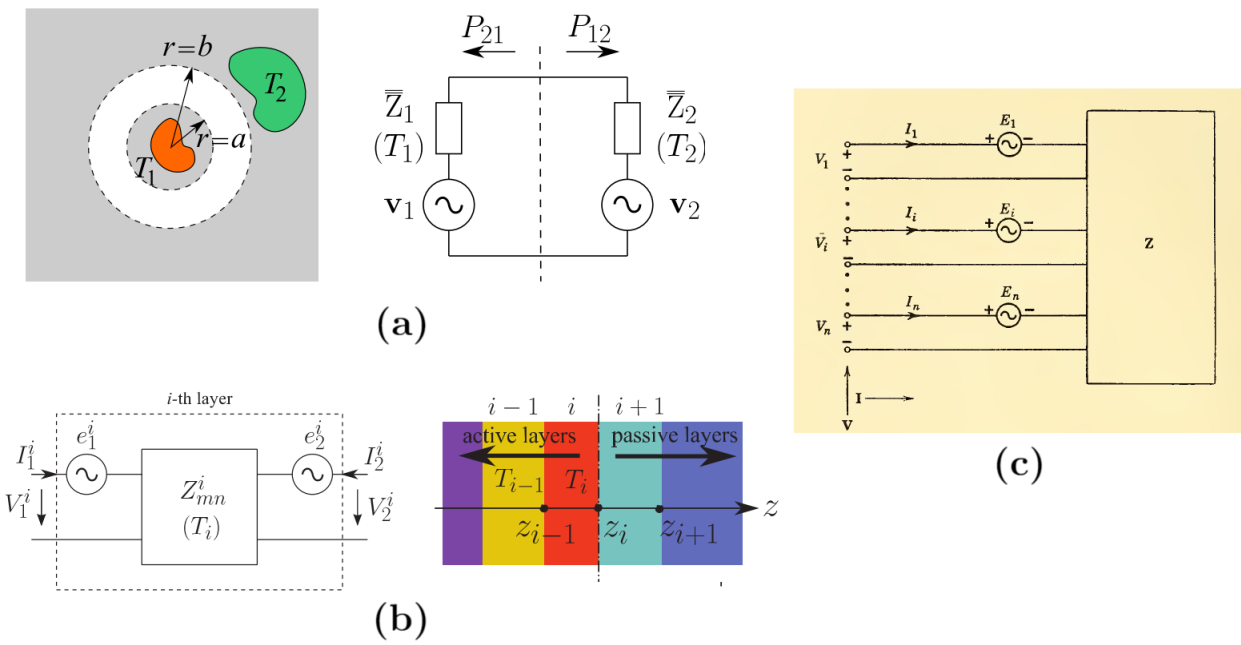

Figure 1.12: (a) A thermal emitter is located $r < a$ exchanging radiative heat with its surroundings located at $r > b$ and an equivalent circuit representing such heat exchange. Figure is adapted from [79].(b) stack of magneto dielectric planar multilayer and the equivalent four-pole network of layer i at thermal equilibrium at temperature $T = T_i$. Figure is adapted from [78]. (c) Thermal noise from N-port network can be used to compute thermal radiation an arbitrary object or a metasurface using their own surface impedance or admittance as it will be shown in chapter V. Figure is adapted from [40].

1.3.4 Near field thermal radiation computation

A lot numerical schemes had been proposed to compute thermal radiation from thermal emitters with arbitrary geometries based on FE [92]. First, analytical computations of thermal radiations are restricted to simple geometries that posses symmetries,i.e: planar [98], cylindrical and spherical [87] geometries. Thermal discrete dipole approximation (TDDA) is a discrete dipole approximation technique with the dipoles are fluctuating according to Eq.(1.21) while thermally radiated power are computed using the electric and magnetic green functions. Method of moments (also called boundary element method) had been reported, where thermal radiation is originated from surface fluctuating current [101]. Mode matching techniques had been

reported, for instance, in [87] radiated heat transfer between two spheres is computed based on the coupling between the spherical bases of both spheres, and coupling (the inner product) between these different set of bases is done using addition theorem. Finally, finite time difference scheme had been used where thermally radiated is time averaged over many simulation loops taking into consideration the statistical nature of the thermal sources.

In this work we make use of TDDA method with Maxwell's equations are solved by COMSOL 3.5A Multiphysics solver which uses finite element method technique. TDDA method with its COMSOl numerical implementation is summarized in appendix D. TDDA method is utilized for its relative simplest and easiness to implement and it is used to verify the different theoretical models proposed in this thesis.

1.4 Duality Transformation

Duality transformation [70], [68] which also recently referred to as Field transformation [71], is transformation in the vector field space. Duality transformation is based on the symmetry of electric and magnetic quantities in the Maxwell equations. Similar to transformation optics, it can be applied to obtain a solution for the dual problem through transforming the solution of the original problem [69]. The difference between transformation optics and duality transformation is shown in Fig.1.13. Duality transformation is limited in the sense that a dielectric media can be only transformed into non reciprocal media and also, in the sense that the transformation is space independent. Actually in [71], field transformation was combined with transformation optics to design an invisibility cloak for a purely dielectric cylinder completely transparent in air for both TE and TM polarizations. This is why in chapter VI, field transformation is investigated while investigating its effect on fluctuation electrodynamics theory.

In what follows duality transformation is summarized while showing its effect on fluctuation electrodynamics. Starting with Maxwell's equation in a medium with no free electric or magnetic charges (assuming time harmonic dependence $e^{i\omega t}$) as following:

$$\begin{aligned} \nabla \times \bar{E} &= -i\omega \bar{B} - \bar{K} \qquad & \nabla \cdot \bar{D} &= 0 \\ \nabla \times \bar{H} &= i\omega \bar{D} + \bar{J} \qquad & \nabla \cdot \bar{B} &= 0 \end{aligned} \tag{1.24}$$

where the bar sign to indicate vector quantity. $\bar{E}$, $\bar{D}$, $\bar{H}$ and$\bar{B}$ are electric and magnetic field intensities and densities respectively, and $\bar{\mathbf{J}}$ and $\bar{K}$ are the electric and magnetic current densities. A general Bi-an-isotropic (an-isotropic chiral) media can be characterized as by the following constitutive relation:

$$\begin{bmatrix} \bar{\mathbf{D}} \\ \bar{\mathbf{B}} \end{bmatrix} = \begin{bmatrix} \underline{\underline{\varepsilon}} & \underline{\underline{\xi}} \\ \underline{\underline{\zeta}} & \underline{\underline{\mu}} \end{bmatrix} \begin{bmatrix} \bar{E} \\ \bar{H} \end{bmatrix} = \underline{\underline{M}} \begin{bmatrix} \bar{\mathbf{E}} \\ \bar{H} \end{bmatrix} \tag{1.25}$$

where $\underline{\underline{\varepsilon}}$, $\underline{\underline{\mu}}$, $\underline{\underline{\zeta}}$ and $\underline{\underline{\xi}}$ are the permeability, permeability, magneto-electric and electromagnetic coupling coefficients. In general, chiral media can be either reciprocal or nonreciprocal depending on the relation between the magneto-electric $\underline{\underline{\xi}}$ and electromagnetic $\underline{\underline{\zeta}}$ coefficients. A reciprocal chiral media (also named Pasteur media) will have the condition $\underline{\underline{\zeta}} = -\underline{\underline{\xi}}^{\tau}$, where τ is a matrix transpose sign. If the former condition is not satisfied then the media is not reciprocal. A special case of the nonreciprocal media is when $\underline{\underline{\zeta}} = \underline{\underline{\xi}}$, this chiral media is named Tellengen media.

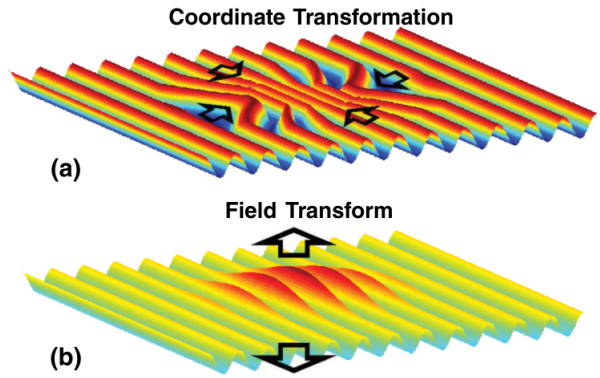

Figure 1.13: Schematic showing the differnec between transformation optics and field transformation. Fig. is adapted from [71]

Duality transformation is defined as following:

$$\begin{bmatrix} \bar{E}' \\ \bar{H}' \end{bmatrix} = \underline{\underline{U}} \begin{bmatrix} \bar{E} \\ \bar{H} \end{bmatrix} = \begin{bmatrix} cos(\alpha) & sin(\alpha) \\ -sin(\alpha) & cos(\alpha) \end{bmatrix} \begin{bmatrix} \bar{E} \\ \bar{H} \end{bmatrix} \tag{1.26}$$

where $\alpha \in$ Re is a real variable with support $[0, 2\pi]$. In general, the variable α is space dependent, $\alpha = \alpha(x, y, z)$. However α is typically assumed to be constant and independent of space so the whole space is transformed [106]. The transformation $\underline{\underline{U}}$ is a rotation in the $E - H$ space with angle α. Also, note that $\underline{\underline{U}}^{-1} = \underline{\underline{U}}^{\tau}$. Maxwell's Eq.s must be invariant upon transformation to physical space, then Maxwell's Eq.s must be written as following:

$$\begin{aligned} \nabla \times \bar{E}' &= -i\omega \bar{B}' - \bar{K}' \\ \nabla \times \bar{H}' &= i\omega \bar{D}' + \bar{J}' \end{aligned} \tag{1.27}$$

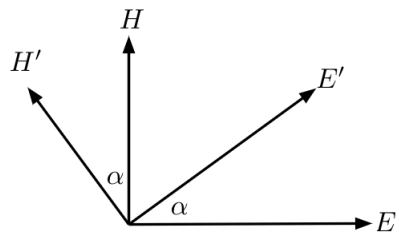

Figure 1.14: Schematic for the Duality transformation of Eq.(1.26).

Starting with Maxwell's Eq.s in the virtual space, and by re-arranging them in a vector form as following:

$$\nabla \times \begin{bmatrix} \bar{E} \\ \bar{H} \end{bmatrix} = i\omega \underline{\underline{R}} \begin{bmatrix} \bar{D} \\ \bar{B} \end{bmatrix} + \underline{\underline{R}} \begin{bmatrix} \bar{J} \\ \bar{K} \end{bmatrix} = j\omega \underline{\underline{R}}\, \underline{\underline{M}} \begin{bmatrix} \bar{E} \\ \bar{H} \end{bmatrix} + \underline{\underline{R}} \begin{bmatrix} \bar{J} \\ \bar{K} \end{bmatrix} \tag{1.28}$$

Note that $\underline{\underline{R}} = \begin{bmatrix} 0 & -1 \\ 1 & 0 \end{bmatrix}$ and $\underline{\underline{R}}^{\tau} = \underline{\underline{R}}^{-1}$. On the other side, Maxwell's Eq in the physical space is arranged in matrix form as following:

$$\nabla \times \begin{bmatrix} \bar{E}' \\ \bar{H}' \end{bmatrix} = i\omega \underline{\underline{R}} \begin{bmatrix} \bar{D}' \\ \bar{B}' \end{bmatrix} + \underline{\underline{R}} \begin{bmatrix} \bar{J}' \\ \bar{K}' \end{bmatrix} = j\omega \underline{\underline{R}}\, \underline{\underline{M}}' \begin{bmatrix} \bar{E}' \\ \bar{H}' \end{bmatrix} + \underline{\underline{R}} \begin{bmatrix} \bar{J}' \\ \bar{K}' \end{bmatrix} \tag{1.29}$$

To ensure the invariance of physics under transformation, the transformation of the fields and sources is as following:

$$\begin{bmatrix} \bar{D}' \\ \bar{B}' \end{bmatrix} = \underline{\underline{U}} \begin{bmatrix} \bar{D} \\ \bar{B} \end{bmatrix} \qquad \begin{bmatrix} \bar{J}' \\ \bar{K}' \end{bmatrix} = \underline{\underline{R}}^{-1}\, \underline{\underline{U}}\, \underline{\underline{R}} \begin{bmatrix} \bar{J} \\ \bar{K} \end{bmatrix} = \underline{\underline{U}} \begin{bmatrix} \bar{J} \\ \bar{K} \end{bmatrix} \tag{1.30}$$

also we find that the media is transformed:

$$\begin{aligned} \underline{\underline{M}}' &= \underline{\underline{R}}^{-1}\, \underline{\underline{U}}\, \underline{\underline{R}}\, \underline{\underline{M}}\, \underline{\underline{U}}^{-1} \\ &= \underline{\underline{U}}\, \underline{\underline{M}}\, \underline{\underline{U}}^{-1} \end{aligned} \tag{1.31}$$

Note that $\underline{\underline{U}} = \underline{\underline{R}}\,\underline{\underline{U}}\,\underline{\underline{R}}^{-1}$. Applying the duality transforming upon a virtual space with a non-chiral dielectric anisotropic media, with the relative constitutive parameters $\underline{\underline{M}}_d = \begin{bmatrix} \underline{\underline{\varepsilon}}_d & \underline{\underline{0}} \\ \underline{\underline{0}} & \underline{\underline{\mu}}_d \end{bmatrix}$ (the subscript d is for dielectric) is transformed into another media $\underline{\underline{M}}' = \begin{bmatrix} \underline{\underline{\varepsilon}}' & \underline{\underline{\xi}}' \\ \underline{\underline{\zeta}}' & \underline{\underline{\mu}}' \end{bmatrix}$, where the relation between the constitutive parameters of both physical and virtual spaces is as following:

$$
\begin{aligned}
\underline{\underline{\varepsilon}}' &= \underline{\underline{\varepsilon}}_d\, cos^2(\alpha) + \underline{\underline{\mu}}_d\, sin^2(\alpha) \\
\underline{\underline{\mu}}' &= \underline{\underline{\varepsilon}}_d\, sin^2(\alpha) + \underline{\underline{\mu}}_d\, cos^2(\alpha) \\
\underline{\underline{\zeta}}' = \underline{\underline{\xi}}' &= (\underline{\underline{\mu}}_d - \underline{\underline{\varepsilon}}_d)\, cos(\alpha) sin(\alpha)
\end{aligned}
\tag{1.32}
$$

The condition $\underline{\underline{\zeta}}' = \underline{\underline{\xi}}'$ indicates that the resulting media is nonreciprocal Tellengen media. It is can be said that duality transforming a reciprocal nonchiral media only results in a nonreciprocal Tellengen media, and there exist no duality transformation that can transform a reciprocal non-chiral media into a reciprocal chiral media (pasteur media), since the $\underline{\underline{M}}$ matrix of a reciprocal media is anti-symmetric and there is no real transformation exist to transform a symmetric matrix into anti-symmetric one [106].

On the other hand, Fluctuation electrodynamics in a nonreciprocal chiral media can be derived by first considering a virtual space with a dielectric media where the spectral correlation of the thermal electric and magnetic currents are already shown

in Eq.(1.21), but they can be rewritten are as following:

$$\left\langle \bar{J}\bar{J}^{\dagger} \right\rangle_{\omega} = \frac{4\omega}{\pi}\theta(\omega,T) Im\{\underline{\epsilon}\}$$
$$\left\langle \bar{K}\bar{K}^{\dagger} \right\rangle_{\omega} = \frac{4\omega}{\pi}\theta(\omega,T) Im\{\underline{\underline{\mu}}\}$$
$$\left\langle \bar{J}\bar{K}^{\dagger} \right\rangle_{\omega} = \left\langle \bar{K}\bar{J}^{\dagger} \right\rangle_{\omega} = 0$$

Now by applying the duality transformation so the virtual space is transformed into a physical space with non reciprocal chiral media. Then the spectral correlation in the physical space is calculated in terms of the spectral correlation in the virtual space. From Eq.(1.30), the transformation of the cross spectral correlation of the thermal electric and magnetic currents from the virtual space into the the physical space is written as following:

$$\left\langle \begin{bmatrix} \bar{J}' \\ \bar{K}' \end{bmatrix} \begin{bmatrix} \bar{J}' & \bar{K}' \end{bmatrix} \right\rangle_{\omega} = \underline{\underline{U}} \left\langle \begin{bmatrix} \bar{J}_d \\ \bar{K}_d \end{bmatrix} \begin{bmatrix} \bar{J}_d & \bar{K}_d \end{bmatrix} \right\rangle_{\omega} \underline{\underline{U}}^{\tau} = \frac{4\,\omega}{\pi}\theta(\omega,T)\underline{\underline{U}}\; Im\{\underline{\underline{M}}\}\; \underline{\underline{U}}^{\tau} \tag{1.33}$$

and since according to FE in the virtual space, the spectral correlation of the thermal current sources in the virtual space are related to the media losses in the same space as following :

$$\left\langle \begin{bmatrix} \bar{J}_d \\ \bar{K}_d \end{bmatrix} \begin{bmatrix} \bar{J}_d & \bar{K}_d \end{bmatrix} \right\rangle_{\omega} = \begin{bmatrix} \left\langle \bar{J}_d \bar{J}_d^{*} \right\rangle_{\omega} & 0 \\ 0 & \left\langle \bar{K}_d \bar{K}_d^{*} \right\rangle_{\omega} \end{bmatrix} = \frac{4\,\omega}{\pi}\theta(\omega,T)\; Im\{\underline{\underline{M}}_d\} \tag{1.34}$$

Note that in the virtual space the electric and magentic currents are uncorrelated. but since the media in the physical is related to that of the virtual space according to Eq.(1.31) and since $\underline{\underline{U}} \in$ Re, then

$$Im\{\underline{\underline{M}}'\} = \underline{\underline{U}}\; Im\{\underline{\underline{M}}\}\; \underline{\underline{U}}^{\tau} \tag{1.35}$$

substituting Eq.(1.35) into Eq.(1.33), then the spectral correlations of the thermal curret sources in the physical space will be as following:

$$\left\langle \begin{bmatrix} \bar{J}' \\ \bar{K}' \end{bmatrix} \begin{bmatrix} \bar{J}' & \bar{K}' \end{bmatrix} \right\rangle_{\omega} = \frac{4\omega}{\pi}\theta(\omega,T)Im\{\underline{\underline{M}}'\} \tag{1.36}$$

the cross correlations are transformed explicitly as following

$$\begin{aligned} \langle J'J'^{*}\rangle_{\omega} &= \langle J_d J_d^{*}\rangle_{\omega}\, cos^2(\theta) + \langle K_d K_d^{*}\rangle_{\omega}\, sin^2(\theta) \\ \langle K'K'^{*}\rangle_{\omega} &= \langle J_d J_d^{*}\rangle_{\omega}\, sin^2(\theta) + \langle K_d K_d^{*}\rangle_{\omega}\, cos^2(\theta) \\ \langle K'J'^{*}\rangle_{\omega} = \langle J'K'^{*}\rangle_{\omega} &= (\langle K_d K_d^{*}\rangle_{\omega} - \langle J_d J_d^{*}\rangle_{\omega})\, cos(\theta)sin(\theta) \end{aligned} \tag{1.37}$$

Eq.(1.37) shows the spectral correlation of thermal currents in the physical space and due to the chirality the thermal electric and magnetic currents are correlated. It is interesting to notice that the cross correlation between thermal electric and magnetic current has the following property

$$\begin{aligned} \langle K'J'^{*}\rangle_{\omega} &= \langle J'K'^{*}\rangle_{\omega} \\ \text{but}\ \ \langle K'J'^{*}\rangle_{\omega} &= \langle J'K'^{*}\rangle_{\omega}^{*} \\ \text{then}\ \ \langle K'J'^{*}\rangle_{\omega} &= \langle J'K'^{*}\rangle_{\omega} \in \mathrm{Re} \end{aligned} \tag{1.38}$$

which is a consequence of the equality of $\underline{\underline{\zeta}}' = \underline{\underline{\xi}}'$ as shown in Eq.(1.32). The former property of the cross correlation is a property of the non-reciprocal media which is different from the spectral cross correlation from reciprocal media as will be shown in chapter VI. It is important to mention FE of nonreciprocal was derived using duality transformation in [12] based on electromagnetic quantization and Similar expressions for FE were derived in [12], the difference between our expressions and those in [11] are due to the way thermal sources are defined, here we defined thermal electric and magnetic currents which are treated on equal footing, while in [11], only fluctuating

electric current densities exist.

CHAPTER II

Controlling Temperature Signature using Transformation Optics

2.1 Introduction

In a typical illusion/ mimicking scenario, a passive thermal emitter is surrounded by some heat sources and sinks where the thermal emitter exchange heat through conduction, convection and radiation. In normal circumstances, heat conduction dominates the energy transport processes inside the thermal emitter, so temperature distribution can be approximated by solving for Fourier's equation of heat diffusion while in the same time convection and radiation are ignored. As it will be discussed in the chapter III, at thermal equilibrium, thermal radiation from thermal emitters is just electromagnetic radiation with the electromagnetic sources of radiation are thermal current sources embedded in the thermal emitters. These thermal currents are random sources of radiation and their statistical properties depend on the local temperature distribution through the implicit dependence of Planck's function of the local temperature according to fluctuation electrodynamics theorem.

In chapter III, it will be shown that, to successfully achieve thermal illusion, the temperature distribution has to be transformed between the two spaces such that

the temperature at each point in one space has to be equal to the temperature at its corresponding image point. In this chapter, we apply transformation optics to space transform between two different objects such that when objects are located in the same thermal environment or the same boundary value problem, they "scatter" or induce the same temperature signature outside their bounding surface. In this frame work we utilize Fourier's law of heat diffusion with the temperature field $T(\bar{r})$ is the equations' dependent quantity of the space coordinates $\bar{r} = \{x, y\}$. Such transformation is implemented by manipulating the thermal conductivity tensors and density-heat capacitance products. Since temperature is a scalar field, It is invariant under transformation, this is why the approach of this chapter can be integrated with Transformational Fluctuation Electrodynamics illustrated in chapter III.

On the other side, in the literature of transformation optics, the objects to cloak or to mimic emphasize arbitrary matrix gradients of their physical parameters, thereby making them difficult to produce. Furthermore, this constraint reduces the field of practical applications because we do not really choose what we are able to hide or camouflage. In practice, one would be interested in working with predefined objects of given shape and conductivity, and these objects would be over-coated to mimic other predefined objects beyond the cloak. Such an inverse engineering problem introduces constraints that restrict the range of space transformations, thereby classifying the set of objects that can be mimicked with another one which is beforehand chosen and must be over-coated. Because all conductivities are forced, the remaining degrees of freedom lie in the shape of the objects and in the set of specific cloaks that surround them. Also, as known, the temperature distribution inside an object depends on its thermal conductivity tensor, heat capacitance and its own shape. When space transforming the object, we find that the object's image parameters (thermal conductivity heat capacitance and shape) are interdependent and specific conditions has

to be satisfied. So We address a general inverse mimicking problem in heat conduction. The objects to cloak and mimic are chosen beforehand; these objects identify a specific set of space transformations. Here we analyze the inverse problem where the thermal parameters are driven and the shape of the objects are derived based on the constraints driven. This chapter is outlined as following , in section (2.2) the inverse transformation scheme is explained, then in section (2.3) the constraints on the thermal parameters of the objects to mimic and cloak are detailed adapting the transformation optics theory which are summarized in appendix B; Then in section (2.4), we will show how to design the illusion coat, in both static and dynamic regimes. At the static or steady state regime $t \Rightarrow \infty$ where it is assumed that the all the transient fluctuations due the starting operation of the external thermal sources had died out. In such case only the frontiers and thermal conductivities are the effective parameters such the constraints due the density-heat capcitance product ρC are excluded. In the case of dynamic regime, the same conditions on the thermal conductivities have to be satisfied beside extra conditions on ρC. In Section section (2.5) results due to performed numerical simulations for both static and time harmonic will be shown and they are in accordance with the analysis depicted in the precedent sections. Finally the chapter's conclusion is included section (2.6).

2.2 Inverse Transformation

Consider in Fig.(2.1) (right side) a thermal object with conductivity matrix κ_Ω resides within domain Ω limited by surface $\partial\Omega$. This object scatters a specific heat flow q_Ω in its surroundings in relation to its geometry $\partial\Omega$ and its thermal parameters, together with the position and nature of thermal sources. Assume now that one aims at mimicking the heat flux q_ω of another thermal object shown in Fig.(2.1) (left side), with conductivity κ_ω within domain ω limited by surface $\partial\omega$. To achieve this goal, a cloak is used to fill domain E/Ω limited by surfaces E and $\partial\Omega$. This cloak surrounds

the thermal object Ω, and its function is to transform its flux q_Ω to mimic outside the cloak the flux q_ω of object ω.

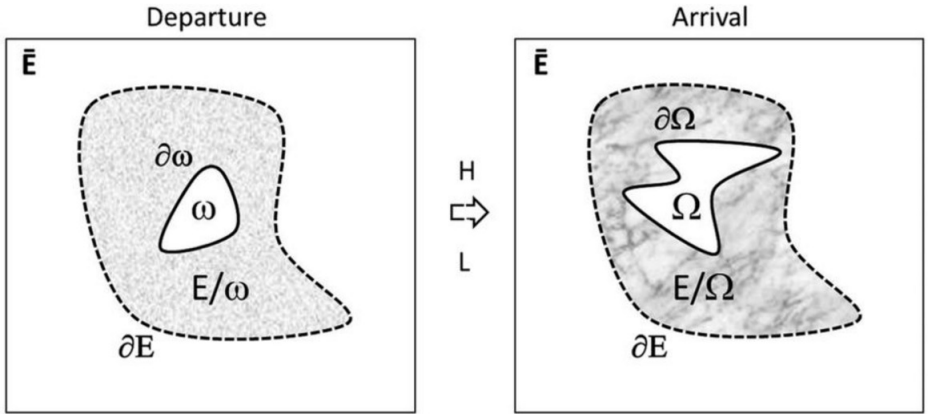

Figure 2.1: left: Departure (virtual) space where the object to be mimicked $\partial\omega$ resides. b) Arrival (physical) space where the object to be mimic $\partial\Omega$ and the coat (cloak) reside. The function of the cloak is to mimic, in the domain $\bar{E}$, the flux of another predefined object ω given on the left side (departure space). H and L are space transformations from the departure space to the arrival space.

In other words, one should have in region $\bar{E}$ outside the cloak (outside ∂E). Following Fig.2.1, one key problem is to find the cloak filling region E/Ω and its thermal parameters. The nature and existence of this cloak depend on the two objects to be cloaked (Ω) and mimicked (ω), including both their thermal parameters and their frontiers (outer surfaces $\partial\Omega$ and $\partial\omega$). In addition, the cloak depends on the object ω surrounding (E/Ω). To solve this problem, we use transformation optics theory (see appendix B), and the necessary conditions to be satisfied in this problem:

- The heat fluxes in at the regions $\bar{E}$ in both spaces is the same

$$q_\Omega(\bar{E}) = q_\omega(\bar{E}) \tag{2.1}$$

- H transformation that transforms ω into Ω:

$$H(\omega) = \Omega. \tag{2.2}$$

- L transformation that transforms E/ω into E/Ω:

$$L(E/\omega) = E/\Omega \tag{2.3}$$

Since the heat flux q_ω is continuous across the boundaries ∂E and $\partial\omega$, then the heat flux q_Ω must be continuous across the corresponding boundary ∂E and $\partial\Omega$, so the transformations H and L must satisfy:

$$H(\partial\omega) = L(\partial\omega) = \partial\Omega \tag{2.4}$$

$$L(\partial E) = \partial E \tag{2.5}$$

Based on the conditions (2.1,2.5), It is expected that not only design of the cloak is constrained but also the objects ω that can be mimicked for a given object Ω. According to transformation optics theory, the thermal parameters of the objects should be related as:

$$[\kappa_\Omega] = \frac{1}{det(M_H)}[M_H][\kappa_\omega][M_H]^\tau \tag{2.6}$$

$$(\rho C)_\Omega = \frac{1}{det(M_H)}(\rho C)_\omega \tag{2.7}$$

where κ is the thermal conductivity tensor, (ρC) is the product of bulk density and heat capacitance, and $[M_H]$ is the Jacobian matrix of the transformation H, M_H is further detailed in section (2.3). $[M_H]^\tau$ is its transposed form (with τ is the transposing operator), and $det(M_H)$ is its determinant. Similar constraints must be satisfied for the cloak, that is:

$$[\kappa_{E/\Omega}] = \frac{1}{det(M_L)}[M_L][\kappa_{E/\omega}][M_L]^\tau \tag{2.8}$$

$$(\rho C)_{E/\Omega} = \frac{1}{det(M_L)}(\rho C)_{E/\omega} \tag{2.9}$$

Based on Eq.s (2.6,2.9), the two objects Ω and ω cannot be predefined with arbitrarily thermal parameters and frontiers, since transformation optics force several relationships between Ω and ω.

Accordingly, we define the inverse as the process of the cloak designing where for given degrees of freedom, we calculate for the dependent parameters. At this step, the degrees of freedom must be analyzed. Let us first consider Eq.(2.6) which relates the anisotropic conductivities of the objects to cloak κ_Ω and to mimic κ_ω. When these two conductivity matrices are fixed, Eq.(2.6) reduces the set of possible H transformations with a constraint in the form:

$$\{H_\sigma\} \mid \{M_H\} = \{M_H(\kappa_\omega, \kappa_\Omega)\} : \sigma \text{ is an index} \tag{2.10}$$

Hence, solutions of Eq.(2.10) will emphasize a specific set $\{H_\sigma\}$ of transformations that connect the two object conductivity matrices in ω and Ω. At this step, the remaining degrees of freedom lie in the frontiers ($\partial\omega$ and $\partial\Omega$), that are, in the outer profiles (shapes) of the objects. Therefore, if we choose one object Ω to cloak with its conductivity κ_Ω and shape $\partial\Omega$ are predefined, then the class of objects ω with given conductivity $\partial\omega$ that can be mimicked exhibits a set of shapes belonging to:

$$\partial\omega_\sigma = H_\sigma^{-1}(\partial\Omega) \tag{2.11}$$

Notice that the roles of the shape and conductivity can be interchanged in this inverse problem. One interesting point is that the cloak introduces no additional constraint on the object to coat and it is deduced from the constraints. Indeed, when all frontiers ($\partial\omega$, $\partial\Omega$ and ∂E) are given, the transformation L can always be

determined, and relation (2.8) gives the matrix conductivity of the cloak.

However, one cannot ignore further constraints resulting from the (ρC) products given in relations (2.7, 2.9) that force the matrix determinants of M_H and M_L. When the (ρC) products are forced, the additional constraints again restrict the set of transformations and may prevent the existence of solutions. Otherwise, one must consider that the (ρC) products are arbitrary, at least for one of the two objects. Another approach to overcome this issue is to start with a problem first limited to the static regime of the heat equation and focus the investigation on the connection between shape and conductivity. Subsequently, the ρC constraints will be analyzed case by case for the dynamic regime. The inverse transformation problem in the static is studied then the dynamic regime in section(2.3).

2.3 Inverse Transformation at the Static regime

Since the constraints on the cloak are mainly imposed by the objects $\omega$and Ω, so in the first part of this section, the analytical formulation of the two-dimensional inverse problem in polar coordinates is outlined , then we study the analytically traceable cases where the two objects to cloak (Ω) and to mimic (ω) are predefined in conductivity, together with the $\partial\Omega$ frontier, which forces the set of possible H transformations and thus the range of $\partial\omega$ shapes.In what follows we focus on the case where ω is of isotropic thermal conductivity.

Analytical formulation of the two-dimensional problem in polar coordinates Here, we focus on searching for the H transformations that can satisfy Eq. (2.6), when the two conductivity matrices are forced. For this purpose, the M_H matrix is first analyzed in detail. An analytical calculation can be developed if we simplify the problem by considering a 2D geometry with polar coordinates (r, θ). The transformation is written as:

$$H(r,\theta) = (r^{'}, \theta^{'}) = [f_H(r,\theta), g_H(r,\theta)] \tag{2.12}$$

where r and $r^{'}$ are the radial distances in the departure and arrival spaces, respectively, and θ and $\theta^{'}$ are the polar angles in the departure and arrival spaces, respectively. The transformation H is expressed in terms of the $r^{'} = f_H(r,\theta)$ and $\theta^{'} = g_H(r,\theta)$ where $f_H$and g_H are the transformation functions to be specified. The M_H matrix is the Jacobian matrix of the transformation and it relates the gradient operators of polar coordinate systems in the departure and arrival spaces as following:

$$\nabla_{r,\theta} T(r,\theta) = [M]^{\tau} \nabla_{r^{'},\theta^{'}} T(r^{'}, \theta^{'}) \tag{2.13}$$

with the temperature T and since,

$$\nabla_{r,\theta} T(r,\theta) = [\frac{\partial T}{\partial r}, (\frac{1}{r})\frac{\partial T}{\partial \theta}] \tag{2.14}$$

$$\nabla_{r^{'},\theta^{'}} T(r^{'}, \theta^{'}) = [\frac{\partial T}{\partial r^{'}}, (\frac{1}{r^{'}})\frac{\partial T}{\partial \theta^{'}}] \tag{2.15}$$

then the Jacobian matrix M_H with dimensionless coefficients will be:

$$M_H = \begin{bmatrix} \partial r^{'} \ / \ \partial r & \partial r^{'} \ / \ r\partial\theta \\ r^{'}\partial\theta^{'} \ / \ \partial r^{'} & r^{'}\partial\theta^{'} \ / \ r\partial\theta \end{bmatrix} \tag{2.16}$$

Case of a heterogeneous isotropic object ω; Let us here consider that the object ω to mimic is isotropic (but still heterogeneous). The result is that κ_ω is a scalar quantity, and this allows us to turn relation (2.6) into:

$$[\kappa_\Omega] = \kappa_\omega [T_\Omega] \ \text{ with } \ [T_\Omega] = \frac{1}{det(M_H)} [M_H][M_H]^{\tau} \tag{2.17}$$

with $[T_\Omega]$ a symmetric tensor with unity determinant, so that:

$$det(T_\Omega) = 1 \Rightarrow det(\kappa_\Omega) = \kappa_\omega^2 \tag{2.18}$$

At this step, the constraint on the H transformation is fully given by this tensor, which is now forced to follow:

$$[T_\Omega] = \frac{1}{\kappa_\omega}[\kappa_\Omega] \Rightarrow H \in \{H_\mu\} \tag{2.19}$$

Because the two conductivities are given, this condition reduces the range of shapes $\partial\omega$ that can be mimicked with a material of frontier $\partial\Omega$ surrounded by a cloak (see Eq. (2.11)). Finally, introducing (2.16) into (2.17) gives the tensor T_Ω in terms of two vectors u and v as follows:

$$[T_\Omega] = \frac{1}{\mathbf{z} \cdot (\mathbf{u} \times \mathbf{v})} \begin{bmatrix} \mathbf{u}^2 & \mathbf{u} \cdot \mathbf{v} \\ \mathbf{u} \cdot \mathbf{v} & \mathbf{v}^2 \end{bmatrix} \tag{2.20}$$

where $(\cdot)$ and $(\times)$ are the vector calculus typical scalar and vector products, respectively, and:

$$\mathbf{u} = \nabla_{r,\theta}(r^{'}) \quad \mathbf{v} = \nabla_{r,\theta}(\theta^{'}) \tag{2.21}$$

In summary, the conductivity matrix $[\kappa_\Omega]$ of the object Ω is entirely given in Eq.(2.20) by the knowledge of two vectors $\mathbf{u}$ and $\mathbf{v}$ resulting from the H transformation. Writing the conductivity as:

$$[\kappa_\Omega] = \begin{bmatrix} \kappa_{rr} & \kappa_{r\theta} \\ \kappa_{\theta r} & \kappa_{\theta\theta} \end{bmatrix} \tag{2.22}$$

we obtain its matrix coefficients as:

$$\frac{\kappa_{rr}}{\kappa_\omega} = \frac{\mathbf{u}^2}{\mathbf{z}\cdot(\mathbf{u}\times\mathbf{v})} \tag{2.23}$$

$$\frac{\kappa_{\theta\theta}}{\kappa_\omega} = \frac{\mathbf{v}^2}{\mathbf{z}\cdot(\mathbf{u}\times\mathbf{v})} \tag{2.24}$$

$$\frac{\kappa_{r\theta}}{\kappa_\omega} = \frac{\mathbf{u}\cdot\mathbf{v}}{\mathbf{z}\cdot(\mathbf{u}\times\mathbf{v})} \tag{2.25}$$

with **(u, v, z)** are independent vectors (**u** and **v** are not necessarily orthogonal). Since all conductivities are chosen beforehand, the unknowns are the two vectors **(u,v)** that are transformation-related according to Eq.s(2.23,2.25) which are the conditions to be satisfied in the inverse transformation problem.In accordance with Eq. (2.18), Eq.s (2.23,2.25) also yield:

$$det(\kappa_\Omega) = \kappa_{rr}\kappa_{\theta\theta} - \kappa_{r\theta}^2 = \kappa_\omega^2 \tag{2.26}$$

We notice that relation (2.25) requires the conductivity matrix to be symmetrical, which has to be always true [93]. In addition, we keep in mind that in the dynamic (temporal) regime, one would also have to consider the transformation of the (ρC) products given as:

$$\frac{(\rho C)_\Omega}{(\rho C)_\omega} = \frac{1}{det(M_H)} = \frac{1}{\mathbf{z}\cdot(\mathbf{u}\times\mathbf{v})} \tag{2.27}$$

Case of Ω with a diagonal conductivity matrix In the previous subsection, we assumed that the object ω to mimic was isotropic (but still can be heterogeneous). In addition, we here consider that the anisotropic object Ω to cloak has a diagonal conductivity matrix, that is:

$$\kappa_{r\theta} = \kappa_{\theta r} = 0 \tag{2.28}$$

Following Eq.(2.26), the two other conductivity coefficients in the matrix follow:

$$\kappa_{rr}\kappa_{\theta\theta} = \kappa_{\omega}^{2} \tag{2.29}$$

Furthermore, relation (2.25) forces the orthogonality of the two real u, v vectors that define the $[T_{\Omega}]$ tensor. The relative angle between them can be quantified as following

$$\mathbf{u} = |\mathbf{u}|(cos\phi_u, sin\phi_u) \text{ and } \mathbf{v} = |\mathbf{v}|(cos\phi_v, sin\phi_v) \tag{2.30}$$

so that the relative angle is the difference $\phi_v - \phi_u$

$$(\mathbf{u} \cdot \mathbf{v}) = 0 \Rightarrow \phi_v - \phi_u = (2k+1)(\frac{\pi}{2}) \tag{2.31}$$

with k is a relative integer. To avoid negative values of the ρC products (see Eq. (2.27), we restrain this direction difference to the condition:

$$det(M_H) > 0 \Rightarrow \phi_v - \phi_u = \frac{\pi}{2} \tag{2.32}$$

In addition, such choice yields the condition:

$$(\frac{\partial r'}{\partial \theta})(\frac{\partial \theta'}{\partial \theta}) = -(\frac{\partial r'}{\partial r})(\frac{\partial \theta'}{\partial r}) \tag{2.33}$$

Among this set of solutions that allow the conductivity matrix $[\kappa_{\Omega}]$ to be diagonal, one can explore a subset with the direction property:

$$\phi_u = 0,\ \phi_v = \frac{\pi}{2} \Rightarrow \mathbf{u} = |\mathbf{u}|(1,0),\ \mathbf{v} = |\mathbf{v}|(1,0) \tag{2.34}$$

Following Eq.(2.21), the final result is:

$$\frac{\partial r'}{\partial \theta} = 0 \text{ with } \frac{\partial \theta'}{\partial r} = 0 \tag{2.35}$$

so that the polar and radial variations are independent in the transformation, that is:

$$r^{'} = f_H(r) \;\; \theta^{'} = g_H(\theta) \tag{2.36}$$

With this last property, the conductivity matrix becomes:

$$[\kappa_\Omega] = \kappa_\omega \begin{bmatrix} \frac{u}{v} & 0 \\ 0 & \frac{v}{u} \end{bmatrix} \tag{2.37}$$

$$u = \frac{\partial r^{'}}{\partial r} = \frac{\partial f_H}{\partial r} \;\text{ and }\; v = \frac{r^{'}}{r}\frac{\partial \theta^{'}}{\partial \theta} = \frac{f_H}{r}\frac{\partial g_H}{\partial \theta} \tag{2.38}$$

As a consequence, the key equations of the inverse problem can now be summarized as:

$$\kappa_{rr}(r,\theta) = \kappa_\omega(r,\theta)\{r\frac{\frac{\partial f_H}{\partial r}}{f_H\frac{\partial g_H}{\partial \theta}}\} \tag{2.39}$$

$$\kappa_{\theta\theta}(r,\theta) = \frac{\kappa_\omega^2(r,\theta)}{\kappa_{rr}(r,\theta)} \tag{2.40}$$

To conclude, Eq.s (2.39,2.40) guarantee the fact that the object Ω with diagonal conductivity matrix $[\kappa_\Omega(\kappa_{rr},\kappa_{\theta\theta})]$ can be cloaked to mimic (in the static regime) a class of isotropic objects ω with heterogeneous isotropic conductivity κ_ω. The shape $\partial\omega$ of these objects can now be discussed because the f_H and g_H functions are given versus the conductivity values. In addition, we notice again that in the dynamic regime, the additional constraint on the ρC product is written as:

$$(\rho C)_\Omega \;/\; (\rho C)_\omega = r \;/\; [f_H(\frac{\partial f_H}{\partial r})(\frac{\partial g_H}{\partial \theta})] \tag{2.41}$$

In some situations, these constraints can be compatible with those of the conductivities, for which reason they are recalled at each step.

Identification of the shapes that can be mimicked: Next, we work with Eq. (2.39), which identifies the H transformation because the two conductivities $[\kappa_\Omega]$ and κ_ω are fixed beforehand. When this transformation is known, we determine the shapes $\partial\omega$ that can be mimicked when $\partial\Omega$ is chosen, on the basis of Eq.s (2.11,2.19). The key equation to satisfy is rewritten as:

$$r\frac{\partial f_H}{\partial r} \,/\, [f_H(r)\frac{\partial g_H}{\partial \theta}] = \kappa_{rr}(r,\theta) \,/\, \kappa_\omega(r,\theta) = \eta(r,\theta) \tag{2.42}$$

In what follows, The unknowns are the f_H and g_H functions to be computed. The conductivity ratio $\eta(r,\theta)$ will be considered for three different cases a

- constant $\eta(r,\theta) = \eta$.
- function of the radial coordinate r only, $\eta(r,\theta) = \eta(\theta)$
- function of the polar coordinate θ only, $\eta(r,\theta) = \eta(\theta)$
- product of functions of the radial only and the polar coordinate only $\eta(r,\theta) = \eta_r(r)\eta_2(\theta)$.

Case of similar heterogeneities in both objects with $\eta(r,\theta) = \eta$: Now η is considered to be a constant; Then terms in Eq. (42) can be separated into θ and r dependent terms:

$$r(\frac{\partial f_H}{\partial r}) \,/\, f_H(r) = \mu \tag{2.43}$$

$$\frac{\partial g_H}{\partial \theta} = \frac{\mu}{\eta} \tag{2.44}$$

which yields the transformation:

$$f_H(r) = f_0(r \,/\, r_0)^\mu \tag{2.45}$$

$$g_H(\theta) = (\mu \,/\, \eta)(\theta - \theta_0) \tag{2.46}$$

with μ,f_0,r_0 and θ_0, are constants of integration, also the condition $|\mu/\eta| \leq 1$ must be satisfied. Such transformations are rather simple since they are a combination of a μth power of the radius with a scaled rotation. At this step, the f_H and g_H functions are known and can be reversed as:

$$r = r_0[f_H \,/\, f_0]^{1/\mu} \tag{2.47}$$

$$\theta = \theta_0 + (\eta \,/\, \mu) g_H(\theta) \tag{2.48}$$

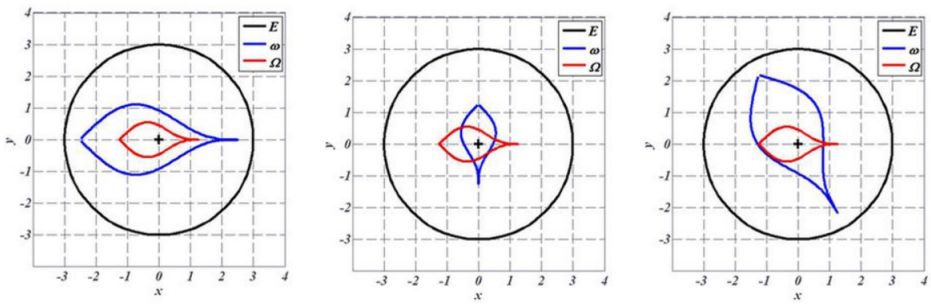

Figure 2.2: Schematic of the transformations mentioned in Eq.s (2.47and2.48) for an objectω (with blue frontiers) that can be mimicked when the same Ω object (with red frontier) is cloaked. (Left Figure):Only radial transformation with $\mu < 1$. (Middle Figure): Only rotational transformation. (Right Figure): Combination of both radial and rotational transformations. The two conductivities are chosen beforehand (with κ_{rr} to be proportional to κ_ω), which forces the nature of the transformation. The external frontier of the cloak is circular and plotted in black.

so that every shape $\partial\Omega$ given by $r' = f_H(r)$ and $\theta' = g_H(\theta)$ gives rise to the range of shapes $\partial\omega(\eta, \mu, f_0, r_0, \theta_0)$ that can be mimicked. Shape illustrations are given in Fig.2.2 below for an arbitrary geometry of the object Ω to cloak. The $\partial\Omega$ frontier is plotted as a red line, whereas the cloak is circular with an external frontier ∂E plotted in black. These arbitrary frontiers ∂E and $\partial\Omega$ are the same for all drafts in Fig.2.2. Alternatively, the frontiers $\partial\omega$ of the objects ω that can be mimicked are plotted as a

blue line and result from the inverse H transformation given in (2.472.48). As seen in Fig.2.2, the objects can be widened (left figure) or reduced, rotated (middle figure), or both (right figure), depending on the set of parameters. Notice that, until now, we did not discuss the cloaks that will allow the thermal illusion (the mimicking effect).

Now that such $\partial\omega$ surfaces and H transformations have been determined from the knowledge of $\eta = \kappa_{rr}(r,\theta)/\kappa_{\omega}(r,\theta)$, we also have to take into account the anisotropic nature of the Ω conductivity. This leads us to analyze the second (polar) conductivity coefficient $\kappa_{\theta\theta}$. In fact, (2.40) and (2.42) give:

$$\kappa_{\theta\theta} = \kappa_{\omega} \,/\, \eta \tag{2.49}$$

so that the object Ω to cloak must be diagonal in the form:

$$[\kappa_{\Omega}] = \kappa_{\omega} \begin{bmatrix} \eta & 0 \\ 0 & 1 \,/\, \eta \end{bmatrix} \tag{2.50}$$

It is also interesting to analyze under which conditions this Ω object can be isotropic. In fact, from relation Eq.(2.42), the value $\eta = 1$ leads to $\kappa_{rr} = \kappa_{\theta\theta} = \kappa_{\omega}$. This last situation indicates that, if the objects ω and Ω have the same heterogeneous isotropic conductivities, then the range of shapes $\partial\omega_{\mu}$ that can be mimicked follows:

$$r = r_0[f_H(r) \,/\, f_0]^{1/\mu} \tag{2.51}$$

$$\theta = \theta_0 + (\frac{1}{\mu})g_H(\theta) \tag{2.52}$$

with $|\mu| \leq 1$. With regard to Eq.(2.472.48), we notice that only the polar variation is modified. This range of surfaces characterizes the transformations that hold the scalar (isotropic) conductivity invariant ($\kappa_{\omega} = \kappa_{\Omega}$). In other words, from Eq.(17), they follow the tensor condition:

$$[T_\Omega] = (\frac{1}{det(M_H)})[M_H][M_H]^\tau = I \tag{2.53}$$

where I is the identity matrix. Hence, when the radial transformation is not linear ($\mu \neq 1$), a scaled rotation in the form ($\theta^{'} = \mu\theta$) is necessary to hold the scalar conductivity. As previously discussed, we also must consider the (ρC) constraints involved in a transient or dynamic regime, to determine whether compatibility can be found with those of conductivity. With $\eta = 1$, these products are related as:

$$\frac{(\rho C)_\Omega}{(\rho C)_\omega} = r \,/\, [f_H(r)\frac{\partial f}{\partial r}\frac{\partial g_H}{\partial \theta}] = [1 \,/\, (f_0^2\mu^2)]r_0^{2\mu} \,/\, r^{2\mu-2} \tag{2.54}$$

Such a relationship could be used to choose the value of μ to fit the (ρC) ratio of the objects in the case where this ratio behaves as a nth power of r, with $n = 2(1-\mu) \geq 0$. In this last situation, all constraints on thermal parameters would be satisfied, allowing for generalization of the previous techniques to the transient regime. However, in practice, the optimal situation is that of a constant (ρC) ratio given by $\mu = 1$, that is:

$$\frac{(\rho C)_\Omega}{(\rho C)_\omega} = (r_0 \,/\, f_0)^2 \tag{2.55}$$

Following (2.512.52) the associated transformation is given by:

$$r = r_0 f_H(r) \,/\, f_0 \tag{2.56}$$

$$\theta = \theta_0 + g_H(\theta) \tag{2.57}$$

These simplified Eq.s (2.56,2.57) are the simplest ones that allow the mimicking technique in the transient regime for given isotropic objects. The transformation is reduced to a simple combination of a rotation and a scaled enlargement.

To conclude, this constant η case, it should be noted that invisibility is usually discussed in the case of the same constant conductivity for ω and its surrounding (E/ω), that is $\kappa_\omega = \kappa_{E/\omega}$, which allows for mimicking the homogeneous region. The result is that the field perturbation (scattering or diffraction) resulting from the Ω object vanishes at the external frontier ∂E of its cloak, as if this cloak were acting as a perfect anti-reflective device, regardless of the excitation conditions. Single H transformations have been widely used in this situation with the range of parameters: $\mu = 1$, $f_0 = 1$, $\theta_0 = 0$, that is, $f(r) = r \,/\, r_0$ and $g(\theta) = \theta$. Furthermore, most often, a circular geometry is considered with a central disk transformed into another one. For all these geometries, the scalar isotropic conductivity is the same in ω and Ω, whereas the ρC product follows $(\rho C)_\Omega = r_0^2 (\rho C)_\omega$. Vanishing values of r_0 leads to zero the ρC product in Ω as in case of Pendry's Cloak. In all situations, the cloak conductivity is anisotropic and heterogeneous (see section 2.4).

Radial dependence case $\eta(r,\theta) = \eta_1(r)$: Here, we consider the situation where this ratio given in (2.42) depends on a only on r. since $\eta(r,\theta) = \eta_1(r)$, then:

$$\eta_1(r) = r\,(\frac{\partial f_H}{\partial r}) \,/\, [f_H(r)\frac{\partial g_H}{\partial \theta}] \tag{2.58}$$

where η_1 is chosen beforehand. The result is:

$$f_1(r) = f_0 exp\left[\mu_1 \int_{r_0}^{r} (\eta_1(u) \,/\, u) du\right] \tag{2.59}$$

$$g_1(\theta) = \mu_1(\theta - \theta_0) \tag{2.60}$$

where f_0, μ_1 and θ_0 are constants and $|\mu_1| \leq 1$. The conductivity matrix $[\kappa_\Omega]$ is anisotropic and diagonal with:

$$\kappa_{rr}(r,\theta) = \kappa_\omega \eta_1 \quad \kappa_{\theta\theta}(r,\theta) = \kappa_\omega \,/\, \eta_1 \tag{2.61}$$

$$[\kappa_\Omega(r,\theta)] = \kappa_\omega(r,\theta) \begin{bmatrix} \eta_1 & 0 \\ 0 & 1 \,/\, \eta_1 \end{bmatrix} \tag{2.62}$$

At this step, it should be noted that the inhomogeneity of conductivity modifies the shape of the object that can be mimicked. Indeed, when $f_1(r)$ and $g_1(\theta)$ are given to fix Ω in the arrival space, ω is rebuilt in the departure space as:

$$r = \eta_1(r) f_1(r)(\frac{\partial g_1}{\partial \theta}) \,/\, (\frac{\partial f_1}{\partial r}) \text{ and } \theta = \theta_0 + g_1(\theta) \,/\, \mu_1 \tag{2.63}$$

Polar dependence case $\eta(r,\theta) = \eta_2(\theta)$: Here, we consider the situation where this ratio given in (2.42) depends on a only on θ. since $\eta(r,\theta) = \eta_2(\theta)$, then:

$$\eta_2(\theta) = r(\frac{\partial f_H}{\partial r}) \,/\, [f_H(r)(\frac{\partial g_H}{\partial \theta})] \tag{2.64}$$

where η_2 is again forced. The result is:

$$f_2(r) = f_0(r \,/\, r_0)^{\mu_2} \qquad g_2(\theta) = \mu_2 \int_{\theta_0}^{\theta} du \,/\, \eta_2 \tag{2.65}$$

The conductivity matrix is still anisotropic with:

$$\kappa_{rr}(r,\theta) = \kappa_\omega(r,\theta)\eta_2(\theta) \quad \kappa_{\theta\theta}(r,\theta) = \kappa_\omega(r,\theta) \,/\, \eta_2(\theta) \tag{2.66}$$

that is:

$$[\kappa_\Omega(r,\theta)] = \kappa_\omega(r,\theta) \begin{bmatrix} \eta_2(\theta) & 0 \\ 0 & 1 \,/\, \eta_2(\theta) \end{bmatrix} \tag{2.67}$$

The inhomogeneous conductivity again modifies the shape of the object to mimic in

the form:

$$r = r_0[f_2(r) \,/\, f_0]^{1/\mu_2} \text{ and } \frac{\partial g_2}{\partial \theta} = \mu_2 \,/\, \eta_2(\theta) \tag{2.68}$$

Product of functions of the radial only and the polar coordinate only $\eta(r,\theta) = \eta_r(r)\eta_2(\theta)$: This more general case is analytically tractable and can be directly found from the previous cases. By considering $\eta(r,\theta) = \eta_1(r)\eta_2(\theta)$, we obtain

$$f_H(r) = f_1(r) \text{ and } g_H(\theta) = g_2(\theta) \text{ with } \mu_1 = \mu_2 \tag{2.69}$$

and the anisotropic conductivity matrix:

$$[\kappa_\Omega(r,\theta)] = \kappa_\omega(r,\theta) \begin{bmatrix} \eta_1(r)\eta_2(\theta) & 0 \\ 0 & 1 \,/\, [\eta_1(r)\eta_2(\theta)] \end{bmatrix} \tag{2.70}$$

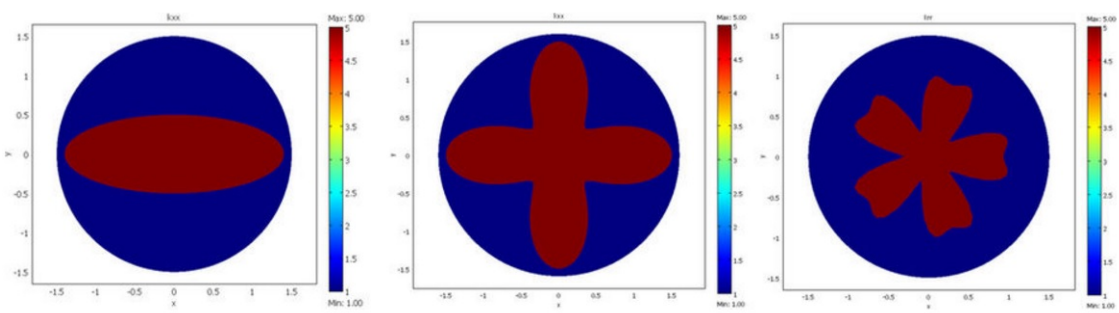

Figure 2.3: Departure (or virtual) space- Three different shapes of the starting object $\partial\omega$ to mimic (from the left to the right): an ellipse, a flower and a butterfly. The color scales are for the conductivity.

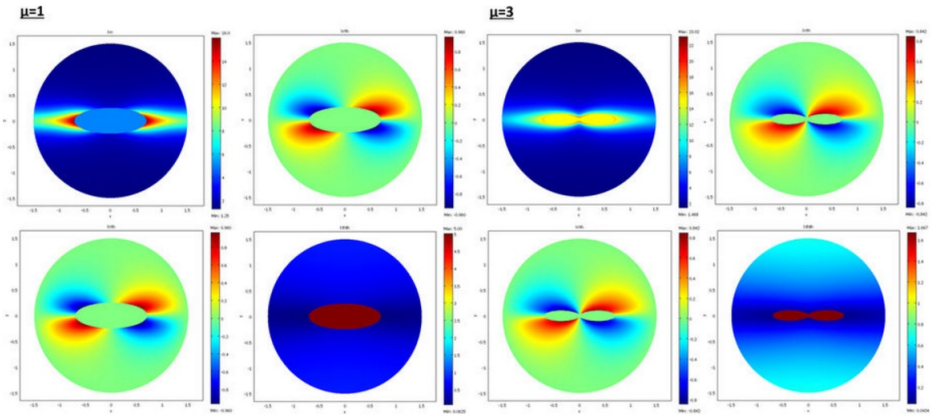

Figure 2.4: Cloak matrix conductivities to mimic the ellipse of Fig.2.3, with parameters $\mu = 1$ (left figure) and $\mu = 3$ (right figure).

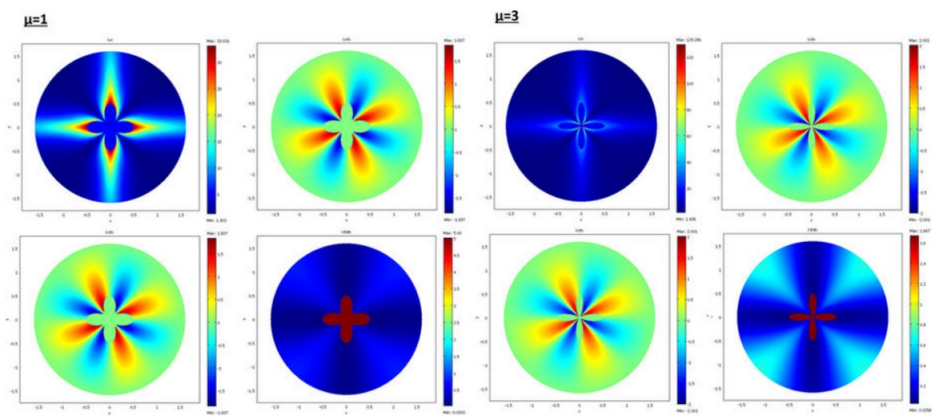

Figure 2.5: Case of the flower, with $\mu = 1$ (left figure) and $\mu = 3$ (right figure).

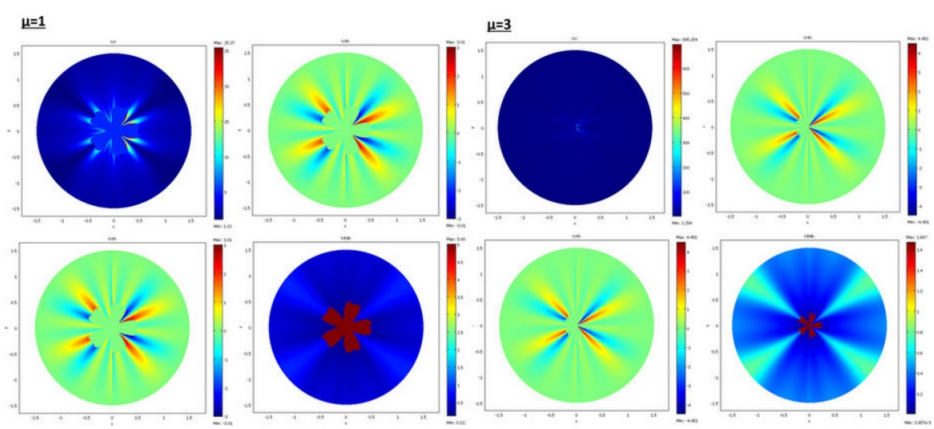

Figure 2.6: Case of the butterfly, with $\mu = 1$ (left figure) and $\mu = 3$ (right figure).

2.4 Cloak Design Procedure

Until now, we considered the H transformations that connect the objects to cloak Ω and mimic ω; however, we did not address the L transformation that gives the cloak E/Ω. The problem of the cloak is different in the sense that there is a large degree of freedom. In fact, the cloak is confined by surface $\partial\Omega$ which is given and by surface ∂E which is arbitrary choice. Furthermore, there is no need apriori for its conductivity matrix to be diagonal, as we had assumed for the Ω object. In the general case, one may address an anisotropic heterogeneous cloak. Following Eq.(2.8), the conductivity matrix of the cloak is known from the L transformation that ensures:

$$L(E/\omega) = E/\omega \Rightarrow L(\partial\omega) = H(\partial\omega) = \partial\Omega \text{ and } L(\partial E) = \partial E \tag{2.71}$$

Emphasizing analytical examples is not an easy task when the two cloak frontiers are arbitrary. This is the reason why well-known geometries are most often addressed. However, analytical calculation can still be performed with specific geometries given by star domains, which we now address. Let us assume that all domains (ω , Ω and E) are star domains and consider that the frontiers $\partial\omega$ and ∂E are given in the form $r_\omega(\theta)$ and $r_E(\theta)$. Next, one can build a simple canonical L function that transforms $E-\omega$ to give the cloak $E-\omega$ as:

$$f_L(r,\theta) = \alpha_1(\theta)r + \beta_1(\theta) \qquad g_L(r,\theta) = \alpha_2(\theta)r + \beta_2(\theta) \tag{2.72}$$

The (α_i, β_i) coefficients can be directly calculated to satisfy (2.71), and this yields:

$$\alpha_1 = [r_E - f_H(r_\omega,\theta)] \,/\, (r_E - r_\omega) \qquad \beta_1 = r_E[f_H(r_\omega,\theta) - r_\omega] \,/\, (r_E - r_\omega) \tag{2.73}$$

$$\alpha_2 = [\theta - g_H(r_\omega,\theta)] \,/\, (r_E - r_\omega) \qquad \beta_2 = [r_E g_H(r_\omega,\theta) - r_\omega\theta] \,/\, (r_E - r_\omega) \tag{2.74}$$

with:

$$f_H(r_\omega, \theta) = f_L(r_\omega, \theta) = r_\Omega(\theta_\Omega) \quad \theta_\Omega = g_H(r_\omega, \theta) = g_L(r_\omega, \theta) \tag{2.75}$$

and:

$$r_E = f_L(r_E, \theta) \qquad \theta_E = g_L(r_E, \theta) = \theta \tag{2.76}$$

Such an L transformation is homothetic for each polar angle. It is fully determined from the two frontier equations ($\partial\omega$ and ∂E) and from the H transformation. It can be used to calculate the cloak conductivity. For that purpose, we must use the general relation (2.8) and not that (2.36) of the diagonal objects because the derivative $\frac{\partial r'}{\partial \theta}$ is not zero for L.

The results are given below in Fig.s 2.3,2.6. The conductivity ratio η is constant, so that the H transformation is given by Eq.s(2.452.46). For the sake of simplicity, we first avoid the rotation in the H transformation, which we obtain with $\mu = \eta$ and $\theta_0 = 0$ (rotation is discussed further). Hence, the H transformation is given by:

$$f_H(r) = f_0(r \,/\, r_0)^{1/\mu} \quad g_H(\theta) = \theta \tag{2.77}$$

and this forces the Ω object diagonal conductivity as:

$$[\kappa_\Omega] = \kappa_\omega \begin{bmatrix} \mu & 0 \\ 0 & \mu \end{bmatrix} \tag{2.78}$$

Note that, since we assumed $\mu = \eta$ to cancel the rotation, this conductivity matrix is now connected to the shape of the object via the η coefficient. The conductivities are scalar and given by $\kappa_\omega = 5$ for the object to mimic and $\kappa_{E/\omega} = \kappa_0 = 1$ for its surrounding medium E/ω. Hence, the departure space is isotropic but non-homogeneous since $\kappa_\omega \neq \kappa_{E/\omega}$.

We considered a circular external frontier ∂E and 3 different shapes (see Fig.2.3)

for $\partial\omega$: an ellipse (left figure), a flower (middle figure) and a butterfly (right figure). Their respective shape equations are as follows:

$$r_\omega(\theta) = [(cos(\theta)\ /\ a)^2 + (sin(\theta)\ /\ b)^2]^{-1}\ \ a = 1.4\ \ b = 0.5 \tag{2.79}$$

$$r_\omega(\theta) = a + b\, cos(4\theta)\ \ a = 1\ \ b = 0.5 \tag{2.80}$$

$$r_\omega(\theta) = 1 + 0.5cos(5\theta) + 0.5(sin5\theta)^2 \tag{2.81}$$

The last parameters to adjust in the H transformation are:

$$r_0 = 1.4\ \ f_0 = 0.7\ \text{ for the ellipse case}$$

$$r_0 = 1.5\ \ f_0 = 0.5\ \text{ for the flower case}$$

$$r_0 = 1.4\ \ f_0 = 0.7\ \text{ for the butterfly case}$$

From relations (2.72,2.76, 2.79,2.81), the cloaks were calculated following (2.8). The resulting conductivity matrices to perform the thermal illusion are given in Fig.s 2.4,2.6 in the polar basis. For each figure the four matrix parameters are given in color scales in the whole arrival space E, that is, for the Ω object and its cloak E/Ω. The colors can be saturated within Ω to emphasize the conductivity variations within the cloaks. In each figure, the matrix coefficients within Ω are constant, with $\kappa_{rr} = \mu\kappa_\omega$, $\kappa_{\theta\theta} = \kappa_\omega/\mu$ and $\kappa_{r\theta} = \kappa_{\theta r} = 0$. In addition, there is an anisotropic gradient of conductivity within the cloak E/Ω.

Fig.2.4 is given for the ellipse of Fig.2.3, with $\mu = 1$ on the left and $\mu = 3$ on the right. We notice in the right figure that the ellipse shape is lost; this results from the fact that, because of the r_μ power variation, the polar radius is increased or decreased, depending on whether $r > 1$ or $r < 1$. Fig.s 2.5,2.6 are given in a similar way for the two other shapes of Fig.2.3 (flower and butterfly). Generally, we observe on a

horizontal axis that, in the cloak E/Ω, the $\kappa_{rr}(r,\theta)$ behavior is connected to the ratio $r_\Omega(\theta)/r_\omega(\theta)$. This is the manner by which the conductivity gradient compensates the $\partial\Omega$ shape to mimic $\partial\omega$.

2.5 Numerical Simulation

Now that all cloaks have been designed, a final validation is required to calculate the resulting heat flow pattern in the two spaces (departure and arrival- see Fig. 2.1), that is:

- Beyond the frontier ∂E limiting the ω object surrounded by E/ω in the departure space.
- Beyond the frontier ∂E limiting the Ω object surrounded with its cloak $E-\Omega$ in the arrival space.

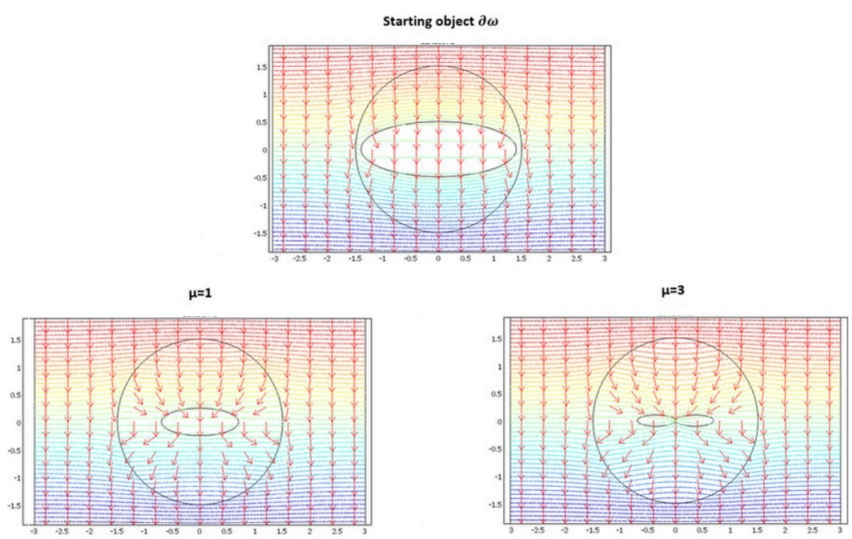

Figure 2.7: Case where $\partial\omega$ is an ellipse. Heat flow patterns are calculated with the conductivity matrices of Fig. 2.4. The top figure is for the scattering pattern of ω , and the bottom figures are for Ω surrounded by its cloak, with $\mu = 1$ (left figure) and $\mu = 3$ (right figure). All patterns are identical beyond the circular cloak ∂E.

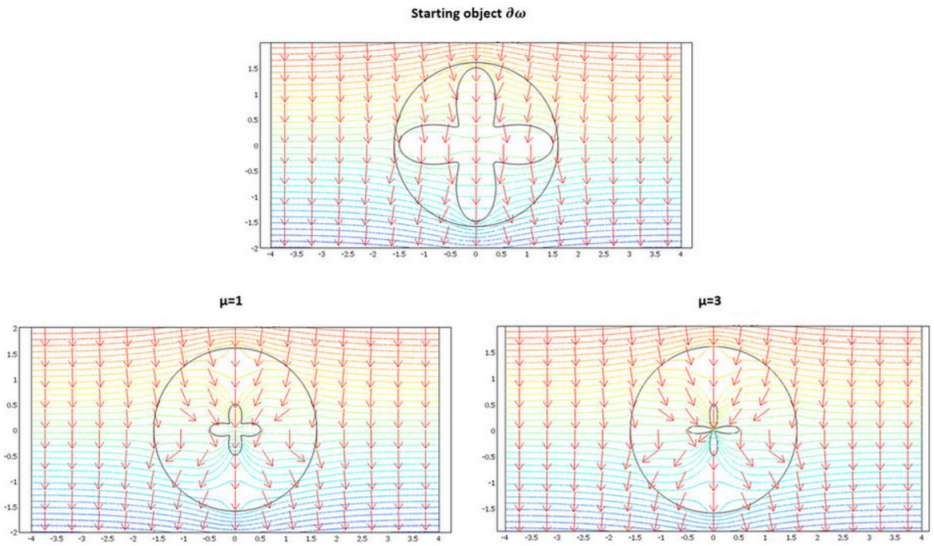

Figure 2.8: Case where $\partial\omega$ is a flower. Heat flow patterns are calculated with the conductivity matrices of 2.5. The top figure is for the scattering pattern of ω , and the bottom figures are for Ω surrounded by its cloak, with $\mu = 1$ (left figure) and $\mu = 3$ (right figure). All patterns are identical beyond the circular cloak ∂E.

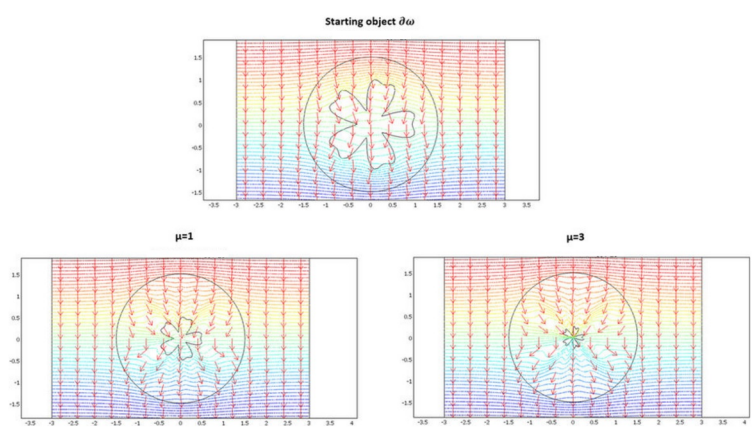

Figure 2.9: Case where $\partial\omega$ is a butterfly. Heat flow patterns are calculated with the conductivity matrices of Fig.2.6. The top figure is for the scattering pattern of ω , and the bottom figures are for Ω surrounded by its cloak, with $\mu = 1$ (left figure) and $\mu = 3$ (right figure). All patterns are identical beyond the circular cloak ∂E.

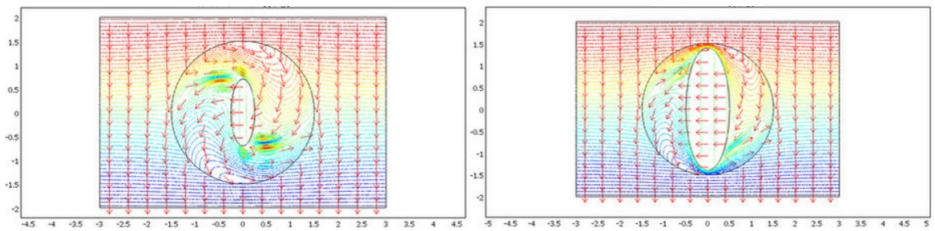

Figure 2.10: Flux pattern calculated for the horizontal ellipse of Fig.2.7 after 90° rotation (right figure) completed by reduction (left figure). All fluxes are identical beyond the circular cloak.

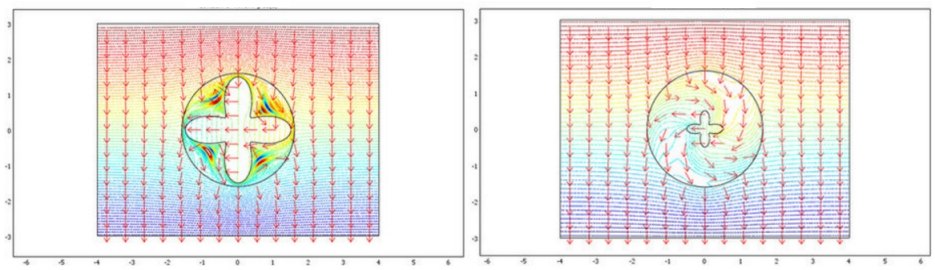

Figure 2.11: Flux pattern calculated for the flower of Fig.2.8 after 90° rotation (left figure) completed by reduction (right figure). All fluxes are identical beyond the circular cloak.

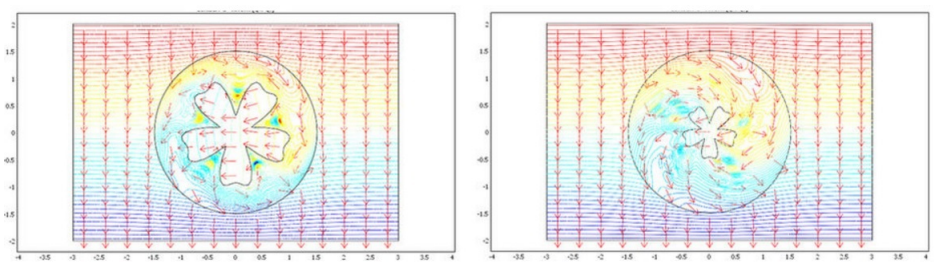

Figure 2.12: Flux pattern calculated for the butterfly of 2.9 after 90° rotation (left figure) completed by reduction (right figure). All fluxes are identical beyond the circular cloak.

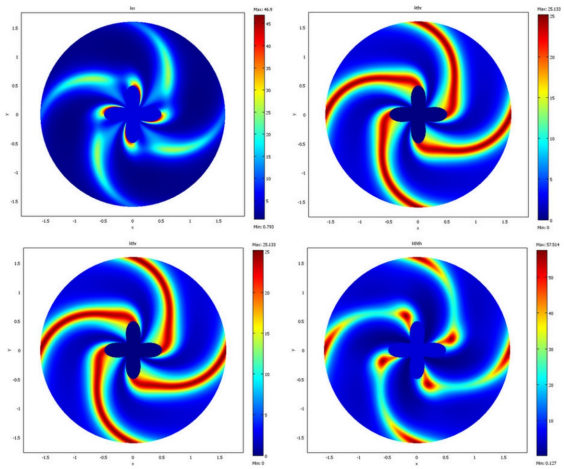

Figure 2.13: Conductivity matrix of the flower in the case of 90° rotation with no scaling.

The validation will be proven if we check that these fluxes beyond ∂E are identical for the two departure and arrival spaces; the results given in Figs. 2.7,2.9 were obtained with Comsol Multiphysics software for all the previously analyzed thermal conductivity matrices. We chose steady state regime with no additional constraints originate from the ρC product. In all figures, the temperature and heat flux fields are calculated and plotted as equi-potential lines and normalized arrows receptively. The temperature field is a solution of a boundary value problem where the domain $\bar{E}$ of the problem has a rectangular shape and the boundary conditions are set as following:

- $T = 1$ at the the top side of the domain $\bar{E}$
- $T = 0$ at the the bottom side of the domain $\bar{E}$ (Dirchlet Boundary condition)
- $q_y = 0$ at both of the lateral sides of the domain $\bar{E}$ (Neumann's Boundary condition)

Fig. 2.7 is given for the ellipse cases whose conductivity matrices are those of Fig. 2.4. The top figure is given in the departure space for the flux to mimic (that of ω), and the bottom figures are for the cloaked object (Ω) in the arrival space. The bottom

left figure is calculated with $\mu = 1$, and the right figure is for $\mu = 3$. We observe for the three drafts that the heat flow pattern is invariant beyond the circular cloak, thereby validating all the results. In a similar manner, Fig.s 2.5,2.6 are given for the butterfly and the flower of Fig.s 2.8,2.9, respectively, providing successful results. All the results confirm that ω is indeed mimicked by Ω and its cloak.

The case of rotation Next, we address the validation in the case of rotation. Although the whole formulation is not modified when the objects are rotated ($\theta^{'} \neq \theta$), numerical implementation raises more difficulties. Indeed, additional intense polar gradients must be introduced (see Eq.s 2.722.76) that reduce the convergence speed in the heat equation and require mesh modification. However, all results are again successful, as shown in Fig.s 2.10,2.12.

In Fig.2.10, the original object to mimic is the horizontal ellipse of Fig. 2.7; in the left of 2.10, the ellipse is rotated by 90° ($\theta_0 = \pi$ / 2), and it is both rotated and reduced in the right figure, with $\mu = 1$, $r_0 = 1.4$ and $f_0 = 0.7$. We observe that, beyond the circular cloak, the heat flux patterns are not modified and remain identical to that of the top Fig.2.7.

Fig.s 2.11 and 2.12 are given for the flower and the butterfly, respectively with $\mu = 1$, $r_0 = 1.5$ and $f_0 = 0.5$. The conclusions are the same. We notice for the flower that because it is invariant by 90° rotation, the mimicking process here occurs as if its anisotropic cloak were invisible. For completeness, we also show the conductivity matrix of the flower in Fig. 2.13.

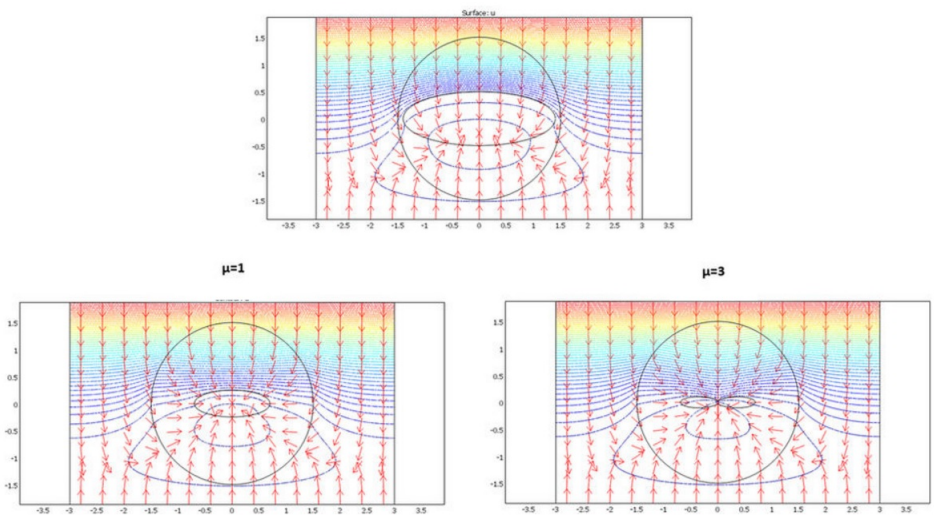

Figure 2.14: Legend analogous to Fig.2.7 , but for the dynamic regime.

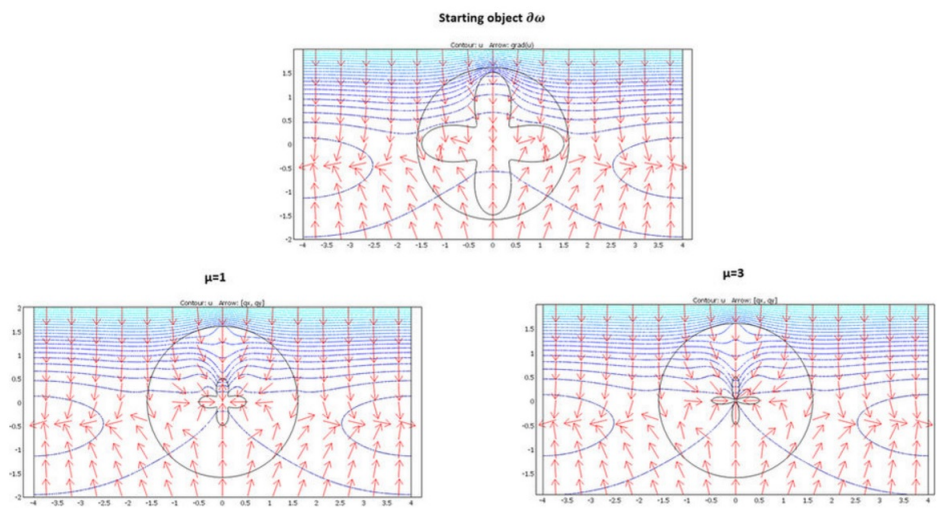

Figure 2.15: Legend analogous to Fig.2.8, but for the dynamic regime.

Dynamic regime Throughout this paper, it was stressed that the additional ρC constraints (Eq. (2.7)) are not compatible with those of the conductivity (Eq. (2.6)) in the general case, which led us to reduce our analysis to the static regime. However, as stated above, there is one transformation that holds both the conductivity and the ρC product, and this transformation is characterized by a single rotation combined with a homothety (see Eq.s (2.56,2.57)). These relations (2.56,2.57) are those that allow the mimicking technique in the transient regime for given isotropic objects,

which we now validate with numerical calculation.

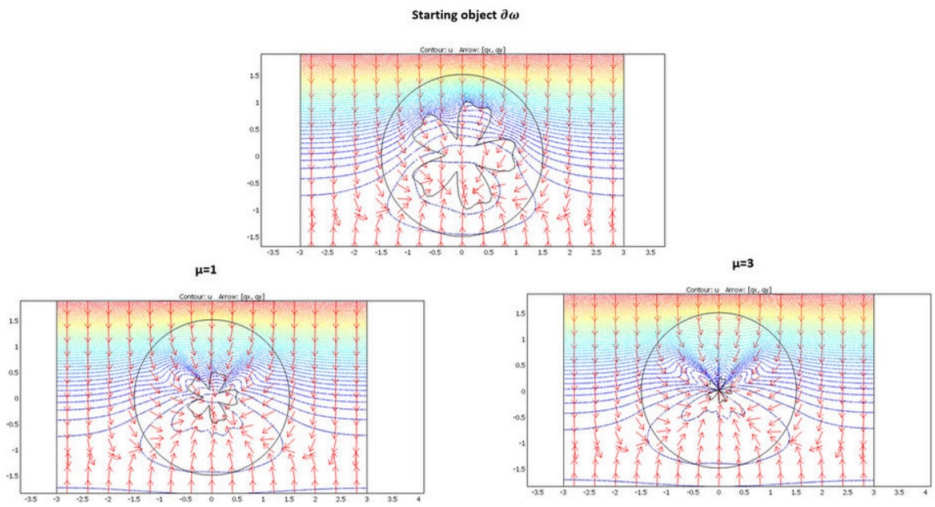

Figure 2.16: Legend analogous to Fig.2.9, but for the dynamic regime.

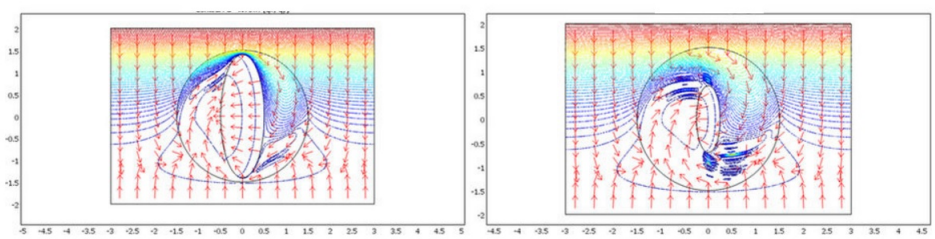

Figure 2.17: Legend analogous to Fig.2.10, but for the dynamic regime. The left figure is for rotation, and the right figure is for rotation and scaling.

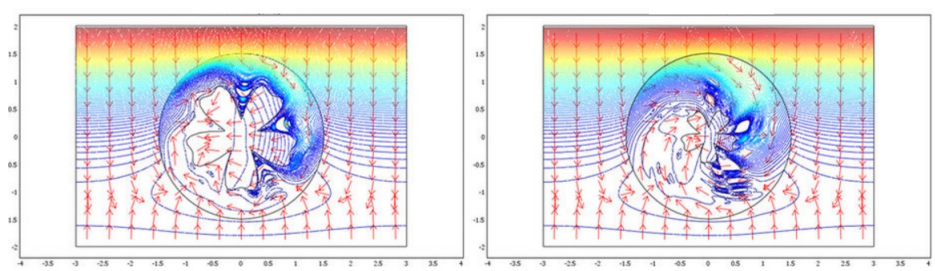

Figure 2.18: Legend analogous to Fig.2.11, but for the dynamic regime. The left figure is for rotation, and the right figure is for rotation and scaling.

For the validation, the heat equation is solved in the dynamic regime. More exactly, we calculated the flux and temperature response of one non-zero Fourier component of the source ($1Hz$) at time $t = 0$. The ρC product is 10 within the

object ω to mimic, whereas it is 1 in its surrounding E/ω . The three shapes of the previous sections (ellipse, flower and butterfly) were considered with the same cloak conductivity matrices.

The results shown in Fig.s 2.14,2.16 confirm that successful data were obtained because all flux patterns are again found to be identical beyond the cloaks. Note that, in regard to the static regime, the heat fluxes above the cloak are far from those of the homogeneous case (scattering is stronger), so that the mimicking effect can be observed with more contrast. Validation of Eq.s (2.562.57) is given by the bottom left figures that involve parameter ($\mu = 1$), which holds both the conductivity and the ρC product. In the bottom right figures calculated with $\mu = 3$, the ρC product was chosen to satisfy Eq. (2.7) and is therefore different from that of the object to mimic.

2.6 Conclusion

We had addressed an inverse problem that consists of cloaking a predefined object (in shape and conductivity) to mimic the conduction heat flow of another object of given conductivity. Because all thermal conductivities are given beforehand, the set of transformations that allow for passing from one object (to mimic) to another object (to cloak) is reduced and was analytically and numerically calculated. This result allowed us to emphasize the class of shapes that can be mimicked when all conductivities are forced. The solutions were first given for the heat flow in the dynamic regime, on the basis of space transformation. To guarantee the existence of solutions, we first dropped a number of constraints related to the (ρC) products, leading us to the static regime with unique conditions on the conductivity matrices. The analytical calculation was fully developed in a 2D polar geometry for a heterogeneous isotropic object to mimic, and a heterogeneous diagonal object to cloak. Among all transformations, a

sub-class was emphasized that allows for camouflaging of the diagonal objects. These transformations hold the conductivity and confer to the objects the adequate thermal illusion, that is, a heat flow pattern identical to that of another predefined object. It was also noticed how specific transformations allowed to match both the conductivity and the (ρC) constraints for the illusion to work in the dynamic regime. Numerical calculation was performed for different object shapes to mimic an ellipse, a flower and a butterfly. Homothetic transformations were used for the cloaks at each polar angle, on the support of space continuity. For simplicity, we assumed that the ratio of the radial conductivity of the object to cloak to the scalar conductivity of the object to mimic was constant. Under these conditions, all mimicking predictions (including rotation and scaling) were confirmed with success, with a heat flow pattern identical for all objects above the cloaks. All these techniques can be directly extended to more general situations of asymmetric objects with arbitrary conductivities. We expect these results to bring added value for applications because they allow the camouflaging of objects that are chosen beforehand. In particular, they should make prototype design easier. In addition, the results open the door to camouflage in thermal radiation, at least for far-infrared wavelengths; indeed, at these wavelengths, where bulk absorption is dominant, the thermal radiation is mainly emitted from the surface of the external cloak, where the temperature has been shown to be invariant. Finally, generalization to other fields (such as waves) can also be directly performed. Notice also that the most general case of a non-diagonal conductivity matrix that should be over-coated to mimic a non-isotropic matrix could be addressed in a similar manner; however, this would require full numerical calculation (including the inverse problem and additional partial differential equations).

CHAPTER III

Transformation Fluctuation Electrodynamics: Application of Transformation Optics upon Thermal Radiation Illusion

3.1 Introduction

Thermal radiation (TR) is a universal property for all objects with temperatures above 0K. Every object with a specific shape and emissivity has its own thermal radiation signature; such signature allows the object to be detected and recognized which can be an undesirable situation. As discussed in chapter I, our main concern is the thermal radiation illusion problem, where one object is coated such that its thermal radiated signature is the same as another arbitrary object in the same range of frequency. In this chapter, we apply transformation optics (TO) theory upon the thermal radiation problem, so the TO based coat can control the thermal radiation signature of the coated emitter. Starting with fluctuation dissipation theorem (FDT) where thermally fluctuating sources are related to the radiative losses, we demonstrate that it is possible for objects residing in two spaces, virtual and physical, to have the same thermal radiation signature if the complex permittivity and permeability satisfy the standard space transformations. We emphasize the invariance of the fluctuation electrodynamics (FE) physics under transformation, and show how this

result allows the mimicking in thermal radiation. We illustrate the concept using the illusion paradigm in the two-dimensional space and a numerical calculation validates all predictions. Finally, we discuss limitations and extensions of the proposed technique.

In this chapter, we first show that FE is invariant under transformations depicted by TO, in the sense that the same fluctuation dissipation theorem is recovered in the physical space after transformation of both the physical parameters and the thermal sources. For that the thermal current sources are first transformed in the same manner as coherent sources according to source transformation, and these transformed sources are then compared to those which are proportional to dissipative losses in the physical space. Hence both ways of transforming the thermal currents are consistent and only constrained by the validity of FDT in both spaces. In order to keep the model relevant to the ongoing literature of near field thermal radiation [42] we illustrate our theoretical demonstration by considering the two-dimensional (2D) space where the electromagnetic radiation is the combination of E- and H-polarizations.

3.2 Transformation optics and Fluctuation Electrodynamics

TO theory states that in order to keep Maxwells equations invariant under a transformation between a virtual (pre-transformation) space with the coordinate set x^m and another physical (post-transformation) space with the coordinate set $x^{m'}$, the materials parameters must comply with the following transformation :

$$\begin{aligned} \varepsilon^{m'n'} &= \frac{1}{detA} A^{m'}_{m} A^{n'}_{n'} \varepsilon^{mn} \\ \mu^{m'n'} &= \frac{1}{detA} A^{m'}_{m} A^{n'}_{n'} \mu^{mn} \end{aligned} \tag{3.1}$$

where $A_m^{m'} = \frac{\partial x^{m'}}{\partial x^m}$and $detA$ are the elements and the determinant of the Jacobian matrix $\underline{\underline{A}}$. ε and μ are the relative permittivity and permeability tensors respectively. Note that m', n', m and n are indices of the space coordinates, respectively used for $\{x, y, z\}$ and $\{x, y, z\}$. Here, we assume that the transformation is real (i.e.: associates with real-valued coordinate systems and in contrast to complex valued transformations [99]). The media in both departure and arrival spaces are lossy so that their permittivity or permeability are complex valued functions. We exclude the cases of bi-anisotropic and optical active media. We consider a $e^{i\omega t}$ time harmonic dependence, where ω is the angular frequency and t is referring to time. We only consider lossy passive media (no gain), so accordingly, the imaginary parts of the permittivity and permeability tensors $Im\{\varepsilon^{mn}\}$ and $Im\{\mu^{mn}\}$ are negative quantities. If the virtual space contains nonzero electric (J) and magnetic (K) volumetric current sources, then these current sources are also transformed to the physical space as follows [58]

$$\begin{aligned} J^{m'} &= \frac{1}{det(A)} A_m^{m'} J^m \\ K^{m'} &= \frac{1}{det(A)} A_m^{m'} K^m \end{aligned} \tag{3.2}$$

FDT theory states that for any dissipative linear system with local temperature T, the spectral density of the generalized force of the system fluctuates in such a way to be proportional to the dissipative part of the transfer function of the system [13]. Here we consider the FDT of second kind [27] (see appendix E) where T.R is the electromagnetic response to the stochastic current sources. The spectral correlation of the volumetric electric J^m and magnetic currents K^m embedded in the object, with relative complex permittivity tensor $\varepsilon^{mn}(x, \omega)$ and relative complex permeability tensor $\mu^{mn}(x, \omega)$ is quantified as follows [34]

$$\langle J^m(x_1,\omega_1)J^{n*}(x_2,\omega_2)\rangle = -4\frac{\omega_1\varepsilon_0}{\pi}\Theta(\omega_1,T)Im\{\varepsilon^{mn}(x_1,\omega_1)\}\delta(x_1-x_2)\delta(\omega_1-\omega_2)$$
$$\langle K^m(x_1,\omega_1)K^{n*}(x_2,\omega_2)\rangle = -4\frac{\omega_1\mu_0}{\pi}\Theta(\omega_1,T)Im\{\mu^{mn}(x_1,\omega_1)\}\delta(x_1-x_2)\delta(\omega_1-\omega_2) \tag{3.3}$$

where $<>_\omega$ represents an ensemble average, $\Theta(\omega,T) = \hbar\omega\left(e^{\hbar\omega/K_BT}-1\right)^{-1}$ corresponds to the mean energy of a single quantum oscillator with angular frequency $\omega > 0$, ignoring vacuum fluctuations. x_1 and x_2 are two different position vectors in the thermal emitter. δ indicates Dirac functions, K_B is Boltzmanns constant, ε_0 and μ_0 are the permittivity and permeability of the free space respectively. The star $(*)$ indicates the complex conjugation operator. Once the thermally fluctuating sources have been quantified, the radiated field can be computed by solving Maxwells equations, or equivalently knowing the Greens function for both electric and magnetic fields.

3.3 Transformation Fluctuation Electrodynamics

In this section, we apply the TO theory to the FE problem. Starting with a lossy object characterized by ε^{mn} and μ^{mn} residing in the virtual space, the correlation of fluctuating electric and magnetic currents is provided according to Eq.s (3.3); Hence these correlations are proportional of the imaginary permittivity and permeability of the virtual space. Now, transforming from the virtual space into the physical space with the transformation $A_m^{m'}$, then, the (post transformation) physical objects parameters $\varepsilon^{m'n'}$ and $\mu^{m'n'}$ are transformed according to Eq.(3.1). Also, since the electric and magnetic currents are transformed according to Eq.(3.2), then, the transformation of the spectral correlation of the fluctuational electric current follows:

$$\left\langle J^{m'}(x_1^{'},\omega_1)J^{n'*}(x_2^{'},\omega_2)\right\rangle = \frac{1}{(det(A))^2}A_m^{m'}A_n^{n'}\left\langle J^m(x_1,\omega_1)J^{n*}(x_2,\omega_2)\right\rangle \tag{3.4}$$

substituting the right-hand side correlation with Eq.(3.3), then

$$\left\langle J^{m'}(x_1^{'},\omega_1)J^{n'*}(x_2^{'},\omega_2)\right\rangle = \frac{1}{(det(A))^2}A_m^{m'}A_n^{n'}|Im\{\varepsilon^{mn}(x_1,\omega_1)\}|\delta(x_1-x_2)\delta(\omega_1-\omega_2) \tag{3.5}$$

due to its scaling property [10], the delta function is transformed as follows:

$$\delta(x_1^{'}-x_2^{'}) = \frac{1}{det(A)}\delta(x_1-x_2) \tag{3.6}$$

substituting Eq.s(3.1) and (3.8) in Eq.(3.7) yields:

$$\left\langle J^{m'}(x_1^{'},\omega_1)J^{n'*}(x_2^{'},\omega_2)\right\rangle = -4\frac{\omega_1\varepsilon_0}{\pi}\Theta(\omega_1,T)Im\{\varepsilon^{m'n'}(x_1^{'},\omega_1)\}\delta(x_1^{'}-x_2^{'})\delta(\omega_1-\omega_2) \tag{3.7}$$

Similarly,

$$\begin{aligned}\left\langle K^{m'}(x_1^{'},\omega_1)K^{n'*}(x_2^{'},\omega_2)\right\rangle &= -4\frac{\omega_1\mu_0}{\pi}\Theta(\omega_1,T)Im\{\mu^{m'n'}(x_1^{'},\omega_1)\}\delta(x_1^{'}-x_2^{'})\delta(\omega_1-\omega_2)\\ &= \frac{1}{(det(A))^2}A_m^{m'}A_n^{n'}\left\langle K^m(x_1,\omega_1)K^{n*}(x_2,\omega_2)\right\rangle\end{aligned} \tag{3.8}$$

These last relations show that after space transformation, the current correlations in the arrival space are again proportional to the imaginary parts of permittivity and permeability of the arrival space. Hence, from Eqs. (3.3), (3.7) and (3.8), FDT has the same form after transformation, that is, the source correlations resulting from the FDT theorem in the arrival space is identical to the transformation of the source correlations resulting from the FDT theorem in the departure space. We therefore conclude that FE is invariant under TO transformations. We also notice that such

invariance requires a real-valued transformation. These last remarks introduce the proposed camouflage technique, which consists in engineering the losses of a given object and its surrounding to control its emitted TR signature.

3.4 Two Dimensional E/H-polarization Thermal Radiation

In the next section, we illustrate for the developed theory in the previous section using a 2D case where the system is invariant along the out of plane $z-$ axis. Two-dimensional electromagnetic scattering cloaking/camouflage was studied previously [35], [65], [26],[49],[89] and [37]. Here, we extend this analysis to its TR counterpart. Starting with Maxwells equations and assuming invariance along z-axis, the TR problem is decomposed into two independent problems that are the H-polarization (Magnetic field is polarized in the z-direction) and the E-polarization (Electric field is polarized in the z-direction). Here we adopt a notation similar to that used in [37], where H and E polarizations were transformed using independent transformations A and B respectively. Let us rewrite all the tensorial quantities in terms of transverse (x and y) components and z-components as follows:

$$\begin{aligned}
\varepsilon^{mn} &= diag\{\underline{\underline{\varepsilon}}_T \; \varepsilon_{zz}\} \\
\mu^{mn} &= diag\{\underline{\underline{\mu}}_T \; \mu_{zz}\} \\
J^m &= [\underline{J}_T \; J_z]^\tau \\
K^m &= [\underline{K}_T \; K_z]^\tau \\
E^m &= [\underline{E}_T \; E_z]^\tau \\
H^m &= [\underline{H}_T \; H_z]^\tau
\end{aligned} \tag{3.9}$$

$$
\begin{aligned}
\varepsilon^{m'n'} &= diag\{\underline{\underline{\varepsilon}}_T^{'}\ \varepsilon_{zz}^{'}\} \\
\mu^{m'n'} &= diag\{\underline{\underline{\mu}}_T^{'}\ \mu_{zz}^{'}\} \\
J^{m'} &= [\underline{J}_T^{'}\ J_z^{'}]^{\tau} \\
K^{m'} &= [\underline{K}_T^{'}\ K_z^{'}]^{\tau} \\
E^{m'} &= [\underline{E}_T^{'}\ E_z^{'}]^{\tau} \\
H^{m'} &= [\underline{H}_T^{'}\ H_z^{'}]^{\tau}
\end{aligned}
\tag{3.10}
$$

where E and H are the electric and the magnetic fields respectively. Single underlining indicate vectors while double underlining indicates matrices, subscript τ indicates transverse components and $m, n = \{x, y, z\}$. Following the typical procedure of transforming Maxwell equations for each polarization, the differential equation for H-polarization virtual space will be as follows:

$$
\nabla \times \underline{\underline{\varepsilon}}_T^{-1} \cdot \nabla \times (H_z\hat{z}) - k_0^2\mu_{zz}(H_z\hat{z}) = \nabla \times \underline{\underline{\varepsilon}}_T^{-1} \cdot \underline{J}_T + i\omega\varepsilon_0(K_z\hat{z}) \tag{3.11}
$$

Notice that $\cdot$ indicates inner tensor product. The differential equation for the physical space at the same H- polarization

$$
\nabla \times \underline{\underline{\varepsilon}}_T^{'-1} \cdot \nabla \times (H_z^{'}\hat{z}) - k_0^2\mu_{zz}^{'}(H_z^{'}\hat{z}) = \nabla \times \underline{\underline{\varepsilon}}_T^{'-1} \cdot \underline{J}_T^{'} + i\omega\varepsilon_0(K_z^{'}\hat{z}) \tag{3.12}
$$

The quantities are transformed for this H- polarization as follows:

$$
\begin{aligned}
\mu_{zz}^{'} &= \frac{\mu_{zz}}{det(\underline{\underline{A}})} \\
\varepsilon_T^{m'n'} &= \frac{1}{det(\underline{\underline{A}})} A_m^{m'} A_n^{n'} \varepsilon_T^{mn} \\
K_z^{'} &= \frac{K_z}{det(\underline{\underline{A}})} \\
J_T^{'m} &= \frac{1}{det(\underline{\underline{A}})} J_T^m \\
\underline{E}_T^{'} &= \underline{\underline{A}}^{-\tau} \underline{E}_T \\
H_z^{'} &= H_z
\end{aligned}
\tag{3.13}
$$

Note that $\underline{\underline{A}}$ is the matrix form for the H-polarization transformation and τ indicates its transpose. Similarly for the E-polarization virtual space we have:

$$
\nabla \times \underline{\underline{\mu}}_T^{-1} \cdot \nabla \times (E_z \hat{z}) - k_0^2 \varepsilon_{zz} (E_z \hat{z}) = \nabla \times \underline{\underline{\mu}}_T^{-1} \cdot \underline{K}_T + i\omega\mu_0 (J_z \hat{z}) \tag{3.14}
$$

and for the E-polarization physical space:

$$
\nabla \times \underline{\underline{\mu}}_T^{'-1} \cdot \nabla \times (E_z^{'} \hat{z}) - k_0^2 \varepsilon_{zz}^{'} (E_z^{'} \hat{z}) = \nabla \times \underline{\underline{\mu}}_T^{'-1} \cdot \underline{K}_T^{'} + i\omega\mu_0 (J_z^{'} \hat{z}) \tag{3.15}
$$

The quantities are transformed for this E-polarization as follows:

$$
\begin{aligned}
\varepsilon_{zz}^{'} &= \frac{\varepsilon_{zz}}{det(\underline{\underline{A}})} \\
\mu_T^{m'n'} &= \frac{1}{det(\underline{\underline{A}})} A_m^{m'} A_n^{n'} \mu_T^{mn} \\
J_z^{'} &= \frac{J_z}{det(\underline{\underline{A}})} \\
K_T^{'m} &= \frac{1}{det(\underline{\underline{A}})} K_T^m \\
\underline{H}_T^{'} &= \underline{\underline{A}}^{-\tau} \underline{H}_T \\
E_z^{'} &= E_z
\end{aligned}
\tag{3.16}
$$

Notice here that B is the matrix form of the E-polarization transformation. It is important to mention that for both polarizations, the z-polarized fields (E_z - H_z) are invariant under transformation. Now we show the analytical basis for calculating the thermally radiated poynting vector (the results of the numerical simulations are shown in next section) and that was used to solve Eq.s (3.11-3.12) and Eq.s (3.14-3.15). We first consider the H-polarization virtual space of Eq. (3.11) and start with the definition of the ensemble averaged time average Poynting vector given as

$$
\langle S \rangle = 4 \times \frac{1}{2} Re\{\langle \underline{E} \times \underline{H}^* \rangle\} \tag{3.17}
$$

The scalar product of this vector with the local normal of a surface gives the elementary flux carried through this surface. The factor 4 is introduced to take into account the fact that only positive frequencies are considered in the ensemble average operator [53]. The magnetic field H_z can be calculated using the Green functions of the operator shown in Eq. (3.11) as follows:

$$H_z(\underline{r}) = \int G_{zz}^{HH}(\underline{r},\underline{r}_1)K_z(\underline{r}_1)d^2\underline{r}_1 + \int G_{zx}^{HE}(\underline{r},\underline{r}_2)J_T^x(\underline{r}_2)d^2\underline{r}_2 + \int G_{zy}^{HE}(\underline{r},\underline{r}_3)J_T^y(\underline{r}_3)d^2\underline{r}_3 \tag{3.18}$$

Similarly, for the Cartesian components of the transverse electric field,

$$\underline{E}_n(\underline{r}) = \int G_{nz}^{EH}(\underline{r},\underline{r}_4)K_z(\underline{r}_4)d^2\underline{r}_4 + \int G_{nx}^{EE}(\underline{r},\underline{r}_5)J_T^x(\underline{r}_5)d^2\underline{r}_5 + \int G_{ny}^{EE}(\underline{r},\underline{r}_6)J_T^y(\underline{r}_6)d^2\underline{r}_6 \tag{3.19}$$

where G_{zz}^{HH} ,G_{zx}^{HE} andG_{zy}^{HE} are the magnetic field Green functions of Eq. (3.11) due to the out of plane magnetic current density and the transverse components of the electric current density and respectively. In a similar manner , and are the transverse electric field components Green functions due to the latter current sources respectively, with $n = \{x, y\}$. r is the position vector of the observation point and $\{r_1, .., r_6\}$ are position vectors inside the thermal emitter volume. Substituting Eq.s(3.18-3.19) in Eq.(3.17), the ensemble averaged Poynting vector will be as follows:

$$\left\langle \underline{S}^H \right\rangle = 2\hat{x}Re\{\langle E_y\, H_z^*\rangle\} - 2\hat{y}Re\{\langle E_x\, H_z^*\rangle\} = \hat{x}\left\langle \underline{S}_x^H \right\rangle + \hat{y}\left\langle \underline{S}_y^H \right\rangle \tag{3.20}$$

Substituting again with Eq.s (3.4) and (3.5) yields,

$$\begin{aligned}\langle E_y\, H_z^*\rangle = &\frac{\omega\mu_0}{\pi}\Theta(\omega,T)\int d^2\underline{r}_1 G_{yz}^{EH}(\underline{r},\underline{r}_1)Im\{\mu_{zz}(\underline{r}_1)\}G_{zz}^{HH*}(\underline{r},\underline{r}_1)\\ &+\frac{\omega\varepsilon_0}{\pi}\Theta(\omega,T)\int d^2\underline{r}_2\sum_{n=x,y}\sum_{m=x,y}G_{yn}^{EE}(\underline{r},\underline{r}_2)Im\{\varepsilon_T^{mn}(\underline{r}_2)\}G_{zm}^{HE*}(\underline{r},\underline{r}_2)\end{aligned} \tag{3.21}$$

Notice here that we used the property $\langle J_T^m\, K^{n*}\rangle$ since the medium is non-chiral. Similarly for the y-component,

$$\langle E_x\, H_z^* \rangle = \frac{\omega\mu_0}{\pi}\Theta(\omega,T)\int d^2\underline{r}_1 G_{xz}^{EH}(\underline{r},\underline{r}_1) Im\{\mu_{zz}(\underline{r}_1)\} G_{zz}^{HH*}(\underline{r},\underline{r}_1) + \frac{\omega\varepsilon_0}{\pi}\Theta(\omega,T)\int d^2\underline{r}_2 \sum_{n=x,y}\sum_{m=x,y} G_{xn}^{EE}(\underline{r},\underline{r}_2) Im\{\varepsilon_T^{mn}(\underline{r}_2)\} G_{zm}^{HE*}(\underline{r},\underline{r}_2) \tag{3.22}$$

The E-polarization of Eq. (3.14) can be treated in a similar way, that is:

$$E_z(\underline{r}) = \int G_{zz}^{EE}(\underline{r},\underline{r}_1) J_z(\underline{r}_1) d^2\underline{r}_1 + \int G_{zx}^{EH}(\underline{r},\underline{r}_2) K_T^x(\underline{r}_2) d^2\underline{r}_2 + \int G_{zy}^{EH}(\underline{r},\underline{r}_3) K_T^y(\underline{r}_3) d^2\underline{r}_3 \tag{3.23}$$

$$\underline{H}_n(\underline{r}) = \int G_{nz}^{HE}(\underline{r},\underline{r}_4) J_z(\underline{r}_4) d^2\underline{r}_4 + \int G_{nx}^{HH}(\underline{r},\underline{r}_5) K_T^x(\underline{r}_5) d^2\underline{r}_5 + \int G_{ny}^{HH}(\underline{r},\underline{r}_6) K_T^y(\underline{r}_6) d^2\underline{r}_6 \tag{3.24}$$

This yields the Poynting vector as:

$$\left\langle \underline{S}^E \right\rangle = -2\hat{x} Re\{\left\langle E_z\, H_y^* \right\rangle\} + 2\hat{y} Re\{\langle E_z\, H_x^* \rangle\} = \hat{x}\left\langle \underline{S}_x^E \right\rangle + \hat{y}\left\langle \underline{S}_y^E \right\rangle \tag{3.25}$$

$$\left\langle E_z\, H_y^* \right\rangle = \frac{\omega\varepsilon_0}{\pi}\Theta(\omega,T)\int d^2\underline{r}_1 G_{zz}^{EE}(\underline{r},\underline{r}_1) Im\{\varepsilon_{zz}(\underline{r}_1)\} G_{yz}^{HE*}(\underline{r},\underline{r}_1) + \frac{\omega\mu_0}{\pi}\Theta(\omega,T)\int d^2\underline{r}_2 \sum_{n=x,y}\sum_{m=x,y} G_{zn}^{EH}(\underline{r},\underline{r}_2) Im\{\mu_T^{mn}(\underline{r}_2)\} G_{ym}^{HH*}(\underline{r},\underline{r}_2) \tag{3.26}$$

And similarly for the y-component:

$$\langle E_z\, H_x^* \rangle = \frac{\omega\varepsilon_0}{\pi}\Theta(\omega,T)\int d^2\underline{r}_1 G_{zz}^{EE}(\underline{r},\underline{r}_1) Im\{\varepsilon_{zz}(\underline{r}_1)\} G_{xz}^{HE*}(\underline{r},\underline{r}_1) + \frac{\omega\mu_0}{\pi}\Theta(\omega,T)\int d^2\underline{r}_2 \sum_{n=x,y}\sum_{m=x,y} G_{zn}^{EH}(\underline{r},\underline{r}_2) Im\{\mu_T^{mn}(\underline{r}_2)\} G_{xm}^{HH*}(\underline{r},\underline{r}_2) \tag{3.27}$$

Note that calculations can be repeated for the physical spaces of H-polarization of Eq.(3.12) and E-polarization of Eq.(3.13).

3.5 Two Dimensional E/H-Polarization Camouflages

In this section, we show how to transform a TR problem between two spaces to produce a TR illusion. We consider an illustrative numerical example of transformation between $2D$ spaces. As shown in Fig. 3.1, the departure space includes a thermally radiating circular shaped object (with radius r_0) surrounded by a circular coating (with radius r_{ex}). It is desired that when thermally radiating, these cylinders mimic the TR signature of a horizontal elliptical shaped object (with the outer boundary defined by the radial distance $\rho(x, y)$) for its E-polarization, and simultaneously mimic the TR signature of a vertical elliptical shaped object (with the outer boundary defined by the radial distance $\eta(x, y)$) for its H-polarization.

The objects in all spaces are assumed to be embedded in a non-absorbing background medium in such a way that the areas surrounding the objects, including the coating, do not contribute to TR (at least the coating can be engineered in such a way that its thermal radiation is appreciably less than the target in the frequency band). Hence the radiated field within an arbitrary line of sight will be the superposition of the thermal radiation of the two polarizations. The departure space is chosen to be the physical space for both polarizations, while the virtual space for each polarization is chosen to be the arrival space of the corresponding assigned transformations. If the detector is polarization insensitive, the observer will detect both the vertical and horizontal elliptical shaped objects simultaneously giving the illusion - for the observer- that the two objects coincide.

In 2D space, H- and E- polarizations are independent. Such property allows

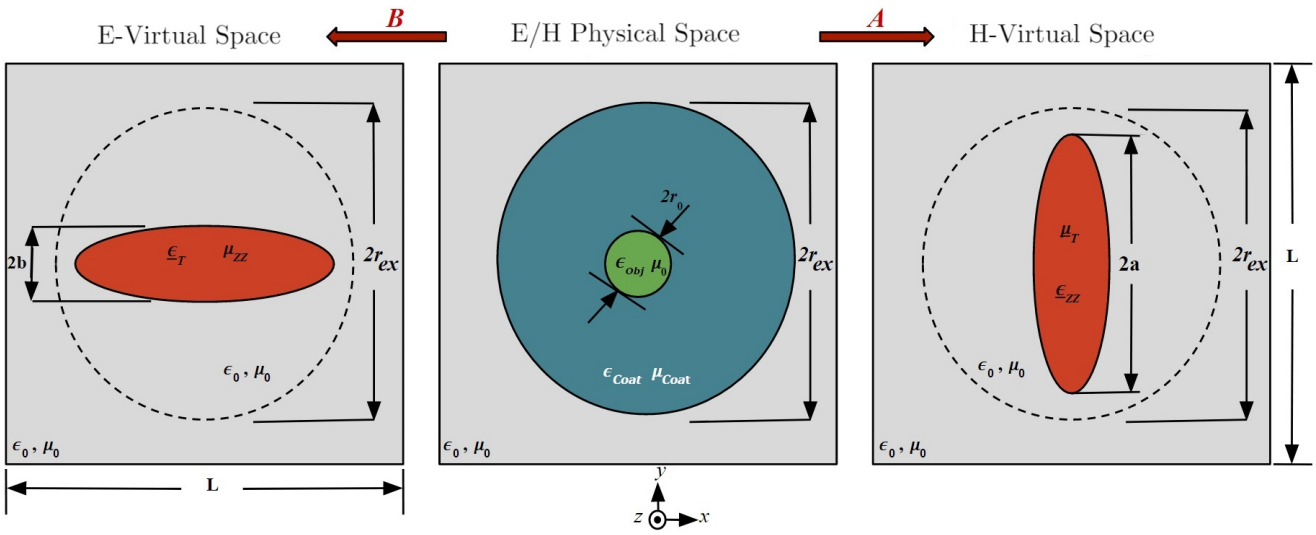

Figure 3.1: schematic of the TR illusion example discussed in section (3.5). The middle figure is for the E/H physical space (departure space) with a homogeneous anisotropic lossy circular object with radiusr_0 [$\varepsilon_{obj}^{mn} = \delta^{mn}(3 + i0.02)$ and $\mu_{obj}^{mn} = \delta^{mn}(1 + i0.02\delta^{mz})$] coated with an inhomogeneous anisotropic circular coat with radius r_{ex}. The left figure is for the E-polarization virtual space with inhomogeneous anisotropic horizontal elliptical shaped object with semi-axes a and b embedded in a homogeneous medium. The right figure is similar but for a vertical ellipse and for H-polarization. The region outside r_{ex} is unity transformed for both polarizations. The areas of all spaces between the dotted external cylinder and the virtual or physical objects, are lossless and do not contribute to the thermal radiation. For numerical calculations, L was set to be 11.1λ with matched boundary conditions at the square frames.

us to design cloaks to mimic one one object for E-polarization and another for H-polarization (horizontal or vertical ellipse) per polarization. It is therefore possible to have two independent transformations A and B for H- and E-polarizations respectively. We provide here an illustration for the H-polarization case but the quantities for the E-polarization case can be retrieved by considering the duality between both polarizations and replacing $\eta(\theta)$ by $\rho(\theta)$. Considering the H-polarization case, the simplest form of the coordinate transformation A can be written as follows:

$$\begin{aligned} r^{'} &= \frac{\eta(\theta)}{r_0} r \\ \theta^{'} &= \theta \ \text{ Object transformation } (0 < r < r_0) \end{aligned} \tag{3.28}$$

Notice here that (x, y) and (r, θ) are the Cartesian and polar coordinates of the departure space, while $(x^{'}, y^{'})$ and $(r^{'}, \theta^{'})$ are the Cartesian and polar coordinates of the arrival space. Now, to design the coat parameters, a transformation is done from the surrounding medium in the virtual space, ensuring continuity at the inner and outer boundaries of the coat $(\eta < r < r_{ex})$ as follows:

$$r = \{ \begin{array}{l} \frac{r_{ex}-r_0}{r_{ex}-\eta}(r^{'} - r_{ex}) + r_{ex} \implies (r_0 < r < r_{ex}) \text{ and } (\eta < r^{'} < r_{ex}) \\ \qquad\qquad r^{'} \implies (r > r_{ex}) \text{ and } (r^{'} > r_{ex}) \end{array} \tag{3.29}$$

$$\theta^{'} = \theta$$

Eq.s (3.30-3.31) are the basis for the T.O transformation of the physical parameters. As a result, the in-homogeneous regions are the two ellipses of the virtual spaces and the cylinder cloak of the physical space, while the cylinder itself and the cloaks of both virtual spaces are homogeneous.

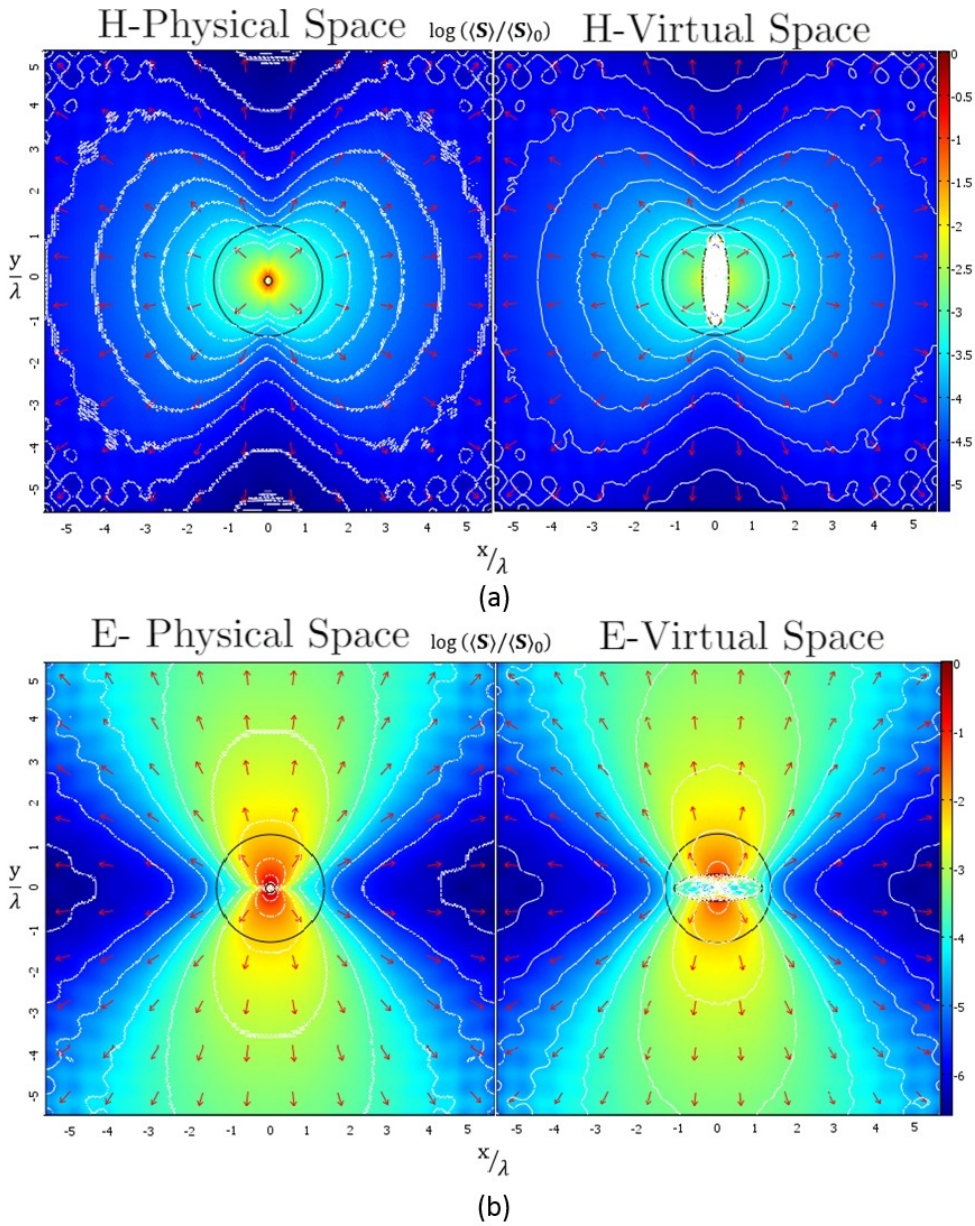

Figure 3.2: Numerical calculation of normalized time averaged radiated poynting vector (log scale) at the virtual and physical spaces of E- and H-polarization as depicted in Fig.3.1, (a) H-polarization physical (left) and virtual (right) (b) E-polarization physical (left) and virtual (right). Colored surfaces, red arrows and white contours indicate the modulus (log scale), direction and isolines of the poynting vector respectively. The left figures consider the circular radiating cylinder given in the middle part of Fig. 3.2. These left figures give the TR pattern of the cylinder coated to mimic the TR patterns of vertical (Fig. 3.2(a)) and horizontal (Fig. 3.2(b)) ellipses for E-and H- polarizations. The right figures consider the vertical and horizontal coated ellipses of 3.1. These right figures give the TR pattern of the ellipses for each polarization and these patterns must be compared to those of the left figures. Normalization constants are: for H-polarization, $< S >_0 = 5.7 \times 10^{-33} \frac{W}{m^2}$, while for E-polarization, $< S >_0 \; 10^{-28} \frac{W}{m^2}$. We notice that the emitted power has the same distribution outside the transformation regions for both polarizations at the physical and virtual spaces.

In general, all media are anisotropic in regions $r < r_{ex}$ but, for simplicity, we assume that the circular object residing inside the E/H physical space of Fig. 3.1 (middle figure) has a diagonal homogeneous permittivity and permeability. Consequently, the electric current densities that are embedded in this object and polarized in orthogonal directions are uncorrelated i.e.: $< J^x J^{y*} >= 0$. Furthermore, following Eq.(3.2), the transverse electric current densities of the H-polarization case are transformed as follows:

$$\begin{aligned} J^{x'} &= \frac{1}{det(A)} A_x^{x'} J^x + \frac{1}{det(A)} A_y^{y'} J^y \\ J^{y'} &= \frac{1}{det(A)} A_x^{y'} J^x + \frac{1}{det(A)} A_y^{x'} J^y \end{aligned} \tag{3.30}$$

Similarly, the z-component of the magnetic current is transformed as:

$$K_z^{'} = \frac{K_z}{det(A)} \tag{3.31}$$

We calculated the harmonic time averaged Poynting vector of the emitted field using thermal discrete dipole approximation (TDDA) and COMSOL Multiphysics was used for the numerical implementation. Appendix D summarizes the way the setup of the numerical calculations were held. As shown in Figs 3.2(a) and 3.2(b), for each polarization the emitted power has the same pattern outside the cloak both in the physical and virtual spaces, which proves that the coat has allowed a successful mimicking as predicted. The imaginary part of the parameters were chosen such that the emitted radiation for both polarizations have distinct patterns. The parameters involved in the physical space object are:

$$\begin{aligned} &\varepsilon_{xx} = \varepsilon_{yy} = \varepsilon_{zz} = 3 + i0.02 \\ &\mu_{xx} = \mu_{yy} = 1 \\ &\mu_{zz} = 1 + i0.02 \end{aligned} \tag{3.32}$$

Hence the permittivity is isotropic but the permeability is not. Notice that ε_{xx}, ε_{yy} and μ_{zz} are involved in the E-polarization problem, while μ_{xx}, μ_{yy} and ε_{zz} are involved in the H-polarization problem. The radial distance for the horizontal and vertical ellipses are respectively.

$$\begin{aligned} \eta(\theta) &= \left[\left(\frac{cos(\theta)}{b}\right)^2 + \left(\frac{sin(\theta)}{a}\right)^2\right]^{-\frac{1}{2}} \\ \rho(\theta) &= \eta(\theta \pm \frac{\pi}{2}) \end{aligned} \tag{3.33}$$

slight differences can be seen and must be attributed to numerical error of discretization. The external coating radius is $r_{ex} = \frac{4}{3}\lambda$, the physical space object radius is $r_0 = (\frac{1}{9})\lambda$, while the semi-axis of the virtual space objects are $a = (\frac{10}{9})\lambda$ and $b = (\frac{1}{3})\lambda$. Calculation is performed for the near field. Such a calculation can be scaled to any arbitrary wavelength, taking into account materials dispersion. The choice of the dimensions (small size of the radiating objects) results from our limited computational power, but similar results would be obtained for micrometer wavelengths and meter objects. To conclude this section, since the Poynting vector of the thermal radiation in the physical and virtual spaces are identical for both polarizations outside the transformation region, then the developed theory is confirmed within our hypothesis framework.

3.6 Limitations and Conclusions

In this chapter, we have introduced and validated a Transformation Optics (TO) based technique to manipulate the Thermal Radiation (TR) signature for camouflage or illusion purposes. We showed that Fluctuation Electrodynamics (FE) is invariant under TO, so that by engineering the parameters of the materials in the physical space, one can get the same TR signature than another one emitted in the virtual space. The concept was illustrated by a numerical example employing a 2D space

transformation. For this example, we used a double mimicking procedure (one per polarization) which is the extension of a previous double cloaking procedure. Although the proposed tool seems promising, limitations must be emphasized. For instance, realizing TO based designs remains a substantial challenge since the resultant parameters after transformation are nonhomogeneous tensorial parameters. Also the dispersion laws of the physical parameters should also be controlled for the TR illusion to work in a wide spectral range. Another limitation lies on the fact that the objects have the same temperature in both virtual and physical spaces; such difficulty could conceptually be overcome by manipulating the chemical potential of photons with an electric potential applied on a semiconductor medium to shift its effective temperature [16] and [33]. The transformations that we used were single valued so that every point in the virtual space was mapped to a unique image in the physical space. Notice that multi-valued transformations were typically used in the context of overlapping illusion optics [128] and anti-cloaks [15] where the image has a larger scattering cross section than that of the virtual space; they were also used for shifting transformations where the image is seen at different locations [61], and size [124] than those of the original object. We restricted the frame to lossy media with positive imaginary parts for permittivity and permeability, and the temperature was assumed positive. To achieve multivalued transformation, such assumptions must be relaxed. For example, a negative real permittivity was employed to produce anticloaks [15]. To implement TR analog of the anti-cloak, a negative imaginary permittivity (permeability) media (gain media) is required. However, the self-correlation of current densities must always be a positive quantity, for which reason a modified version of FDT must be used [55]. It was mentioned in [55] that a population inverted two level system gain media exhibits a negative effective temperature such that Planck distribution is negative. Negative Planck distribution can be also achieved by controlling the photonic chemical potential [16] and [33]. Finally, Thermal radiation illusion

of objects with graded temperature is possible by simultaneous transformation of thermal conductivities and electromagnetic constitutive parameters.

CHAPTER IV

Cloaking and Scattering Camouflage using Transformation Optics based Mantle Meta-surfaces

4.1 Introduction

Transformation optics (TO) have been shown to be an exact design tool for invisibility and Scattering Illusion cloaks; However, TO based cloaks are hard to be fabricated as they are bulky objects with highly anisotropic, in-homogeneous media. On the other side, cloaking using meta-surfaces (also called mantle cloaks) was first proposed by Alu, the main advantage for such mantle cloaks is their simplicity and easiness for fabrication when compared to the T.O based cloaks. Mantle cloaks are thin meta-surfaces (ideally zero thickness) which separate the object to be cloaked and the surrounding where an observer can be located. Mantle cloaks are designed based on scattering cancellation technique (SCT). The main idea of SCT technique, is to design the mantle cloak such that its scattered field for a specific incident field, destructively interferes with the scattering due the object to be cloaked in order to give the illusion of invisibility. Although this technique is relatively simple, mantle cloaks suffer from two main limitations when compared with T.O based cloaks:

1. In case of invisibility, SCT based mantle cloaks are designed for a specific incident field pattern (typically the lowest order cylindrical wave or spherical

harmonic), while T.O based cloaks are independent of the exact nature of the incident field as the cloak's constitutive parameters depend solely on the space transformation.

2. SCT assumes the knowledge of the scattering of both objects (to be cloaked and to be mimicked) for a specific incident field. This is why SCT based mantle cloaks are typically restricted to circular (2D) or spherical (3D) geometry. The circularly (spherically) symmetry condition requires the shape of the scatterer to be circle (2D) or sphere in 3D and its permeability and permeability tensors are diagonal in the polar (spherical) coordinates and also they can be only radial dependent function.

In order to overcome these two limitations, one may be interested to combine both approaches, that is, SCT and TO. Although in literature SCT and TO are different techniques, in this chapter we show that these two techniques are equivalent, which allows us to propose a new procedure to design Mantle cloaks based on transformation optics theory (we call them **TO based Mantle cloaks**). In order to understand the equivalence it is important to consider the following points

- A meta-surface is an electromagnetic device that is used to manipulate the electromagnetic field. Its main property is to introduce a jump or discontinuity for one tangential component of electric $\bar{E}_{\parallel}$ or magnetic $\bar{H}_{\parallel}$ fields or both simultaneously.

- A discontinuous space transformation can induce a jump or discontinuity $\Delta\bar{E}_{\parallel}$ and $\Delta\bar{H}_{\parallel}$ for the tangential field components.

- By equating the two field jumps, we can relate the metasurface susceptibility to the discontinuous space transformation.

Actually based on the former point of view, any meta-surface is a discontinuity in the electromagnetic space (also commonly named virtual space). In other words, a zero thickness meta-surface (with arbitrary susceptibility tensors) located in a physical space is equivalent to a discontinuity in the corresponding virtual space. The procedure to design the proposed TO based Mantle cloaks is the same as the standard procedure of TO is used where one transforms between a virtual and physical space using a discontinuous transformation, and the necessary meta-surface is introduced to ensure the continuity of the spaces where such TO based Mantle cloaks can replace the TO classical cloaks. To model such TO based MS, we make use of two different but equivalent descriptions for the electromagnetic response of a general passive metasurface namely *Generalized sheet Transverse Condition* (**GSTC** condition) and Impedance Matrix network representation. In both cases the metasurface will be represented as a linear operator which connects the electric and magnetic fields at its sides. Impedance representation, which is a typical circuit design tool in microwave and RF engineering, provides a simple interface for both electromagnetic reflection and thermal radiation. Also, we will introduce the meta-surface susceptibility tensors in order to implement the meta-surface; here the GSTC model is used where it relates the electric and magnetic fields. The advantage of GSTC is that it paves the way for a physical realization of the necessary unit cell topology and material properties and etc as the Susceptibility tensors provided by GSTC can be easily related to collective polarizabilities of such unit cell physical realizations.

This chapter is arranged as following; First section (4.2) includes the derivation of the impedance matrix elements and the corresponding susceptibility surface tensors for arbitrary planar and circular (cylindrical) shaped Meta-surface. In section (4.3), we show the equivalence between a thin meta-surface separating two regions and a discontinuous space transformation that yields these two space regions. It is shown

that the former point of view is applied to scattering camouflage where a T.O-based mantle cloak is designed to replace the classic typical bulky transformation optics cloak of chapter (2). Numerical simulations are done using *COMSOL 3.5A* and results provided are consistent with the theoretical models shown in this chapter.

4.2 Meta-surface models: GSTC versus Impedance Matrix

In this section both Impedance Matrix and GSTC representations of a MS are considered. For both representations, planar and cylindrical MS.s are highlighted.

4.2.1 Impedance matrix representation

SC based mantle cloaks are typically a simple surface impedance or equivalently electric susceptibility, however this cloak is a special case of more general "matching" network. In order to set the stage for using TO based Mantle cloaks, the general case of a MS must be formulated first. In this work, we are mainly dealing with problems in 2D space which are invariant along the out of plane axis z-axis, so accordingly, the fields are typical decomposed in (TM_z/E) and (TE_z/H)-Polarizations with the field components $\{E_z, \bar{H}_T\}$ and $\{H_z, \bar{E}_T\}$ respectively. For either case the desired MS can be represented as two port network with the impedance matrix and the sides of the M.S are represented as ports. Such Network relates the electric (voltage) and Magnetic (current) field amplitudes located on both M.S sides 1 and 2 or equivalently connected to ports 1 and 2 respectively as following :

$$\begin{aligned} E_{1,\parallel}(\bar{r}_s) &= \int_{\bar{r}_s^{'}\in S} \Big(Z_{11}(\bar{r}_s^{'}, \bar{r}_s - \bar{r}_s^{'}) H_{1,\parallel}(\bar{r}_s^{'}) - Z_{12}(\bar{r}_s^{'}, \bar{r}_s - \bar{r}_s^{'}) H_{2,\parallel}(\bar{r}_s^{'}) \Big)\, d\bar{r}_s^{'} \\ \bar{E}_{2,\parallel}(\bar{r}_s) &= \int_{\bar{r}_s^{'}\in S} \Big(Z_{21}(\bar{r}_s^{'}, \bar{r}_s - \bar{r}_s^{'}) H_{1,\parallel}(\bar{r}_s^{'}) - Z_{22}(\bar{r}_s^{'}, \bar{r}_s - \bar{r}_s^{'}) H_{2,\parallel}(\bar{r}_s^{'}) \Big)\, d\bar{r}_s^{'} \end{aligned} \tag{4.1}$$

Equation (4.1) is a generalized form of a convolution integral where the electric

and magnetic fields at different locations $\bar{r}_s$ and $\bar{r}_s^{'}$ along the MS are related by the arguments of the impedance matrix Z whose value changes all over the MS.

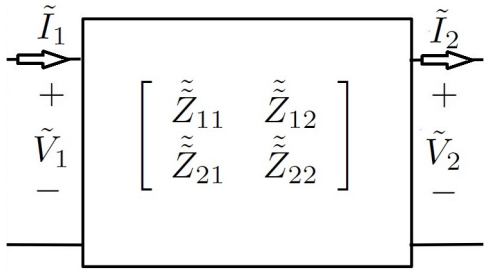

Figure 4.1: Representation of Z-matrix in the Fourier space for a homogeneous (planar or cylindrical) MS.

It is customary to choose an appropriate basis to describe the electromagnetic scattering problems, and such choice is highly dependent on the symmetry of the problem's geometry; it is typical to expand electromagnetic fields in plane and cylindrical wave bases when dealing with unbounded planar slabs and bounded 2D objects respectively.

Z-matrix for Planar MS For a planar MS, The fields are typically expanded in terms of plane waves basis. By applying a Fourier transform with respect to the transverse coordinate along the metasurface $\bar{r}_s$, the Impedance matrix representation will be :

$$\begin{aligned}
\tilde{E}_{1,\parallel}(\bar{k}_\parallel) &= \frac{1}{2\pi} \int\limits_{\bar{k}_\parallel^{'} \in \mathbb{R}^2} \left(\tilde{\tilde{Z}}_{11}(\bar{k}_\parallel - \bar{k}_\parallel^{'}, \bar{k}_\parallel^{'}) \tilde{H}_{1,\parallel}(\bar{k}_\parallel^{'}) - \tilde{\tilde{Z}}_{12}(\bar{k}_\parallel - \bar{k}_\parallel^{'}, \bar{k}_\parallel^{'}) \tilde{H}_{2,\parallel}(\bar{k}_\parallel^{'}) \right) d\bar{k}_\parallel^{'} \\
\tilde{E}_{2,\parallel}(\bar{k}_\parallel) &= \frac{1}{2\pi} \int\limits_{\bar{k}_\parallel^{'} \in \mathbb{R}^2} \left(\tilde{\tilde{Z}}_{21}(\bar{k}_\parallel - \bar{k}_\parallel^{'}, \bar{k}_\parallel^{'}) \tilde{H}_{1,\parallel}(\bar{k}_\parallel^{'}) - \tilde{\tilde{Z}}_{22}(\bar{k}_\parallel - \bar{k}_\parallel^{'}, \bar{k}_\parallel^{'}) \tilde{H}_{2,\parallel}(\bar{k}_\parallel^{'}) \right) d\bar{k}_\parallel^{'}
\end{aligned} \tag{4.2}$$

where the tilde, double tilde indicates a 1D and 2D Fourier transform with respect to $\bar{r}_s$, as following:

$$
\begin{aligned}
\tilde{E}_{1,\parallel}(\bar{k}_\parallel) &= \int_{\bar{r}_s} E_{1,\parallel}(\bar{r}_s) e^{-i\bar{k}_\parallel \cdot \bar{r}_s} d\bar{r}_s \\
&= \iint \left[Z_{11}(\bar{r}_s^{'}, \bar{r}_s - \bar{r}_s^{'}) H_{1,\parallel}(\bar{r}_s^{'}) - Z_{12}(\bar{r}_s^{'}, \bar{r}_s - \bar{r}_s^{'}) H_{2,\parallel}(\bar{r}_s^{'}) \right] e^{-i\bar{k}_\parallel \cdot \bar{r}_s} d\bar{r}_s d\bar{r}_s^{'} \quad \bar{\lambda} = \bar{r}_s^{'} - \bar{r}_s \\
&= \int_0^{2\pi} \left(\frac{1}{2\pi} \int_0^{2\pi} \left[Z_{11}(\bar{r}_s^{'}, \bar{\lambda}) H_{1,\parallel}(\bar{r}_s^{'}) - Z_{12}(\bar{r}_s^{'}, \bar{\lambda}) H_{2,\parallel}(\bar{r}_s^{'}) \right] e^{-i\bar{k}\cdot\lambda} d\lambda \right) e^{-i\bar{k}\cdot\bar{r}_s^{'}} d\bar{r}_s^{'} \\
&= \int_0^{2\pi} \left[\tilde{Z}_{11}(\bar{r}_s^{'}, \bar{k}_\parallel) H_{1,\parallel}(\bar{r}_s^{'}) - \tilde{Z}_{12}(\bar{r}_s^{'}, \bar{k}_\parallel) H_{2,\parallel}(\bar{r}_s^{'}) \right] e^{-i\bar{k}_\parallel \cdot \bar{r}_s^{'}} d\bar{r}_s^{'} \quad \textit{Multiplication in } \bar{r}_s \textit{ space} \\
&= \frac{1}{2\pi} \int_{\bar{k}_\parallel^{'} \in \mathbb{R}^2} \left(\tilde{\tilde{Z}}_{11}(\bar{k}_\parallel - \bar{k}_\parallel^{'}, \bar{k}_\parallel^{'}) \tilde{H}_{1,\parallel}(k_\parallel^{'}) - \tilde{\tilde{Z}}_{12}(\bar{k}_\parallel - \bar{k}_\parallel^{'}, \bar{k}_\parallel^{'}) \tilde{H}_{2,\parallel}(\bar{k}_\parallel^{'}) \right) d\bar{k}_\parallel^{'}
\end{aligned}
\tag{4.3}
$$

The last terms in Eq.(4.3) is a Fourier transform of a multiplication between the magnetic fields and the Z-parameters leading to Eq.(4.2). Similar treatment is done for $E_{2,\parallel}$. In the case of local MS, the impedance matrix representation becomes as following (Fig.(4.1)):

$$
\begin{aligned}
\tilde{E}_{1,\parallel}(k_\parallel) &= \tilde{\tilde{Z}}_{11}(k_\parallel) \tilde{H}_{1,\parallel}(k_\parallel) - \tilde{\tilde{Z}}_{12}(k_\parallel) \tilde{H}_{2,\parallel}(k_\parallel) \\
\tilde{E}_{2,\parallel}(k_\parallel) &= \tilde{\tilde{Z}}_{21}(k_\parallel) \tilde{H}_{1,\parallel}(k_\parallel) - \tilde{\tilde{Z}}_{22}(k_\parallel) \tilde{H}_{2,\parallel}(k_\parallel)
\end{aligned}
\tag{4.4}
$$

which is the classical Z-matrix form of two port network.

Z-matrix for cylindrical MS By using cylindrical waves as basis for the incident field, at cylindrical boundary of radius $\rho = \rho_0$, Eq.(4.1) is rewritten in terms of the azimuthal angle coordinateϕ.

$$
\begin{aligned}
E_{1,\parallel}(\rho_0, \phi) &= \frac{1}{2\pi} \int Z_{11}(\phi', \phi - \phi') H_{1,\parallel}(\rho_0, \phi^{'}) - Z_{12}(\phi', \phi - \phi') H_{2,\parallel}(\rho_0, \phi^{'}) d\phi^{'} \\
E_{2,\parallel}(\rho_0, \phi) &= \frac{1}{2\pi} \int Z_{21}(\phi', \phi - \phi') H_{1,\parallel}(\rho_0, \phi^{'}) - Z_{22}(\phi', \phi - \phi') H_{2,\parallel}(\rho_0, \phi^{'}) d\phi^{'}
\end{aligned}
\tag{4.5}
$$

The impedance matrix representation for a generically non local and in-homogeneous cylindrical MS will have the following form(Fig.(4.1)):

$$\begin{aligned}\tilde{E}_{1,\parallel}[n] &= \sum_{m\in\mathbb{Z}} \left(\tilde{\tilde{Z}}_{11}[n-m,m]\tilde{H}_{1,\parallel}[m] - \tilde{\tilde{Z}}_{12}[n-m,m]\tilde{H}_{2,\parallel}[m]\right) \\ \tilde{E}_{2,\parallel}[n] &= \sum_{m\in\mathbb{Z}} \left(\tilde{\tilde{Z}}_{21}[n-m,m]\tilde{H}_{1,\parallel}[m] - \tilde{\tilde{Z}}_{22}[n-m,m]\tilde{H}_{2,\parallel}[m]\right)\end{aligned} \tag{4.6}$$

where the tilde indicates a Fourier transform with respect to ϕ defined as following:

$$E(\rho_0,\phi) = \sum_n \tilde{E}[\rho_0,n]e^{in\phi} \tag{4.7}$$

and n is the corresponding discrete conjugate variable (also the order of the cylindrical wave). The impedance matrix representation for a homogeneous cylindrical MS (but in general order dispersive) will be reduced to the following:

$$\begin{aligned}\tilde{E}_{1,\parallel}[n] &= \tilde{\tilde{Z}}_{11}[n]\tilde{H}_{1,\parallel}[n] - \tilde{\tilde{Z}}_{12}[n]\tilde{H}_{2,\parallel}[n] \\ \tilde{E}_{2,\parallel}[n] &= \tilde{\tilde{Z}}_{21}[n]\tilde{H}_{1,\parallel}[n] - \tilde{\tilde{Z}}_{22}[n]\tilde{H}_{2,\parallel}[n]\end{aligned} \tag{4.8}$$

The main properties of the meta-surface can be emphasized from the impedance matrix of such network as:

- The meta-surface is reciprocal if $\tilde{\tilde{Z}}_{21} = \tilde{\tilde{Z}}_{12}$.
- The meta-surface is symmetric if $\tilde{\tilde{Z}}_{11} = \tilde{\tilde{Z}}_{22}$.
- The meta-surface is loss-less if $\tilde{\tilde{Z}}_{ab} = j\tilde{\tilde{X}}_{ab}$ with $a,b = \{1,2\}$ and $\tilde{\tilde{X}}_{ab} \in \mathbb{R}$.

Y-matrix for cylindrical The relation between the electric (voltage) field and the magnetic (current) field can be also written in an inverse way to the impedance matrix method depicted earlier. Such inverse relation is called $Y-$matrix. For a

cylindrical meta-surface the relation between the electric and magnetic fields will be written as following:

$$\begin{aligned} H_{1,\parallel}(\rho_0,\phi) &= \frac{1}{2\pi}\int Y_{11}(\phi',\phi-\phi')E_{1,\parallel}(\rho_0,\phi^{'}) + Y_{12}(\phi',\phi-\phi')E_{2,\parallel}(\rho_0,\phi^{'})d\phi^{'} \\ H_{2,\parallel}(\rho_0,\phi) &= \frac{1}{2\pi}\int Y_{21}(\phi',\phi-\phi')H_{1,\parallel}(\rho_0,\phi^{'}) + Y_{22}(\phi',\phi-\phi')E_{2,\parallel}(\rho_0,\phi^{'})d\phi^{'} \end{aligned} \tag{4.9}$$

The admittance matrix representation for a generically non local cylindrical MS will have the following form:

$$\begin{aligned} \tilde{H}_{1,\parallel}[n] &= \sum_{m\in\mathbb{Z}}\left(\tilde{\tilde{Y}}_{11}[n-m,m]\tilde{E}_{1,\parallel}[m] + \tilde{\tilde{Y}}_{12}[n-m,m]\tilde{E}_{2,\parallel}[m]\right) \\ \tilde{H}_{2,\parallel}[n] &= \sum_{m\in\mathbb{Z}}\left(\tilde{\tilde{Y}}_{21}[n-m,m]\tilde{E}_{1,\parallel}[m] + \tilde{\tilde{Y}}_{22}[n-m,m]\tilde{E}_{2,\parallel}[m]\right) \end{aligned} \tag{4.10}$$

4.2.2 GSTC

Since the Z-matrix representation is a variant of a transfer matrix, it is sufficient to predict the electromagnetic response of the meta-surface; however, it says nothing on the detailed nature of this metasurface (the shape of the constituting unit cells, the materials to be used for fabrication,...). An intermediate step towards a successful design is to calculate for the MS's susceptibility tensor elements. Such elements can be calculated using *Generalized sheet Transverse Condition* (**GSTC** condition). GSTC and Z-matrix representations are different but equivalent descriptions for the electromagnetic response of a MS. Since, although, a meta-surface is considered to be a generalization of lumped circuit elements in higher dimensions, mathematically speaking, it is a linear operator that maps between the electric and magnetic field amplitudes along both its sides. In this section, we show the correspondence between both (Z- and GSTC) representations and then we show how the metasurface's susceptibility can be calculated for different circuit configurations. Note that in what follows we use the terms " electric field, voltage wave" and "magnetic field, current

wave" interchangeably. According to GSTC, the field discontinuities across the MS are linearly related to these fields' average values with proportionality factors that are the MS's susceptibility tensor elements. This dependence is written following:

Assuming $e^{i\omega t}$ harmonic time dependence and assuming time invariant MS, then

$$\begin{aligned}
\hat{e}_n(\bar{r}_s) \times \Delta\bar{H}_{\parallel}(\bar{r}_s) &= j\omega\bar{P}_{\parallel}(\bar{r}_s) \\
\Delta\bar{E}_{\parallel}(\bar{r}_s) \times \hat{e}_n(\bar{r}_s) &= j\omega\bar{M}_{\parallel}(\bar{r}_s) \\
&\text{Where:} \\
\bar{E}(\bar{r}_s) &= \bar{E}_{\parallel}(\bar{r}_s) + \hat{e}_n(\bar{r}_s)E_{\perp}(\bar{r}_s) \\
\bar{H}(\bar{r}_s) &= \bar{H}_{\parallel}(\bar{r}_s) + \hat{e}_n(\bar{r}_s)H_{\perp}(\bar{r}_s) \\
\bar{P}(\bar{r}_s) &= \bar{P}_{\parallel}(\bar{r}_s) + \hat{e}_n(\bar{r}_s)P_{\perp}(\bar{r}_s) \\
\bar{M}(\bar{r}_s) &= \bar{M}_{\parallel}(\bar{r}_s) + \hat{e}_n(\bar{r}_s)M_{\perp}(\bar{r}_s) \\
&\text{Also } \Delta A = A_1 - A_2 \text{ for } A = \{\bar{E}, \bar{H}\}
\end{aligned} \tag{4.11}$$

where P and M are the MS Electric polarization and magnetic magnetization vectors respectively, Δ is the difference operator for the jump of the fields value on both sides 1 and 2 of the M.S, ($\parallel$ and $\perp$) are parallel and normal to the metasurface; $\hat{e}_n(\bar{r}_s)$ is the local normal unit vector to the metasurface at $\bar{r}_s$ which is the position vector for points on the metasurface. It is clear that GSTC conditions are an integral form of Maxwell's equations on both sides of the M.S discontinuity. The constitutive relations that relates the electric and magnetic polarizabilities to the electric and magnetic fields is determined based on the exact nature of the constitutive unit cells (atoms) that constitutes the M.S. Different special cases can be retrieved by choosing a combination of the following set of properties [(Non)Locality, (In)Homogenity,(Bi and/or An) Isotropicity, Active/Passive]. For a general M.S which is constrained to be **linear, time invariant, reciprocal, bi-anisotropic and inhomogenous,**

spatial dispersive (non-local), the MS polarizabilities are linearly related to the fields on both sides of the M.S as following:

$$
\begin{aligned}
\bar{P}(\bar{r}_s) &= \int\limits_{\bar{r}_s^{'}\in S} \left(\epsilon_0 \, \underline{\underline{\chi}}^{ee}(\bar{r}_s, \bar{r}_s - \bar{r}_s^{'})\bar{E}_{av}(\bar{r}_s^{'}) + \sqrt{\epsilon_0\mu_0} \, \underline{\underline{\chi}}^{em}(\bar{r}_s, \bar{r}_s - \bar{r}_s^{'})\bar{H}_{av}(\bar{r}_s)\right) d\bar{r}_s^{'} \\
\bar{M}(\bar{r}_s) &= \int\limits_{\bar{r}_s^{'}\in S} \left(\sqrt{\epsilon_0\mu_0} \, \underline{\underline{\chi}}^{me}(\bar{r}_s, \bar{r}_s - \bar{r}_s^{'})\bar{E}_{av}(\bar{r}_s^{'}) + \mu_0 \, \underline{\underline{\chi}}^{mm}(\bar{r}_s, \bar{r}_s - \bar{r}_s^{'})\bar{H}_{av}(\bar{r}_s^{'})\right) d\bar{r}_s^{'} \\
\text{where: } \bar{E}_{av}(\bar{r}_s) &= \frac{1}{2}\left(E_1(\bar{r}_s) + E_2(\bar{r}_s)\right) \\
\bar{H}_{av}(\bar{r}_s) &= \frac{1}{2}\left(H_1(\bar{r}_s) + H_2(\bar{r}_s)\right)
\end{aligned}
\tag{4.12}
$$

where av for averaging the field values on both sides 1 and 2 and the double underline is to indicate 2nd rank tensor so $\underline{\underline{\chi}}^{ee}$, $\underline{\underline{\chi}}^{mm}$, $\underline{\underline{\chi}}^{em}$, $\underline{\underline{\chi}}^{me} \in \mathbb{C}$ are the electric, magnetic, magneto-electric and electromagnetic susceptibility tensors describing the M.S. The components of the latter susceptibility tensors are described in Cartesian and cylindrical coordinates respectively as following:

$$
\begin{aligned}
\underline{\underline{\chi}} = \begin{bmatrix} \underline{\underline{\chi}}_{TT} & \underline{\chi}_{Tz} \\ \underline{\chi}_{zT} & \chi_{zz} \end{bmatrix} &= \begin{bmatrix} \chi_{xx} & \chi_{xy} & \chi_{xz} \\ \chi_{yx} & \chi_{yy} & \chi_{yz} \\ \chi_{zx} & \chi_{zy} & \chi_{zz} \end{bmatrix} \quad \bar{r} = \{x, y, z\} \\
&= \begin{bmatrix} \chi_{\rho\rho} & \chi_{\rho\phi} & \chi_{\rho z} \\ \chi_{\phi\rho} & \chi_{\phi\phi} & \chi_{\phi z} \\ \chi_{z\rho} & \chi_{z\phi} & \chi_{zz} \end{bmatrix} \quad \bar{r} = \{\rho, \phi, z\} \\
T : \textit{Transverse}
\end{aligned}
\tag{4.13}
$$

Note that Eq.(4.12) show all the properties except reciprocity which need separate condition. For instance, a reciprocal MS must fulfill the following:

$$
\begin{aligned}
\underline{\underline{\chi}}^{em} &= -\left(\underline{\underline{\chi}}^{me}\right)^{\tau} \quad \tau : \text{transpose} \\
\underline{\underline{\chi}}^{ee} &= \left(\underline{\underline{\chi}}^{ee}\right)^{\tau} \\
\underline{\underline{\chi}}^{mm} &= \left(\underline{\underline{\chi}}^{mm}\right)^{\tau}
\end{aligned}
\tag{4.14}
$$

GSTC for planar MS Assuming a planar metasurface, and using plane waves as basis for the incident field by applying the Fourier transform of Eq.(4.12) with respect to the tangent of the surface coordinate, the constitutive relation becomes:

$$
\begin{aligned}
\bar{\tilde{P}}(k_{\parallel}) &= \frac{1}{2\pi} \int\limits_{k_{\parallel}^{'} \in \mathbb{R}^2} \left(\epsilon_0 \, \underline{\underline{\tilde{\chi}}}^{ee}(k_{\parallel} - k_{\parallel}^{'}, k_{\parallel}^{'}) \bar{\tilde{E}}_{av}(k_{\parallel}^{'}) + \sqrt{\epsilon_0 \mu_0} \, \underline{\underline{\tilde{\chi}}}^{em}(k_{\parallel} - k_{\parallel}^{'}, k_{\parallel}^{'}) \bar{\tilde{H}}_{av}(k_{\parallel}^{'}) \right) dk_{\parallel}^{'} \\
\bar{\tilde{M}}(k_{\parallel}) &= \frac{1}{2\pi} \int\limits_{k_{\parallel}^{'} \in \mathbb{R}^2} \left(\sqrt{\epsilon_0 \mu_0} \, \underline{\underline{\tilde{\chi}}}^{me}(k_{\parallel} - k_{\parallel}^{'}, k_{\parallel}^{'}) \bar{\tilde{E}}_{av}(k_{\parallel}^{'}) + \mu_0 \, \underline{\underline{\tilde{\chi}}}^{mm}(k_{\parallel} - k_{\parallel}^{'}, k_{\parallel}^{'}) \bar{\tilde{H}}_{av}(k_{\parallel}^{'}) \right) dk_{\parallel}^{'}
\end{aligned}
\tag{4.15}
$$

where the tilde indicates a Fourier transform with respect to $\bar{r}_s$ with $k_{\parallel}$ is the corresponding conjugate variable. In the particular case of local M.S the convolution integrals in Eq.(4.15) is removed and are rewritten to be as following:

$$
\begin{aligned}
\bar{\tilde{P}}(k_{\parallel}) &= \epsilon_0 \, \underline{\underline{\tilde{\chi}}}^{ee}(k_{\parallel}) \bar{\tilde{E}}_{av}(k_{\parallel}) + \sqrt{\epsilon_0 \mu_0} \, \underline{\underline{\tilde{\chi}}}^{em}(k_{\parallel}) \bar{\tilde{H}}_{av}(k_{\parallel}) \\
\bar{\tilde{M}}(k_{\parallel}) &= \sqrt{\epsilon_0 \mu_0} \, \underline{\underline{\tilde{\chi}}}^{me}(k_{\parallel}) \bar{\tilde{E}}_{av}(k_{\parallel}) + \mu_0 \, \underline{\underline{\tilde{\chi}}}^{mm}(k_{\parallel}) \bar{\tilde{H}}_{av}(k_{\parallel})
\end{aligned}
\tag{4.16}
$$

GSTC for cylindrical Metasurface Assuming a cylindrical shaped metasurface located at $\rho = \rho_0$ and the transverse coordinate is specified by the azimuthal angle ϕ, so using cylindrical waves as basis for the incident field by considering the Fourier transform of Eq.(4.12) with respect to ϕ, the constitutive relation becomes

$$
\begin{aligned}
\tilde{\bar{P}}[n] &= \frac{1}{2\pi}\sum_{m\in\mathbb{Z}}\left(\epsilon_0\,\underline{\underline{\tilde{\chi}}}^{ee}[n-m,m]\tilde{\bar{E}}_{av}[m] + \sqrt{\epsilon_0\mu_0}\,\underline{\underline{\tilde{\chi}}}^{em}[n-m,m]\tilde{\bar{H}}_{av}[m]\right)\\
\tilde{\bar{M}}[n] &= \frac{1}{2\pi}\sum_{m\in\mathbb{Z}}\left(\sqrt{\epsilon_0\mu_0}\,\underline{\underline{\tilde{\chi}}}^{me}[n-m,m]\tilde{\bar{E}}_{av}[m] + \mu_0\,\underline{\underline{\tilde{\chi}}}^{mm}[n-m,m]\tilde{\bar{H}}_{av}[m]\right)
\end{aligned}
\tag{4.17}
$$

where the tilde, double tilde indicates a 1D and 2D fourier transform with respect to ϕ defined at Eq.(4.7) with n is the corresponding discrete conjugate variable(also the cylindrical wave order). Note that m was used twice, once as an index and other as superscript and used as an abbreviation for magnetic and the significance should be clear within the context. In the particular case of local M.S the convolution sum in Eq.(4.17) is removed and are rewritten to be as following

$$
\begin{aligned}
\tilde{\bar{P}}[n] &= \epsilon_0\,\underline{\underline{\tilde{\chi}}}^{ee}[n]\tilde{\bar{E}}_{av}[n] + \sqrt{\epsilon_0\mu_0}\,\underline{\underline{\tilde{\chi}}}^{em}[n]\tilde{\bar{H}}_{av}[n]\\
\tilde{\bar{M}}[n] &= \sqrt{\epsilon_0\mu_0}\,\underline{\underline{\tilde{\chi}}}^{me}[n]\tilde{\bar{E}}_{av}[n] + \mu_0\,\underline{\underline{\tilde{\chi}}}^{mm}[n]\tilde{\bar{H}}_{av}[n]
\end{aligned}
\tag{4.18}
$$

Conversion of Impedance Matrix into GSTC representation For a local MS the GSTC polarizability tensors in Eq.(4.16)and (4.18) are directly related to the elements of the impedance matrix in Eq.s(4.4) and (4.18) for planar and cylindrical metasurfaces respectively. By algebraically manipulating the impedance matrix we can find that

$$
\begin{aligned}
\tilde{\chi}^{ee} &= \frac{1}{j\omega}\frac{4}{\tilde{\bar{Z}}_{11}+\tilde{\bar{Z}}_{12}+\tilde{\bar{Z}}_{21}+\tilde{\bar{Z}}_{22}}\\
\tilde{\chi}^{em} &= -\frac{2}{j\omega}\frac{\tilde{\bar{Z}}_{11}-\tilde{\bar{Z}}_{12}+\tilde{\bar{Z}}_{21}-\tilde{\bar{Z}}_{22}}{\tilde{\bar{Z}}_{11}+\tilde{\bar{Z}}_{12}+\tilde{\bar{Z}}_{21}+\tilde{\bar{Z}}_{22}} \qquad \tilde{\chi}^{me} = \frac{2}{j\omega}\frac{\tilde{\bar{Z}}_{11}+\tilde{\bar{Z}}_{12}-\tilde{\bar{Z}}_{21}-\tilde{\bar{Z}}_{22}}{\tilde{\bar{Z}}_{11}+\tilde{\bar{Z}}_{12}+\tilde{\bar{Z}}_{21}+\tilde{\bar{Z}}_{22}}\\
\tilde{\chi}^{mm} &= \frac{1}{j\omega}\left((\tilde{\bar{Z}}_{11}-\tilde{\bar{Z}}_{12}-\tilde{\bar{Z}}_{21}+\tilde{\bar{Z}}_{22})-(\tilde{\bar{Z}}_{11}-\tilde{\bar{Z}}_{12}+\tilde{\bar{Z}}_{21}-\tilde{\bar{Z}}_{22})(\frac{\tilde{\bar{Z}}_{11}-\tilde{\bar{Z}}_{12}+\tilde{\bar{Z}}_{21}-\tilde{\bar{Z}}_{22}}{\tilde{\bar{Z}}_{11}+\tilde{\bar{Z}}_{12}+\tilde{\bar{Z}}_{21}+\tilde{\bar{Z}}_{22}})\right)
\end{aligned}
\tag{4.19}
$$

from the former parameter conversion, we note that if $\tilde{\tilde{Z}}_{12} = \tilde{\tilde{Z}}_{21}$ then $\tilde{\tilde{\chi}}^{me} = -\tilde{\tilde{\chi}}^{em}$ which guarantees reciprocity.

Topology of Special MS Since we are only concerned with reciprocal MS.s then the circuit topologies and the corresponding susceptibility tensors discussed in this section are constrained to be reciprocal.

1) Series Impedance As shown in Fig.(4.2), the current ($\tilde{H}_{1,\|} = \tilde{H}_{2,\|}$) is continuous while a voltage drop ($\Delta\tilde{E}_{\|}$) is induced across the impedance Z_s so

$$\Delta\tilde{E}_{\|} = \tilde{E}_{1,\|} - \tilde{E}_{2,\|} = \tilde{\tilde{Z}}_s \tilde{H}_{av,\|}$$

$$\tilde{H}_{av,\|} = \tilde{H}_{1,\|} = \tilde{H}_{2,\|} \quad \Delta\tilde{H}_{\|} = 0$$

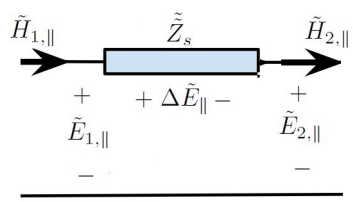

Figure 4.2: Series connected impedance Z_s causing an electric field discontinuity while the magnetic field is continuous.

Comparing with the GSTC condition in Eq.(4.11), we find that

$$\tilde{\tilde{\chi}}^{mm} = \frac{\tilde{\tilde{Z}}_s}{j\omega} \tag{4.20}$$

2) Parallel Admittance (inverse of Surface Impedance) A local Metasurface is quantified as a parallel admittance when introducing a discontinuous magnetic field. As shown in Fig. (4.3), the voltage across the metasurface is continuous ($\tilde{E}_{1,\|} = \tilde{E}_{2,\|}$) while there is a current discontinuity ($\Delta\tilde{H}_{\|}$) is induced across the parallel connected

admittance Y_p so

$$\Delta\tilde{H}_{\parallel} = \tilde{H}_{1,\parallel} - \tilde{H}_{2,\parallel} = Y_p \tilde{E}_{av,\parallel}$$

$$\tilde{E}_{av,\parallel} = \tilde{E}_{1,\parallel} = \tilde{E}_{2,\parallel} \quad \Delta\tilde{E}_{\parallel} = 0$$

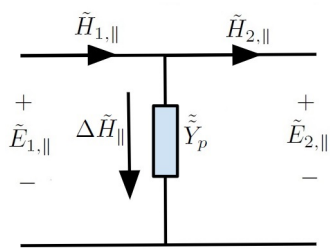

Figure 4.3: Parallel connected Admittance Y_p causing a magnetic field discontinuity while the electric field is continuous.

Comparing with the GSTC condition in Eq.(4.11), we find that

$$\chi^{ee} = \frac{\tilde{\tilde{Y}}_p}{j\omega} \tag{4.21}$$

3) T-Network In general any passive network with no dependent sources (circuit representation of Bi-isotropicity) can be reduced to be a Pi or T-Network. Here we consider a general T-Network as shown in Fig(4.4) with arbitrary series impedances $Z_{s,1}$ and $Z_{s,2}$ causing collective voltage drop $\Delta\tilde{E}_{\parallel}$ and in between parallel impedance Y_p causing a current discontinuity $\Delta\tilde{H}_{\parallel}$.

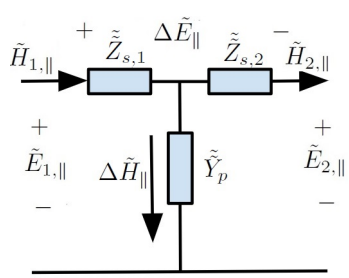

Figure 4.4: T-Network with arbitrary impedances $\{Z_{s,1}, Z_{s,2}, \frac{1}{Y_p}\}$ causing simultaneous electric and magnetic discontinuities.

$$
\begin{aligned}
\Delta\tilde{E}_{\parallel} &= \tilde{\tilde{Z}}_{s,1}\tilde{H}_{1,\parallel} + \tilde{\tilde{Z}}_{s,2}\tilde{H}_{2,\parallel} \\
\Delta\tilde{H}_{\parallel} &= \tilde{E}_{1,\parallel} - \tilde{\tilde{Z}}_{s,1}\tilde{H}_{1,\parallel} = \tilde{E}_{2,\parallel} + \tilde{\tilde{Z}}_{s,2}\tilde{H}_{2,\parallel}
\end{aligned}
\tag{4.22}
$$

Actually the conversion to susceptibility tensor can be retrieved from Eq.(4.19) by substituting

$\tilde{\tilde{Y}}_p = \frac{1}{\tilde{\tilde{Z}}_{21}} = \frac{1}{\tilde{\tilde{Z}}_{12}}$, $\tilde{\tilde{Z}}_{s,1} = \tilde{\tilde{Z}}_{11} - \tilde{\tilde{Z}}_{12}$ and $\tilde{\tilde{Z}}_{s,2} = \tilde{\tilde{Z}}_{22} - \tilde{\tilde{Z}}_{12}$, then

$$
\begin{aligned}
\tilde{\tilde{\chi}}^{ee} &= \frac{1}{j\omega}\frac{2}{\frac{2}{\tilde{\tilde{Y}}_p} + \frac{1}{2}(\tilde{\tilde{Z}}_{s,1} + Z_{s,2})} \qquad \tilde{\tilde{\chi}}^{mm} = \frac{1}{j\omega}\left(\tilde{\tilde{Z}}_{s,1} + \tilde{\tilde{Z}}_{s,2} - \frac{(\tilde{\tilde{Z}}_{s,1} - \tilde{\tilde{Z}}_{s,2})^2}{\frac{2}{Y_p} + \frac{1}{2}(\tilde{\tilde{Z}}_{s,1} + \tilde{\tilde{Z}}_{s,2})}\right) \\
\tilde{\tilde{\chi}}^{em} &= \frac{1}{j\omega}\frac{\tilde{\tilde{Z}}_{s,2} - \tilde{\tilde{Z}}_{s,1}}{\frac{2}{\tilde{\tilde{Y}}_p} + \frac{1}{2}(\tilde{\tilde{Z}}_{s,1} + \tilde{\tilde{Z}}_{s,2})} \qquad \tilde{\tilde{\chi}}^{me} = \frac{1}{j\omega}\frac{\tilde{\tilde{Z}}_{s,1} - \tilde{\tilde{Z}}_{s,2}}{\frac{2}{\tilde{\tilde{Y}}_p} + \frac{1}{2}(\tilde{\tilde{Z}}_{s,1} + \tilde{\tilde{Z}}_{s,2})}
\end{aligned}
\tag{4.23}
$$

Special Case: Symmetric T-Network In the case when $\tilde{\tilde{Z}}_{s,1} = \tilde{\tilde{Z}}_{s,2} = \tilde{\tilde{Z}}_s$, we find that the corresponding susceptibilities are significantly reduced as following :

$$
\begin{aligned}
\tilde{\tilde{\chi}}^{ee} &= \frac{1}{j\omega}\frac{2}{\frac{2}{\tilde{\tilde{Y}}_p} + \tilde{\tilde{Z}}_s} \qquad \chi^{mm} = \frac{2}{j\omega}\tilde{\tilde{Z}}_s \\
\tilde{\tilde{\chi}}^{em} &= \tilde{\tilde{\chi}}^{me} = 0
\end{aligned}
\tag{4.24}
$$

4.3 Equivalence between Scattering Cancellation and Discontinuous T.O

In this section we show that a meta-surface can also viewed as a result of discontinuous space transformation between virtual and physical spaces. We will consider such discontinuous space transformation in both Cartesian and polar coordinates, where two arbitrary regions of the virtual (electromagnetic) space are transformed with different transformations such that they are adjacent in the physical (coordinate) space and separated by a surface boundary. The MS will be located at that boundary introducing the specific electromagnetic field discontinuity. Space discontinuous transformation are discussed in details in this section, first, we will clarify the concept of discontinuous space transformations in 1D space, then, it will be explored for 2D spaces for both Cartesian or cylindrical coordinates respectively. In what follows we consider the E-polarization as a study case, with similar conclusions for H-polarization using the known duality.

4.3.1 1D discontinuous space transformation

Consider a homogeneous transmission line aligned along y as shown in Fig.(4.5). A transmission line is a wave-guide where the cross section is invariant along the propagation direction. The transmission line is characterized by the wave impedance $\eta = \frac{\mu}{\epsilon}$ and propagation wave-number $\beta_y = \omega\sqrt{\mu\epsilon}$. A plane wave is assumed to be propagating along such transmission line at frequency ω and its electric field is polarized along $z-$ axis so $\bar{E} = \hat{z}E_z$ and its magnetic field is polarized along $x-$axis so $\bar{H} = \hat{x}H_x$, and its wave front and phase is independent of the transverse coordinate so its propagation is a 1D problem. In case of transformation $y' = y'(y)$ between a virtual space y and physical space y', we have the following properties:

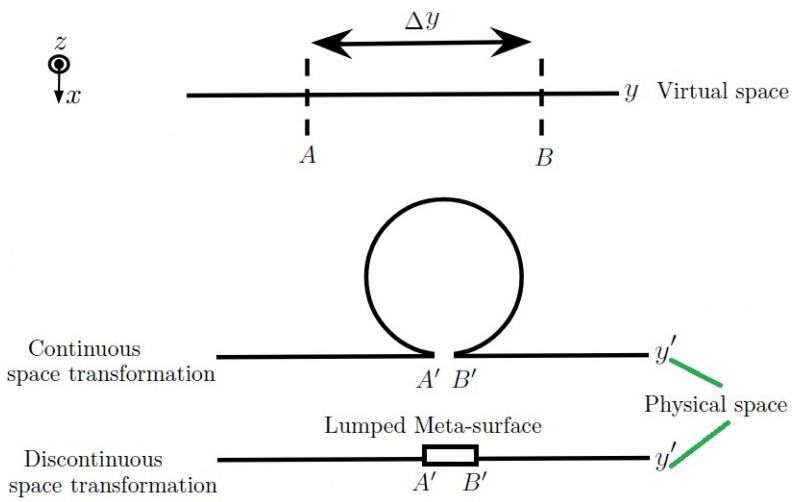

Figure 4.5: Schematic showing the equivalence between a discontinuous 1D space with lumped TO based MS, where a region in the 1D transmission line with length Δy is compressed to be a point or a lumped network of the MS. Up: Continuous 1D virtual space. Middle: Intermediate space. Bottom: The physical space including the metasurface.

$$\begin{aligned}
&\text{The Jacobian } \underline{\underline{J}} = J = \frac{dy'}{dy} \\
&\text{Field transformation } E_z^{'} = E_z \quad H_x^{'} = J^{-1} H_x = \frac{dy}{dy'} H_x \\
&\text{Media transformation } \epsilon^{'} = \frac{1}{det(J)}\epsilon = \frac{dy}{dy'}\epsilon \quad \mu^{'} = \frac{JJ^{\tau}}{det(J)}\mu = \frac{dy'}{dy}\mu
\end{aligned} \tag{4.25}$$

Due to the media transformation, then the transmission line properties (η, β) are transformed as following:

$$\begin{aligned}
&\text{Wave impedance transformation} \quad \eta' = \sqrt{\frac{\mu'}{\epsilon'}} = \frac{dy'}{dy}\sqrt{\frac{\mu}{\epsilon}} = \frac{dy'}{dy}\eta \\
&\text{Wave number transformation} \quad \beta' = \omega\sqrt{\mu'\epsilon'} = \omega\sqrt{\mu\epsilon} = \beta
\end{aligned} \tag{4.26}$$

4.3.1.1 1D compression (distributed TL into dispersive lumped metasurface located at a point):

Consider the following general transformation (expressed in a polynomial form for generality)

$$y' = \{ \begin{array}{ll} \sum_n \alpha_n (y - \Delta y)^n & y \geq \Delta y \\ y & y \leq 0 \end{array} \text{ with } n = [1, 2, ...] \tag{4.27}$$

where α_n is a constant that determine the specific details of the transformation. As shown in Fig(4.6), the discontinuity of such transformation can be seen as following: the region located at $y \geq \Delta y$ is transformed and shifted into $y' \geq 0$, while the other region $y \leq 0$ is unity transformed into $y' \leq 0$ and the region $0 < y < \Delta y$ is transformed (compressed) into a point $y' = 0$. Since the two regions $y \geq \Delta y$ and $y \leq \Delta y$ are transformed differently, the transmission line parameters of these two regions change under transformation according to Eq.(4.25) such that the transmission parameters are $\eta'(y' > 0) = \eta \frac{dy'}{dy}|_{y=\Delta y} = \alpha_1 \eta$ and $\beta'(y' > 0) = \beta$ and similarly $\eta'(y' < 0) = \eta$ and $\beta'(y' < 0) = \beta$. Notice that we have used the fact that $\frac{dy'}{dy}|_{y=\Delta y} = \alpha_1$.

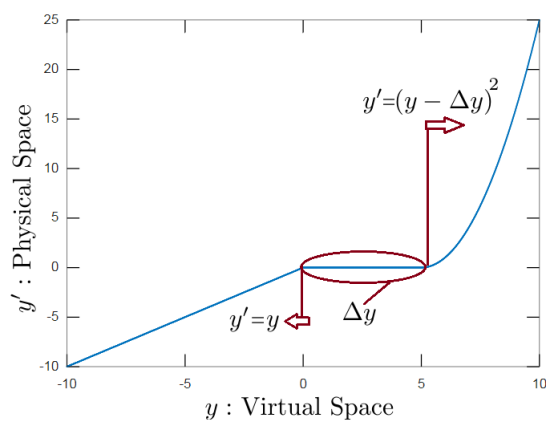

Figure 4.6: Schematic for the discontinuous transformation of Eq.(4.27) where two regions of the virtual space y are transformed differently, while the region of length Δy is compressed into a point $y' = 0$ in the physical space. In this graph the transformation is plotted for $y' = (y - \Delta y)^2$ for $y \geq \Delta y$ and $\Delta y = 5$.

Now we make use of the notion of lumped elements in transmission line theory as the correspondent of the compressed region Δy in the virtual space. Actually lumped elements have no counterpart in optics as it is a low frequency notion and typically used in RF and Microwave engineering. Also, it is known that a piece transmission line length Δy is equivalent to a lumped network with the following impedance matrix representation which relates the electric and magnetic fields at two locations separated by distance Δy. As shown in Fig(4.7), the electric field $\tilde{E}_{1,z}$and magnetic field $\tilde{H}_{1,x}$ amplitudes at $y = 0$ are related to the electric field $\tilde{E}_{2,z}$ and the magnetic field $\tilde{H}_{2,x}$ at $y = \Delta y$ as following:

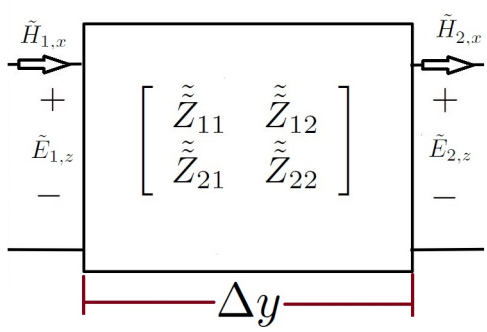

Figure 4.7: Z-matrix relating the electric and magnetic fields of the terminals of a transmission line of length Δy.

$$\begin{aligned} \tilde{E}_{1,z}(\beta_y) &= \tilde{\tilde{Z}}_{11}(\beta_y)\tilde{H}_{1,x}(\beta_y) - \tilde{\tilde{Z}}_{12}(\beta_y)\tilde{H}_{2,x}(\beta_y) \\ \tilde{E}_{2,z}(\beta_y) &= \tilde{\tilde{Z}}_{21}(\beta_y)\tilde{H}_{1,x}(\beta_y) - \tilde{\tilde{Z}}_{22}(\beta_y)\tilde{H}_{2,x}(\beta_y) \end{aligned} \tag{4.28}$$

with

$$\begin{aligned} \tilde{\tilde{Z}}_{11} &= j\eta\, cot(\beta_y \Delta y) \quad \tilde{\tilde{Z}}_{12} = j\eta\, csc(\beta_y \Delta y) \\ \tilde{\tilde{Z}}_{21} &= j\eta\, csc(\beta_y \Delta y) \quad \tilde{\tilde{Z}}_{22} = j\eta\, cot(\beta_y \Delta y) \end{aligned} \tag{4.29}$$

By transforming from virtual space into physical space the Z-parameters will be

(substituting the transformation of the field amplitudes of Eq.(4.25) into Eq.(4.29))

$$\begin{aligned}\tilde{E}_{1,z}(\beta_y) &= \tilde{Z}_{11}^{MS}(\beta_y)\tilde{H}_{1,x}(\beta_y) - \tilde{Z}_{12}^{MS}(\beta_y)\tilde{H}_{2,x}^{'}(\beta_y)\\ \tilde{E}_{2,z}(\beta_y) &= \tilde{Z}_{21}^{MS}(\beta_y)\tilde{H}_{1,x}(\beta_y) - \tilde{Z}_{22}^{MS}(\beta_y)\tilde{H}_{2,x}^{'}(\beta_y)\end{aligned} \tag{4.30}$$

where

$$\begin{aligned}\tilde{\tilde{Z}}_{11}^{MS} &= \frac{dy^{'}}{dy}|_{y=0}\tilde{\tilde{Z}}_{11} = j\eta\, cot(\Phi) \quad \tilde{\tilde{Z}}_{12}^{MS} = \frac{\partial y^{'}}{\partial y}|_{y=\Delta y}\tilde{\tilde{Z}}_{12} = j\alpha_1\eta\, csc(\Phi)\\ \tilde{\tilde{Z}}_{21}^{MS} &= \frac{dy^{'}}{dy}|_{y=0}\tilde{\tilde{Z}}_{21} = j\eta\, csc(\Phi) \quad \tilde{\tilde{Z}}_{22}^{MS} = \frac{dy^{'}}{dy}|_{y=\Delta y}\tilde{\tilde{Z}}_{22} = j\alpha_1\eta\, cot(\Phi)\\ &\text{where } \Phi = \beta_y\Delta y\end{aligned} \tag{4.31}$$

Although the MS was expected to be asymmetric $\tilde{\tilde{Z}}_{11}^{MS} \neq \tilde{\tilde{Z}}_{22}^{MS}$ due to the different transformations at $y' = 0^+$ and $y' = 0^-$ but the surprising result is that the resultant MS is also non-reciprocal $\tilde{\tilde{Z}}_{12}^{MS} \neq \tilde{\tilde{Z}}_{21}^{MS}$. The case where the MS can be reciprocal and symmetric is when $\alpha_1 = 1$ so the space transformation in Eq.(4.27) becomes as following

$$y' = \{ \begin{matrix} y - \Delta y + \sum_n \alpha_n (y-\Delta y)^n & y > \Delta y \\ y & y < 0 \end{matrix} \quad \text{with } n = [2, 3, ...] \tag{4.32}$$

In this case the impedance matrix is invariant under transformation and $\underline{\underline{Z}}^{MS} = \begin{bmatrix} \tilde{\tilde{Z}}_{11} & \tilde{\tilde{Z}}_{12} \\ \tilde{\tilde{Z}}_{21} & \tilde{\tilde{Z}}_{22} \end{bmatrix}$. This means that the compressed region $0 < y < \Delta y$ is exactly equivalent to the lumped network with the same impedance matrix representation.

Numerical Example: Here we consider a numerical example to clarify the concept of compressing a region of space into a lumped MS. Consider a parallel plate waveguide with its walls are perfect magnetic conductors as shown in Fig.(4.8). A normal incident plane wave is excited from the left side and is matched at the right end. The wave guide is divided into three parts by planes A and B, the middle parts between the two planes A and B is desired to be compressed into a MS.

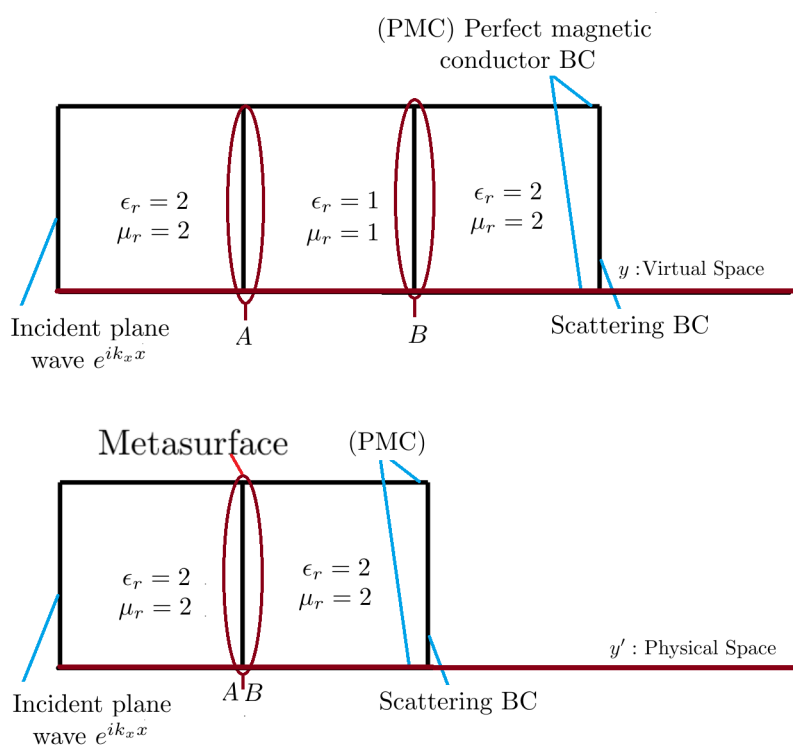

Figure 4.8: Numerical simulation setup for examining the concept of compressing a region of space into a lumped meta surface. A plane wave is incident from the right into a parallel plate wave guide with PMC walls (to guarantee planar wave front). In the virtual space, the wave-guide has three sections and it is terminated by a matched boundary condition. It is required to compress the middle section (between planes A and B) into a lumped meta-surface in the physical space. Up: Virtual space. Bottom: Physical space.

As shown in Fig.(4.9), the region between planes A and B can be replaced by a $Z-$matrix with parameters quantified at Eq.(4.29), then compressing the region $A-B$

into a MS with $Z-$matrix quantified according to Eq.(4.31). Numerical calculations were done using COMSOL3.5A. The effect of compressing the region between planes A-B in a MS discontinuity can be traced by investigating the phase of the propagating plane wave as shown in Fig.(4.9). Results agree with the proposed theory.

4.3.1.2 1D expansion: a point is expanded into a distributed TL and a complementary MS

This case is exactly the opposite to the former case of Eq.(4.27), where starting with the point $y = 0$ can be replaced by two dual networks connected in series (in literature, they are also named as "parity time symmetric" network). As shown in Fig.(4.10), two Dual networks when connected in series are equivalent to a short circuit such that the electric and magnetic fields amplitudes are have the same values at the terminals of the combined network (A and B in Fig.(4.10)). We start with a 1D plane wave propagation represented by a transmission line aligned along $y-$axis. The transmission line is characterized by the wave impedance η and wave number $beta$. Now we introduce a discontinuous transformation which breaks a continuous transmission line into two lines separated by Δy as following:

$$y' = \{ \begin{array}{cc} \Delta y + \sum_n \alpha_n y^n & y > 0 \\ \sum_n \gamma_n y^n & y < 0 \end{array} \text{ with } n = [0, 1, 2, ...] \tag{4.33}$$

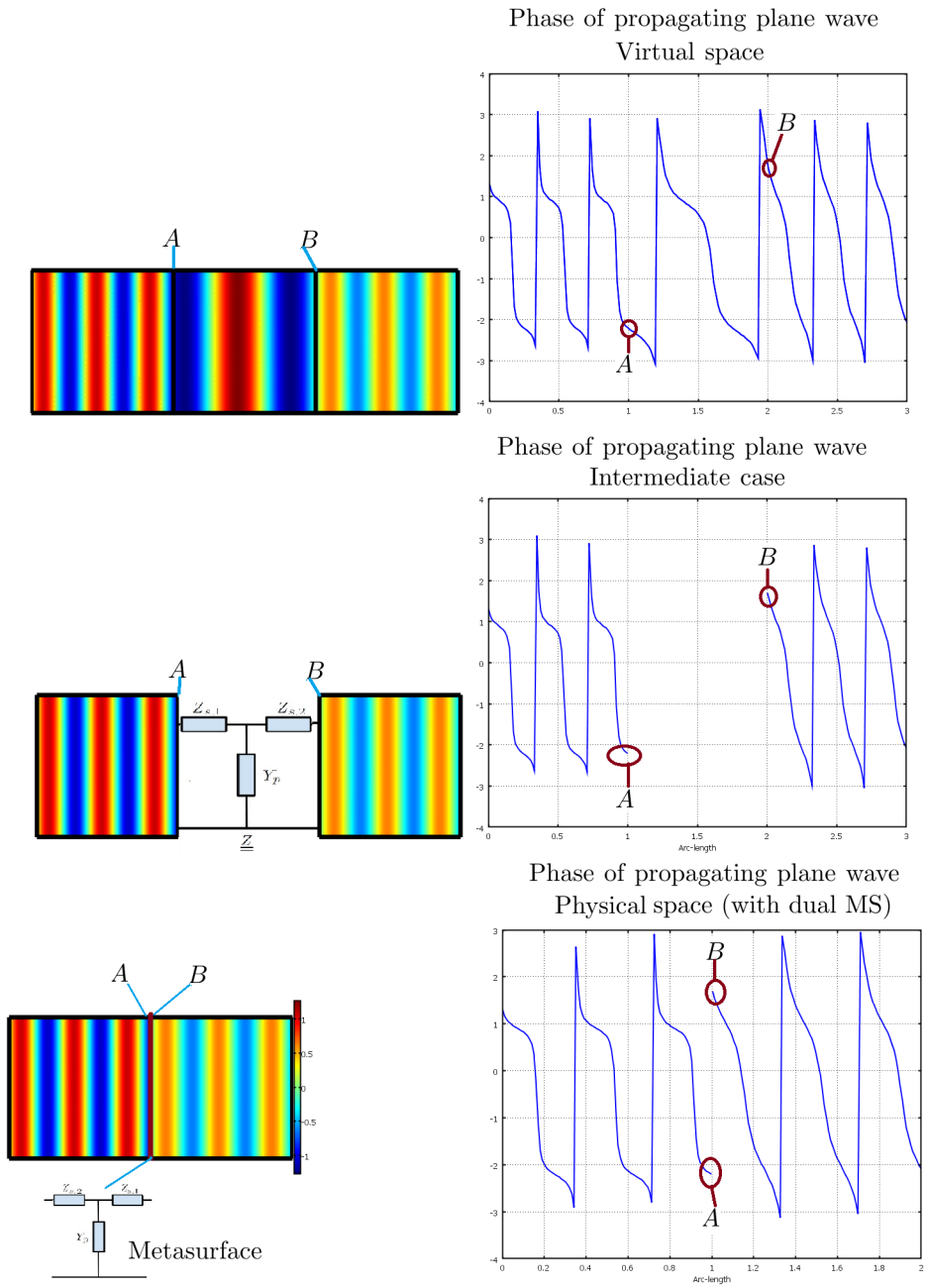

Figure 4.9: Up: Virtual space Electric field and its phase plots. Middle: Intermediate Electric field and its phase plots (the space is still the same as the virtual space but with replacing the $A - B$ space region with its equivalent circuit for a normal incident plane wave). Down:Physical space-(including the MS) Electric field and its phase plots.

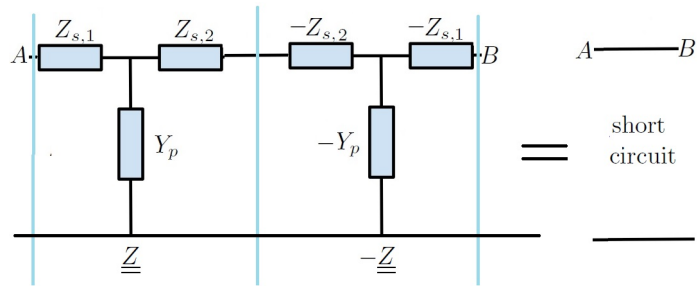

Figure 4.10: Two consecutive connected dual networks are equivalent to a short circuit.

where α_n and γ_n are constants of the transformation. The transformation indicates that the region located at $y > 0$ are transformed and shifted into $y' > \Delta y$, while the other region $y < 0$ is transformed into $y' < 0$. Since the two regions $y < 0$ and $y > 0$ are transformed differently, then the transmission line parameters of these two regions change under transformation will be η_1 and β_1 for $y' < 0$ and η_2 and β_2 for $y' > 0$.The region $0 < y' < \Delta y$ should be the expansion of the point $y = 0$.

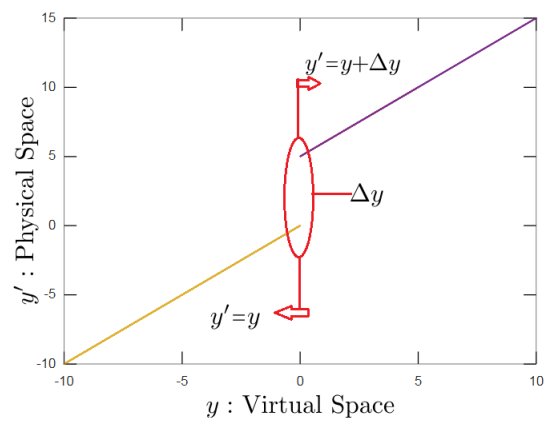

Figure 4.11: Schematic for the discontinuous transformation of Eq.(4.33) where two regions of the virtual space y are transformed differently and the point $y = 0$ is expanded into the region $0 \leq y' \leq \Delta y$ in the physical space. In this graph the transformation is plotted for $y' = y + \Delta y$ for $y \geq 0$ and $\Delta y = 5$.

One can fill the region $0 < y' < \Delta y$ with any arbitrary cascaded dual transmission lines (with arbitrary impedance and wave number) such that the combined effect is the same as of a point (short circuit). Actually there is an infinite number of arrangements of finite length cascaded transmission lines such that the total combined

effect resembles that of the point. We choose to use a homogeneous transmission line of impedance η_0' and wave number β_0' with a Z-matrix $\underline{\underline{Z}}^{(TL)}$, to fill the void region $0 < y' < \Delta y$ and cascaded by a lumped MS with the Z-matrix given by $\underline{\underline{Z}}^{(MS)} = -\underline{\underline{Z}}^{(TL)}$.

Numerical Example: Now, we consider a numerical example to clarify the concept of expanding a zero area region (point or a line) into space region cascaded with a dual lumped MS. Consider a parallel plate wave guide with its walls are perfect magnetic conductors as shown in Fig.(4.12). First in virtual space, the wave-guide is filled with homogeneous and non-magnetic media of permittivity $\epsilon = 2$. The space is transformed according to the graph in Fig.(4.33), and the plane located AB is desired to be expanded into two dual media as shown in the middle of Fig(4.12). Finally the media with negative permittivity and permeability is replaced with a dual MS. A normal incident plane wave is excited from the left side and is matched at the right end. The effect of expansion of a point into two dual networks can be investigated by following the phase of the propagating plane wave as shown in Fig.(4.13). Results agree with the proposed theory.

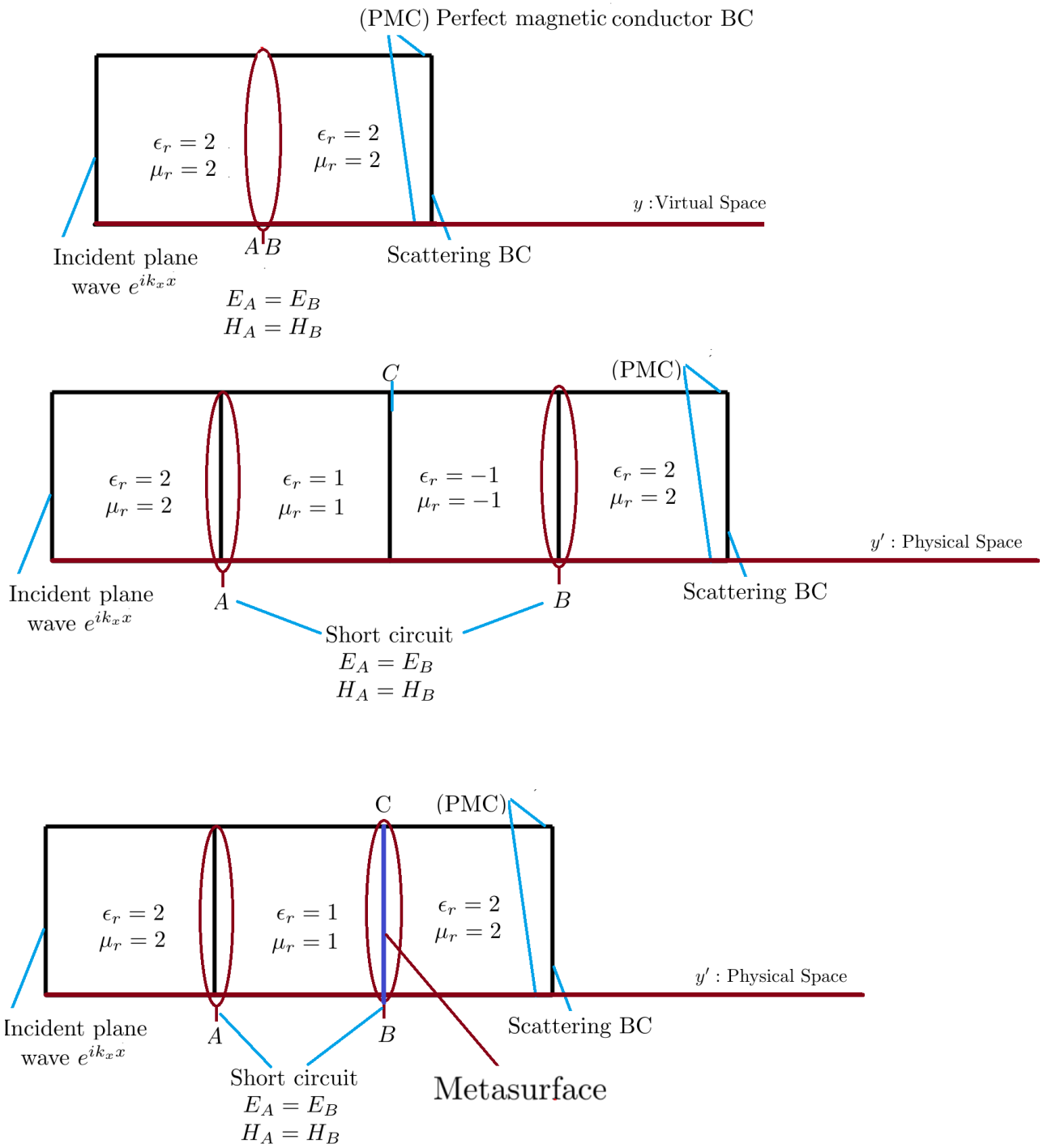

Figure 4.12: Numerical simulation Setup for examining the concept of 1D Expansion or replacing a plane/point by two dual media or a space region and dual meta-surface. A plane wave is incident from the right into a parallel plate wave guide with PMC walls (to guarantee planar wave front). The wave-guide has four sections and it is terminated by a matched boundary condition. It is required to compress the third section (between planes C and B) to a meta-surface.Up: Virtual space. Middle: Intermediate space. Bottom: Physical space.

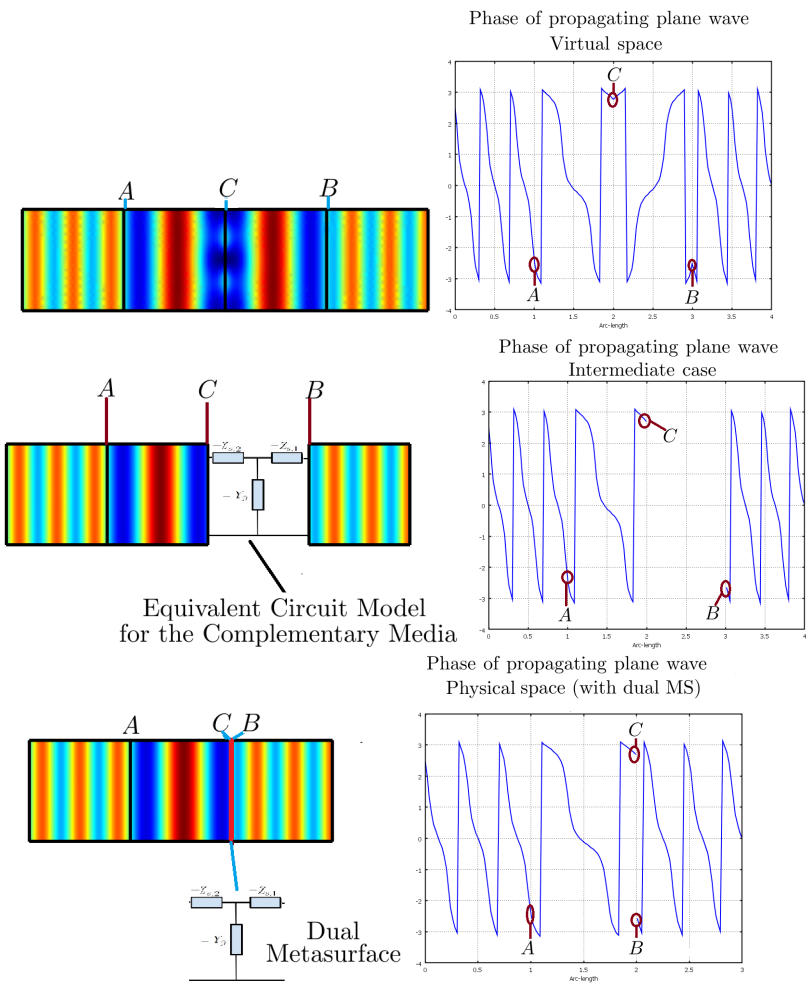

Figure 4.13: Up: Plot of the amplitude and phase of the Electric field propagating in an intermediate space including two dual media of the same thickness. Middle: Plot of the amplitude and phase of the Electric field propagating in the same intermediate space but with replacing the media with negative permittivity and permeability space region with its equivalent circuit for a normal incident plane wave). Down: Plot of the amplitude and phase of the Electric field propagating in the physical space including the MS.

4.3.2 2D polar/cylindrical discontinuous space transformation

Here we consider the 2D generalization of the two 1D cases of discontinuous space transformation introduced in the previous section. The analysis used in section(4.3.1) can be used in the corresponding 2D case but with replacing the plane wave basis by cylindrical wave basis. Considering 2D virtual space, there are two cases of discon-

tinuous space transformations in polar coordinates as following:

1. **Compression** the region $\rho_1 < \rho < \rho_2$ is compressed into a meta-surface located at $\rho' = \rho_2$, while the region A at $\rho < \rho_1$ in virtual space is expanded into A' at $\rho' < \rho_2$ in the physical space, with $\phi = \phi'$ invariant under transformation (no rotation). See Fig.(4.14).

2. **Expansion** Starting with the virtual space, the cylindrical boundary $\rho = \rho_2$ into an arbitrary media resides at $\rho_1 < \rho' < \rho_2$ in contact with a complementary (dual) meta-surface located at $\rho' = \rho_2$ and the region $\rho < \rho_2$ in virtual space is compressed into $\rho' < \rho_1$ while $\phi = \phi'$ is invariant under transformation (no rotation). See Fig.(4.23).

4.3.2.1 Discontinuous radial compression: (cylindrical shell into cylindrical meta-surface)

Starting with a 2D virtual space divided into three regions (see Fig.(4.14)):

1. Region B located at $\rho > \rho_2$.

2. Region A located at $\rho < \rho_1$.

3. Annulus ring located at $\rho_1 < \rho < \rho_2$ with width $\Delta\rho = \rho_2 - \rho_1$.

Transforming the area A located in $\rho \leq \rho_1$ at the virtual space into A' located at $\rho^{'} \leq \rho_2$ in the physical space and since there is no rotation then $\phi' = \phi$. Note that the object A is transformed into A' for $\rho' < \rho_2$ and the annulus ring located at $\rho_1 < \rho < \rho_2$ is compressed into zero thickness layer which will be replaced by a MS located at $\rho' = \rho_2$. The discontinuous space transformation is defined as following:

$$\rho'(\rho, \phi) = \{ \begin{array}{ll} \frac{\rho_2(\phi)}{\rho_1(\phi)}\rho & \rho \leq \rho_1 \\ \rho & \rho > \rho_2 \end{array} \tag{4.34}$$

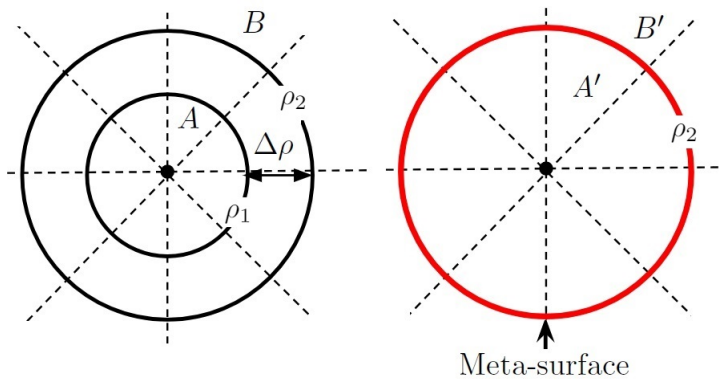

Figure 4.14: Schematic of the discontinuous radial transformation where the cylindrical shell located at $\rho_1 < \rho < \rho_2$ ($\Delta\rho = \rho_2 - \rho_1$) in the virtual space is compressed into a cylindrical MS at $\rho' = \rho_2$ in the physical space. Note that A is transformed into A' and B is unity transformed into B' ($B = B'$).

The Jacobian of the transformation will be as following

$$\text{For } \rho < \rho_1 \quad \underline{\underline{J}} = J_m^{m'} = \begin{bmatrix} \frac{\partial\rho'}{\partial\rho} & 0 \\ 0 & \frac{\rho'}{\rho} \end{bmatrix} = \frac{\rho_2}{\rho_1}\begin{bmatrix} 1 & 0 \\ 0 & 1 \end{bmatrix} \quad \text{then } \underline{\underline{J}}^{-\tau} = \frac{\rho_1}{\rho_2}$$

$$\text{For } \rho > \rho_2 \quad \underline{\underline{J}} = \begin{bmatrix} 1 & 0 \\ 0 & 1 \end{bmatrix}$$

The media are transformed as following: $\varepsilon_{zz}^{'} = \dfrac{\varepsilon_{zz}}{det(\underline{\underline{J}})} \qquad \mu_T^{m'n'} = \dfrac{1}{det(\underline{\underline{J}})} J_m^{m'} J_n^{n'} \mu_T^{mn}$

The fields are transformed as following: $\underline{H}_T^{'}(\rho' = \rho_2^-) = \underline{\underline{J}}^{-\tau}\underline{H}_T(\rho = \rho_1) = \dfrac{\rho_1}{\rho_2}\underline{H}_T(\rho = \rho_1)$

$$E_z^{'}(\rho' = \rho_2^-) = E_z(\rho = \rho_1) \tag{4.35}$$

For simplicity assume a homogeneous isotropic media is located in the annulus ring

region, so the electromagnetic field propagating in this region is expressed in terms the cylindrical waves orthogonal basis. The propagation of a cylindrical wave of order n along the annulus ring can be modeled using a Z-matrix defined as following:

$$\begin{aligned}
\tilde{V}_1[n] = \sqrt{\rho_1}\tilde{E}_{1,z}[n] &= \tilde{\tilde{Z}}_{11}^{shell}[n]\tilde{I}_1 - \tilde{\tilde{Z}}_{12}^{shell}[n]\tilde{I}_2 \\
&= \tilde{\tilde{Z}}_{11}^{shell}[n]\left(-\sqrt{\rho_1}\tilde{H}_{1,\phi}[n]\right) - \tilde{\tilde{Z}}_{12}^{shell}[n]\left(-\sqrt{\rho_2}\tilde{H}_{2,\phi}[n]\right) \\
\tilde{V}_2[n] = \sqrt{\rho_2}\tilde{E}_{2,z}[n] &= \tilde{\tilde{Z}}_{21}[n]\tilde{I}_1 - \tilde{\tilde{Z}}_{22}^{shell}[n]\tilde{I}_2 \\
&= \tilde{\tilde{Z}}_{21}^{shell}[n]\left(-\sqrt{\rho_1}\tilde{H}_{1,\phi}[n]\right) - \tilde{\tilde{Z}}_{22}^{shell}[n]\left(-\sqrt{\rho_2}\tilde{H}_{2,\phi}[n]\right)
\end{aligned} \tag{4.36}$$

Note that the square root of the metric of the cylindrical coordinate is included in the definition of voltage as $\tilde{V} = \sqrt{\rho}\tilde{E}_z$ and the current $\tilde{I} = \sqrt{\rho}\tilde{H}_\phi$ in order to guarantee that the Z-matrix is reciprocal.

Z-matrix for radial cylindrical annular shell ($\rho_1 < \rho < \rho_2$): Here we derive the Z-matrix for a E-polarization cylindrical wave propagating along a cylindrical shell bounded between two cylinders $\rho_1 < \rho < \rho_2$. Considering the medium to be homogeneous and isotropic media with permittivity ϵ and permeability μ then $k = \omega\sqrt{\epsilon\mu}$ is the propagation wave number. Defining voltage and currents at the inner $\rho = \rho_1$ and outer $\rho = \rho_2$ sides of the annulus ring as following:

$$\begin{aligned}
\tilde{V}_1^n &= \sqrt{\rho_1}\tilde{E}_{z,1}^n = \sqrt{\rho_1}\left(E_n^+ H_n^{(2)}(k\rho_1) + E_n^- H_n^{(1)}(k\rho_1)\right)e^{jn\phi} \\
\tilde{I}_1^n &= -\sqrt{\rho_1}\tilde{H}_{\phi,1}^n = j\frac{\sqrt{\rho_1}}{\eta}\left(E_n^+ \dot{H}_n^{(2)}(k\rho_1) + E_n^- \dot{H}_n^{(1)}(k\rho_1)\right)e^{jn\phi} \\
\tilde{V}_2^n &= \sqrt{\rho_2}\tilde{E}_{z,2}^n = \sqrt{\rho_2}\left(E_n^+ H_n^{(2)}(k\rho_2) + E_n^- H_n^{(1)}(k\rho_2)\right)e^{jn\phi} \\
\tilde{I}_2^n &= -\sqrt{\rho_2}\tilde{H}_{\phi,2}^n = j\frac{\sqrt{\rho_2}}{\eta}\left(E_n^+ \dot{H}_n^{(2)}(k\rho_2) + E_n^- \dot{H}_n^{(1)}(k\rho_2)\right)e^{jn\phi}
\end{aligned} \tag{4.37}$$

where $H_n^{(1)}$ and $H_n^{(2)}$ are Hankel functions of order n of 1st and 2nd types, E_n^+ and E_n^- are the amplitude of outgoing ($+\rho$ direction) and in-going ($-\rho$ direction) of cylindrical waves of order n. In order to construct Z-Matrix representation , Eq.(A.58) is

arranged as following:

$$
\begin{aligned}
\begin{bmatrix} \tilde{V}_1^n \\ \tilde{V}_2^n \end{bmatrix} &= \begin{bmatrix} \sqrt{\rho_1} H_n^{(2)}(k\rho_1) & \sqrt{\rho_1} H_n^{(1)}(k\rho_1) \\ \sqrt{\rho_2} H_n^{(2)}(k\rho_2) & \sqrt{\rho_2} H_n^{(1)}(k\rho_2) \end{bmatrix} \begin{bmatrix} E_n^+ \\ E_n^- \end{bmatrix} \\
&= \begin{bmatrix} \sqrt{\rho_1} H_n^{(2)}(k\rho_1) & \sqrt{\rho_1} H_n^{(1)}(k\rho_1) \\ \sqrt{\rho_2} H_n^{(2)}(k\rho_2) & \sqrt{\rho_2} H_n^{(1)}(k\rho_2) \end{bmatrix} \begin{bmatrix} j\frac{\sqrt{\rho_1}}{\eta} \dot{H}_n^{(2)}(k\rho_1) & j\frac{\sqrt{\rho_1}}{\eta} \dot{H}_n^{(1)}(k\rho_1) \\ j\frac{\sqrt{\rho_2}}{\eta} \dot{H}_n^{(2)}(k\rho_2) & j\frac{\sqrt{\rho_2}}{\eta} \dot{H}_n^{(1)}(k\rho_2) \end{bmatrix}^{-1} \begin{bmatrix} \tilde{I}_1^n \\ \tilde{I}_2^n \end{bmatrix} \\
&= \begin{bmatrix} \tilde{\tilde{Z}}_{11}^{shell}[n] & -\tilde{\tilde{Z}}_{12}^{shell}[n] \\ \tilde{\tilde{Z}}_{21}^{shell}[n] & -\tilde{\tilde{Z}}_{22}^{shell}[n] \end{bmatrix} \begin{bmatrix} \tilde{I}_1^n \\ \tilde{I}_2^n \end{bmatrix}
\end{aligned}
\tag{4.38}
$$

where the Z-Matrix elements are evaluated as following:

$$
\begin{aligned}
\tilde{\tilde{Z}}_{11}^{shell}[n] &= -j\eta \frac{H_n^{(2)}(k\rho_1)\dot{H}_n^{(1)}(k\rho_2) - H_n^{(1)}(k\rho_1)\dot{H}_n^{(2)}(k\rho_2)}{\dot{H}_n^{(2)}(k\rho_1)\dot{H}_n^{(1)}(k\rho_2) - \dot{H}_n^{(1)}(k\rho_1)\dot{H}_n^{(2)}(k\rho_2)} \\
\tilde{\tilde{Z}}_{12}^{shell}[n] &= -j\eta \sqrt{\frac{\rho_1}{\rho_2}} \frac{H_n^{(2)}(k\rho_1)\dot{H}_n^{(1)}(k\rho_1) - H_n^{(1)}(k\rho_1)\dot{H}_n^{(2)}(k\rho_1)}{\dot{H}_n^{(2)}(k\rho_1)\dot{H}_n^{(1)}(k\rho_2) - \dot{H}_n^{(1)}(k\rho_1)\dot{H}_n^{(2)}(k\rho_2)} \\
&= \frac{\eta}{\sqrt{\rho_1\rho_2}} \frac{4\,/\,(\pi k)}{\dot{H}_n^{(2)}(k\rho_1)\dot{H}_n^{(1)}(k\rho_2) - \dot{H}_n^{(1)}(k\rho_1)\dot{H}_n^{(2)}(k\rho_2)} \\
\tilde{\tilde{Z}}_{21}^{shell}[n] &= -j\eta \sqrt{\frac{\rho_2}{\rho_1}} \frac{H_n^{(2)}(k\rho_2)\dot{H}_n^{(1)}(k\rho_2) - H_n^{(1)}(k\rho_2)\dot{H}_n^{(2)}(k\rho_2)}{\dot{H}_n^{(2)}(k\rho_1)\dot{H}_n^{(1)}(k\rho_2) - \dot{H}_n^{(1)}(k\rho_1)\dot{H}_n^{(2)}(k\rho_2)} \\
&= \frac{\eta}{\sqrt{\rho_1\rho_2}} \frac{4\,/\,(\pi k)}{\dot{H}_n^{(2)}(k\rho_1)\dot{H}_n^{(1)}(k\rho_2) - \dot{H}_n^{(1)}(k\rho_1)\dot{H}_n^{(2)}(k\rho_2)} \\
\tilde{\tilde{Z}}_{22}^{shell}[n] &= +j\eta \frac{H_n^{(1)}(k\rho_2)\dot{H}_n^{(2)}(k\rho_1) - H_n^{(2)}(k\rho_2)\dot{H}_n^{(1)}(k\rho_1)}{\dot{H}_n^{(2)}(k\rho_1)\dot{H}_n^{(1)}(k\rho_2) - \dot{H}_n^{(1)}(k\rho_1)\dot{H}_n^{(2)}(k\rho_2)}
\end{aligned}
\tag{4.39}
$$

Note that $H_n^{(2)}(k\rho)\dot{H}_n^{(2)*}(k\rho) = J_n(k\rho)\dot{J}_n(k\rho) + Y_n(k\rho)\dot{Y}_n(k\rho) - j\frac{2}{\pi k\rho}$

Z-matrix of the MS: In order to calculate of the $Z-$ matrix of the required MS , it is needed to transform the electric and magnetic fields from virtual space into physical space according to Eq.(4.35), substituting the field transformation in Eq.(4.35), then the Z-parameters in the physical space will be:

$$\begin{aligned}\sqrt{\rho_2}\tilde{E}_z^{'}[n,\rho_2^-] &= \tilde{\tilde{Z}}_{11}^{MS}[n]\left(-\sqrt{\rho_2}\tilde{H}_\phi^{'}[n,\rho_2^-]\right) - \tilde{\tilde{Z}}_{12}^{MS}[n]\left(-\sqrt{\rho_2}\tilde{H}_\phi^{'}[n,\rho_2^-]\right)\\ \sqrt{\rho_2}\tilde{E}_z^{'}[n,\rho_2^+] &= \tilde{\tilde{Z}}_{21}^{MS}[n]\left(-\sqrt{\rho_2}\tilde{H}_\phi^{'}[n,\rho_2^-]\right) - \tilde{\tilde{Z}}_{22}^{MS}[n]\left(-\sqrt{\rho_2}\tilde{H}_\phi^{'}[n,\rho_2^-]\right)\end{aligned} \tag{4.40}$$

such that the Z-matrix matrix elements are expressed as following:

$$\begin{aligned}\tilde{\tilde{Z}}_{11}^{MS}[n] &= \frac{\rho_2}{\rho_1}\tilde{\tilde{Z}}_{11}[n] = -j\eta\frac{\rho_2}{\rho_1}\frac{H_n^{(2)}(k\rho_1)\dot{H}_n^{(1)}(k\rho_2) - H_n^{(1)}(k\rho_1)\dot{H}_n^{(2)}(k\rho_2)}{\dot{H}_n^{(2)}(k\rho_1)\dot{H}_n^{(1)}(k\rho_2) - \dot{H}_n^{(1)}(k\rho_1)\dot{H}_n^{(2)}(k\rho_2)}\\ \tilde{\tilde{Z}}_{12}^{MS}[n] &= \sqrt{\frac{\rho_2}{\rho_1}}\tilde{\tilde{Z}}_{12}[n] = -j\eta\frac{H_n^{(2)}(k\rho_1)\dot{H}_n^{(1)}(k\rho_1) - H_n^{(1)}(k\rho_1)\dot{H}_n^{(2)}(k\rho_1)}{\dot{H}_n^{(2)}(k\rho_1)\dot{H}_n^{(1)}(k\zeta) - \dot{H}_n^{(1)}(k\rho_1)\dot{H}_n^{(2)}(k\rho_2)}\\ \tilde{\tilde{Z}}_{21}^{MS}[n] &= \sqrt{\frac{\rho_2}{\rho_1}}\tilde{\tilde{Z}}_{21}[n] = -j\eta\frac{\rho_2}{\rho_1}\frac{H_n^{(2)}(k\rho_1)\dot{H}_n^{(1)}(k\rho_2) - H_n^{(1)}(k\rho_1)\dot{H}_n^{(2)}(k\rho_2)}{\dot{H}_n^{(2)}(k\rho_1)\dot{H}_n^{(1)}(k\rho_2) - \dot{H}_n^{(1)}(k\rho_1)\dot{H}_n^{(2)}(k\rho_2)}\\ \tilde{\tilde{Z}}_{22}^{MS}[n] &= \tilde{\tilde{Z}}_{22}[n] = +j\eta\frac{H_n^{(1)}(k\rho_2)\dot{H}_n^{(2)}(k\rho_1) - H_n^{(2)}(k\rho_2)\dot{H}_n^{(1)}(k\rho_1)}{\dot{H}_n^{(2)}(k\rho_1)\dot{H}_n^{(1)}(k\rho_2) - \dot{H}_n^{(1)}(k\rho_1)\dot{H}_n^{(2)}(k\rho_2)}\end{aligned} \tag{4.41}$$

Numerical Results: In this section, two simulation setups are done to investigate the concept of compression a cylindrical shell into a lumped radial MS. In both setups, a 2D discontinuous space transformation is introduced and the discontinuity of the transformation is implemented by a spatial dispersive homogeneous cylindrical meta-surface.

Simulation Setup (1): As shown in Fig.(4.15), in the Virtual space (left figure), a surface current $Js = e^{in\phi}$ is flowing at the surface of a PMC cylinder of radius ρ_0 and surrounded by vacuum. Such surface current launches cylindrical waves of the same order n. It is desired to transform the region $\rho_0 < \rho < \rho_1$ radially into $\rho_0' < \rho' < \rho_2$ with the annulus ring $\rho_1 < \rho < \rho_2$ is compressed into a MS in the physical space. The space transformation can be written as following:

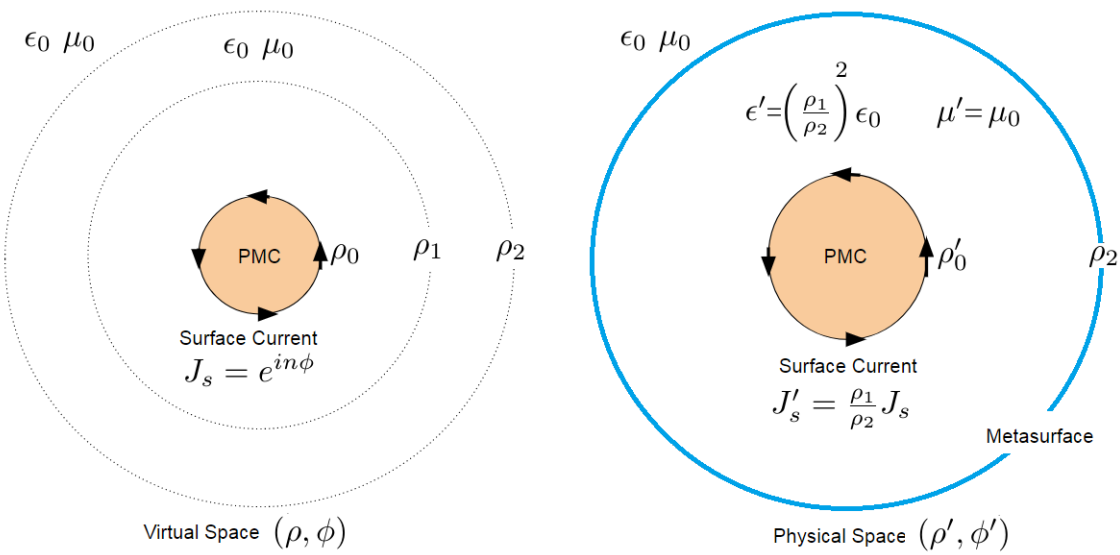

$$\rho' = \{ \begin{array}{ll} \frac{\rho_2}{\rho_1}\rho & \rho_0 < \rho < \rho_1 \\ \rho & \rho \geq \rho_2 \end{array} \qquad \phi' = \phi$$

Figure 4.15: A simulation setup : left: Virtual space. Right: Physical space. A Surface electric current $J_s = e^{in\phi}$ is flowing on the surface of a cylindrical perfect magnetic conductor with radius ρ_0. The emitted radiation is of the same order n. The space is transformed such that the annulus shell $\rho_1 < \rho < \rho_2$ is compressed into a cylindrical boundary $\rho' = \rho_2$.

$$\rho' = \{ \begin{array}{ll} \frac{\rho_1}{\rho_2}\rho & 0 < \rho < \rho_1 \\ \rho & \rho \geq \rho_2 \end{array} \qquad \phi' = \phi \tag{4.42}$$

The details of the setup is shown in Fig.(4.15). Numerical simulations are shown in Fig.s (4.16-4.18) for $n = 1, 2$ and 10 respectively. In the physical space, For each order n, a MS with the $Z-$parameters is determined according to Eq.(4.41). The electric fields are plotted in Fig.s (4.16-4.18) for three cases, the virtual space, the virtual space with the ring $\rho_1 < \rho < \rho_2$ replaced by the equivalent Z-matrix of Eq.(A.60) and finally the physical space where the regions of space are transformed where the MS is introduced and its $Z-$matrix matches the corresponding cylindrical order. The simulation is done with the following parameters: $\rho_0 = 10\mu m$, $\rho_1 = 30\mu m$ and $\rho_2 = 2\rho_1$. The wavelength is chosen to be $\lambda = 9\mu m$.

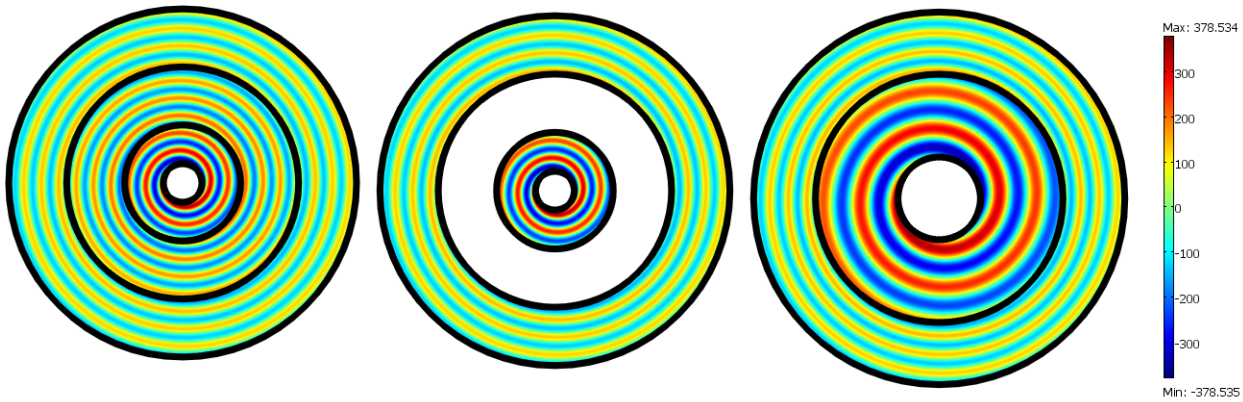

Figure 4.16: Plot of the radiated electric field E_z from electric surface current $J_s = e^{in\phi}$ with $n = 1$. Left: full virtual space, Middle: discontinuous virtual space, Right:physical space.

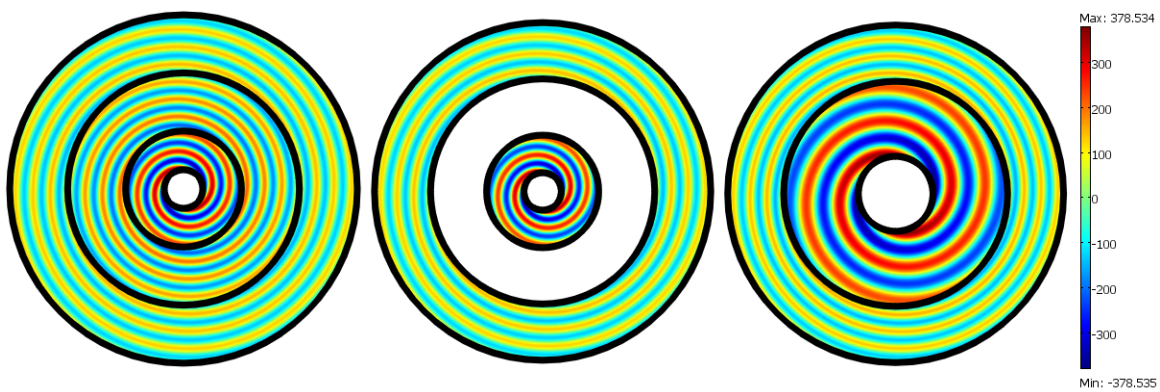

Figure 4.17: Plot of the radiated electric field E_z from electric surface current $J_s = e^{in\phi}$ with $n = 2$. Left: full virtual space, Middle: discontinuous virtual space, Right: physical space.

It is important to notice that the electric field E_z in the left and middle figures are unchanged for both regions $\rho < \rho_1$ and $\rho > \rho_2$, while in the physical space, in the right figure, the field value and distribution are the same for the region $\rho' > \rho_2$ while for the inner region $\rho' < \rho_2$, the same field E_z got stretched due to the radial transformation (enlargement).

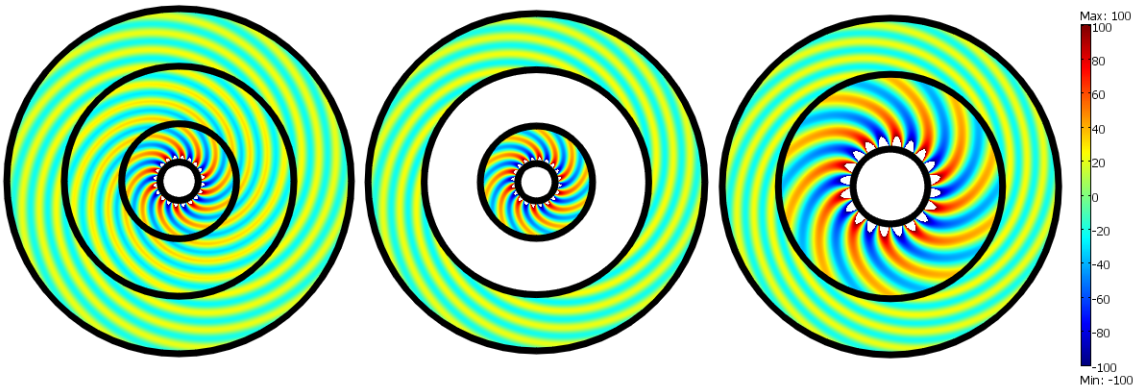

Figure 4.18: Plot of the radiated electric field E_z from electric surface current $J_s = e^{in\phi}$ with $n = 10$. left: full virtual space, middle: discontinuous virtual space, right:physical space.

Simulation Setup (2): Now, we consider the space transformation as the previous case, but instead of examining each cylindrical harmonic separately, we design the MS in order to compress the phase due to multiple cylindrical harmonics simultaneously. We consider the virtual space to be vacuum inside parallel plate waveguide with PMC walls as shown in Fig.(4.19). A plane wave is launched from the top side to be propagating in y direction. In the virtual space, at the surface $\rho = \rho_2$, a plane wave can be expanded as a superposition of infinite number of cylindrical waves of all orders as following:

$$e^{-ik_0 y}_{y=\rho_2 sin(\phi)} = \sum_{n=-\infty}^{\infty} (-1)^n J_n(k_0\rho_2) e^{in\phi} \tag{4.43}$$

where J_n is Bessel function of 1st type and order n. Although the plane wave expansion includes infinite number of cylindrical waves, actually depending on the size-to-wavelength ratio, only a finite number N of cylindrical waves are dominant and the series can be truncated for all cylindrical waves of order $n > N$. The smaller $\frac{\rho}{\lambda}$, the less N cylindrical waves that contribute to the incident plane wave and consequently the less N cylindrical waves that contribute to the scattered field.

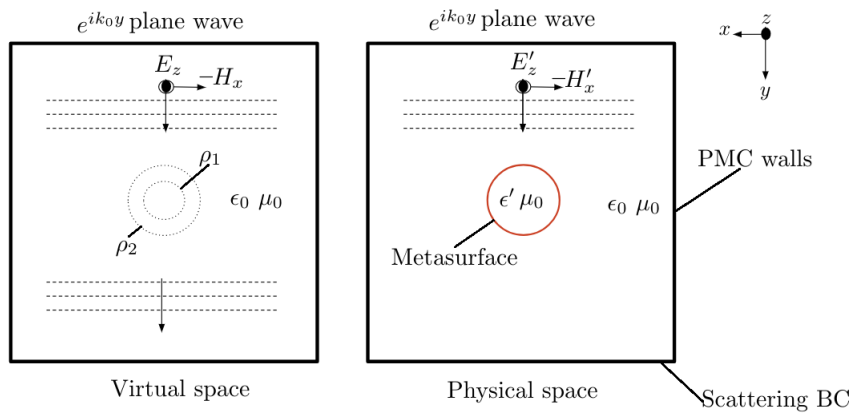

Figure 4.19: Simulation setup (2) : left: Virtual space. Right: Physical space. A plane wave is propagating in y direction in a PMC parallel plate wave guide. The space is transformed according to Eq.(4.47) such that the annulus ring $\rho_1 < \rho < \rho_2$ is compressed into a MS located at $\rho' = \rho_2$ in the physical space. The MS is designed to be spatial dispersive (non local) with respect to ϕ (see Fig.(4.15)).

Since the region the annulus ring $\rho_1 < \rho < \rho_2$ is compressed into a MS located at $\rho' = \rho_2$, the spatial dispersion of the annulus ring must to be taken into account in the physical space MS in order to ensure the invariance of physics under space transformation. The spatial dispersive meta-surface located at ρ_2 is required to relate the electric and magnetic fields on its inner ρ_2^- and outer ρ_2^+ sides as following:

$$E'_z(\rho_2^-,\phi) = \sum_{n=-N}^{n=N} \tilde{\tilde{E}}'_z[\rho_2^-,n]e^{in\phi} = \sum_{n=-N}^{n=N} \left[\tilde{\tilde{Z}}_{11}^{MS}[\rho_2,n](-\tilde{H}'_\phi[\rho_2^-,n]) - \tilde{\tilde{Z}}_{12}^{MS}[\rho_2,n](-\tilde{H}'_\phi[\rho_2^+,n])\right] e^{in\phi}$$
$$E'_z(\rho_2^+,\phi) = \sum_{n=-N}^{n=N} \tilde{\tilde{E}}'_z[\rho_2^+,n]e^{in\phi} = \sum_{n=-N}^{n=N} \left[\tilde{\tilde{Z}}_{21}^{MS}[\rho_2,n](-\tilde{H}'_\phi[\rho_2^-,n]) - \tilde{\tilde{Z}}_{22}^{MS}[\rho_2,n](-\tilde{H}'_\phi[\rho_2^+,n])\right] e^{in\phi} \tag{4.44}$$

where N is the number of cylindrical orders included in the $Z-$matrix of the MS. Simulation results are shown in Fig.(4.20), for $N = 0, 5, 10, 15$ and 20 respectively. In the physical space, as N increases both the scattered field at $\rho' < \rho_2$ and $\rho' > \rho_2$ gets more closer to the plane wave electric field distribution plotted at Fig(4.20.f). As shown in Fig.(4.21), when $N = 50$, the field distribution outside the $\rho' > \rho_2$ has

the same exact electric field distribution and both cases become in-distinguishable. Simulations are done at wavelength $\lambda = 9\mu m$.

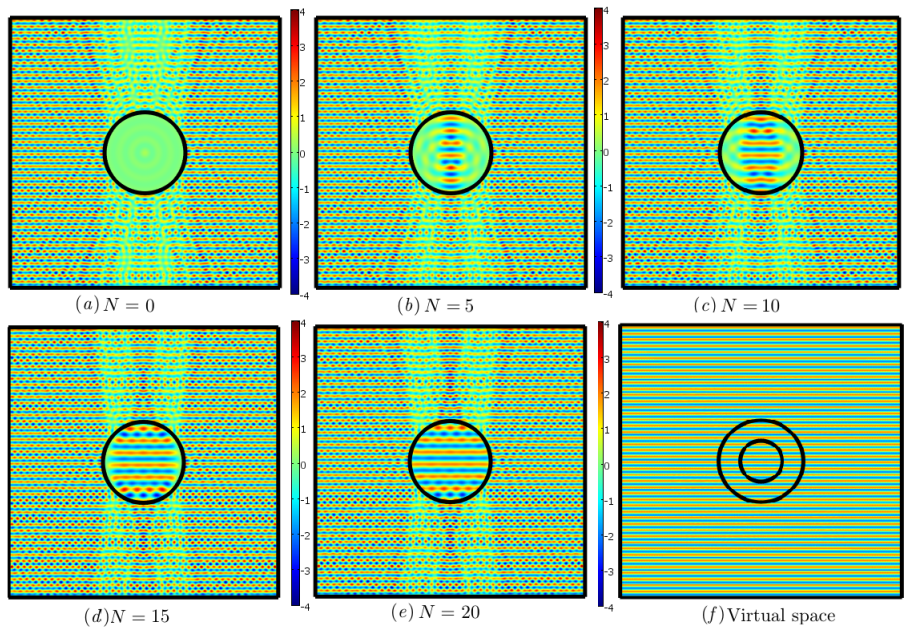

Figure 4.20: Simulation results of the simulation setup shown in Fig.(4.19). Figs.(a-e) show the electric field distribution in the physical space for $N = \{0, 5, 10, 15, 20\}$. Fig.(f) is the virtual space with a propagating plane wave.

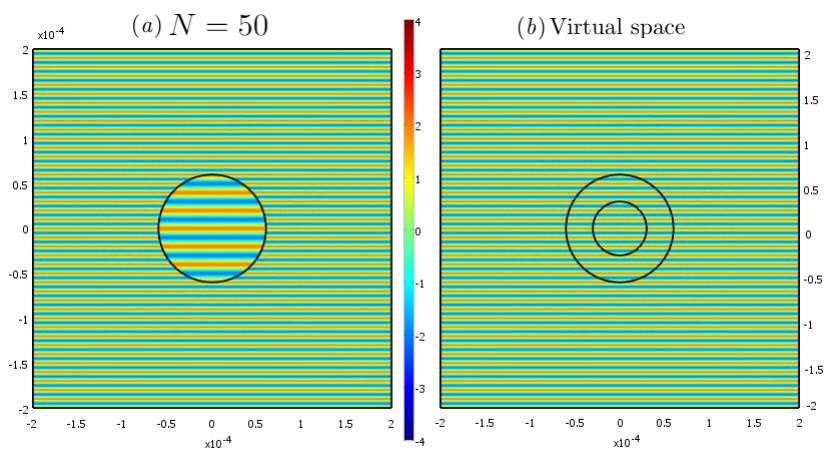

Figure 4.21: Comparison between the electric field E_z distribution. (a) Non-local MS with $N = 50$. (b) Homogeneous virtual space.

A spatial dispersive (non local) MS is hard to be implemented. Instead, it is customary to approximate such MS with another local MS including only the zeroth

cylindrical order which is the dominant term in the expansion of Eq.(4.43). The simulation results of Fig.(4.22) show a comparison between the electric field distribution of the non-local MS including $N = 20$ cylindrical wave orders and a zeroth order local MS with the plane wave's electric field of the virtual space for three different wavelength $\lambda = 1mm, 100\mu m$ and $10\mu m$. It is noticeable that for small $\frac{\rho_2}{\lambda}$ (large λ), the zeroth order local MS provides a good approximation, however as $\frac{\rho_2}{\lambda}$ increases the scattered field distribution for both the local and non-local MS.s deviates. On the other hand, the 20th order non-local MS provides a good approximation of the infinite order MS required for the discontinuous space transformation.

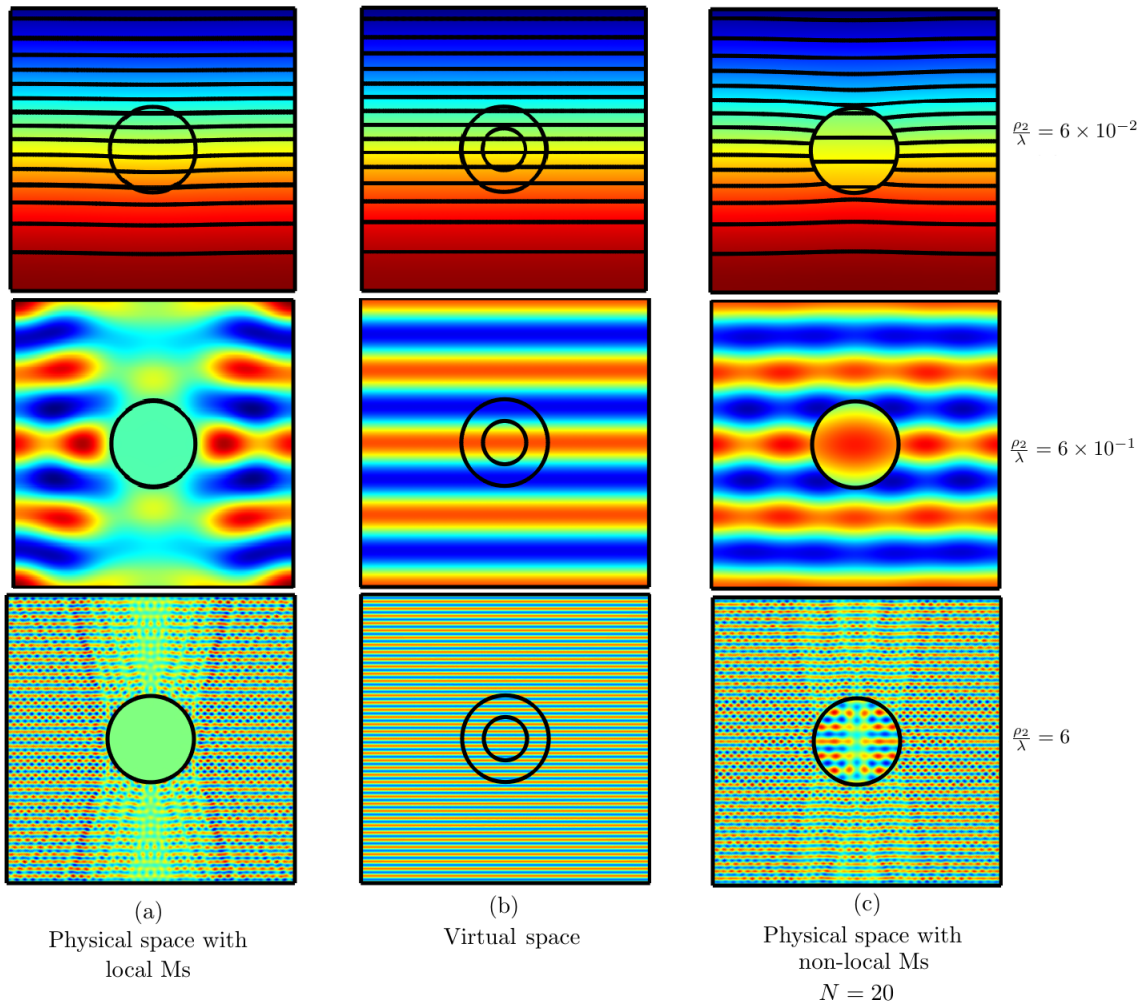

Figure 4.22: Comparison of the performance of the local and spatial Metasurfaces when compared with the virtual space for different wave lengths $\{1mm, 10\mu m$ and$10\mu m$ $\}$and $\Delta\rho = \rho_2 - \rho_1$. left: Local MS. Middle: Virtual space. Right: Non local MS.

4.3.2.2 Discontinuous radial expansion: (cylindrical boundary into cylindrical shell and dual meta-surface)

Similarly to the 1-D Expansion Discontinuous space transformation, a cylindrical shaped boundary can be replaced by a cylindrical shell and dual MS. Consider the boundary $\rho = \rho_2$ and a discontinuous transformation which breaks a continuous virtual space into two cylindrical regions $\rho' < \rho_1$ and $\rho' > \rho_2$ in the physical space as

following:

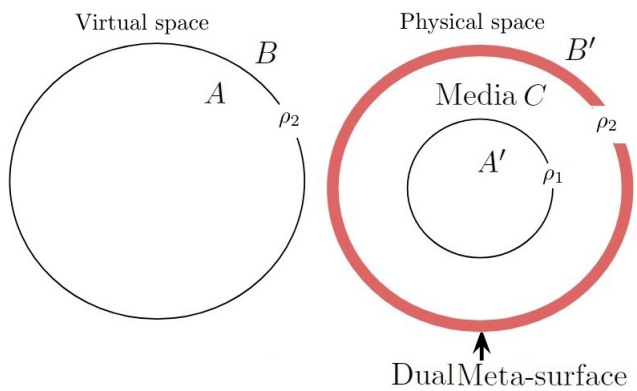

Figure 4.23: Schematic of the discontinuous radial space transformation shown in Eq.(4.46) where the cylindrical boundary $\rho < \rho_2$ in the virtual space is expanded into the cylindrical shell $\rho_1 < \rho' < \rho_2$ cascaded with a dual cylindrical Meta-surface at in the physical space

$$\rho'(\rho,\phi) = \{ \begin{array}{ll} \frac{\rho_1}{\rho_2}\rho & \rho \leq \rho_2 \\ \rho & \rho > \rho_2 \end{array} \tag{4.45}$$

such that the region located at $\rho \leq \rho_2$ are compressed into $\rho' \leq \rho_1$, while the outer region $\rho \geq \rho_2$ is unity transformed into $\rho' \geq \rho_2$. The void region $\rho_1 \leq \rho' \leq \rho_2$ is filled by arbitrary media (we assume it is homogeneous and isotropic for simplicity) and place a dual lumped cylindrical MS located at $\rho' = \rho_2$. Note that both the media and the location (radius) of the Meta-surface are arbitrary. The $Z-$ matrix of the homogeneous isotropic cylindrical shell was given in Eq.(A.60) and the $Z-$matrix of the resultant MS upon compressing such shell was given in Eq.(4.41). The $Z-$matrix of the dual MS is related to the $Z-$matrix of MS of the compressed annulus shell as as following:

$$\begin{array}{ll} \tilde{\tilde{Z}}_{11}^{DMS} = -\tilde{\tilde{Z}}_{22}^{MS} & \tilde{\tilde{Z}}_{12}^{DMS} = -\tilde{\tilde{Z}}_{21}^{MS} \\ \tilde{\tilde{Z}}_{21}^{DMS} = -\tilde{\tilde{Z}}_{12}^{MS} & \tilde{\tilde{Z}}_{22}^{DMS} = -\tilde{\tilde{Z}}_{11}^{MS} \end{array} \tag{4.46}$$

Numerical Results: In this section, two simulation setups are done to investigate the concept of expanding a cylindrical boundary into a cylindrical shell and a dual lumped radial MS. In both setups, a 2D discontinuous space transformation is introduced and the discontinuity of the transformation is implemented by a spatial dispersive homogeneous cylindrical meta-surface.

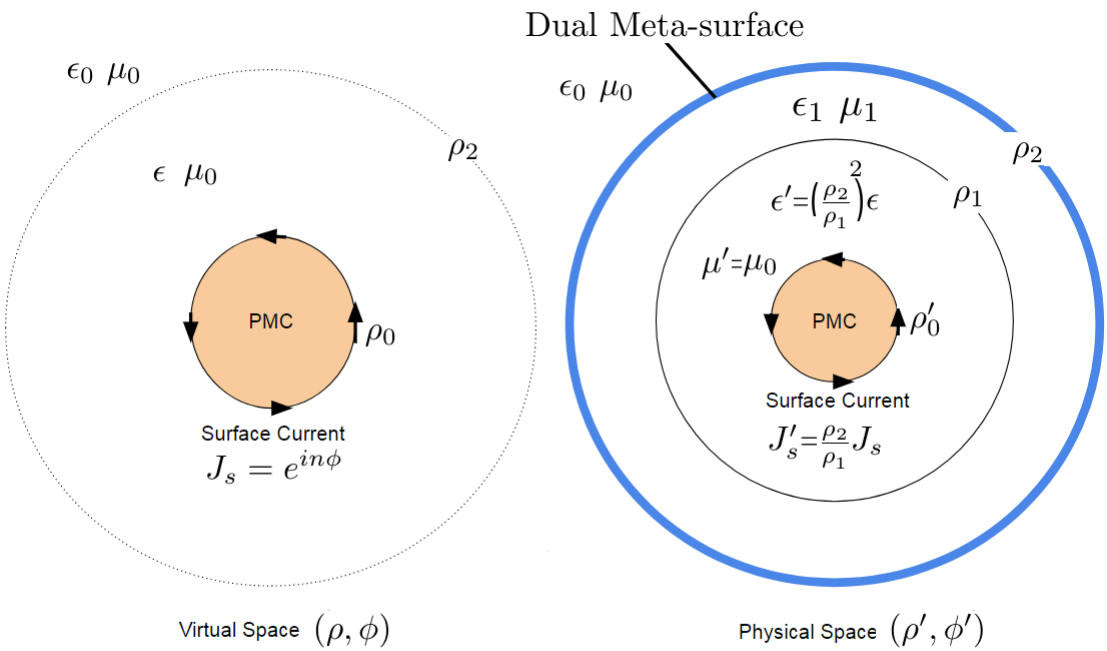

$$\phi' = \phi \quad \rho' = \begin{cases} \frac{\rho_1}{\rho_2}\rho & \rho_0 < \rho < \rho_1 \\ \rho & \rho \geq \rho_2 \end{cases}$$

Figure 4.24: A simulation setup : left: Virtual space. Right: Physical space. A Surface electric current $J_s = e^{in\phi}$ is flowing on the surface of a cylindrical perfect magnetic conductor with radius ρ_0. The emitted radiation is of the same order n. The space is transformed such that the cylindrical boundary $\rho = \rho_2$ is replaced by an annulus shell $\rho_1 < \rho' < \rho_2$ and consequent dual MS located at $\rho' = \rho_2$ in the physical space.

Simulation Setup (1) As shown in Fig.(4.24), in the Virtual space (left figure), a surface current $Js = e^{in\phi}$ is flowing at the surface of a PMC cylinder of radius ρ_0 and surrounded by a dielectric cylindrical shell $\rho_0 < \rho < \rho_2$ of permittivity ϵ and vacuum for $^{\rho} > \rho_2$. Such surface current launches cylindrical waves of the same order

n. It is desired to compress the region $\rho_0 < \rho < \rho_2$ is transformed radially into $\rho_0' < \rho' < \rho_1$ with the boundary $\rho = \rho_2$ is transformed into an annulus shell located at $\rho_1 < \rho' < \rho_2$ and a dual MS in the physical space. The space transformation can be written as following:

$$\rho' = \{ \begin{array}{c} \frac{\rho_2}{\rho_1}\rho \;\; 0 < \rho < \rho_1 \\ \rho \;\; \rho \geq \rho_2 \end{array} \qquad \phi' = \phi \tag{4.47}$$

The details of the setup is shown in Fig.(4.24). Numerical simulations are shown in Fig.s (4.25-4.27) for $n = 0, 2$ and 10 respectively. In the physical space, For each order n, a MS with the $Z-$parameters determined according to Eq.(4.46). The electric field are plotted in Fig.s (4.25-4.27) for three cases $n = 0, 2$ and 10, where the boundary $\rho = \rho_2$ in the virtual space is expanded into the cylindrical shell of vacuum with permittivity $\epsilon_1 = \epsilon_0$ and permeability $\mu_1 = \mu_0$ located at $\rho_1 < \rho' < \rho_2$ with a dual MS located at $\rho' = \rho_2$with its Z-matrix according to Eq.(4.46). The simulation was done with the following parameters: $\epsilon = \frac{1}{4}$, $\epsilon' = 1$, $\rho_0 = 10\mu m$, $\rho_1 = 30\mu m$ and $\rho_2 = 2\rho_1$. The wavelength is chosen to be $\lambda = 9\mu m$.

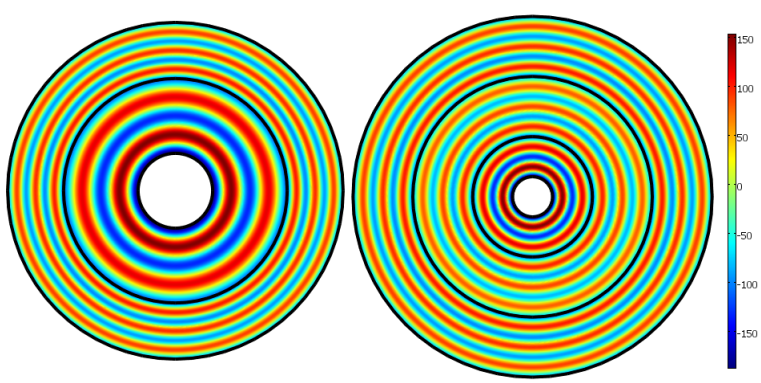

Figure 4.25: Plot of the radiated electric field E_z from electric surface current $J_s = e^{in\phi}$ with $n = 0$. left: full virtual space, right:physical space.

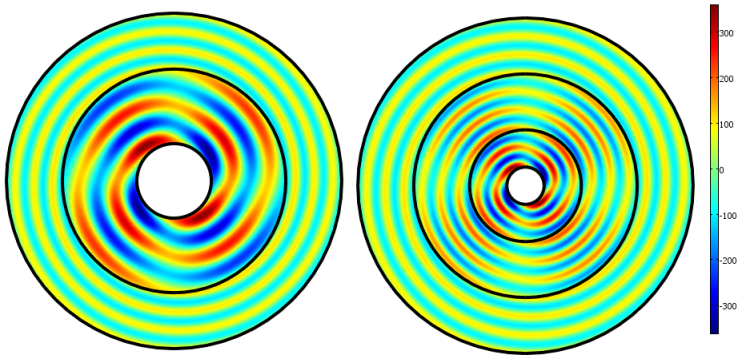

Figure 4.26: Plot of the radiated electric field E_z from electric surface current $J_s = e^{in\phi}$ with $n = 2$. left: full virtual space, right:physical space.

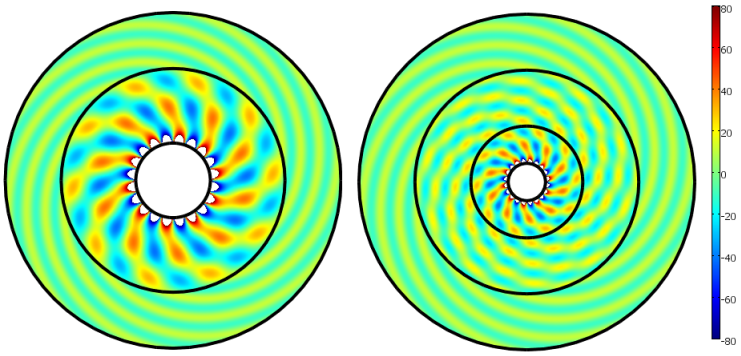

Figure 4.27: Plot of the radiated electric field E_z from electric surface current $J_s = e^{in\phi}$ with $n = 10$. left: full virtual space, right:physical space.

Simulation Setup 2 Now we examine the case of expanding a cylindrical boundary into a cylindrical ring cascaded by a dual metasurface as shown in Fig.(4.28). We consider the virtual space to be vacuum inside parallel plate waveguide with PMC walls as shown in Fig.(4.28). A plane wave is launched from the top side to be propagating in y direction. A plane wave can be expanded as a superposition of infinite number of cylindrical waves of all orders according to Eq.(4.43). The dual MS is spatial dispersive (non local) and in-homogenous is hard to be implemented. Fig.s(4.29-4.30) compare the performance of a Dual MS includes $N = 50$ orders with another dual MS which includes only the zeroth cylindrical order which is the

dominant term in the expansion of Eq.(4.43). The simulation results of Fig.s (4.29-4.30) show a comparison between the electric field distribution of the non-local MS including $N = 50$ cylindrical wave orders and a zeroth order local MS with the plane wave's electric field of the virtual space for three different wave length $\lambda = 100\mu m$ and $10\mu m$ respectively. It is clear that the Dual MS with 50 orders shows complete agreement with the theory. The local in-homogenous MS shows to be a good approximations where for large wavelengths and its performance decline as the wave length decreases since higher cylindrical orders become more significant.

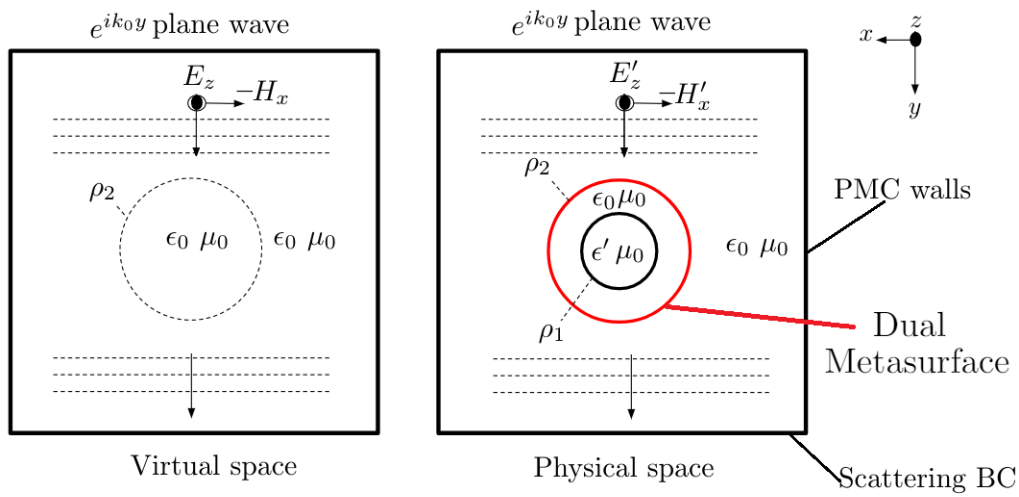

Figure 4.28: Simulation setup (2) : left: Virtual space. Right: Physical space. A plane wave is propagating in y direction in a PMC parallel plate wave guide. The space is transformed according to Eq.(4.45) such that the cylindrical region $\rho \leq \rho_2$ in the virtual space is compressed into the cylindrical region $\rho' \leq \rho_1$ while the region $\rho \geq \rho_2$ is unity transformed into $\rho' \geq \rho_2$. The boundary $\rho = \rho_2$ is expanded into a cylindrical shell (chosen to be vacuum) surrounded by a cylindrical dual MS located $\rho' = \rho_2$. The MS is designed to be spatial dispersive (non local) and homogenous.

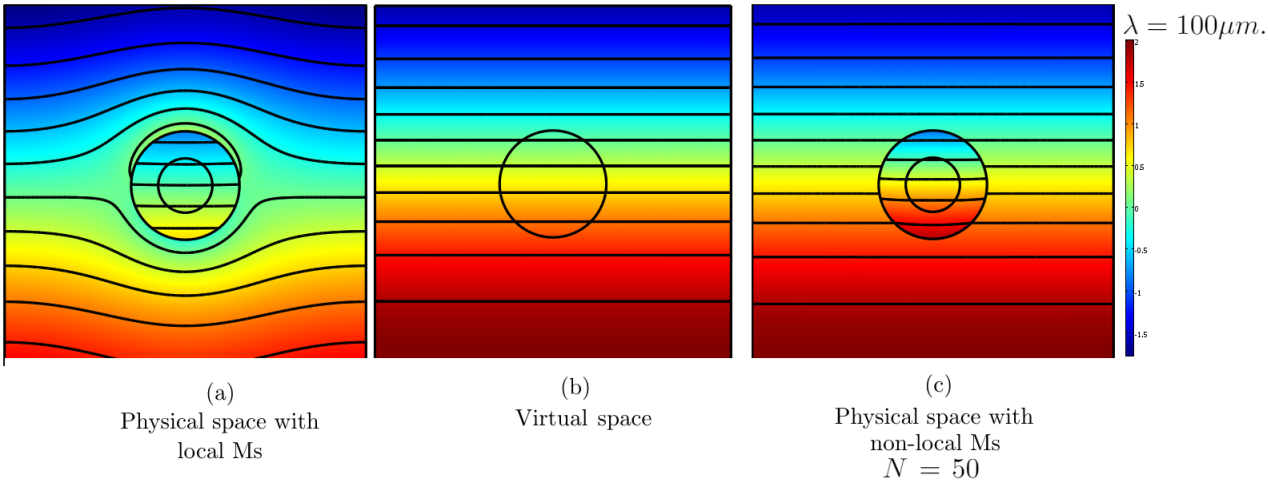

Figure 4.29: Comparison of the performance of the local and spatial Metasurfaces when compared with the virtual space for wave length $100\mu m$. left: Local MS. Middle: Virtual space. Right: Non local MS.

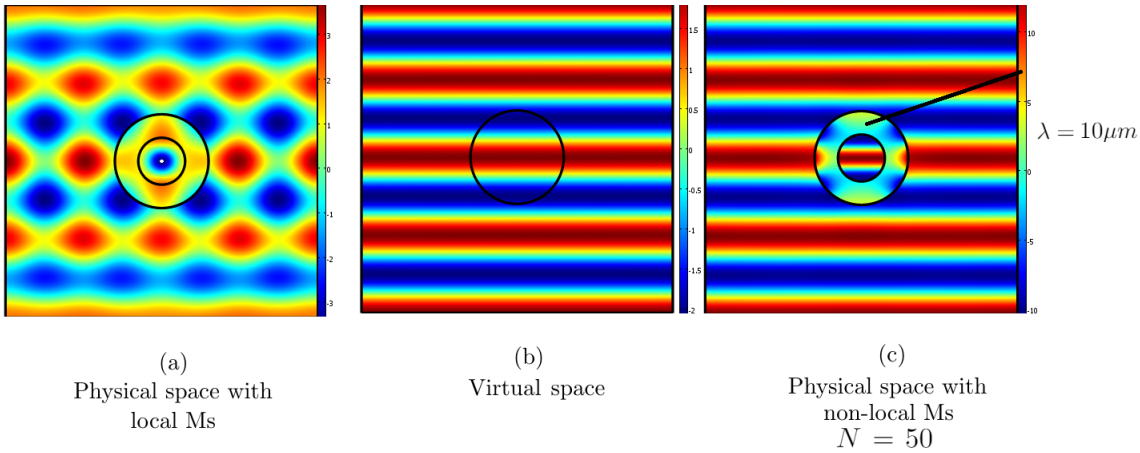

Figure 4.30: Comparison of the performance of the local and spatial Metasurfaces when compared with the virtual space for wave length $10\mu m$. left: Local MS. Middle: Virtual space. Right: Non local MS.

4.3.3 Compression of non cylindrical shell into an inhomogeneous and spatial dispersive MS:

Till now, we have considered discontinuous space transformation where either a cylindrical shell is compressed into a MS or expanding a cylindrical boundary into a

cylindrical shell in contact with a dual MS. In this subsection, we consider a further generalization where we apply discontinuous space transformation but utilizing non cylindrical shells as following:

1. **Compression:** As shown in Fig.(4.31), the region $\sigma(\phi) < \rho < \rho_s$ at the virtual space is compressed into a meta-surface located at $\rho' = \rho_s$ in the physical space. The region A at $\rho < \sigma(\phi)$ in virtual space is expanded into A' at $\rho' < \rho_s$ in the physical space, with $\phi = \phi'$ invariant under transformation (no rotation).

2. **Expansion:** As shown in Fig.(4.39), starting with the virtual space, the cylindrical boundary $\rho = \rho_s$ into an arbitrary media resides at $\sigma(\phi) < \rho' < \rho_s$ in contact with a complementary (dual) meta-surface located at $\rho' = \rho_s$ and the region $\rho < \rho_s$ in virtual space is compressed into $\rho' < \sigma$ while $\phi = \phi'$ is invariant under transformation (no rotation).

The resulting meta-surface from both former cases will be both spatial dispersive and in the same time in-homogeneous or ϕ-dependent MS. The in-homogeneity stems from the inner surface $\sigma(\phi)$. Note that the latter two cases are the same as the cylindrical shell cases of previous subsections, where we substitute for $\rho_1 \longrightarrow \sigma(\phi)$ and $\rho_2 \longrightarrow \rho_s$.

4.3.3.1 Discontinuous radial compression: (non-cylindrical shell into cylindrical Meta-surface)

Starting with a 2D virtual space divided into three regions (see Fig.(4.31)):

1. Region B located at $\rho > \rho_s$.

2. Region A located at $\rho < \sigma(\phi)$.

3. Annulus ring located at $\sigma(\phi) < \rho < \rho_s$.

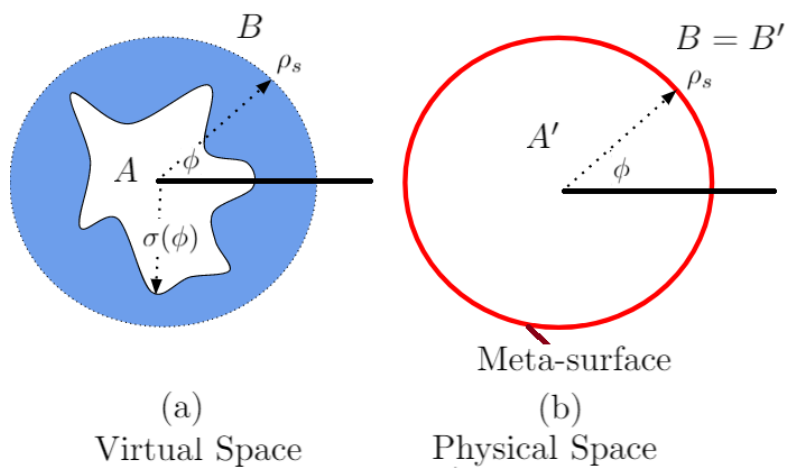

Figure 4.31: Schematic of the discontinuous radial transformation where the blue coloured shell located at $\sigma(\phi) < \rho < \rho_s$ in the virtual space in Fig.(a) is compressed into the red coloured cylindrical shaped MS located at $\rho' = \rho_s$ in the physical space in Fig.(b). Note that A is transformed into A' and B is unity transformed into B' $(B = B')$.

Transforming the area A located in $\rho \leq \sigma(\phi)$ at the virtual space into A' located at $\rho^{'} \leq \rho_s$ in the physical space and since there is no rotation then $\phi' = \phi$. Note that the object A is transformed into A' for $\rho' < \rho_s$ and the shell located at $\sigma(\phi) < \rho < \rho_s$ is compressed into zero thickness layer which will be replaced by a MS located at $\rho' = \rho_s$. The discontinuous space transformation is defined as following:

$$\rho'(\rho, \phi) = \{ \begin{array}{ll} \frac{\rho_s}{\sigma(\phi)}\rho & \rho \leq \sigma(\phi) \\ \rho & \rho > \rho_s \end{array} \tag{4.48}$$

The Jacobian of the transformation will be as following

$$\text{For } \rho < \sigma(\phi) \quad \underline{\underline{J}} = J_m^{m'} = \begin{bmatrix} \frac{\partial \rho'}{\partial \rho} & \frac{\partial \rho'}{\rho \partial \phi} \\ 0 & \frac{\rho'}{\rho} \end{bmatrix} = \frac{\rho_s}{\sigma(\phi)} \begin{bmatrix} 1 & -\frac{1}{\sigma(\phi)} \frac{\partial \sigma(\phi)}{\partial \phi} \\ 0 & 1 \end{bmatrix}$$

$$\text{then } \underline{\underline{J}}^{-\tau} = \begin{bmatrix} \frac{\sigma(\phi)}{\rho_s} & 0 \\ \frac{1}{\rho_s}\frac{\partial\sigma(\phi)}{\partial\phi} & \frac{\sigma(\phi)}{\rho_s} \end{bmatrix}$$

$$\text{For } \rho > \rho_s \quad \underline{\underline{J}} = \begin{bmatrix} 1 & 0 \\ 0 & 1 \end{bmatrix}$$

The media are transformed as following: $\varepsilon_{zz}^{'} = \dfrac{\varepsilon_{zz}}{det(\underline{\underline{J}})}$ $\qquad \mu_T^{m'n'} = \dfrac{1}{det(\underline{\underline{J}})} J_m^{m'} J_n^{n'} \mu_T^{mn}$

while the fields are transformed as following: $\underline{H}_T^{'}(\rho' = \rho_s^-) = \underline{\underline{J}}^{-\tau}\underline{H}_T(\rho = \sigma(\phi))$

$$\underline{H}_T^{'}(\rho' = \rho_s^+) = \underline{H}_T(\rho = \rho_s)$$

$$E_z^{'}(\rho' = \rho_s^-) = E_z(\rho = \sigma(\phi)) \tag{4.49}$$

Note that a major difference between the space transformation between this case and the case of cylindrical symmetric is the transformation of the magnetic field azimuthal component $H'_\phi = H'_\phi(H_\phi)$ where the H'_ϕ is written in terms of the magnetic field components of the virtual space as following:

$$H'_\phi = \frac{1}{\rho_s}\frac{\partial\sigma(\phi)}{\partial\phi}H_\rho + \frac{\sigma(\phi)}{\rho_s}H_\phi \tag{4.50}$$

In the case of compressing a cylindrical shell $\sigma = constant$ so $\frac{\partial\sigma(\phi)}{\partial\phi} = 0$. The former transformation will alter the way to calculate for the impedance(Z) or equivalently the admittance (Y) matrix.

Y-matrix of the MS: In order to calculate of the $Y-$ matrix of the required MS , it is needed to transform the electric and magnetic fields from virtual space into physical space according to Eq.(4.49), then the Y-parameters in the physical space will be calculated as following:

starting with the virtual space which is assumed to be contain a homogeneous and isotropic media with permittivity ϵ and permeability μ for the region $\rho < \rho_s$. For E-polarization case, the expressions of the electromagnetic field components (E_z,H_ϕ and H_ρ) in the virtual space in terms of the cylindrical basis are written as following:

$$\begin{aligned}
\tilde{E}_z[n] &= \left(E_n^+ H_n^{(2)}(k\rho) + E_n^- H_n^{(1)}(k\rho)\right) e^{jn\phi} \\
\tilde{H}_\phi[n] &= -j\frac{1}{\eta}\left(E_n^+ \dot{H}_n^{(2)}(k\rho) + E_n^- \dot{H}_n^{(1)}(k\rho)\right) e^{jn\phi} \\
\tilde{H}_\rho[n] &= \frac{n}{k\eta\rho}\left(E_n^+ H_n^{(2)}(k\rho) + E_n^- H_n^{(1)}(k\rho)\right) e^{jn\phi}
\end{aligned} \tag{4.51}$$

where n is the cylindrical order and η is the wave impedance, $k = \omega\sqrt{\epsilon\mu}$ is the propagation wave, E_n^+ and E_n^- are the amplitudes of the out-going and in-going cylindrical waves. Now by space transforming the virtual space into the physical space according to Eq.(4.49), then the electromagnetic field components (E'_z,H'_ϕ and H'_ρ)in the physical space will have the following form:

$$\begin{aligned}
\tilde{E}'_z[n] &= \tilde{E}'_z[n] = \left(E_n^+ H_n^{(2)}(k\rho) + E_n^- H_n^{(1)}(k\rho)\right) e^{jn\phi} \\
\tilde{H}'_\phi[n] &= \frac{1}{\rho_s}\frac{\partial\sigma(\phi)}{\partial\phi}H_\rho + \frac{\sigma(\phi)}{\rho_s}H_\phi \\
&= \left[\frac{1}{\rho_s}\frac{\partial\sigma(\phi)}{\partial\phi}\frac{n}{\omega\mu\rho}\left(E_n^+ H_n^{(2)}(k\rho) + E_n^- H_n^{(1)}(k\rho)\right) - \frac{\sigma(\phi)}{\rho_s}j\frac{1}{\eta}\left(E_n^+ \dot{H}_n^{(2)}(k\rho) + E_n^- \dot{H}_n^{(1)}(k\rho)\right)\right] e^{jn\phi} \\
\tilde{H}'_\rho[n] &= \frac{\sigma(\phi)}{\rho_s}\tilde{H}_\rho[n] = \frac{\sigma(\phi)}{\rho_s}\frac{n}{\omega\mu\rho}\left(E_n^+ H_n^{(2)}(k\rho) + E_n^- H_n^{(1)}(k\rho)\right) e^{jn\phi}
\end{aligned} \tag{4.52}$$

Similarly to the cylindrical shell, to calculate for the $Y-$ matrix of the MS, currents and voltages are needed to be defined in terms of the tangential electric and magnetic field components as following:

$$
\begin{aligned}
\tilde{V}_1'[n,\phi] &= \sqrt{\rho_s}\tilde{E}_{z,1}'[n] = \sqrt{\rho_s}\left(E_n^+ H_n^{(2)}(k\sigma(\phi)) + E_n^- H_n^{(1)}(k\sigma(\phi))\right)e^{jn\phi} \\
\tilde{I}_1'[n,\phi] &= -\sqrt{\rho_s}\tilde{H}_{\phi,1}'[n] \\
&= -\sqrt{\rho_s}E_n^+\left[\frac{1}{\rho_s}\frac{\partial\sigma(\phi)}{\partial\phi}\frac{n}{\omega\mu\sigma(\phi)}H_n^{(2)}(k\sigma(\phi)) - \frac{\sigma(\phi)}{\rho_s}j\frac{1}{\eta}\dot{H}_n^{(2)}(k\sigma(\phi))\right]e^{in\phi} \\
&\quad - \sqrt{\rho_s}E_n^-\left[\frac{1}{\rho_s}\frac{\partial\sigma(\phi)}{\partial\phi}\frac{n}{\omega\mu\sigma(\phi)}H_n^{(1)}(k\sigma(\phi)) - \frac{\sigma(\phi)}{\rho_s}j\frac{1}{\eta}\dot{H}_n^{(1)}(k\sigma(\phi))\right]e^{in\phi} \\
\tilde{V}_2'[n,\phi] &= \sqrt{\rho_s}\tilde{E}_{z,2}'[n] = \sqrt{\rho_s}\left(E_n^+ H_n^{(2)}(k\rho_s) + E_n^- H_n^{(1)}(k\rho_s)\right)e^{jn\phi} \\
\tilde{I}_2'[n,\phi] &= -\sqrt{\rho_s}\tilde{H}_{\phi,2}'[n] = j\frac{\sqrt{\rho_s}}{\eta}\left(E_n^+\dot{H}_n^{(2)}(k\rho_s) + E_n^-\dot{H}_n^{(1)}(k\rho_s)\right)e^{jn\phi}
\end{aligned}
\tag{4.53}
$$

Note that the subscripts 1 and 2 are indices for inner and outer sides of the shell. Arranging the previous equation in a matrix form while relating the current and voltages by an admitttance matrix as following:

$$
\begin{aligned}
&\begin{bmatrix} \tilde{I}_1'[n,\phi] \\ \tilde{I}_2'[n,\phi] \end{bmatrix} \\
&= \begin{bmatrix} \frac{-1}{\sqrt{\rho_s}} \frac{\partial \sigma(\phi)}{\partial \phi} \frac{n}{k\eta\sigma(\phi)} H_n^{(2)}(k\sigma(\phi)) & \frac{-1}{\sqrt{\rho_s}} \frac{\partial \sigma(\phi)}{\partial \phi} \frac{n}{k\eta\sigma(\phi)} H_n^{(1)}(k\sigma(\phi)) \\ 0 & 0 \end{bmatrix} \\
&\qquad \begin{bmatrix} \sqrt{\rho_s} H_n^{(2)}(k\sigma(\phi)) & \sqrt{\rho_s} H_n^{(1)}(k\sigma(\phi)) \\ \sqrt{\rho_s} H_n^{(2)}(k\rho_s) & \sqrt{\rho_s} H_n^{(1)}(k\rho_s) \end{bmatrix}^{-1} \begin{bmatrix} \tilde{V}_1'[n,\phi] \\ \tilde{V}_2'[n,\phi] \end{bmatrix} \\
&+ \begin{bmatrix} \frac{\sigma(\phi)}{\sqrt{\rho_s}} j \frac{1}{\eta} \dot{H}_n^{(2)}(k\sigma(\phi)) & \frac{\sigma(\phi)}{\sqrt{\rho_s}} j \frac{1}{\eta} \dot{H}_n^{(1)}(k\sigma(\phi)) \\ j \frac{\sqrt{\rho_s}}{\eta} \dot{H}_n^{(2)}(k\rho_s) & j \frac{\sqrt{\rho_s}}{\eta} \dot{H}_n^{(1)}(k\rho_s) \end{bmatrix} \begin{bmatrix} \sqrt{\rho_s} H_n^{(2)}(k\sigma(\phi)) & \sqrt{\rho_s} H_n^{(1)}(k\sigma(\phi)) \\ \sqrt{\rho_s} H_n^{(2)}(k\rho_s) & \sqrt{\rho_s} H_n^{(1)}(k\rho_s) \end{bmatrix}^{-1} \begin{bmatrix} \tilde{V}_1'[n,\phi] \\ \tilde{V}_2'[n,\phi] \end{bmatrix} \\
&= \begin{bmatrix} \tilde{Y}_{11}^{MS}[n,\phi] & \tilde{Y}_{12}^{MS}[n,\phi] \\ \tilde{Y}_{21}^{MS}[n,\phi] & \tilde{Y}_{22}^{MS}[n,\phi] \end{bmatrix} \begin{bmatrix} \tilde{V}_1'[n,\phi] \\ \tilde{V}_2'[n,\phi] \end{bmatrix}
\end{aligned}
\tag{4.54}
$$

where the elements of the admittance matrix are written as following:

$$
\begin{aligned}
\tilde{Y}_{11}^{MS}[n,\phi] &= \frac{j}{\eta} \frac{\sigma(\phi)}{\rho_s} \frac{\dot{H}_n^{(2)}(k\sigma(\phi)) H_n^{(1)}(k\rho_s) - \dot{H}_n^{(1)}(k\sigma(\phi)) H_n^{(2)}(k\rho_s)}{H_n^{(2)}(k\sigma(\phi)) H_n^{(1)}(k\rho_s) - H_n^{(1)}(k\sigma(\phi)) H_n^{(2)}(k\rho_s)} - \frac{j}{\eta} \frac{n}{k} \frac{\frac{d\sigma(\phi)}{d\phi}}{\rho_s \sigma(\phi)} \\
\tilde{Y}_{12}^{MS}[n,\phi] &= \frac{j}{\eta} \frac{\sigma(\phi)}{\rho_s} \frac{\dot{H}_n^{(1)}(k\sigma(\phi)) H_n^{(2)}(k\sigma(\phi)) - \dot{H}_n^{(2)}(k\sigma(\phi)) H_n^{(1)}(k\sigma(\phi))}{H_n^{(2)}(k\sigma(\phi)) H_n^{(1)}(k\rho_s) - H_n^{(1)}(k\sigma(\phi)) H_n^{(2)}(k\rho_s)} \\
\tilde{Y}_{21}^{MS}[n,\phi] &= \frac{j}{\eta} \frac{\dot{H}_n^{(2)}(k\rho_s) H_n^{(1)}(k\rho_s) - \dot{H}_n^{(1)}(k\rho_s) H_n^{(2)}(k\rho_s)}{H_n^{(2)}(k\sigma(\phi)) H_n^{(1)}(k\rho_s) - H_n^{(1)}(k\sigma(\phi)) H_n^{(2)}(k\rho_s)} \\
\tilde{Y}_{22}^{MS}[n,\phi] &= \frac{j}{\eta} \frac{\dot{H}_n^{(1)}(k\rho_s) H_n^{(2)}(k\sigma(\phi)) - \dot{H}_n^{(2)}(k\rho_s) H_n^{(1)}(k\sigma(\phi))}{H_n^{(2)}(k\sigma(\phi)) H_n^{(1)}(k\rho_s) - H_n^{(1)}(k\sigma(\phi)) H_n^{(2)}(k\rho_s)}
\end{aligned}
\tag{4.55}
$$

Note the difference between the elements of the former $Y-$matrix and the $Z-$matrix in Eq.(4.41) of the Ms due to compressing a cylindrical shell. The main difference lies in the extra term found in $\tilde{Y}_{11}^{MS}$. It is also clear that the $Y-$ matrix elements are both order dependent (non-local) and in-homogeneous in ϕ, as it was shown in Eq.(4.9), the admittance matrix will relate the voltages and currents at the sides of the MS as following:

$$\begin{aligned} I_1'(\rho_s,\phi) &= \frac{1}{2\pi}\int Y_{11}^{MS}(\phi',\phi-\phi')V_1'(\rho_s,\phi') + Y_{12}^{MS}(\phi',\phi-\phi')V_{2,\|}'(\rho_s,\phi')d\phi' \\ I_2'(\rho_s,\phi) &= \frac{1}{2\pi}\int Y_{21}^{MS}(\phi',\phi-\phi')V_1'(\rho_0,\phi') + Y_{22}^{MS}(\phi',\phi-\phi')V_2'(\rho_s,\phi')d\phi' \end{aligned} \tag{4.56}$$

where $I_{1,2}(\rho_s,\phi)$ and $V_{1,2}(\rho_s,\phi)$ are the current (magnetic) and the voltage (electric) fields at the sides of the MS respectively and they are calculated through Fourier transform relation as following:

$$\begin{aligned} I_1'(\rho_s,\phi) &= \sum_n \tilde{I}_1'[n]e^{in\phi} \qquad & I_2'(\rho_s,\phi) &= \sum_n \tilde{I}_2'[n]e^{in\phi} \\ V_1'(\rho_s,\phi) &= \sum_n \tilde{V}_1'[n]e^{in\phi} \qquad & V_2'(\rho_s,\phi) &= \sum_n \tilde{V}_2'[n]e^{in\phi} \end{aligned} \tag{4.57}$$

also the admittance elements are also calculated through Fourier transform relation as following:

$$\begin{aligned} Y_{11}^{MS}(\phi',\phi-\phi') &= \sum_n \tilde{Y}_{11}^{MS}[n,\phi]e^{in(\phi-\phi')} \qquad & Y_{12}^{MS}(\phi',\phi-\phi') &= \sum_n \tilde{Y}_{12}^{MS}[n,\phi]e^{in(\phi-\phi')} \\ Y_{21}^{MS}(\phi',\phi-\phi') &= \sum_n \tilde{Y}_{21}^{MS}[n,\phi]e^{in(\phi-\phi')} \qquad & Y_{22}^{MS}(\phi',\phi-\phi') &= \sum_n \tilde{Y}_{22}^{MS}[n,\phi]e^{in(\phi-\phi')} \end{aligned} \tag{4.58}$$

Numerical Results: Here, two simulation setups are done to examine the concept of compressing a non-cylindrical shell into a zero thickness MS. In both setups, a 2D discontinuous space transformation is introduced and the discontinuity of the trans-

formation is implemented by a a spatial frequency dispersive and in-homogeneous cylindrical meta-surface.

Simulation Setup (1): As shown in Fig.(4.32), a virtual space (left figure) is filled by vacuum. considering an incident cylindrical wave of order n . Such surface current launches cylindrical waves of the same order n, then the scattered field will be also a cylindrical wave of the same order n. It is desired to transform the elliptic region $\rho < \sigma(\phi)$ radially into $\rho' < \rho_s$ with the shell $\sigma(\phi) < \rho < \rho_s$ is compressed into a MS in the physical space located at $\rho' = \rho_s$. The space transformation can be written as following:

$$\rho' = \{ \begin{array}{c} \frac{\rho_s}{\sigma(\phi)}\rho \;\; \rho < \rho_s \\ \rho \;\; \rho \geq \rho_s \end{array} \qquad \phi' = \phi \tag{4.59}$$

where $\sigma(\phi) = \left[\left(\frac{cos(\phi)}{a}\right)^2 + \left(\frac{sin(\phi)}{b}\right)^2\right]^{-\frac{1}{2}}$ is the equation of the ellipse, where a and b are the semi-major and semi-minor axes of the ellipse.

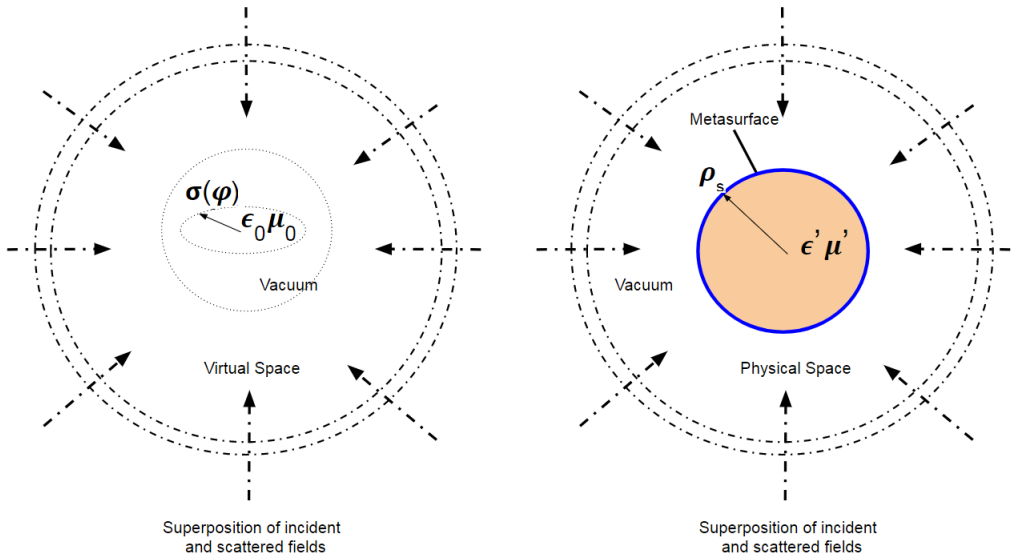

Figure 4.32: Schematic of a simulation setup: left: Virtual space filled with vacuum. Right: Physical space. In the vacuum filled virtual space, an incident cylindrical wave of order n is reflected so the distribution of the electric field $\tilde{E}_z[n] = A_n J_n(k\rho)e^{in\phi}$ where J_n is Bessel function of 1st type and order n. The virtual space is transformed into the physical space through Eq.(4.59)such that the non-cylindrical shell $\sigma(\phi) < \rho < \rho_s$ is compressed into a MS located at $\rho' = \rho_s$ in the physical space. Note the electric field E_z is transformed as a scalar quantity and is expected to be unity transformed for the regions $\rho' > \rho_s$ and $\rho' > \rho_s$.

The details of the setup is shown in Fig.(4.32). Numerical simulations are shown in Fig.s (4.33-4.36) for incident cylindrical waves of order $n = 0, 1$ and 10 respectively with the electric fields are plotted in Fig.s (4.33-4.36) for the three cases. In the physical space the $Y-$ matrix of the MS is calculated according to Eq.s (4.55) and (4.58).The simulation is done with the following parameters: $\rho_0 = 10\mu m$, $a = 50\mu m$, $b = 30\mu m$ and $\rho_s = 60\mu m$. The wavelength is chosen to be $\lambda = 10\mu m$. It is clear from Figs (4.33-4.36) that the electric field distributions of the virtual space at $\rho > \rho_s$ is the same as the the electric field distributions of the physical space $\rho' > \rho_s$ which is consistent with the fact that regions are unity transformed. Fig.(4.34) shows the field distribution in the virtual and physical spaces for the regions $\rho < \sigma(\phi)$ and $\rho' < \rho_s$ respectively, for an incident cylindrical wave of order $n = 0$, which is consistent with the fact that the electric field E_z is a scalar and invariant under space transformation

so that $E_z = E'_z$. It is important to note that the MS is in-homogeneous and non-local while the region $\rho' < \rho_s$ is an-isotropic and in-homogeneous. The combination of both the MS and the region $\rho' < \rho_s$ give the effect that the scattering of an incident cylindrical wave of order n is of the same order.

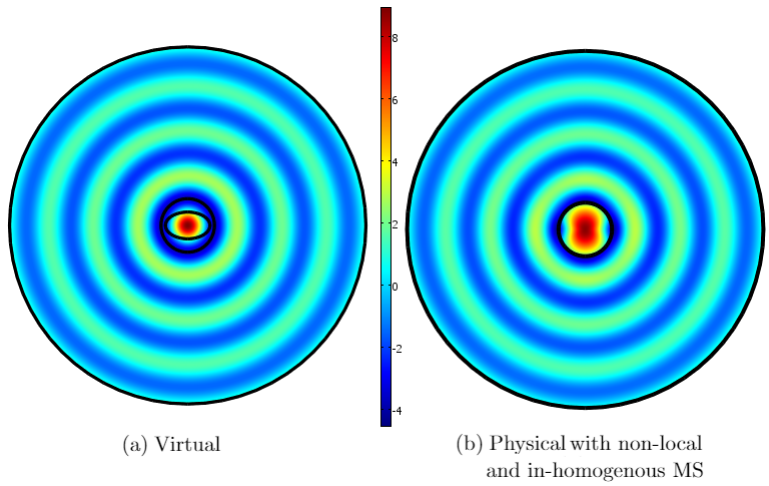

Figure 4.33: Plot of the electric field E_z with $n = 0$. (a) full virtual space, (b) physical space. The electric field at $\rho = \rho' > \rho_s$ is a standing cylindrical wave of order $n = 0$ with the following form $E_z = A_0 J_0(k\rho)e^{i\phi}$ where A_0 is a constant.

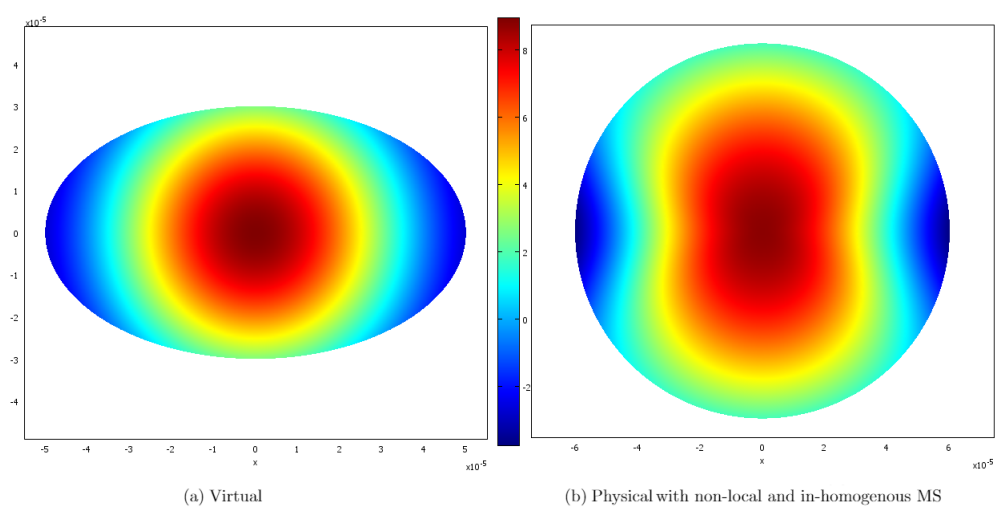

Figure 4.34: Plot of the electric fields E_z of virtual space for $\rho < \sigma(\phi)$ and E'_z of physical space for $\rho' < \rho_s$ with $n = 0$. (a) virtual space, (b) physical space. It is clear the $E_z(\rho) = E'_z(\rho')$.

Simulation Setup (2): Now, we consider the space transformation as the previous case, but instead of examining each cylindrical harmonic separately, we consider the case where the incident field is a plane wave that contains theoretically infinite cylindrical harmonics. We consider the virtual space to be vacuum inside parallel plate waveguide with PMC walls as shown in Fig.(4.37). A plane wave is launched from the top side to be propagating in y direction. A plane wave can be expanded as a superposition of infinite number of cylindrical waves of all orders as shown in Eq.(4.43).

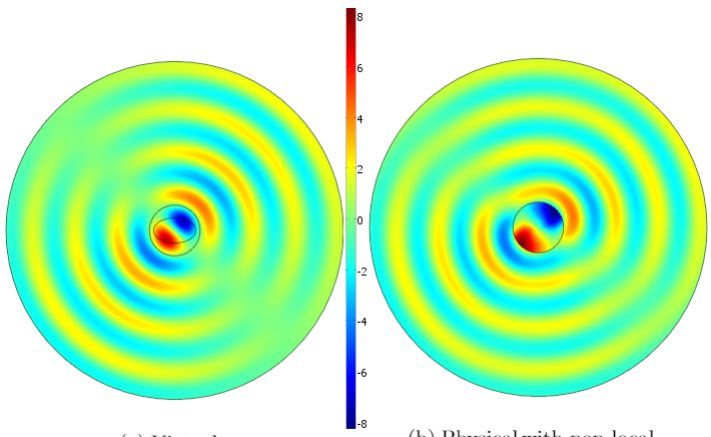

(a) Virtual

(b) Physical with non-local and in-homogenous MS

Figure 4.35: Plot of the electric field E_z with $n = 1$. (a) full virtual space, (b) physical space. The electric field at $\rho = \rho' > \rho_s$ is a standing cylindrical wave of order $n = 1$ with the following form $E_z = A_1 J_1(k\rho)e^{i\phi}$ where A_1 is a constant.

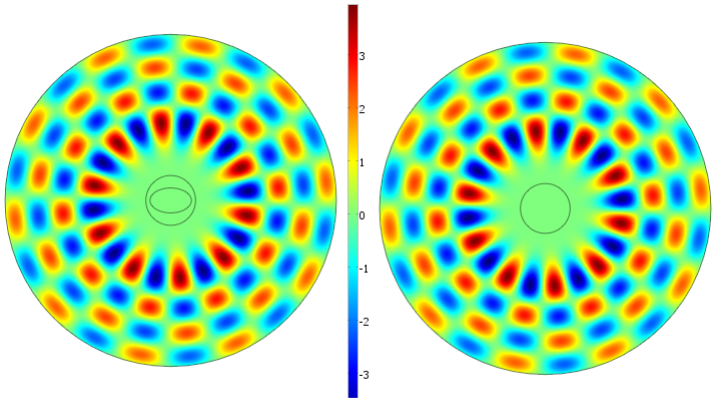

(a) Virtual

(b) Physical with non-local and in-homogenous MS

Figure 4.36: Plot of the electric field E_z with $n = 10$. (a) full virtual space, (b) physical space.The electric field at $\rho = \rho' > \rho_s$ is a standing cylindrical wave of order $n = 10$ with the following form $E_z = A_{10}J_{10}(k\rho)e^{i10\phi}$ where A_{10} is a constant.

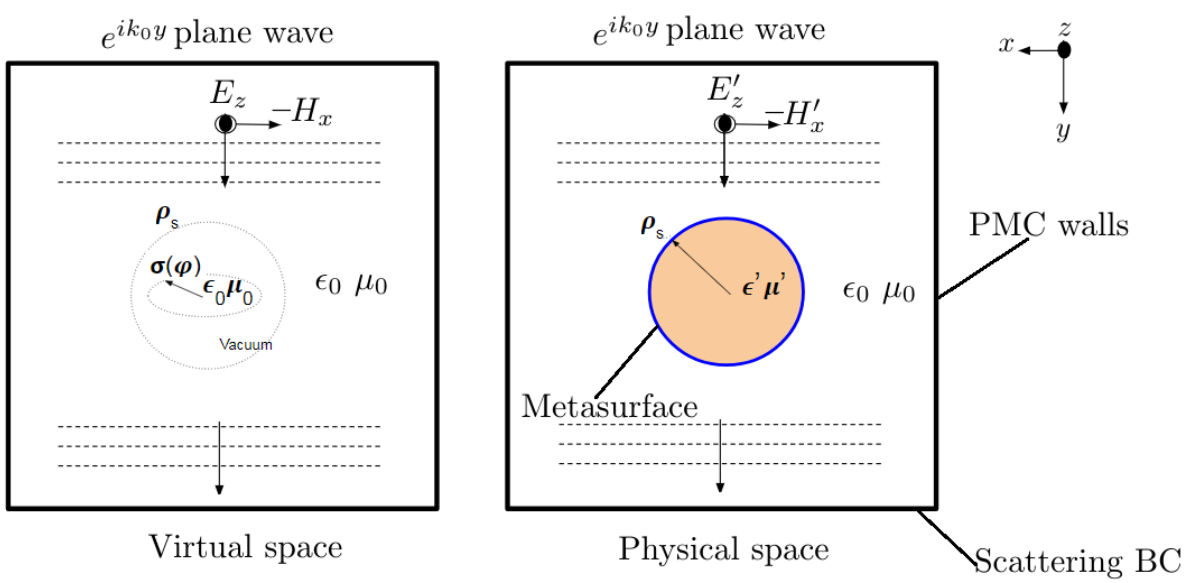

Figure 4.37: Simulation setup (2) : left: Virtual space. Right: Physical space. A plane wave is propagating in y direction in a PMC parallel plate wave guide. The space is transformed according to Eq.(4.59) such that the non-cylindrical ring $\sigma(\phi) < \rho < \rho_s$ is compressed into a MS located at $\rho' = \rho_s$ in the physical space. The MS is designed to be spatial dispersive (non local) and in-homogenous with respect to ϕ (see Fig.(4.15)).

The $Y-$matrix of the MS is calculated according to Eq.s (4.55) and (4.58) using $N = 50$ cylindrical orders such that $n \in [-50, -50]$. Simulation is done at wave length $\lambda = 100\mu m$. The field distributions in both virtual and physical spaces are

shown in Fig.(4.38). We notice that the isolines of the electric field in the physical are slightly different from those of the virtual space. It is believed that such difference can be attributed to the usage of limited number of cylindrical orders. Due to the in-homogeneity of the MS, different cylindrical orders are coupled to each other and by truncation a residual effect is unavoidable.

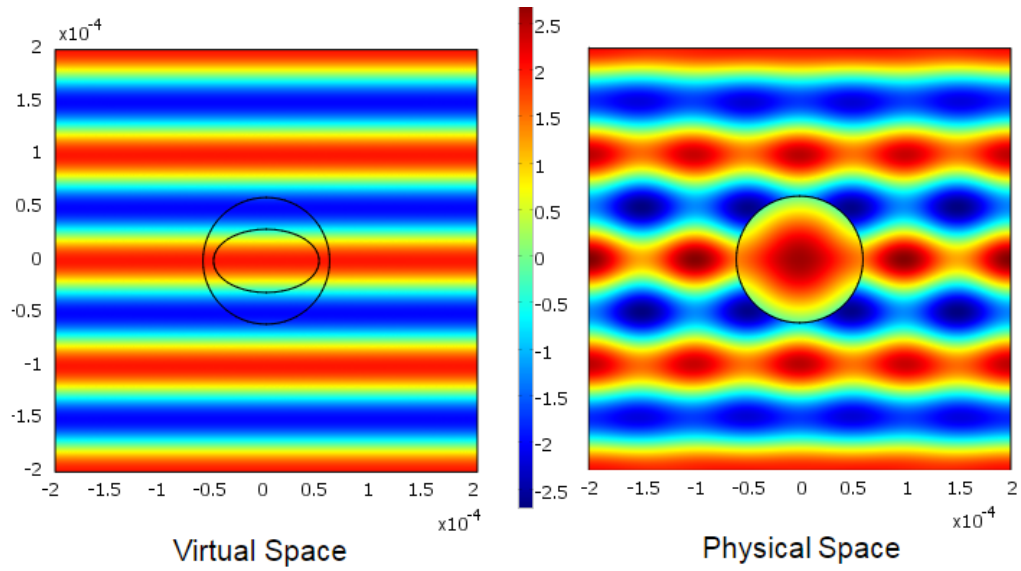

Figure 4.38: with non-local and in-homogeneous MS with $N = 50$ cylindrical orders. simulation is done at wavelength $\lambda = 100\mu m$.

4.3.3.2 Discontinuous radial expansion: (cylindrical boundary into cylindrical shell and Dual Meta-surface)

In the opposite direction to the previous case, a cylindrical shaped boundary can be replaced by a dual MS at the same boundary with a shell of an outer cylindrical and non-cylindrical inner boundary as shown in Fig.(4.39). Consider the boundary $\rho = \rho_s$ and a discontinuous transformation which breaks a continuous virtual space into two regions $\rho' < \sigma(\phi)$ and $\rho' > \rho_s$ in the physical space as following:

$$\rho'(\rho, \phi) = \{ \begin{array}{ll} \frac{\sigma(\phi)}{\rho_s}\rho & \rho \leq \rho_s \\ \rho & \rho > \rho_s \end{array} \tag{4.60}$$

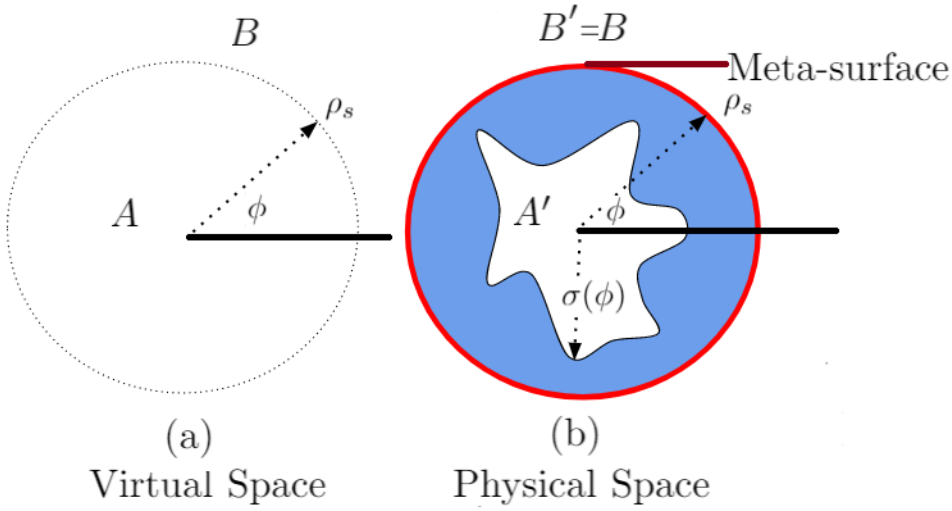

Figure 4.39: Schematic of the discontinuous radial space transformation of Eq.(4.60), where the cylindrical boundary $\rho < \rho_s$ in the virtual space of Fig.(a) is expanded into a blue coloured non-cylindrical shell $\sigma(\phi) < \rho' < \rho_s$ cascaded with a red coloured dual cylindrical Meta-surface at in the physical space of Fig.(b). Note that the cylindrical region A in the virtual is transformed into A' of the outer surface $\sigma(\phi)$ in the physical space, while the outer region is unity transformed $B' = B$.

such that the region located at $\rho \leq \rho_s$ are compressed into $\rho' \leq \sigma(\phi)$, while the outer region $\rho \geq \rho_s$ is unity transformed into $\rho' \geq \rho_s$. The void region $\sigma(\phi) \leq \rho' \leq \rho_s$ is filled by arbitrary media (we assume it is homogeneous and isotropic for simplicity) and place a dual lumped cylindrical MS located at $\rho' = \rho_s$. Note that both the media and the location (radius) of the Meta-surface are arbitrary. The $Y-$matrix of the resultant MS due to compressing a homogeneous isotropic non cylindrical shell was given in Eq.(4.55). The $Y-$matrix of the dual MS is related to the $Y-$matrix of the $Y - matrix$ of the MS due to compressing the annulus shell as as following:

$$\begin{aligned} \tilde{Y}_{11}^{DMS}[n,\phi] &= -\tilde{Y}_{22}^{shell}[n,\phi] \quad \tilde{Y}_{12}^{DMS}[n,\phi] = -\tilde{Y}_{21}^{shell}[n,\phi] \\ \tilde{Y}_{21}^{DMS}[n,\phi] &= -\tilde{Y}_{12}^{shell}[n,\phi] \quad \tilde{Y}_{22}^{DMS}[n,\phi] = -\tilde{Y}_{11}^{shell}[n,\phi] \end{aligned} \tag{4.61}$$

In what follows we examine the concept of expanding a boundary into a non-

cylindrical shell cascaded by a dual MS by two simulation setups as following:

Simulation Setup (1) In a similar manner to the setup shown in Fig.(4.59). consider the virtual space to be filled by vacuum and considering an incident cylindrical wave of order $n = 0$. It is desired to transform the cylindrical region $\rho < \rho_s$ radially into $\rho' < \sigma(\phi)$ with the boundary located at $\rho = \rho_s$ is expanded into the non cylindrical shell $\sigma(\phi) < \rho' < \rho_s$ with a dual MS located at $\rho' = \rho_s$ in the physical space . The space transformation can be written as following:

$$\rho' = \{ \begin{array}{c} \frac{\sigma(\phi)}{\rho_s}\rho \;\; \rho \leq \rho_s \\ \rho \;\; \rho \geq \rho_s \end{array} \qquad \phi' = \phi \tag{4.62}$$

where $\sigma(\phi) = \left[\left(\frac{cos(\phi)}{a}\right)^2 + \left(\frac{sin(\phi)}{b}\right)^2\right]^{-\frac{1}{2}}$ is the equation of the ellipse, where a and b are the semi-major and semi-minor axes of the ellipse. Simulation results are shown in Fig.s(4.40-4.41). The simulation is done with the following parameters: $\rho_0 = 10\mu m$, $a = 50\mu m$, $b = 30\mu m$ and $\rho_s = 60\mu m$. The wavelength is chosen to be $\lambda = 10\mu m$. It is clear from Fig (4.41) that the electric field distributions of the virtual space at $\rho > \rho_s$ is the same as the the electric field distributions of the physical space $\rho' > \rho_s$ which is consistent with the fact that regions are unity transformed. Fig.(4.41) shows the field distribution in the virtual and physical spaces for the regions $\rho < \rho_s$ and $\rho' < \sigma(\phi)$ respectively, for an incident cylindrical wave of order $n = 0$, which is consistent with the fact that the electric field E_z is a scalar and invariant under space transformation so that $E_z = E'_z$. It is important to note that the MS is in-homogeneous and non-local while the region $\rho' < \sigma(\phi)$ is an-isotropic and in-homogeneous. The combination of both the MS and the region $\rho' < \rho_s$ give the effect that the scattering of an incident cylindrical wave of order n is of the same order.

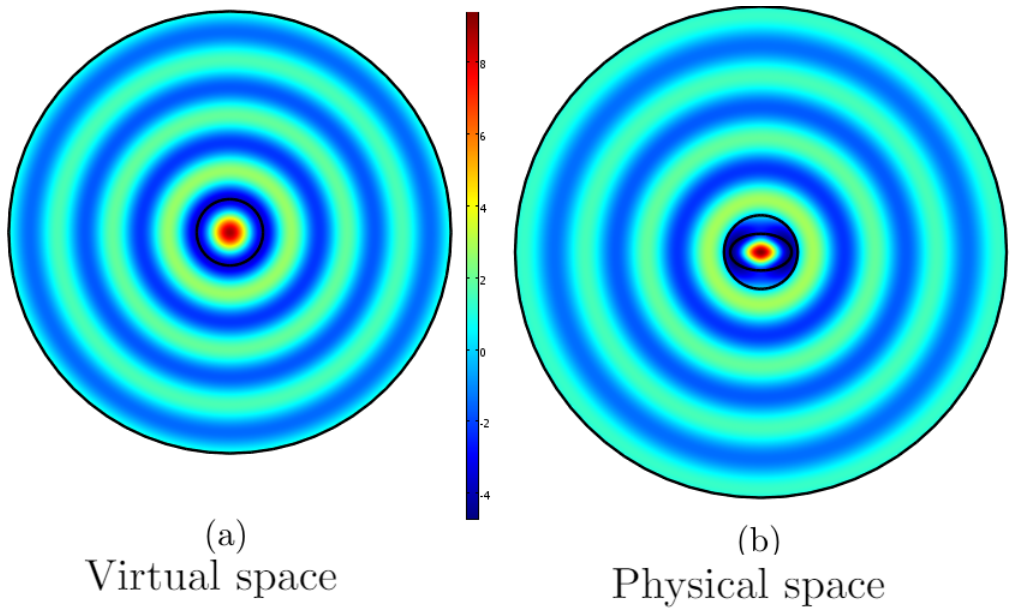

Figure 4.40: Plot of the electric field E_z with $n = 0$. (a) full virtual space, (b) physical space. The electric field at $\rho = \rho' > \rho_s$ is a standing cylindrical wave of order $n = 0$ with the following form $E_z = A_0 J_0(k\rho)e^{i\phi}$ where A_0 is a constant.

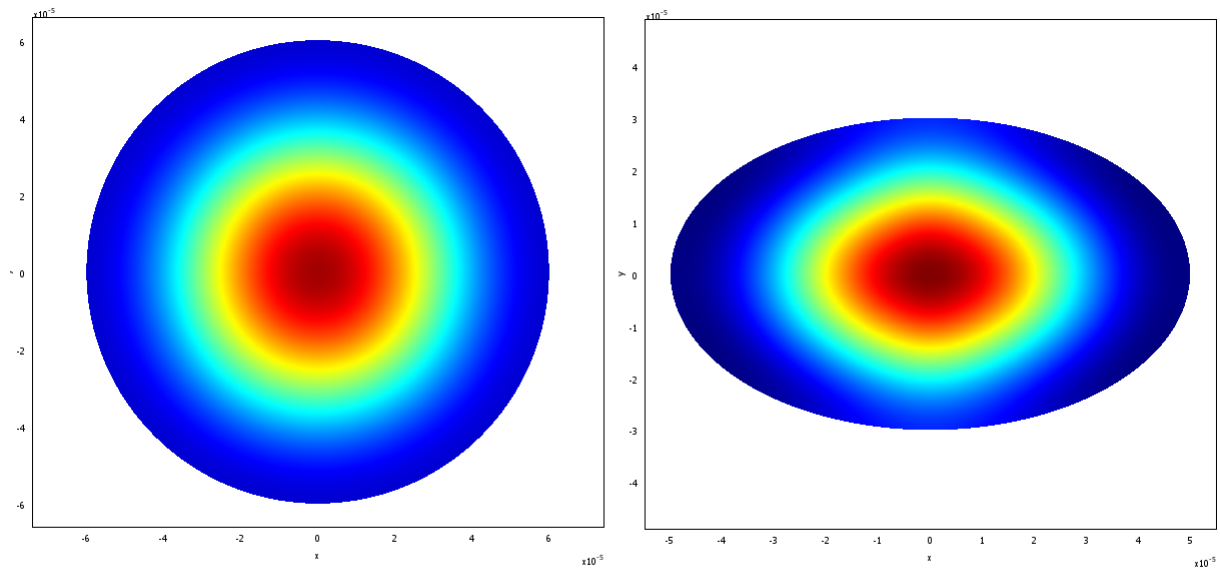

(a) Virtual space (b) Physical space

Figure 4.41: Plot of the electric fields E_z of virtual space for $\rho < \rho_s$ and E'_z of physical space for $\rho' < \sigma(\phi)$ with $n = 0$. (a) virtual space, (b) physical space. It is clear the $E_z(\rho) = E'_z(\rho')$.

Simulation Setup 2 Now we examine the case of expanding a cylindrical boundary into a non-cylindrical ring cascaded by a dual metasurface as shown in Fig.(4.42). We consider the virtual space to be vacuum inside parallel plate waveguide with PMC walls as shown in Fig.(4.42). A plane wave is launched from the top side to be propagating in y direction. A plane wave can be expanded as a superposition of infinite number of cylindrical waves of all orders according to Eq.(4.43). Fig.s(4.43-4.44) compare the performance of a dual MS includes $N = 50$ orders with another dual MS which includes only the zeroth cylindrical order which is the dominant term in the expansion of Eq.(4.43). The simulation results of Fig.s (4.43-4.44) show a comparison between the electric field distribution of the non-local MS including $N = 50$ cylindrical wave orders and a zeroth order local MS with the plane wave's electric field of the virtual space for three different wave length $1mm$ and $\lambda = 100\mu m$ respectively. It

is clear that the dual MS with 50 orders shows a good agreement with the theory. However, we notice that the isolines of the electric field in the physical are not flat as it should be in the virtual space. such discrepancy can be explained as following: due to the in-homogeneity of the MS, different cylindrical orders are coupled to each other and by truncation a residual effect is unavoidable. The local in-homogeneous dual MS shows to be a good approximations for the spatial dispersive dual MS for both cases examined.

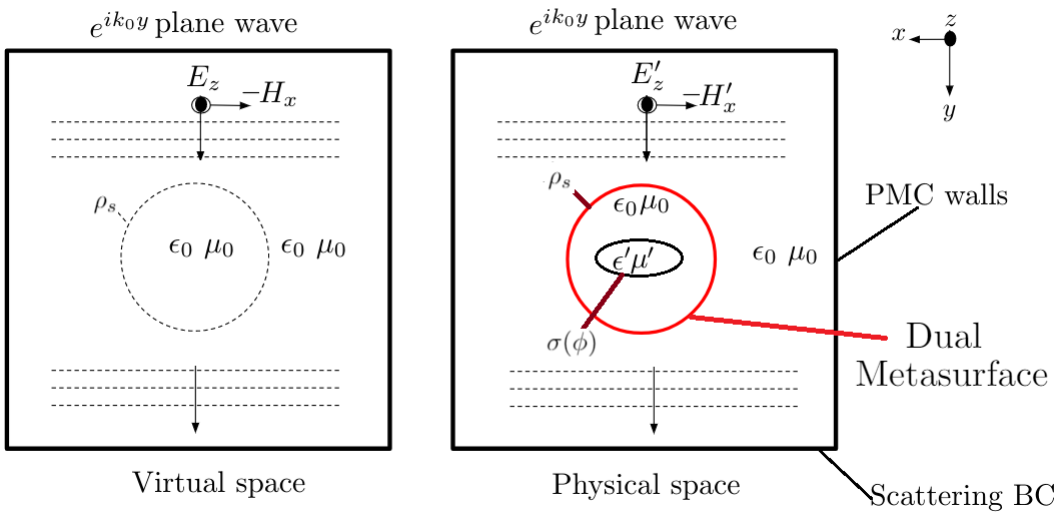

Figure 4.42: Simulation setup (2) : left: Virtual space. Right: Physical space. A plane wave is propagating in y direction in a PMC parallel plate wave guide. The space is transformed according to Eq.(4.60) such that the cylindrical boundary $\rho = \rho_s$in the virtual space is expanded into the non-cylindrical shell $\sigma(\phi) \leq \rho' \leq \rho_s$ cascaded with the dual MS, while the region $\rho \geq \rho_s$ is unity transformed into $\rho' \geq \rho_s$. The dual MS is designed to be both spatial dispersive (non local) and in-homogenous.

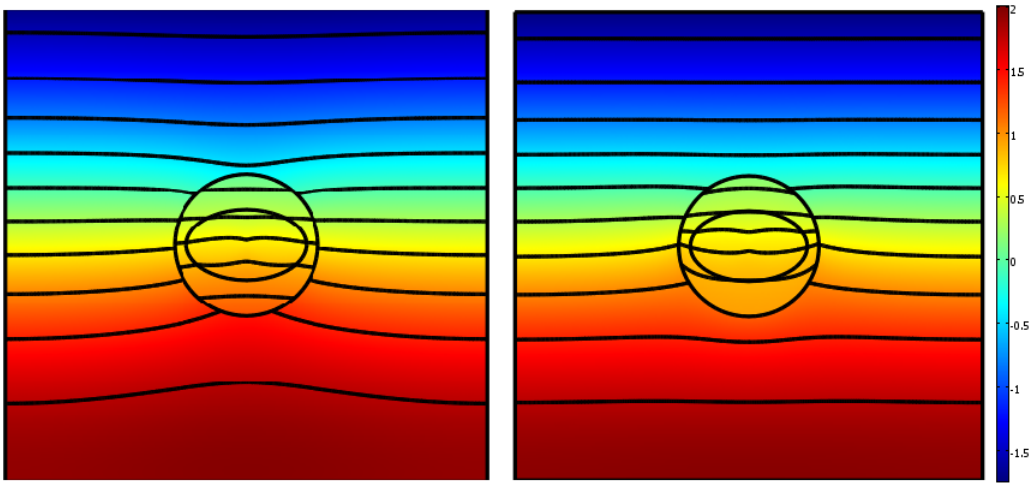

(a)
Physical space with
local Ms

(b)
Physical space with
non-local Ms
$N = 50$

Figure 4.43: Comparison of the performance of the local and spatial dispersive dual Metasurfaces for wave length $1mm$. (a) Local MS. (b) Non local MS.

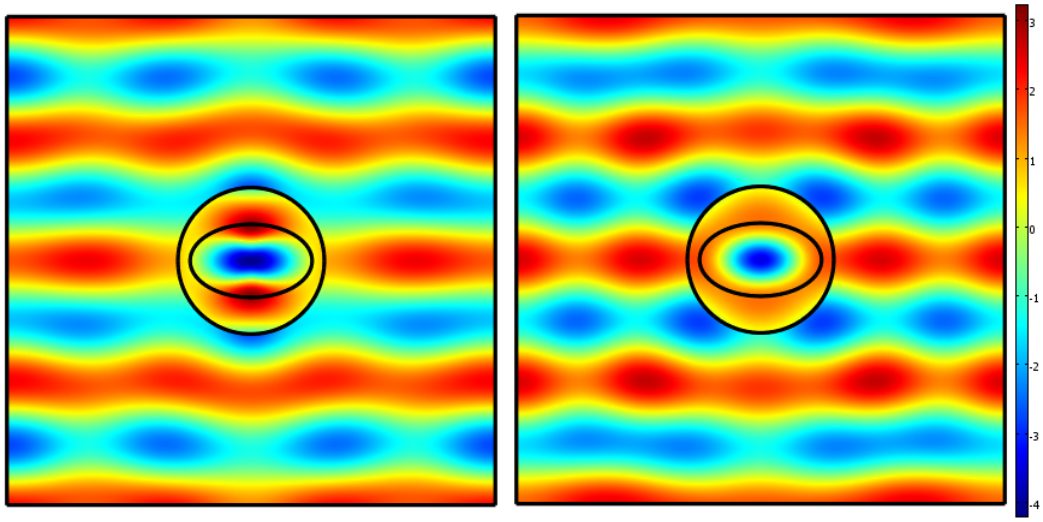

(a)
Physical space with
local Ms

(b)
Physical space with
non-local Ms
$N = 50$

Figure 4.44: Comparison of the performance of the local and spatial dispersive dual Metasurfaces for wave length $100\mu m$. (a) Local MS. (b) Non local MS.

4.4 Conclusion

In this chapter, we proposed a new technique to design mantle cloaks based on discontinuous space transformation for the purposes of electromagnetic cloaking and scattering illusion and camouflage. The main techniques used in cloaking technology are transformation optics (TO) and scattering cancellation technique (SCT). TO is a space transformation technique which is an exact theory, however the resultant cloaks are bulky, highly anisotropic and hard to be fabricated. On the other side, in case of invisibility cloaking, SCT is a field cancellation technique where a mantle cloak is designed such that upon scattering of an incident field, suitable surface currents are induced on the cloak surface, which radiates scattered fields that cause destructive interference with the scattered fields produced by the object to be cloaked. In case of scattering illusion, the mantle cloak will be designed such that the overall scattering cross section of the cloak with the cloaked object is the same as another desired object. In both cases, SCT is typically constrained to optically small circularly and spherically symmetric scatterers. Also, the mantle cloaks calculated based on SCT are typically constrained to be local and homogeneous as only the lowest order spherical or cylindrical waves are assumed to be dominant.

We propose a technique that combines both TO and SCT. The technique is similar to TO as it makes use of the standard procedure of TO, where a discontinuous space transformation is used and it is allowed to be discontinuous and it is similar to SCT as it uses a mantle metasurface to replace the space transformation discontinuity. We proposed two different procedures to design mantle cloaks depending on the shape of the discontinuity. In order to account for the space discontinuity, SCT based procedure is used to calculate for the mantle cloak/ meta-surface. The main idea of such procedure is that a meta-surface is a generalization of the concept of lumped impedance of the circuit theory. With in electrical network theory, a lumped impedance is an electrical component that introduces a jump or a discontinuity of the

voltage or the flowing current or both simultaneously. Similarly, a meta-surface introduces a discontinuity in the electric or the magnetic fields or both simultaneously across the surface. In general, a lumped network is characterize by an impedance $Z-$matrix or equivalently admittance $Y-$ matrix. We showed that a meta-surface can also be characterized by $Z-$ or $Y-$ matrices where we made use of the modal transmission line model (described in appendix A).

The proposed technique combines the advantages of TO and SCT techniques. On one hand, space transformation can be employed while the cloak is a zero-thickness meta-surface. On the other hand, the proposed meta-surfaces depend solely on the shape of the space discontinuity which is much simpler than SCT calculation procedure.

Although we didn't address the physical implementation of the proposed meta-surface, we paved the way for their design by calculating for the required susceptibility tensors. The correspondence between the impedance matrix of a meta-surface and its susceptibility tensors using generalized sheet transition condition (GSTC) was highlighted.

CHAPTER V

Circuit Model for Thermal Radiation from Arbitrary Thermal Emitter at Constant Temperature

5.1 Introduction

Thermal radiation (T.R) is an implicit property of a thermal emitter. T.R has two main measurable quantities, the thermal radiated power and the radiation pattern which is the distribution of the thermally radiated power in space. Both quantities at specific wavelength depend on its absolute temperature, the constitutive material and the outer surface shape of the thermal emitter. Considering two dimensional space, a thermal emitter made of a reciprocal, local and linear media, the thermally radiated power is closely bounded to the losses of the media through Kirchhoff's reciprocity. Due to the locality, the Kirchoff's reciprocity between the losses and the electromagnetic fluctuations is a point-wise and it is independent of the global shape and geometry of the object. On the other hand, the thermally radiated pattern is strongly dependent on the specific shape of the emitter's surface. For instance, if we consider a lossy circularly symmetric cylindrical thermal emitter of media with constitutive parameters that are only radially dependent, such emitter is expected to thermally radiate azimuthally symmetric and the pattern is independent of azimuthal

angle (ϕ). Such circular symmetry can be broken either due to a non cylindrical outer surface profile or due to the dependence of the media's parameters on ϕ.

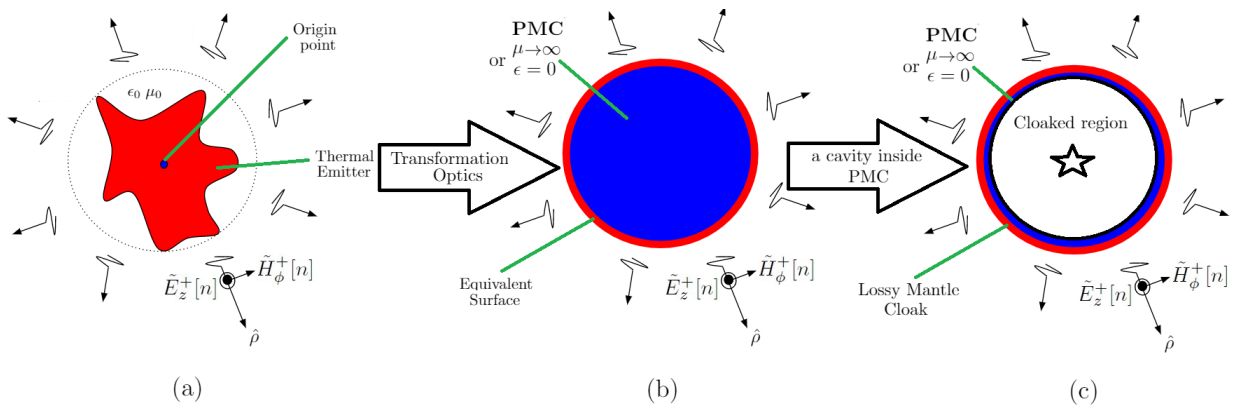

Figure 5.1: Schematic of discontinuous space transformation where a mantle cloak is designed to coat an isolated cloaked region so as to thermally radiate and scatter the electromagnetic field as another target object. (a) Target object. (b) After application of discontinuous TO (chapter(3)). (c) An isolated cloaked region is introduced. A target thermal emitter (red) and surrounding vacuum (white) are compressed into an equivalent surface (red) for E-polarization case. The origin is expanded into a finite cylindrical region occupied with perfect magnetic conductor media. Finally a cavity can be introduced inside the the PMC which can include an arbitrary object to be cloaked.

The main aim of this chapter is to design a mantle meta-surface to cloak an arbitrary object such that their combined scattering and thermal radiation signatures are the same as those of another target object. The working principle is shown in Fig.(5.1) employing the discontinuous space transformation proposed in chapter(3). As shown in Fig.(5.1), an arbitrary shaped thermal emitter can be space transformed such that it is compressed into an equivalent surface or a meta-surface located at the boundary of the compressed area.We constraint the outer boundary to be a cylindrical boundary. In this case where the whole thermal emitter is going to be compressed into a zero thickness meta-surface, the origin point is to be stretched into cylindri-

cal perfect magnetic conductor as shown in Fig.(5.1). The equivalent surface will be backed by a perfect magnetic conductor (perfect electric conductor) in the case of E-(H-) polarization due to the expansion the origin point into a finite area. In general, an arbitrary shaped thermal emitter can be compressed into an equivalent surface or mantle cloak with surface impedance (admittance) which is non-local and in-homogeneous. Accordingly, the equivalent surface will be described in terms of a surface impedance (admittance) which is the equivalent surface impedance (admittance) for the target thermal emitter. Finally a cavity can be introduced inside the volume occupied by the PEC or PMC which can include an arbitrary object o be cloaked. In such case, the equivalent surface is the cloaking mantle cloak.

On other hand, an analytical model to compute for thermal radiation using the circuit model was proposed by Maslovski et al, the model is summarized in appendix(A). The model make use of the notion of transmission line and surface impedance, while introducing the thermal noise through Nyquist's theorem for thermal noise in electrical resistors. Although the model as proposed for arbitrary shaped objects [79], it was only used to compute for thermal radiated power for thermal emitters that have continuous translational, circular and spherical symmetry i.e planar [78], cylindrical and spherical emitters[80]. In order to verify the usage of the mantle cloaks shown in Fig.(5.1) to achieve thermal radiation illusion, we extend the circuit model proposed by Masloviski et al, so as to compute T.R from an arbitrary shaped target thermal emitter or equivalently from a lossy mantle cloak as both has the same surface impedance. The main advantage of the proposed circuit model is it allows to relate thermal pattern to the surface impedance. It will be shown that the dependence of the thermally radiated poynting vector is closely related to the homogeneity of the surface impedance or admittance of the radiating surface.

Also, it known that by using the equivalence theorem [39], the volumetric thermal current sources fluctuating in the bulk volume of a thermal emitter can replaced by other corresponding surface thermal electric or magnetic currents while fluctuate at the outer surface of the thermal emitter. In order to relate the bulk and the surface thermal currents, we first relate the the thermal radiated power to the surface impedance (admittance), then we relate surface impedance (admittance) to the surface susceptibilities through GSTC model [2]. In order to do so, we make use of both formulations for the electromagnetic responses of a surface (discussed in more details in ChapterIV) where:

- **Surface Impedance/Admittance Representation:**

  Given the surface impedance (admittance) of the surface, the losses are given by the real part of such surface impedance (admittance) and the spectral correlations of associated voltage (or current) sources are computed according to Nyquist theorem of electrical noise associated with lossy resistors (conductors).

- **Generalized Sheet transverse Condition (GSTC)or Susceptibility Representation:**

  The electromagnetic response of a surface can be expressed in terms of a combination of electric, magnetic, electromagnetic and magneto-electric susceptibilities where the losses will be given by the imaginary part of such susceptibilities and the spectral correlations of associated thermally fluctuating electric and magnetic surface currents are computed according to fluctuation electrodynamics (FE) theorem. Notice that for an equivalent surface impedance (admittance), there is more than one possible GSTC representation, or in other words, the GSTC representation of an equivalent surface impedance (admittance) is not unique.

Both models are equivalent descriptions for the electromagnetic responses of an equiv-

alent surface or a meta-surface and both provide equivalent descriptions for the thermal surface current fluctuations that causes the thermal radiation. By relating the two models, one can easily make a correspondence between the surface thermal surface currents which correlations are provided by FE and the corresponding circuit voltage and current sources which correlations are provided by Nyquist's theorem.

This chapter is arranged as following: in section (5.2), the properties of the thermally radiating poynting vector radiated from arbitrary shaped thermal emitter is analyzed in terms of cylindrical waves. The role of the cross terms of cylindrical waves of different orders in the calculation of the radiated power is highlighted. In section (5.3), the notion of surface impedance (admittance) is revised, and we focus on the most general case where the surface impedance (admittance) is non-local and in-homogeneous (i.e: space dependent). Also, it will be shown that an arbitrary surface admittance can be quantified as an admittance matrix representing a network coupling different cylindrical orders. Finally, the necessary conditions to be satisfied for an equivalent surface admittance to be Lorentz reciprocal will derived and discussed. In section (5.4), the GSTC description of the equivalent surface is discussed. While in section (5.5), we consider T.R from circularly symmetric thermal emitters whose equivalent surface impedance (admittance) is homogeneous and non-local in space. We use such case to demonstrate the equivalence between both the GSTC and the equivalent surface impedance (admittance) highlighting the equivalence between thermally fluctuating surface magnetic (electric) currents and the circuit thermal noise voltage (current) sources.implemented using COMSOL solver. In section (5.6), we generalize the circuit model of Masloviski to calculate for the TR from an arbitrary shaped thermal emitter whose equivalent surface impedance (admittance) is, in general, in-homogeneous and spatial cylindrical order dispersive, where the in-homogeneity of the equivalent surface is due to the broken circular

symmetry. Finally, in section (5.7) numerical calculation according to the proposed model is compared with the numerical calculations due to thermal discrete dipole approximation (TDDA) previously discussed in appendix D. In appendix C, the circuit model proposed is verified analytically by comparing the analytical expression of the thermal radiated poynting vector with that using Kirchhoff's reciprocity within a Landauer like formalism[7]. In this chapter we consider T.R in 2D space, where the E- and H- polarizations are uncoupled. In what follows, we only consider E-polarization and same conclusions for H-polarization can be drawn by duality. Finally, since the impedance and the admittance are equivalent quantities, we choose to use the admittance as the main quantity of computation in the foregoing analysis, but the same results can be got using the impedance quantities instead.

5.2 TR Pattern for Arbitrary Thermal Emitter

In this section, the properties of the thermally radiating poynting vector radiated from arbitrary shaped thermal emitter is detailed. The starting point is to consider thermally radiated poynting vector from an arbitrary thermal emitter centered at the origin and radiating into vacuum. We consider a 2D thermal emitter that have arbitrary shape and constitutive media but it is constrained to be linear, reciprocal and the emitter is with constant temperature. Assuming the thermal emitter is confined in $\rho \leq \rho_s$ and surrounded by vacuum and since the electromagnetic thermal radiation is radiated away from the thermal emitter, for E-polarization, the electric fields (voltage waves) and magnetic fields (current waves) can be written in terms of orthogonal cylindrical waves basis as following :

$$V(\rho_s,\phi)=\sum_n \tilde{V}[n]e^{in\phi}=\sqrt{\rho_s}E_z=\sum_n \tilde{V}^+[n]H_n^{(2)}(k_0\rho_s)e^{in\phi}$$
$$I(\rho_s,\phi)=\sum_n \tilde{I}[n]e^{in\phi}=-\sqrt{\rho_s}H_\phi=\sum_n j\frac{1}{\eta}\tilde{V}^+[n]\dot{H}_n^{(2)}(k\rho_s)e^{in\phi}$$

$Where:$

$$\tilde{V}[n]=\tilde{V}^+[n]H_n^{(2)}(k\rho_s)=\frac{1}{2\pi}\int_0^{2\pi}V(\rho_s,\phi)e^{-in\phi}d\phi \tag{5.1}$$
$$\tilde{I}[n]=-j\frac{1}{\eta}\tilde{V}^+[n]H_n^{(2)}(k\rho_s)=\frac{1}{2\pi}\int_0^{2\pi}I(\rho_s,\phi)e^{-in\phi}d\phi$$
$$\tilde{I}[n]=\tilde{Y}_n^+\tilde{V}[n]\quad \tilde{Y}_n^+=j\frac{\dot{H}_n^{(2)}(k\rho_s)}{\eta H_n^{(2)}(k\rho_s)}$$

here we utilize the same notations as in chapter IV where $V(\rho_s,\phi)=\sqrt{\rho_s}E_z(\rho_s,\phi)$ and $I(\rho_s,\phi)=-\sqrt{\rho_s}H_\phi(\rho_s,\phi)$. Note that $-$ is to indicate propagation in $+\rho$ direction and the current $I=-\sqrt{\rho}H_\phi$ is defined to be flowing in $+\rho$ direction. $\tilde{Y}_n^+$ is the wave admittance for an outgoing cylindrical wave of order n. A single tilde indicates a 1-D Fourier transform with respect to ϕ . The ensemble and time averaged thermally radiated complex power per unit angle ϕ (or complex poynting vector times the ρ) for such radiated field **at** $\rho=\rho_s$ is calculated as following:

$$\begin{aligned}\langle\mathbb{P}(\phi)\rangle_\omega &= 4\times\frac{1}{2}\langle V(\rho_s,\phi)I^*(\rho_s,\phi)\rangle_\omega = 4\times\frac{1}{2}\sum_n\sum_m\left\langle\tilde{V}[n]\tilde{I}^*[m]\right\rangle_\omega e^{j(n-m)\phi}\\ &= 4\times\frac{-j}{2\eta}\sum_n\sum_m\left(\left\langle\tilde{V}^+[n]\tilde{V}^{+*}[n]\right\rangle_\omega[m]H_n^{(2)}(k\rho_s)\dot{H}_m^{(2)*}(k\rho_s)\right)e^{j(n-m)\phi}\\ &= \sum_n\sum_m\left\langle\tilde{\mathbb{P}}_{nm}\right\rangle_\omega e^{j(n-m)\phi}\\ with\ \ \tilde{\mathbb{P}}_{nm} &= \frac{1}{2}\tilde{V}[n]\tilde{I}^*[m]\in\mathbb{C}\end{aligned} \tag{5.2}$$

where $\langle\rangle_\omega$ represents an ensemble average and the factor 4 is introduced because we only consider positive harmonic frequency components. It is important to recognize that the thermal radiated $\left\langle \tilde{\mathbb{P}}_{nm} \right\rangle_\omega$ is a complex quantity, however when $n = m$ then $\tilde{\mathbb{P}}_{nn} \in \mathbb{R}$.

The only physical measurable quantity is the radiative thermal radiated poynting vector which is the real part of $< \mathbb{P} >_\omega$. It is clear from Eq.(5.2) that the radiated power is the sum of the total power carried by every cylindrical wave and the cross interference between different cylindrical orders. It is also important to recognize that the cross terms don't contribute to the total power radiated which is only the sum of the power carried of each order solely due to orthogonality between modes as shown as following:

$$\langle \mathbb{P}_{total} \rangle_\omega = \int_0^{2\pi} \langle \mathbb{P}(\phi) \rangle_\omega \, d\phi = \int_0^{2\pi} \sum_n \sum_m \left\langle \tilde{\mathbb{P}}_{nm} \right\rangle_\omega e^{j(n-m)\phi} d\phi = 2\pi \sum_n \left\langle \tilde{\mathbb{P}}_{nn} \right\rangle_\omega \tag{5.3}$$

On the other side the cross terms are responsible to shape the radiation pattern of the radiation. This is clear since the components $\tilde{\mathbb{P}}_{nm}$ are closely related to the qth harmonic of the thermally radiated pattern $\langle \mathbb{P}(\phi) \rangle_\omega$ where $q = n - m$. while for a general emitter (azimuthally asymmetric), the time averaged complex emitted power per unit angle is written as following:

$$\langle \mathbb{P}(\phi) \rangle_\omega = \sum_q \left\langle \tilde{\mathbb{P}}_q \right\rangle_\omega e^{iq\phi} = \sum_n \sum_{m=n-q} \left\langle \tilde{\mathbb{P}}_{nm} \right\rangle_\omega e^{i(n-m)\phi} \tag{5.4}$$

then the qth component $\tilde{\mathbb{P}}_q$ is computed as following:

$$\begin{aligned}\left\langle \tilde{\mathbb{P}}_q \right\rangle_\omega &= \frac{1}{2\pi}\int_0^{2\pi} \langle \mathbb{P}(\phi)\rangle_\omega \, e^{-iq\phi} d\phi = \frac{1}{2\pi}\int_0^{2\pi} \sum_n \sum_m \langle \mathbb{P}_{nm}\rangle_\omega \, e^{j(n-m)} e^{-iq\phi} d\phi \\ &= \sum_n \sum_{m=n-q} \langle \mathbb{P}_{nm}\rangle_\omega \qquad q = n-m\end{aligned} \tag{5.5}$$

As mentioned previously, the thermal radiation from azimuthally symmetric thermal emitters is independent of ϕ, for such objects, the time averaged emitted power per unit angle is written as following

$$\langle \mathbb{P}\rangle_\omega = \sum_n \left\langle \tilde{\mathbb{P}}_{nn} \right\rangle_\omega \quad \text{where} \quad \left\langle \tilde{\mathbb{P}}_{nm} \right\rangle_\omega = 0 \text{ for } n \neq m \tag{5.6}$$

At distances $\rho > \rho_s$, the thermally emitted complex power per unit angle will be computed as following

$$\langle \mathbb{P}(\rho,\phi)\rangle_\omega = \sum_n \sum_m \left\langle \tilde{\mathbb{P}}_{nm} \right\rangle_\omega \frac{H_n^{(2)}(k\rho)\dot{H}_m^{(2)*}(k\rho)}{H_n^{(2)}(k\rho_s)\dot{H}_m^{(2)*}(k\rho_s)} e^{j(n-m)\phi} \tag{5.7}$$

note that the measurable physical quantity be is the radiated power per unit angle which is the real part of the former quantities.

5.3 Equivalent Surface Admittance

In this section, we first review qualitatively the notion of surface admittance, then quantitatively, we consider that notion to include the surface admittance of an equivalent surface of arbitrary shaped scatterer or thermal emitter, where a surface admittance is in-homogeneous and non-local in space. Also, we show that an arbitrary surface admittance can be represented as a network that couples different cylindrical

orders and such network is quantified by an admittance matrix. Finally, we show the necessary conditions to be satisfied for an equivalent surface admittance to be Lorentz reciprocal.

5.3.1 Surface impedance/admittance: Quick Review

In the electrical network theory, ohm's law is defined as a linear relation between the voltage across an impedance (admittance) and the current flowing through it and the value of impedance (admittance) is the constant of proportionality. The same concept can generalized for higher dimensions, for example, a boundary or a surface in 2D or 3D spaces. Indeed the surface impedance (admittance) of a boundary linearly relates the tangential components of the electric and magnetic fields at the surface in a similar manner.

The simplest and most common configuration is Fresnel reflection of plane waves from planar surfaces. It is known that, for a plane wave, the tangential component of the momentum vector of the photons or the parallel component of propagation wave vector is conserved under Fresnel reflection due to the continuous translational symmetry of the planar surface where the height of the surface profile is constant. For instance, as shown in Fig.(5.2.a), consider a planar slab aligned along x-axis, when illuminated by a plane wave with k_{x0} tangential component of propagation wave vector, the reflected field propagates with the same tangential k_{x0}. Fresnel reflection is typically modelled as a mismatch problem or as a jump in the value of the wave admittance of the propagating plane wave as shown in Fig.(5.2.a). The surface admittance of the slab at the entrance plane can be written as $\tilde{Y}_s(k_x)$. The surface admittance $\tilde{Y}_s(k_x)$ as a function of k_x is spatial frequency frequency dispersive as it value changes for different incident angles. Note that k_x is also called spatial frequency as it is the conjugate variable to the space coordinate x. On the other

hand, if the translational symmetry is broken and the profile's height varies in space, an incident plane wave is diffracted into multiple plane waves. For instance, consider Fig.(5.2.b), a plane wave with k_{x0} tangential component of propagation wave vector, is diffracted into N plane waves with different spatial frequencies ($k_{x,-1}$, k_{x1} and k_{x2}) where $N = 3$ in such example. At some reference level plane, The surface admittance of such slab can be calculated and it is represented as a network of $N-$ports, where each port is defined by a unique value of the tangential wave number k_x as shown in Fig.(5.2.b).

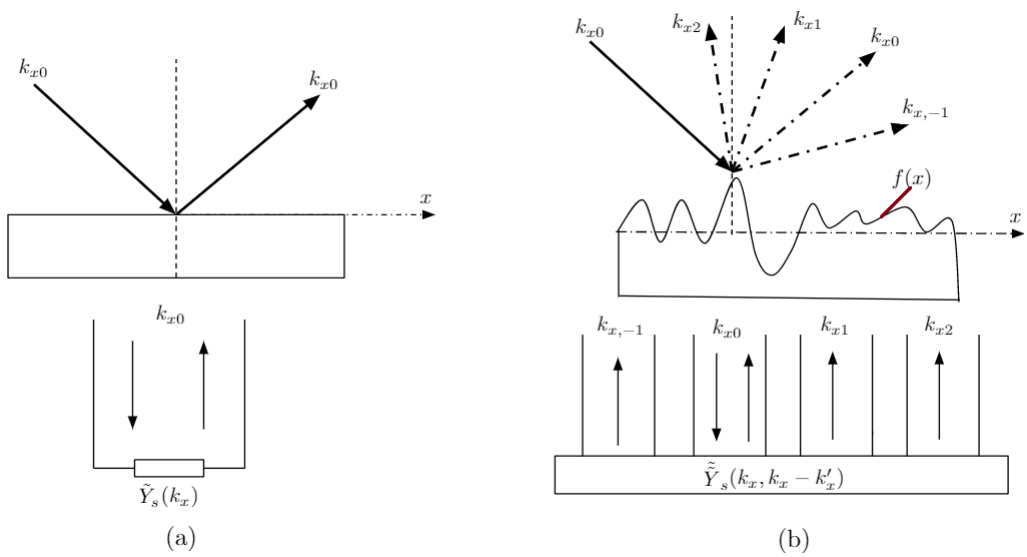

Figure 5.2: Illustration of the effect of translation symmetry upon the surface impedance representation of semi-infinite scatterer. (a) Tangential wave number k_x is conserved under Fresnel's reflection from planar slab and the reflection from such planar surface can be modelled as reflection of an incident plane wave from a surface impedance which is homogeneous but spatial frequency dispersive. (b) The scattering of an incident plane wave by a non-planar profile can be modelled as the reflection by a $N-$ port network quantified by the surface admittance which will be spatial frequency dispersive and in-homogeneous.

The same concept can be extended to 2D bounded scatterers with the space described by cylindrical coordinates. Consider a circular symmetric scatterer, so that its properties are independent of the azimuthal angle ϕ. Now, if we consider an incident cylindrical wave of order n, due to the circular symmetry, the scattered field will also

be a cylindrical wave of the same order n as shown in Fig.(5.3.a). In other words, cylindrical order n is conserved due to the circular symmetry. In such case the scattering process can be modelled as a reflection or a mismatch problem between the in-going cylindrical wave impedance (admittance) and the equivalent surface impedance (admittance) of the scatterer. The equivalent surface impedance (admittance) of such scatterer will have the form $\tilde{Y}_s[n]$, and its value depends solely on the order of the incident cylindrical wave. On the other side, if the circular symmetry is broken, the scattered field due to an incident cylindrical wave of order n, will be a linear combination of multiple cylindrical waves of different cylindrical orders as shown in Fig.(5.3.b). In such case, the surface admittance, calculated at some reference cylindrical boundary, will be a network of $N-$ports, where each port is defined by a unique value of the cylindrical order n. The equivalent surface impedance (admittance) of such scatterer will have the form $\tilde{\tilde{Y}}_s[n, n-m]$, where m is another cylindrical order. The notion of $\tilde{\tilde{Y}}_s[n, n-m]$ will be discussed quantitatively in section(5.3.2).

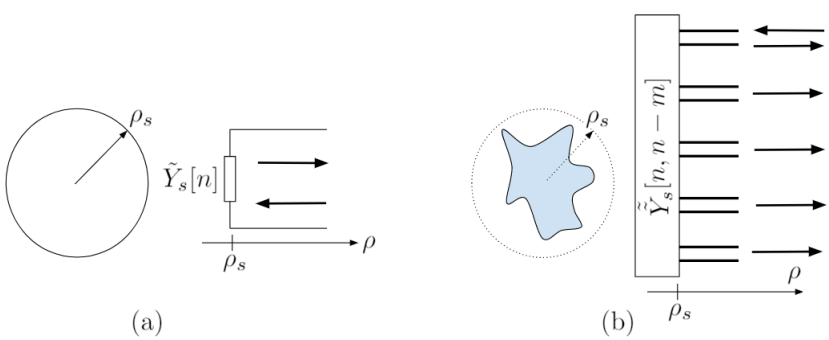

Figure 5.3: Illustration of the effect of circular symmetry upon the surface impedance representation of a bounded scatterer. (a) cylindrical order n is conserved when an incident cylindrical wave is scattered by a circular symmetric scatterer and the scatterer is represented by a surface impedance which is homogeneous but spatial frequency dispersive $\tilde{Y}_s[n]$. (b) The scattering of an incident cylindrical wave by a non-circular shaped profile can be modelled as the reflection from a $N-$ port network quantified by the surface admittance which will be spatial frequency dispersive and in-homogeneous $\tilde{\tilde{Y}}_s[n, n-m]$. Note that the quantities $\tilde{Y}_s[n]$ and $\tilde{\tilde{Y}}_s[n, n-m]$ are defined in section(5.3.2).

5.3.2 Equivalent surface admittance for arbitrary shaped emitter

An equivalent surface impedance (admittance) defined at the surface of an arbitrary scatterer or a thermal emitter includes all the necessary information to compute both its electromagnetic scattering or its thermal emission properties. Now, assume that the equivalent surface admittance (or equivalently the surface impedance) is known for a thermal emitter enclosed in $\rho < \rho_s$. Assuming E-polarization, a general linear in-homogeneous and non-local surface admittance relates the tangential electric E_z and magnetic H_ϕ field components through a generalized form of Ohm's law as following:

$$\begin{aligned} E_z(\rho_s, \phi) &= \frac{1}{2\pi} \int_0^{2\pi} Z_s(\phi, \phi') H_\phi(\rho_s, \phi') d\phi' \\ H_\phi(\rho_s, \phi) &= \frac{1}{2\pi} \int_0^{2\pi} Y_s(\phi, \phi') E_z(\rho_s, \phi') d\phi' \end{aligned} \tag{5.8}$$

The two relations are equivalent, however we choose the surface admittance relation. Then, a similar relation relates the radial voltage and currents as following:

$$I(\rho_s, \phi) = \frac{1}{2\pi} \int_0^{2\pi} Y_s(\phi, \phi') V(\rho_s, \phi') d\phi' \tag{5.9}$$

where the subscript s is to indicate surface. The factor $\frac{1}{2\pi}$ is included so that the quantity $\frac{d\phi}{2\pi}$ becomes unit-less. **Note that the current I is defined to be flowing into the surface admittance along $-\rho$ direction**. The former generalizations of Ohm's law were proposed by L. Zadeh [127] and [126] with in the context the circuit theory of the time varying electrical networks, here we replaced time by the azimuthal angle ϕ. The surface admittance $Y_s(\phi, \phi')$ is in-homogeneous as its value changes along ϕ' and non local in space as the voltage field (electric field) at location ϕ' induces current (magnetic field) at location ϕ. Note that both the fields and the admittance

Y_s are periodic with respect to ϕ with period 2π, so the Fourier transform with respect to ϕ of both the fields and the admittance is expected to be discrete. The discrete variable which is the conjugate variable for ϕ, is identical to that of the cylindrical order n. This relation suggests that using Fourier transformation with respect to ϕ allows investigating the coupling between different cylindrical orders. Also, in order to use the circuit analysis tools when dealing with the surface admittance quantity, one has to decompose the field at the surface into the cylindrical wave orthogonal basis. For a cylindrical boundary, the set of functions $e^{in\phi}$ is an orthogonal basis on the support $\phi \in [0, 2\pi]$ where $n \in \mathbb{Z}$. This decomposition of the fields in terms of the set $e^{in\phi}$ is done by a 1D Fourier transform with respect to ϕ defined as following:

$$\tilde{I}[\rho_s, n] = \frac{1}{2\pi} \int_0^{2\pi} I(\rho_s, \phi) e^{-in\phi} d\phi \tag{5.10}$$

while the inverse Fourier transform is defined as following:

$$I(\rho_s, \phi) = \sum_n \tilde{I}[\rho_s, n] e^{+in\phi} \tag{5.11}$$

Now we use the 1D Fourier transform to examine Ohm's law of Eq.(5.9) as following:

$$\begin{aligned}
\frac{1}{2\pi} \int_0^{2\pi} I(\rho_s, \phi) e^{-in\phi} d\phi &= \frac{1}{(2\pi)^2} \iint_0^{2\pi} Y_s(\phi, \phi') V(\rho_s, \phi') e^{-in\phi} d\phi' d\phi \\
&= \frac{1}{2\pi} \int_0^{2\pi} \tilde{Y}_s(n, \phi') V(\rho_s, \phi') d\phi'
\end{aligned}$$

Since $V(\rho_s, \phi) = \sum_m \tilde{V}[\rho_s, m] e^{im\phi}$ then

$$\begin{aligned}
\tilde{I}[n] &= \sum_m \tilde{V}[\rho_s, m] \frac{1}{2\pi} \int_0^{2\pi} \tilde{Y}_s(n, \phi') e^{i(m)\phi'} d\phi' \\
&= \sum_m \tilde{\tilde{Y}}_s[n, -m] \tilde{V}[\rho_s, m]
\end{aligned}$$

Note that the $\frac{1}{2\pi}\int_0^{2\pi}\left[\tilde{Y}_s(n,\phi')V(\rho_s,\phi')\right]e^{-in\phi'}d\phi'$ term is the 1-D Fourier transform of $\tilde{Y}_s(\phi',n)V(\rho_s,\phi')$ which is a multiplication term in the ϕ' space, so this term will be transformed into a convolution term in the discrete Fourier space as following:

$$\tilde{I}[n] = \sum_{m\in\mathbb{Z}} \tilde{\tilde{Y}}_s[n,-m]\tilde{V}[m] \quad \textit{Convolution in n space} \tag{5.12}$$

The dependence of $\tilde{I}$ and $\tilde{V}$ upon ρ_s is dropped as it understood implicitly from the context. The single and double tilde signs indicate single (1-D) and double (2-D) Fourier transformed quantities respectively. $\tilde{\tilde{Y}}_s$ is the two dimensional Fourier transform of its space correspondence Y_s as following:

$$\begin{aligned} \tilde{\tilde{Y}}_s[n,-m] &= \frac{1}{(2\pi)^2}\iint_0^{2\pi} Y_s(\phi,\phi')e^{-in\phi}e^{im\phi'}\,d\phi\,d\phi' \\ Y_s(\phi,\phi') &= \sum_n\sum_m \tilde{\tilde{Y}}_s[n,-m]e^{jn\phi}e^{-jm\phi'} \end{aligned} \tag{5.13}$$

$\tilde{\tilde{Y}}_s[n,-m]$ is the $(n,m)^{th}$ component of the 2-D Fourier transform of the non-local and space dependent surface impedance $Y_s(\phi,\phi')$. This quantity $\tilde{\tilde{Y}}_s[n,-m]$ is in general complex and can be decomposed into real and imaginary parts as following:

$$\tilde{\tilde{Y}}_s[n,-m] = \tilde{\tilde{G}}_s[n,-m] + j\tilde{\tilde{B}}_s[n,-m] \tag{5.14}$$

where the real part $\tilde{\tilde{G}}_s$ is the conductive component and the imaginary part $\tilde{\tilde{B}}_s[n,m]$ is the susceptance component.

Notional and Nomenclature remark The quantity surface impedance $Y_s(\phi,\phi')$ is a multi-variable function and can be expressed in different Fourier spaces, where we can treat the variables ϕ and $\phi'-\phi$ as two independent variables and apply Fourier

transform upon them independently. In order to avoid confusion, it is important to clarify the notation and the nomenclature of the surface admittance with respect to its non-locality, spatial cylindrical order dispersion, homogeneity and in-homogeneity. By applying a 1D-Fourier transform with respect to ϕ' or ϕ variable upon the multi-variable function $Y_s(\phi, \phi')$, one gets another function $\tilde{Y}_s$, while by applying a 2D-Fourier transform with respect to ϕ' and ϕ variables upon Y_s, one gets another function $\tilde{\tilde{Y}}_s$. Accordingly a surface admittance Y_s is both in-homogeneous and non-local in space ϕ if:

1. $Y_s = Y_s(\phi, \phi')$.
2. $\tilde{Y}_s = \tilde{Y}_s(\phi, -m) \quad \text{or} \quad \tilde{Y}_s = \tilde{Y}_s(n, \phi')$.
3. $\tilde{\tilde{Y}}_s = \tilde{\tilde{Y}}_s[n, -m]$.

While a surface admittance Y_s is both homogeneous and non-local (spatial cylindrical order dispersive) in space ϕ if

1. $Y_s = Y_s(\phi' - \phi)$.
2. $\tilde{Y}_s = \tilde{Y}_s[n]$.
3. $\tilde{\tilde{Y}}_s = \tilde{Y}_s[n]\delta[n - m]$, where δ is Kronecker delta function.

Also a surface admittance Y_s is both in-homogeneous and local in space ϕ if

1. $Y_s = Y_s(\phi)\delta(\phi - \phi')$.
2. $\tilde{Y}_s = \frac{1}{2\pi} Y_s(\phi)$.
3. $\tilde{\tilde{Y}}_s = \frac{1}{2\pi} \tilde{Y}_s[n - m]$, Note that the in-homogeneity in space ϕ is non-locality in the frequency $n-$ space.

Finally, a surface admittance Y_s is both homogeneous and local in space ϕ if

1. $Y_s = C\delta(\phi - \phi')$, where C is a constant and δ is Dirac's delta function.

2. $\tilde{Y}_s = \frac{1}{2\pi}C$.

3. $\tilde{\tilde{Y}}_s = \frac{1}{2\pi}C\delta[n-m]$, where δ is Kronecker delta function.

5.3.3 Admittance matrix representation

The electromagnetic scattering by a general in-homogeneous and non-local surface admittance can be seen from Eq.(5.12) where different cylindrical orders are coupled to each other. Actually the generalized convolution in Eq.(5.12) can be written as a matrix multiplication form. By defining a rectangular admittance matrix such that

$$\underline{\underline{\tilde{\tilde{Y}}}}_s = \left[\tilde{\tilde{Y}}_s[n,-m]\right] = \left[\tilde{\tilde{Y}}_s\right]_{n\times m} \tag{5.15}$$

Also, Defining the collection of the cylindrical harmonics of the voltage and current such that $\underline{\tilde{V}} = \left[\tilde{V}[m]\right] = [\tilde{V}_m]$ and $\underline{\tilde{I}} = \left[\tilde{I}[n]\right] = [\tilde{I}_n]$ are column vectors of the same length. Then Eq.(5.12) is written in matrix multiplication form as following:

$$\underline{\tilde{I}} = \underline{\underline{\tilde{\tilde{Y}}}}_s \, \underline{\tilde{V}} \tag{5.16}$$

Note the change in notation such that the indices n and m are placed as subscripts which is a customary convention of linear algebra. Eventually, Eq.(5.12) can be rewritten as following:

$$\tilde{I}_n = \sum_m \tilde{\tilde{Y}}_{s,nm}\tilde{V}_m \tag{5.17}$$

5.3.4 Reciprocal surfaces

In general, meta-surfaces or equivalent surfaces do not have to be Lorentz reciprocal [39]. However, if the surface is an equivalent surface of a reciprocal media, the equivalent surface must be Lorentz reciprocal as well. A generic Lorentz reciprocal

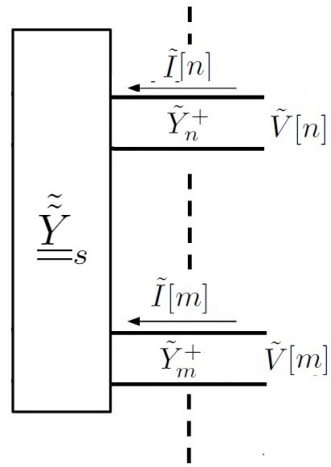

Figure 5.4: The 2D Fourier transform of the surface admittance is represented as an admittance matrix such that at each port of order n..

in-homogeneous and non-local surface admittance $Y_s(\phi, \phi')$ should be invariant under swap of variables ϕ and ϕ' , then

$$Y_s(\phi', \phi) = Y_s(\phi, \phi') \tag{5.18}$$

using Eq.(5.13), the implication of such property in the frequency domain can be seen as following:

$$\tilde{\tilde{Y}}_s[m, -n] = \tilde{\tilde{Y}}_s[n, -m] \tag{5.19}$$

This means that the coupling between different ports (different cylindrical orders) of the network $\tilde{\tilde{Y}}_s$ is Lorentz reciprocal. The former equation can be rewritten in admittance matrix form as following:

$$\tilde{\tilde{Y}}_s = \tilde{\tilde{Y}}_s^{\tau} \tag{5.20}$$

where τ is matrix transpose operator.

In what follows we show a proof of this Lorentz reciprocity property at Eq.(5.18)

based on Lorentz reciprocity theorem [39]. Lorentz's reciprocity is the equality of the reaction of the fields produced by different current sources upon each others. Consider electric current densities $\{J_a, J_b\}$ and magnetic current densities $\{K_a, K_b\}$ located at different points a and b. The sources J_a and K_a radiate an electric field E_a and magnetic field H_a, similarly the sources J_b and K_b radiate an electric field E_b and magnetic field H_b. The reaction of the fields E_a and H_a on the sources at point b is defined as following:

$$< a, b >= \int_{\mathbb{R}^2} \left(E_a(\bar{r})J_b(\bar{r}) - H_a(\bar{r})K_b(\bar{r})\right) d^2\bar{r} \tag{5.21}$$

similarly the reaction of the fields E_b and H_b on the sources at point a is defined as following:

$$< b, a >= \int_{\mathbb{R}^2} \left(E_b(\bar{r})J_a(\bar{r}) - H_b(\bar{r})K_a(\bar{r})\right) d^2\bar{r} \tag{5.22}$$

It was shown in [39] that a reciprocal media is the media where both reactions equates as following

$$< a, b >=< b, a > \tag{5.23}$$

Now, since the Lorentz reciprocity of a surface is under question, we calculate the reactions between different magnetic current point sources reside at the points located on the surface itself. Consider a cylindrical MS located at $\rho = \rho_s$, as shown in Fig.(5.5), and then consider two separate configurations described as following:

1. Case(A): A point magnetic current source is located on the MS at point a with azimuthal angle ϕ_a. Then, the magnetic current source can be written as following:

$$K_a(\rho_s, \phi) = K_s(\phi_a)\delta(\phi - \phi_a) \tag{5.24}$$

The generated magnetic field $H_a(\rho_s, \phi)$ at the MS is related to the surface "point" magnetic current source $K_a(\rho, \phi)$ by the surface admittance in Eq.(5.8) as following:

$$\begin{aligned} H_a(\rho_s, \phi) &= \frac{1}{2\pi} \int_0^{2\pi} Y_s(\phi, \phi') K_a(\rho_s, \phi') d\phi' \\ &= \frac{1}{2\pi} \int_0^{2\pi} Y_s(\phi, \phi') K_s(\phi_a) \delta(\phi' - \phi_a) d\phi' \\ &= \frac{1}{2\pi} Y_s(\phi, \phi_a) K_s(\phi_a) \end{aligned} \tag{5.25}$$

where we have made use of the equivalence theorem [39] where the tangential component of the electric field at surface equates a surface magnetic current as following

$$\hat{z} E_z = \hat{\rho} \times \hat{\phi} K_s \tag{5.26}$$

where $\hat{z}$, $\hat{\rho}$ and $\hat{\phi}$ are the cylindrical coordinates unit vectors. Note that the magnetic current K_s is flowing azimuthally along the surface.

2. Case(B): A point current source is located on the MS at point b with azimuthal angle ϕ_b, then the magnetic current source can be written as following:

$$K_b(\rho_s, \phi) = K_s(\phi_b) \delta(\phi - \phi_b) \tag{5.27}$$

The generated magnetic field $H_b(\rho_s, \phi)$ at the MS is related to the surface "point" magnetic current source $K_b(\rho, \phi)$ by the surface admittance in Eq.(5.8) as following:

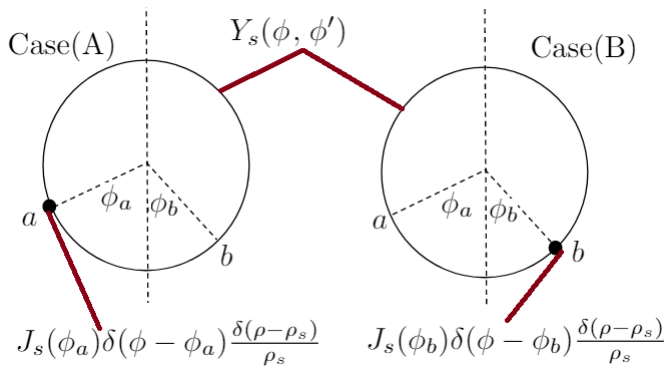

Figure 5.5: Schematic for the proof of Eq.(5.18). Two reciprocal situations are considered. Case(A): a point current sources is located on the surface at point a with polar coordinates (ρ_s, ϕ_a). Case(B): a point current sources is located on the surface at point b with polar coordinates (ρ_s, ϕ_b). For both cases, The reactions $< a, b >$ and $< b, a >$ are calculated. If the surface is Lorentz reciprocal then the reaction is reciprocal or $< a, b >=< b, a >$.

$$\begin{aligned} H_b(\rho_s, \phi) &= \frac{1}{2\pi} \int_0^{2\pi} Y_s(\phi, \phi') K_b(\rho_s, \phi') d\phi' \\ &= \frac{1}{2\pi} \int_0^{2\pi} Y_s(\phi, \phi') K_s(\phi_b) \delta(\phi' - \phi_b) d\phi' \\ &= \frac{1}{2\pi} Y_s(\phi, \phi_b) K_s(\phi_b) \end{aligned} \tag{5.28}$$

Then reaction $< a, b >$ of the field E_a due to the magnetic current source K_a located at a on the current source K_b located at point b will be:

$$\begin{aligned} < a, b > &= -\int_\phi H_a(\rho_s, \phi) K_b(\phi) d\phi \\ &= -\frac{1}{2\pi} \int_\phi Y_s(\phi, \phi_a) K_s(\phi_a) K_s(\phi_b) \delta(\phi - \phi_b) d\phi \\ &= -\frac{1}{2\pi} Y_s(\phi_a, \phi_b) K_s(\phi_a) K_s(\phi_b) \end{aligned} \tag{5.29}$$

Similarly, the reaction $< b, a >$ of the field H_b due to the current source K_b located at b on the current source K_a located at point b will be:

$$< b, a > = -\frac{1}{2\pi} Y_s(\phi_b, \phi_a) K_s(\phi_b) K_s(\phi_a) \tag{5.30}$$

If the surface is Lorentz reciprocal, then the two reactions equate $< b, a >=< a, b >$, then

$$Y_s(\phi_a, \phi_b - \phi_a) = Y_s(\phi_b, \phi_a - \phi_b) \tag{5.31}$$

by replacing ϕ_a and ϕ_b with ϕ and ϕ', one retrieves Eq.(5.18).

5.4 GSTC description of an Equivalent Surface

In this section, using the GSTC description, we relate the electric and magnetic susceptibilities of an equivalent surface to the surface impedance and admittance of the same surface. GSTC is a way to characterize the susceptibility tensors of a surface that introduce a jump or discontinuity for either the tangential components of electric $\bar{E}_z$ and/or magnetic H_ϕ fields. Such field discontinuities are the z-directed surface electric polarizability P_z and angular directed surface magnetic polarizability M_ϕ. The dependence of the field discontinuities on the surface polarizabilities can be described by the so called (**GSTC** condition) as following:

Considering a cylindrical shaped surface and considering the E-polarization case then

$$\begin{aligned} \Delta H_\phi(\phi) &= j\omega \bar{P}_z(\phi) \\ \Delta E_z(\phi) &= j\omega M_\phi(\phi) \end{aligned} \tag{5.32}$$

where Δ is the difference operator for the jump of the fields value across the surface. The surface's polarizabilities are assumed to be linearly related to the fields on both sides of the surface as following:

$$
\begin{aligned}
P_z(\phi) &= \frac{1}{2\pi}\int_0^{2\pi} \epsilon_0\, \chi_{ee}^{zz}(\phi,\phi')\bar{E}_{z,av}(\phi')\phi' \\
M_\phi(\phi) &= \frac{1}{2\pi}\int_0^{2\pi} \mu_0\, \chi_{mm}^{\phi\phi}(\phi,\phi')\bar{H}_{\phi,av}(\phi')d\phi' \\
\text{where: } E_{z,av}(\phi) &= \frac{1}{2}\left(E(\rho_s^-,\phi)+E(\rho_s^+,\phi)\right) \\
H_{\phi,av}(\phi) &= \frac{1}{2}\left(H(\rho_s^-,\phi)+H(\rho_s^+,\phi)\right)
\end{aligned}
\tag{5.33}
$$

where $\rho_s^{\pm} = lim_{\rho\to\rho_s^{\pm}}\ \rho$ and the subscript av indicates averaging of the field values on both sides of the surface. In the current case, the surface under consideration is an equivalent surface of a thermal emitter or a scatterer and it is backed by a PMC (for the E-polarization case) as depicted in Fig.(5.1). Due to the PMC, the electromagnetic field vanishes at $\rho < \rho_s$ so $E_{z,1}(\rho_s^-,\phi) = H_{\phi,1}(\rho_s^-,\phi) = 0$, then

$$
\begin{aligned}
E_{z,av}(\phi) &= \Delta E_z(\phi) = E_z(\rho_s^+,\phi) \\
H_{\phi,av}(\phi) &= \Delta H_\phi(\phi) = H_\phi(\rho_s^+,\phi)
\end{aligned}
\tag{5.34}
$$

Then the GSTC condition of Eq.s(5.32-5.33) is re-written as following:

$$
\begin{aligned}
H_\phi(\rho_s^+,\phi) = j\omega P_z(\phi) &= \frac{1}{2\pi}\int_0^{2\pi} j\omega\epsilon_0\, \chi_{ee}^{zz}(\phi,\phi')E_z(\rho_s^+,\phi')\phi' \\
E_z(\phi) = j\omega M_\phi(\phi) &= \frac{1}{2\pi}\int_0^{2\pi} j\omega\mu_0\, \chi_{mm}^{\phi\phi}(\phi,\phi')H_\phi(\rho_s^+,\phi')d\phi'
\end{aligned}
\tag{5.35}
$$

Now comparing the former equation with Eq.(5.8), we find that

$$Z_s(\phi,\phi') = j\omega\mu_0\chi_{mm}^{\phi\phi}(\phi,\phi') \qquad Y_s(\phi,\phi') = j\omega\epsilon_0\chi_{ee}^{zz}(\phi,\phi') \tag{5.36}$$

The same relation between the surface susceptibilities, impedance and admittance is valid in the Fourier space. Such relation is found by applying 2D-Fourier transform as defined in Eq.(5.13) as following:

$$\tilde{\tilde{Z}}_s[n,m] = j\omega\mu_0\tilde{\tilde{\chi}}_{mm}^{\phi\phi}[n,m] \qquad \tilde{\tilde{Y}}_s[n,m] = j\omega\epsilon_0\tilde{\tilde{\chi}}_{ee}^{zz}[n,m] \tag{5.37}$$

5.5 TR from Circularly Symmetric Object

In this section, we study the T.R from a circularly symmetric thermal emitter by considering its homogeneous and non-local equivalent surface admittance. We show the equivalence between the surface impedance (admittance) and the GSTC descriptions highlighting the correspondence between thermal circuit sources and thermal surface currents. The thermal radiation from circularly symmetric object is first considered since it is the special case of the proposed model discussed in section(5.6) which already exists in the literature [80] and it can be used as a benchmark to test the validity of the proposed model for the more general cases. At the end of this section, numerical calculation is done where a comparison is held between results of numerical calculation of T.R from a circular symmetric object using three different techniques: Thermal discrete dipole approximation(TDDA), the circuit model proposed by Masloviski and the surface thermal surface electric and magnetic currents based on the equivalence discussed in this section.

5.5.1 Equivalence between surface admittance and GSTC descriptions:

Consider a cylindrical symmetric thermal emitter, with a cylindrical shape with radius $\rho = \rho_s$ and only radial dependent media's permittivity and permeability. As long as we are concerned with its electromagnetic scattering and T.R properties, such object can be replaced by an equivalent homogeneous cylindrical surface impedance, located at $\rho = \rho_s$. The equivalent surface must be also non-local as its surface impedance (admittance) has different value for each nth order cylindrical wave, then the surface impedance (admittance) will be written as following:

$$\begin{aligned} Y_s(\phi, \phi') = Y_s(\phi - \phi') \qquad & Z_s(\phi, \phi') = Z_s(\phi - \phi') \\ \tilde{\tilde{Y}}_s[n-m, n] = \tilde{Y}_s[n]\delta_{nm} \qquad & \tilde{\tilde{Z}}_s[n, m] = \tilde{Z}_s[n]\delta_{nm} \end{aligned} \tag{5.38}$$

where $\tilde{\tilde{Y}}_s[n, m]$ and $\tilde{\tilde{Z}}_s[n, m]$ are 2-D Fourier transform according to Eq.(5.13). Since we consider T.R from cylindrical emitters utilizing polar coordinates then in order to make use of the circuit model of Masloviski, the metric of space has to be included in the definition of the voltage and current waves. The voltage and current waves are defined in terms of the tangential electric E_z and magnetic H_ϕ fields as following:

$$\begin{aligned} V(\phi) = \sqrt{\rho_s} E_z(\phi) \qquad & I(\phi) = \sqrt{\rho_s} H_\phi(\phi) \\ \tilde{V}[n] = \sqrt{\rho_s} \tilde{E}_z[n] \quad & \tilde{I}[n] = \sqrt{\rho_s} \tilde{H}_\phi[n] \end{aligned} \tag{5.39}$$

Note that for each cylindrical order n, an equivalent surface impedance (admittance) relates linearly the voltage $\tilde{V}[n]$ or equivalently the tangential electric field $\tilde{E}_z$ to the current $\tilde{I}$ or equivalently the tangential magnetic field $\tilde{H}_\phi$ as following:

$$\begin{aligned} \tilde{V}[n] &= \tilde{Z}_s[n]\tilde{I}[n] \\ \text{or equivalently } \tilde{I}[n] &= \tilde{Y}_s[n]\tilde{V}[n] \\ \text{where } \tilde{Z}_s[n] &= \frac{1}{\tilde{Y}_s[n]} \end{aligned} \tag{5.40}$$

The spatial frequency dispersion of such equivalent surface becomes more evident when considering the inverse Fourier transform of the former relation as following:

$$
\begin{aligned}
I(\phi) &= \frac{1}{2\pi}\int_{0}^{2\pi} Y_s(\phi-\phi')V(\phi')d\phi' \\
V(\phi) &= \frac{1}{2\pi}\int_{0}^{2\pi} Z_s(\phi-\phi')I(\phi')d\phi'
\end{aligned}
\tag{5.41}
$$

Since the thermal emitter is lossy, then its equivalent surface is also lossy and in such case, the equivalent surface impedance (admittance) are complex quantities Z_s and $Y_s \in \mathbb{C}$. The real part $\mathrm{Re}\{Z_s\}$ ($\mathrm{Re}\{Y_s\}$) represent a resistive (conductive) part of the surface impedance (admittance). Consequently, according to Nyquist's theorem of electrical noise, at thermal equilibrium, such resistive (conductive) part is associated with thermal voltage (current) fluctuations represented by a noisy voltage (current) source whose spectral auto-correlation is written as following:

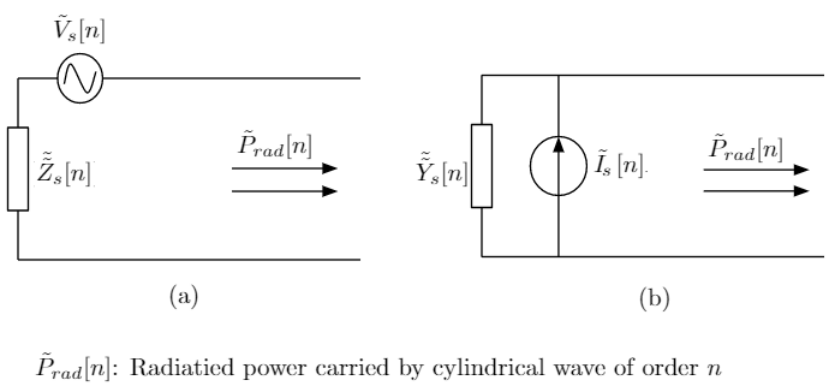

Figure 5.6: Two equivalent circuit models for thermally radiated n^{th} order cylindrical wave from lossy homogeneous equivalent surface, (a) Thevinin representation (b) Norton representation. The thermal noise sources are represented as voltage (current) sources connected in series (parallel) to the losses represented as series impedance (parallel admittance) at Thevenin (Norton) equivalent circuits respectively.

$$\left\langle \tilde{V}_s[n]\tilde{V}_s^*[m]\right\rangle_\omega = \frac{4}{\pi}\Theta(\omega,T)\,\mathrm{Re}\{\tilde{\tilde{Z}}_s[n]\}\delta_{nm}$$
$$\left\langle \tilde{I}_s[n]\tilde{I}_s^*[m]\right\rangle_\omega = \frac{4}{\pi}\Theta(\omega,T)\,\mathrm{Re}\{\tilde{\tilde{Y}}_s[n]\}\delta_{nm} \tag{5.42}$$

where $\Theta(\omega, T)$ is the mean energy of a single quantum oscillator with angular frequency ω, ignoring vacuum fluctuations, δ indicates Dirac functions and $<>_\omega$ is the ensemble average and $*$ is the conjugation operators. The Thevenin or Norton equivalent representations for Nyquist thermal sources as shown in Fig.(5.6). In Thevenin representation, the thermal source is represented by a voltage $\tilde{V}_s$ source series connected to surface impedance, while in Norton representation the thermal source is represented by a current source $\tilde{I}_s$ parallel connected to the surface admittance as shown in Fig(5.6). Finally, the thermally radiated poynting vector carried by the cylindrical wave of order n to the surrounded media can be simply calculated by representing the surrounding as loads connected on the free terminals of the circuit model shown in Fig. (5.6).

Thermal Radiation due to Surface Currents utilizing GSTC Model: The electromagnetic response of a surface can be quantified in terms of elements of the susceptibility tensor. Losses associated with a surface are quantified by the imaginary part of the susceptibility tensor. Fluctuation electrodynamics relates the fluctuations of the thermal electric and magnetic currents to the losses embedded in the surface through Kirchhoff's reciprocity. For simplicity assume that the magneto-electric and electro-magnetic susceptibilities of the surface vanish, so thermal surface electric and magnetic currents are uncoupled. Using the second form of Fluctuation electrodynamics, the spectral auto and cross-correlations between the thermally fluctuating electric and magnetic surface currents for a general non-local, in-homogeneous equivalent surface at constant temperature T (the same temperature at all over the

equivalent surface) will have the following form:

$$\begin{aligned}\langle J_s^z(\rho_s,\phi)J_s^{z*}(\rho_s,\phi')\rangle_\omega &= 4\frac{\omega\epsilon_0}{\pi}\Theta(\omega,T)\frac{1}{\rho_s}Im\{\chi_{ee}^{zz}(\phi-\phi')\}\\ \left\langle K_s^\phi(\rho_s,\phi)K_s^{\phi*}(\rho_s,\phi')\right\rangle_\omega &= 4\frac{\omega\mu_0}{\pi}\Theta(\omega,T)\frac{1}{\rho_s}Im\{\chi_{mm}^{\phi\phi}(\phi-\phi')\}\end{aligned} \tag{5.43}$$

where χ_{ee}^{zz} and $\chi_{mm}^{\phi\phi} \in \mathbb{C}$ are the electric, magnetic susceptibility tensors manipulating the tangential electric E_z and magnetic H_ϕ. J_s^z is the thermal surface electric current flowing in out of plane z direction and K_s^ϕ is the thermal surface magnetic current flowing in azimuthal ϕ direction. We use Fourier transform with respect to ϕ to re-express the former correlations as correlations in the Fourier space or in other words, to calculate for the spectral cross correlations of the harmonic thermal currents that produce cylindrical waves of different orders. The Fourier transform and inverse Fourier transform of the current densities with respect to ϕ and ϕ' are defined as following:

$$\begin{aligned} J_s^z(\rho_s,\phi) &= \sum_n \tilde{J}_s^z[n]e^{in\phi} & \tilde{J}_s^z[n] &= \frac{1}{2\pi}\int_0^{2\pi} J_s^z(\rho_s,\phi)e^{-in\phi}\\ J_s^{z*}(\rho_s,\phi') &= \sum_n \tilde{J}_s^{z*}[m]e^{-im\phi'} & \tilde{J}_s^{z*}[m] &= \frac{1}{2\pi}\int_0^{2\pi} J_s^z(\rho_s,\phi')e^{im\phi'}\end{aligned} \tag{5.44}$$

by substituting Eq.(5.44) in Eq.(5.43), the spectral cross correlations between

different cylindrical orders is written as following:

$$\begin{aligned}\left\langle \tilde{J}_s^z[n]\tilde{J}_s^{z*}[m]\right\rangle_\omega &= \frac{1}{(2\pi)^2}\iint_0^{2\pi} \left\langle J_s^z(\rho_s,\phi)J_s^{z*}(\rho_s,\phi')\right\rangle_\omega e^{-i(n\phi-m\phi')}d\phi d\phi' \\ &= \frac{1}{(2\pi)^2}4\frac{\omega\epsilon_0}{\pi}\Theta(\omega,T)\frac{1}{\rho_s}\iint_0^{2\pi} Im\{\chi_{ee}^{zz}(\phi-\phi')\}e^{-i(n\phi-m\phi')}d\phi d\phi'\end{aligned} \tag{5.45}$$

but since $Im\{\chi_{ee}^{zz}(\phi-\phi')\} = \frac{1}{2j}\left[\chi_{ee}^{zz}(\phi-\phi') - \chi_{ee}^{zz*}(\phi-\phi')\right]$ and since $\chi_{ee}^{zz}(\phi-\phi') = \chi_{ee}^{zz}(\phi'-\phi)$, then

$$\begin{aligned}\left\langle \tilde{J}_s^z[n]\tilde{J}_s^{z*}[m]\right\rangle_\omega &= \frac{1}{(2\pi)^2}4\frac{\omega\epsilon_0}{\pi}\Theta(\omega,T)\frac{1}{2j}\left[\tilde{\chi}_{ee}^{zz}[n] - \tilde{\chi}_{ee}^{zz*}[n]\right]\frac{1}{\rho_s}\int_0^{2\pi} e^{-i(n-m)\phi}d\phi' \\ &= \frac{1}{2\pi}4\frac{\omega\epsilon_0}{\pi}\Theta(\omega,T)Im\{\tilde{\chi}_{ee}^{zz}[n]\}\frac{1}{\rho_s}2\pi\delta_{nm} \\ &= 4\frac{\omega\epsilon_0}{\pi}\Theta(\omega,T)Im\{\tilde{\chi}_{ee}^{zz}[n]\}\frac{\delta_{nm}}{\rho_s}\end{aligned} \tag{5.46}$$

Then the spectral cross correlations of the electric and magnetic are written as following:

$$\begin{aligned}\left\langle \tilde{J}_s^z[n]\tilde{J}_s^{z*}[m]\right\rangle_\omega &= 4\frac{\omega\epsilon_0}{\pi}\Theta(\omega,T)Im\{\tilde{\chi}_{ee}^{zz}[n]\}\frac{\delta_{nm}}{\rho_s} \\ \left\langle \tilde{K}_s^\phi[n]\tilde{K}_s^{\phi*}[m]\right\rangle_\omega &= 4\frac{\omega\mu_0}{\pi}\Theta(\omega,T)Im\{\tilde{\chi}_{mm}^{\phi\phi}[n]\}\frac{\delta_{nm}}{\rho_s}\end{aligned} \tag{5.47}$$

where n and m are cylindrical orders.

Relation between Thermal Surface currents and Circuit model sources: In general, the relation between the thermal electric and magnetic surface currents of a lossy homogeneous surface and the corresponding thermal voltage and current sources are not unique. However, it is closely related to the relation between the surface's susceptibilities (derived using GSTC) and the corresponding surface impedance

(admittance)which was found in Eq.s (5.36-5.37) such that

$$\tilde{\tilde{Z}}_s[n,m] = j\omega\mu_0\tilde{\tilde{\chi}}^{\phi\phi}_{mm}[n,m] \qquad \tilde{\tilde{Y}}_s[n,m] = j\omega\epsilon_0\tilde{\tilde{\chi}}^{zz}_{ee}[n,m$$

The spectral correlation of the thermal fluctuating surface electric and magnetic current in Eq.(5.46) is closely related to the corresponding correlation of the voltage and current sources of Eq.(5.42). Note that, during calculation, one utilizes either surface admittance or impedance representation, similarly, because of Eq.(5.36), one can use either electric susceptibility χ^{zz}_{ee} or magnetic susceptibility $\chi^{\phi\phi}_{mm}$ description representation. Now we show the correspondence between the thermal surface currents and their circuit counterparts based on Eq.(5.36) as following:

Series Impedance: Considering the Thevenin representation, then since $\tilde{\tilde{Z}}_s = j\omega\mu_0\tilde{\tilde{\chi}}^{\phi\phi}_{mm}$ then $\mathrm{Re}\{\tilde{\tilde{Z}}_s\} = \omega\mu_0 Im\{\tilde{\tilde{\chi}}^{\phi\phi}_{mm}\}$, then from Eq.s (5.42) and (5.46), we get that

$$\left\langle \tilde{K}^{\phi}_s[n]\tilde{K}^{\phi *}_s[m]\right\rangle_\omega = \frac{1}{\rho_s}\left\langle \tilde{V}_s[n]\tilde{V}^*_s[m])\right\rangle_\omega \tag{5.48}$$

since only time averaged power is the physically observable quantity, then it is acceptable to write

$$\tilde{V}_s[n] = \sqrt{\rho_s}\tilde{K}^{\phi}_s[n] \tag{5.49}$$

so for a surface with a series impedance, for a cylinder wave with order (n), the series connected Nyquist voltage source is equivalent to the thermal fluctuating surface magnetic current source.

Parallel Admittance: Considering the Norton representation, Since $\tilde{\tilde{Y}}_s = j\omega\epsilon_0\tilde{\chi}^{zz}_{ee}$ then $\mathrm{Re}\{\tilde{\tilde{Y}}_s\} = \omega\epsilon_0 Im\{\tilde{\tilde{\chi}}^{zz}_{ee}\}$ then from Eq.s (5.42) and (5.46), we find that:

$$\left\langle \tilde{J}^{z}_s[n]\tilde{J}^{z*}_s[m]\right\rangle_\omega = \frac{1}{\rho_s}\left\langle \tilde{I}_s[n]\tilde{I}^*_s[m]\right\rangle_\omega \tag{5.50}$$

since only time averaged power is the physically observable quantity, then it is acceptable to write

$$\tilde{I}_s[n] = \sqrt{\rho_s}\tilde{J}_s^z[n] \tag{5.51}$$

So for as parallel admittance MS, for a cylinder wave with order (n), the parallel connected Nyquist current source is equivalent to the thermal fluctuating surface electric current source.

5.5.2 Numerical example

Assuming $e^{i\omega t}$ time harmonic dependence, we consider thermal radiation, at $9\mu m$ wavelength, from cylindrical symmetric nonmagnetic dielectric object at temperature $T = 50C$, with cylindrical boundary of radius $\rho_s = 50\mu m$, and relative permittivity $\epsilon_{zz} = 3 - i0.02$. According to Fluctuation Electrodynamics, the thermal radiation is originated by thermal electric current density $J^z(\bar{r})$ fluctuating in the bulk volume of the thermal emitter with spectral correlation is given by:

$$\langle J^z(\bar{r})J^{z*}(\bar{r'})\rangle_\omega = 4\frac{\omega\epsilon_0}{\pi}\Theta(\omega,T)Im\{\epsilon_{zz}(\bar{r})\}\delta(\bar{r}-\bar{r}') \tag{5.52}$$

where $\bar{r}$ and $\bar{r}'$ are position vectors of two different locations in the thermal emitter. In order to calculate for the thermally radiated poynting vector, we utilize **Thermal Discrete Dipole Approximation (TDDA)** technique. In such technique, the thermal emitter is meshed and the thermal electric current density is discretized and thermal radiated Poynting vector is calculated according to the procedure depicted appendix D and as shown in Fig.(5.7).

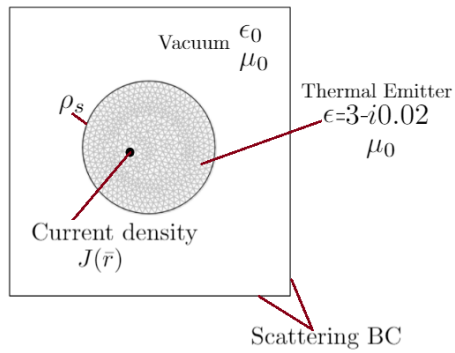

Figure 5.7: Thermal discrete dipole approximation (TDDA) simulation setup: the thermal emitter is meshed and the thermal electric current density is discretized and thermal radiated Poynting vector is calculated according to the procedure used in appendix D. Note that for the E polarization, since permeability is real, and the permittivity is complex, only a thermal electric current exist.

In order to validate the equivalence between the circuit model and GSTC proposed previously in this section, first we compare the calculated thermal radiation from TDDA with that calculated by the circuit model. To do that we consider two ways of calculation, semi analytical and fully analytical calculations. The semi-analytical approach is to replace the electrical current density of Eq.(5.52) with an equivalent surface current $J_s^z(\rho_s, \phi)$ flowing on the surface. The spectral cross correlation of such surface thermal electric current is depicted as following:

$$\langle J_s^z(\rho_s, \phi) J_s^{z*}(\rho_s, \phi') \rangle_\omega = 4\frac{\omega\epsilon_0}{\pi}\Theta(\omega, T)\frac{1}{\rho_s} Im\{\chi_{ee}^{zz}(\phi - \phi')\} \tag{5.53}$$

where $\chi_{ee}^{zz}(\phi - \phi')$ is the electric susceptibility of the equivalent surface. The setup of such calculation is shown in Fig.(5.8). The radiated electric and magnetic fields are related to the surface current as following:

$$\begin{aligned} E_z(\underline{r}) &= \sum_n G_{zz}^{EE}(\underline{r}, n)\tilde{J}_s^z[n]e^{in\phi} \\ H_\phi(\underline{r}) &= \sum_m G_{\phi z}^{HE}(\underline{r}, m)\tilde{J}_s^z[m]e^{im\phi} \end{aligned} \tag{5.54}$$

where G_{zz}^{EE} and $G_{\phi z}^{HE}$ are the Green functions of the electric and magnetic field due to the z-polarized surface electric current. Accordingly the poynting vector is calculated as following:

$$\left\langle \underline{S}^E \right\rangle = -2\hat{\rho} Re\{\left\langle E_z \, H_\phi^* \right\rangle\} = \hat{\rho} \left\langle \underline{S}_r^E \right\rangle \tag{5.55}$$

where by substituting Eq.(5.46), we find that

$$\begin{aligned}
\left\langle E_z \, H_\phi^* \right\rangle &= \sum_n \sum_m G_{zz}^{EE}(\underline{r}, n) \left\langle \tilde{J}_s^z[n] \tilde{J}_s^{z*}[m] \right\rangle_\omega G_{\phi z}^{HE*}(\underline{r}, m) e^{i(n-m)\phi} \\
&= \frac{4}{\pi} \theta(\omega, T) \frac{1}{\rho_s} \sum_n \sum_m \omega \epsilon_0 Im\{\tilde{\chi}_{ee}^{zz}[n]\} \delta_{nm} G_{zz}^{EE}(\underline{r}, n) G_{\phi z}^{HE*}(\underline{r}, m) e^{i(n-m)\phi} \\
&= \frac{4}{\pi} \theta(\omega, T) \frac{1}{\rho_s} \sum_n \omega \epsilon_0 Im\{\tilde{\chi}_{ee}^{zz}[n]\} G_{zz}^{EE}(\underline{r}, n) G_{\phi z}^{HE*}(\underline{r}, n) e^{i(n-m)\phi}
\end{aligned} \tag{5.56}$$

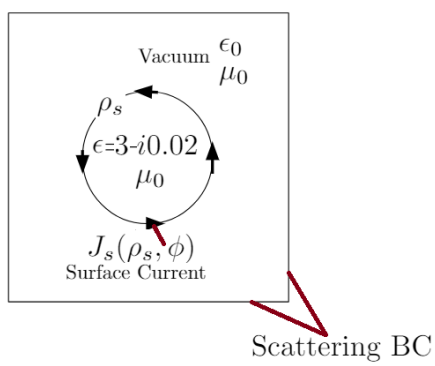

Figure 5.8: Equivalent thermal surface current (semi-analytical) simulation setup. The thermal electric current density is replaced by an equivalent surface thermal electric current flowing on the surface of the thermal emitter. Note that only the permittivity is complex, then only thermal electric surface current exist.

On the other hand, the circuit model based calculation is depicted in Fig.(5.9). Since the thermal emitter is circularly symmetric, cylindrical waves with different orders are uncoupled such that each cylindrical order n has its own equivalent circuit. For each order, the thermal source is represented by electric current source $\tilde{I}_s[n]$

which is related to $\tilde{Y}_s[n]$ according to Nyquist theorem of electrical noise. The thermal radiated poynting vector for each cylindrical wave n is calculated as following: The circuit model of Maslovisky is shown in Fig.(5.9). For each cylindrical order n, the current source $\tilde{I}_s[n]$ is connected in parallel with both the admittance of the equivalent surface $\tilde{Y}_s[n]$ and the input admittance of the surrounding vacuum $\tilde{Y}^+[n]$. The radiated power can be calculated by finding the voltage and current flowing outwards through the admittance $\tilde{Y}^+[n]$. Using basic circuit analysis of the circuit as shown in Fig.(5.9) we find:

$$\begin{aligned} \tilde{V}^+[n] &= \frac{\tilde{I}_s[n]}{\tilde{Y}_s[n] + \tilde{Y}^+[n]} \\ \tilde{I}^+[n] &= \tilde{Y}^+[n]\tilde{V}^+[n] = \tilde{Y}^+[n]\frac{\tilde{I}_s[n]}{\tilde{Y}_s[n] + \tilde{Y}^+[n]} \end{aligned} \tag{5.57}$$

then the the total radiating time and ensemble averaged poynting vector radiated at this cylindrical order and computed at $\rho = \rho_s$ will be

$$\begin{aligned} \mathrm{Re}\{< \mathbb{P}_{nn} >_\omega\} &= 4 \times \frac{1}{2} < \tilde{V}^+[n]\tilde{I}^{+*}[n] > \\ &= 4 \times \frac{1}{2}\,\mathrm{Re}\left\{\tilde{Y}^+[n]\frac{< \tilde{I}_s^+[n]\tilde{I}_s^{+*}[n] >}{|\tilde{Y}_s[n] + \tilde{Y}^+[n]|^2}\right\} \\ &= 4 \times \frac{1}{2} \times \frac{4\theta(\omega, T)}{\pi}\frac{\mathrm{Re}\left\{\tilde{Y}_s[n]\right\}\mathrm{Re}\left\{\tilde{Y}^+[n]\right\}}{|\tilde{Y}[n] + \tilde{Y}^+[n]|^2} \end{aligned} \tag{5.58}$$

Then by summing the power radiated over all cylindrical order, we retrieve total radiated poynting vector.

Numerical results The radial thermal radiated poynting vector calculated from the three ways is shown in Fig.(5.10). Although the plots show a close agreement, the TDDA calculated poynting vector needs to be scaled with 0.7 to match the same value as the other poynting vectors.

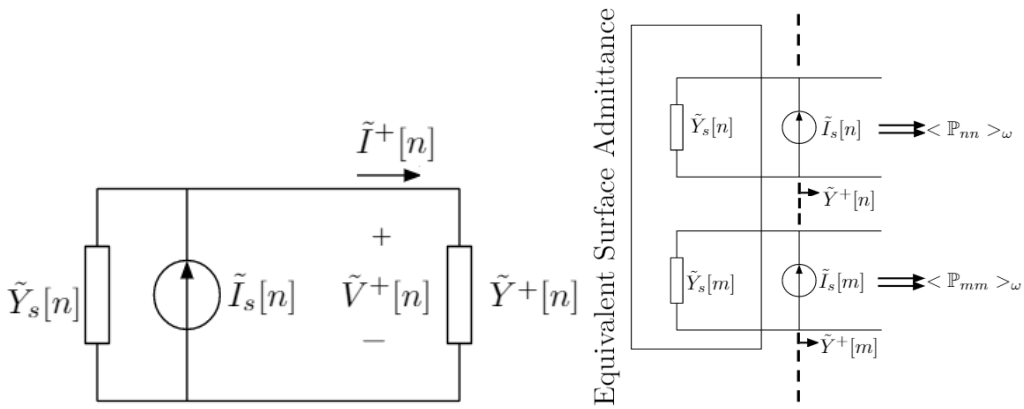

Figure 5.9: Left: schematic of the circuit model of the thermal radiation for cylindrical order n. The radiated Power per unit angle is calculated from the circuit as following: $\mathrm{Re}\{< \mathbb{P}_{nn} >_\omega\} = 4 \times \frac{1}{2} < \tilde{V}^+[n]\tilde{I}^{+*}[n] >$. Right: circuit model simulation setup with the equivalent surface admittance of the thermal emitter is used to calculate the thermal radiated poynting vector.

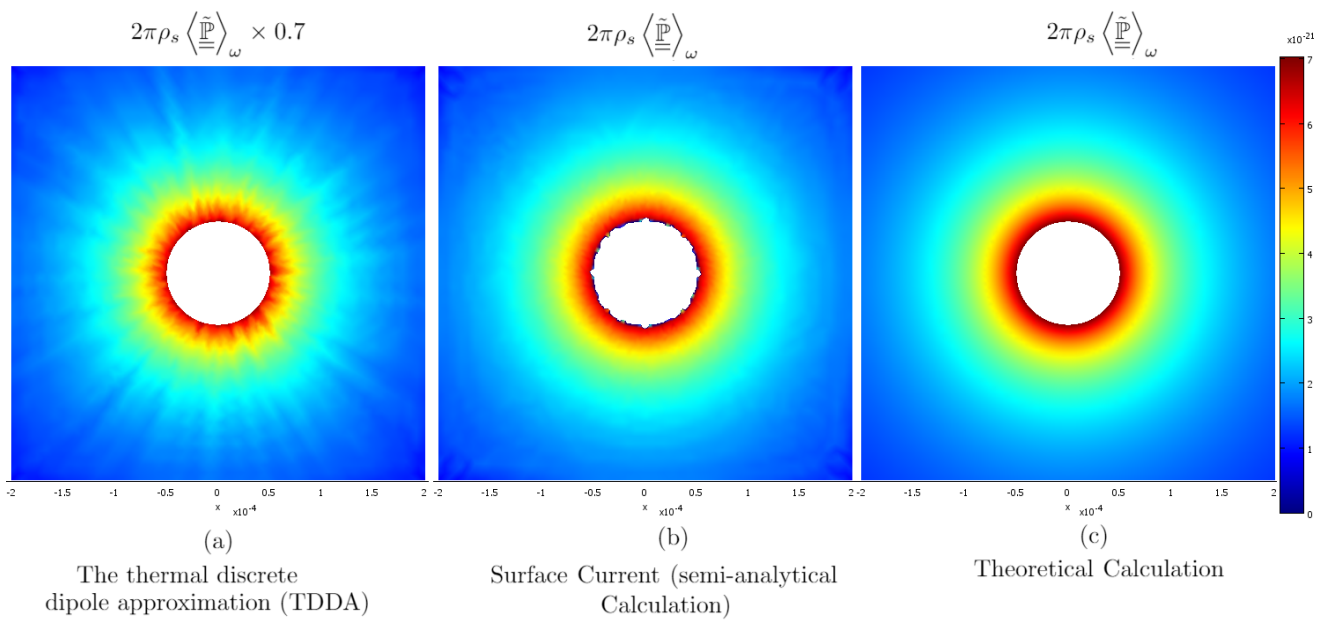

Figure 5.10: Plot of the thermal radiated Poynting vector multiplied by $2\pi\rho_s$ due to the following simulation setups: (a)The thermal discrete dipole approximation (TDDA) of Fig.(5.7) (b) Equivalent thermal surface current (semi-analytical Calculation) of Fig.(5.8) (c)Theoretical calculation of Fig.(5.9) using Eq.(5.58).

5.6 TR from arbitrary thermal emitter characterized by a Surface Impedance

In this section, the circuit model for TR from arbitrary shaped emitter is proposed. The method proposed here is an extension of the model developed by Masloviski et al [78]. An arbitrary thermal emitter is quantified by in-homogeneous and spatial dispersive surface admittance. Starting by the spectral cross correlation of the electric and magnetic current in such general case:

$$\langle J_s^z(\rho_s,\phi)J_s^{z*}(\rho_s,\phi')\rangle_\omega = 4\frac{\omega\epsilon_0}{\pi}\Theta(\omega,T)\frac{1}{\rho_s}Im\{\chi_{ee}^{zz}(\phi,\phi')\} \tag{5.59}$$

since $Y_s = j\omega\epsilon_0\chi_{ee}^{zz}$, then

$$\langle J_s^z(\rho_s,\phi)J_s^{z*}(\rho_s,\phi')\rangle_\omega = \frac{4}{\pi}\Theta(\omega,T)\frac{1}{\rho_s}Re\{Y_s(\phi,\phi')\} \tag{5.60}$$

and making use of the Lorentz reciprocity property of Eq.(5.18) , then:

$$\langle J_s^z(\rho_s,\phi)J_s^{z*}(\rho_s,\phi')\rangle_\omega = \frac{4}{\pi}\Theta(\omega,T)\frac{1}{\rho_s}Re\{Y_s(\phi,\phi')\} \tag{5.61}$$

similarly for thermal magnetic current density, then

$$\left\langle K_s^\phi(\rho_s,\phi)K_s^{\phi*}(\rho_s,\phi')\right\rangle_\omega = 4\frac{\omega\mu_0}{\pi}\Theta(\omega,T)\frac{1}{\rho_s}Im\{\chi_{mm}^{\phi\phi}(\phi,\phi')\} \tag{5.62}$$

since $Z_s = j\omega\mu_0\chi_{mm}^{\phi\phi}$, then

$$\left\langle K_s^\phi(\rho_s,\phi)K_s^{\phi*}(\rho_s,\phi')\right\rangle_\omega = \frac{4}{\pi}\Theta(\omega,T)\frac{1}{\rho_s}Re\{Z_s(\phi',\phi,\phi')\} \tag{5.63}$$

Applying the Fourier transform of Eq.(5.44), then the spectral cross correlation between different cylindrical orders is as following:

$$\begin{aligned}
\left\langle \tilde{J}_s^z[n]\tilde{J}_s^{z*}[m]\right\rangle_\omega &= \frac{1}{(2\pi)^2}\iint_0^{2\pi} \langle J_s^z(\rho_s,\phi)J_s^{z*}(\rho_s,\phi'))\rangle_\omega\, e^{-i(n\phi-m\phi')}d\phi d\phi' \\
&= \frac{1}{(2\pi)^2}\frac{4}{\pi}\Theta(\omega,T)\frac{1}{\rho_s}\iint_0^{2\pi} Im\{\omega\epsilon_0\chi_{ee}^{zz}(\phi,\phi')\}e^{-i(n\phi-m\phi')}d\phi d\phi' \quad (5.64)\\
&= \frac{1}{(2\pi)^2}\frac{4}{\pi}\Theta(\omega,T)\frac{1}{\rho_s}\iint_0^{2\pi} Re\{Y_s(\phi,\phi')\}e^{-i(n\phi-m\phi')}d\phi d\phi'
\end{aligned}$$

Where $Y_s = j\omega\epsilon_0\chi_{ee}^{zz}$, then

$$\begin{aligned}
\left\langle \tilde{J}_s^z[n]\tilde{J}_s^{z*}[m]\right\rangle_\omega &= \frac{1}{(2\pi)^2}\frac{2}{\pi}\Theta(\omega,T)\frac{1}{\rho_s}\iint_0^{2\pi} \left[Y_s(\phi,\phi') + Y_s^*(\phi,\phi')\right] e^{-i(n\phi-m\phi')}d\phi d\phi' \\
&= \frac{1}{(2\pi)^2}\frac{2}{\pi}\Theta(\omega,T)\frac{1}{\rho_s}\iint_0^{2\pi} \left[Y_s(\phi,\phi') + Y_s^*(\phi',\phi)\right] e^{-i(n\phi-m\phi')}d\phi d\phi' \\
&= \frac{2}{\pi}\Theta(\omega,T)\frac{1}{\rho_s}\left[\tilde{\tilde{Y}}_s[n,-m] + \left(\tilde{\tilde{Y}}_s[m,-n]\right)^*\right]
\end{aligned}$$

where we used the Lorentz reciprocity relation of Eq.(5.18).Similarly

$$\begin{aligned}
\left\langle \tilde{K}_s^\phi[n]\tilde{K}_s^{\phi*}[m])\right\rangle_\omega &= \frac{1}{(2\pi)^2}\frac{2}{\pi}\Theta(\omega,T)\frac{1}{\rho_s}\iint_0^{2\pi} \left[Z_s(\phi,\phi') + Z_s^*(\phi,\phi')\right] e^{-i(n\phi-m\phi')}d\phi d\phi' \\
&= \frac{2}{\pi}\Theta(\omega,T)\frac{1}{\rho_s}\left[\tilde{\tilde{Z}}_s[n,-m] + \left(\tilde{\tilde{Z}}_s[m,-n]\right)^*\right]
\end{aligned} \tag{5.65}$$

Spectral of Nyquist Sources for an Equivalent Surface of arbitrary shaped Emitter: The spectral cross correlations of the Nyquist voltage and current can be retrieved from the previous correlations of the equivalent electric and magnetic surface

current of Eq.s (**??**-5.65) using the equivalence shown previously at Eq.s(5.49-5.51); then since

$$\tilde{I}_s = \sqrt{\rho_s}\tilde{J}_s^z \quad \tilde{V}_s = \sqrt{\rho_s}\tilde{K}_s^\phi$$

the spectral cross correlations of the electric current and voltage of different cylindrical orders can be written as following :

$$\begin{aligned} \left\langle \tilde{I}_s[n]\tilde{I}_s^*[m] \right\rangle_\omega &= \frac{2}{\pi}\Theta(\omega,T)\left[\tilde{\tilde{Y}}_s[n,-m] + \left(\tilde{\tilde{Y}}_s[m,-n]\right)^*\right] \\ \left\langle \tilde{V}_s[n]\tilde{V}_s^*[m] \right\rangle_\omega &= \frac{2}{\pi}\Theta(\omega,T)\left[\tilde{\tilde{Z}}_s[n,-m] + \left(\tilde{\tilde{Z}}_s[m,-n]\right)^*\right] \end{aligned} \tag{5.66}$$

5.6.1 Nyquist thermal sources

Now we introduce the thermal electric current sources to the surface admittance network of Eq.(5.16) as following:

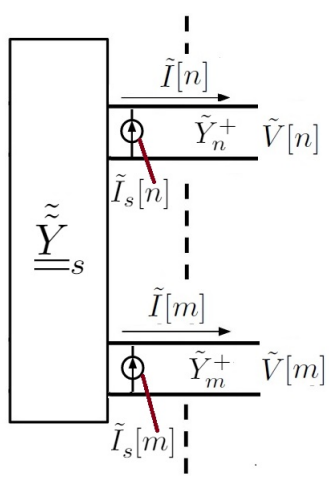

Figure 5.11: The circuit configuration as Fig.(5.4) but with the associated thermal sources represented as Nyquist voltage sources $\tilde{e}_n$.

$$\underline{\tilde{I}} = -\tilde{\tilde{\underline{\underline{Y}}}}_s\,\underline{\tilde{V}} + \underline{\tilde{I}}_s \tag{5.67}$$

where $\underline{\tilde{I}}_s = \tilde{I}_s[n]$ is a column vector representing the Nyquist's current source of the electromagnetic fluctuation launching cylindrical wave of order n. Notice that the negative sign is introduced with respect to Eq.(5.1) to accommodate $+\rho$ flowing current as shown in Fig.(5.67). The spectral cross correlation of the thermal electric surface currents of different cylindrical orders of Eq.(5.66) can be rewritten as following:

$$< \tilde{I}_s[n]\tilde{I}_s^*[m] >_\omega = \frac{2}{\pi}\theta(\omega, T)\left(\underline{\underline{\tilde{\tilde{Y}}}}_{s,nm} + \underline{\underline{\tilde{\tilde{Y}}}}^*_{s,mn}\right) \tag{5.68}$$

defining

$$\underline{\underline{L}} = \underline{\underline{\tilde{\tilde{Y}}}}_s + \underline{\underline{\tilde{\tilde{Y}}}}^\dagger_s \tag{5.69}$$

where $\dagger$ is the matrix adjoint operator. The spectral cross correlation will be in a matrix form as following:

$$< \underline{\tilde{I}}_s\underline{\tilde{I}}_s^\dagger >_\omega = \frac{2}{\pi}\theta(\omega, T)\underline{\underline{L}} \tag{5.70}$$

5.6.2 TR from Nyquist sources

To calculate for the thermal radiation, we use $\tilde{I}[n] = \tilde{Y}_n^+\tilde{V}[n]$ where $\tilde{Y}_n^+ = j\frac{\dot{H}_n^{(2)}(k\rho_s)}{\eta H_n^{(2)}(k\rho_s)}$ is the wave admittance of outward propagating cylindrical wave of order n. Then in matrix form

$$\underline{\tilde{I}} = \underline{\underline{\tilde{Y}}}^+\underline{\tilde{V}} \tag{5.71}$$

where $\underline{\underline{\tilde{Y}}}^+ = \left[\tilde{Y}_n^+\right]$ is a diagonal rectangular matrix. Substituting Eq.(5.71) in Eq.(5.67) then we get:

$$\left[\underline{\underline{\tilde{Y}}}^+ + \underline{\underline{\tilde{\tilde{Y}}}}_s\right]\underline{\tilde{V}} = \underline{\tilde{I}}_s \tag{5.72}$$

rewriting $\underline{V}$ in terms of the $\underline{I}_s$ as following:

$$\tilde{\underline{V}} = \left[\tilde{\underline{\underline{Y}}}^{+} + \tilde{\tilde{\underline{\underline{Y}}}}_s\right]^{-1} \tilde{\underline{I}}_s \tag{5.73}$$

and similarly for $\underline{I}$,

$$\tilde{\underline{I}} = \tilde{\underline{\underline{Y}}}^{+} \left[\tilde{\underline{\underline{Y}}}^{+} + \tilde{\tilde{\underline{\underline{Y}}}}_s\right]^{-1} \tilde{\underline{I}}_s \tag{5.74}$$

Now, we define a time averaged complex power matrix as following

$$\underline{\underline{\mathbb{P}}} = 4 \times \frac{1}{2} \left\langle \tilde{\underline{V}} \ \tilde{\underline{I}}^{\dagger} \right\rangle_{\omega} \tag{5.75}$$

then by substituting Eqs.(5.70), (5.73) and (5.74) in the latter equation we get

$$\begin{aligned} \underline{\underline{\mathbb{P}}} &= 4 \times \frac{1}{2} \left[\tilde{\underline{\underline{Y}}}^{+} + \tilde{\tilde{\underline{\underline{Y}}}}_s\right]^{-1} \left\langle \tilde{\underline{I}}_s \tilde{\underline{I}}_s^{\dagger} \right\rangle_{\omega} \left[\tilde{\underline{\underline{Y}}}^{+} + \tilde{\tilde{\underline{\underline{Y}}}}_s\right]^{-\dagger} \left(\tilde{\underline{\underline{Y}}}^{+}\right)^{\dagger} \\ &= \frac{4}{\pi} \theta(\omega, T) \left[\tilde{\underline{\underline{Y}}}^{+} + \tilde{\tilde{\underline{\underline{Y}}}}_s\right]^{-1} [\underline{\underline{L}}]_{nm} \left[\tilde{\underline{\underline{Y}}}^{+} + \tilde{\tilde{\underline{\underline{Y}}}}_s\right]^{-\dagger} \left(\tilde{\underline{\underline{Y}}}^{+}\right)^{\dagger} \end{aligned} \tag{5.76}$$

Note that $\underline{\underline{\mathbb{P}}}$ is a square matrix whose elements are $[\mathbb{P}_{nm}]$ which was previously defined in Eq.(5.2). The $\underline{\underline{\mathbb{P}}}$ has the following form:

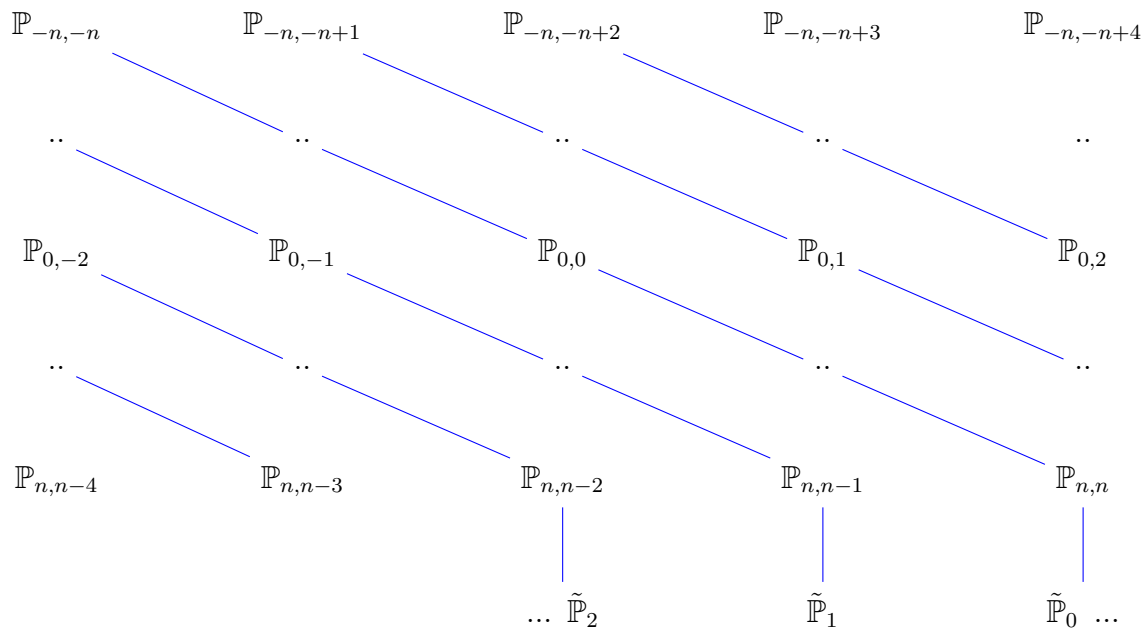

The thermally radiated power can be computed from the former power matrix $\underline{\underline{\mathbb{P}}}$ as following:

1. The total thermally radiated power $\langle \mathbb{P}_{total} \rangle_\omega$ is computed through the trace (summation over the main diagonal) of $\underline{\underline{\mathbb{P}}}$ as following:

$$\begin{aligned}\langle \mathbb{P}_{total} \rangle_\omega &= \mathrm{Re}\left\{ trace\{\underline{\underline{\mathbb{P}}}\} \right\} \\ &= 4 \times \frac{1}{2} \times \frac{4}{\pi}\theta(\omega, T)\,\mathrm{Re}\left\{ trace\left\{ \left[\underline{\underline{\tilde{Y}}}^{+} + \underline{\underline{\tilde{\tilde{Y}}}}_s\right]^{-1} [\underline{\underline{L}}]_{nm} \left[\underline{\underline{\tilde{Y}}}^{+} + \underline{\underline{\tilde{\tilde{Y}}}}_s\right]^{-\dagger} \left(\underline{\underline{\tilde{Y}}}_s^{+}\right)^{\dagger} \right\} \right\}\end{aligned} \tag{5.77}$$

   Note the $\langle \mathbb{P}_{total} \rangle_\omega$ is defined as the dc constant of the thermally radiated as shown in fig.(5.3).

2. In order to calculate for the thermal radiated pattern at the outer surface of the thermal emitter, we need to sum over the diagonals (other than the main diagonal)of the matrix $\underline{\underline{\mathbb{P}}}$ scaled with $e^{iq\phi}$, where q is the index of the diagonal

on which the summation is performed as following:

$$\langle \mathbb{P}(\rho_s, \phi) \rangle_\omega = \sum_q \tilde{\mathbb{P}}_q e^{iq\phi} = \sum_q \left(\sum_n \sum_{m=n-q} \mathbb{P}_{nm} \right) e^{iq\phi} \quad q = n - m \tag{5.78}$$

The quantity $\langle \mathbb{P}(\phi) \rangle_\omega$ is the thermally radiated complex power per unit angle computed at the surface of the equivalent surface and is defined in Eq.(5.2). It is interesting to note that the computation of $\langle \mathbb{P}_{total} \rangle_\omega$ is the same as the computation of $\langle \mathbb{P}(\phi) \rangle_\omega$ but for $n = m$.

3. The thermal emitted radiated (real) power per unit angle at locations in vacuum of radial distance ρ from the origin is calculated according to Eq.(5.7) as following:

$$\mathrm{Re}\left\{ \langle \mathbb{P}(\rho, \phi) \rangle_\omega \right\} = \mathrm{Re}\left\{ \sum_n \sum_m \left\langle \tilde{\mathbb{P}}_{nm} \right\rangle_\omega \frac{H_n^{(2)}(k\rho) \dot{H}_m^{(2)*}(k\rho)}{H_n^{(2)}(k\rho_s) \dot{H}_m^{(2)*}(k\rho_s)} e^{j(n-m)\phi} \right\}$$

5.7 Numerical Calculation

Now, we consider thermal radiation from a lossy non-circularly symmetric emitters where we test the validity of the proposed analytical model. We compare between the numerical simulation of the proposed model and the results of numerical calculation done by TDDA. Consider the same emitter as the previous case in section (5.5.2) but with an embedded elliptic perfect magnetic conductor (PMC) core. This elliptic core is located inside $\rho < \sigma(\phi)$ as shown in Fig.(5.12), while $\sigma(\phi) = \left(\frac{cos^2(\phi)}{a^2} + \frac{sin^2(\phi)}{b^2} \right)^{-\frac{1}{2}}$, where a and b are semi-major and semi-minor axes of the ellipse. In what follows the numerical calculation procedure is summarized as following:

1. First the surface admittance is calculated using COMSOL 3.5A, where a boundary condition $E_z = e^{in\phi}$ is imposed on the boundary $\rho = \rho_s$ for $n = [-N, N]$. Then the surface admittance $\tilde{Y}[n, \phi]$ is computed through $\tilde{Y}[n, \phi] = H_\phi$, where

H_ϕ is provided by the electromagnetic solver.

2. Having the surface admittance calculated $\tilde{Y}_s[n,\phi]$, its Fourier transform with respect to ϕ is computed as following: $\tilde{\tilde{Y}}_s[n,-m] = \frac{1}{2\pi}\int_0^{2\pi} \tilde{Y}_s[n,\phi]e^{i(m)\phi}d\phi$.

3. The matrices $\underline{\underline{\tilde{\tilde{Y}}}}_s$ and $[\underline{\underline{L}}]_{nm}$ are constructed according to Eq.s (5.69) and (5.15). Finally the thermal radiated power for each cylindrical order is calculated according to Eq.(5.76).

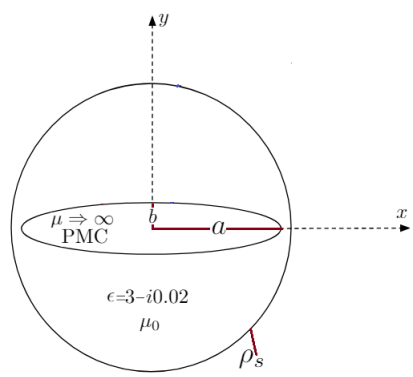

Figure 5.12: Schematic for the numerical example used to validate the proposed circuit model. The thermal emitter consists of a cylindrical dielectric with permittivity $\epsilon = 3 - i0.02$ with an elliptic shaped PMC (infinite permeability). Due to the broken circular symmetry, thermally radiated power is expected to have a pattern which is not circularly symmetric.

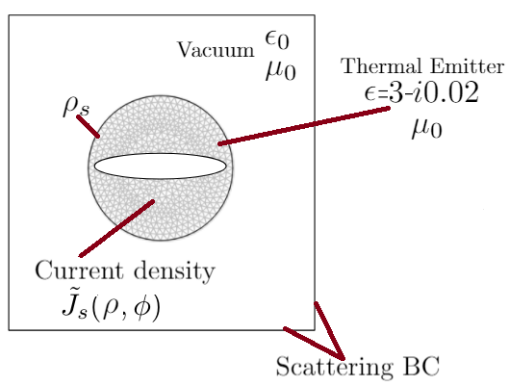

Figure 5.13: Thermal discrete dipole approximation (TDDA) simulation setup

To test the validity of the proposed model, TDDA calculation of the thermal radiation is implemented and its setup is as shown in Fig.(5.13). The thermal emitter located at $\rho_s < \rho < \sigma(\phi)$ is meshed and the thermal electric current density is discretized and thermal radiated poynting vector is calculated according to the procedure used in Chapter (2).The calculated thermal radiated radial power computed a the surfacez $\rho = \rho_s$, is shown in Fig.(5.14) for both TDDA and the proposed model. While Fig.(5.15) shows the thermal radiated radial poynting vector for both TDDA and the proposed circuit model. The results show good agreement and confirms the proposed circuit model. Calculations are done using $\pm$ 20 cylindrical orders, the temperature of the thermal emitter is $T = 50\, C^0$. The elliptic PMC is with $a = 50\mu m$, $b = 30\mu m$. Calculation is done at $100\mu m$ wavelength and $\rho_s = 60\mu m$.

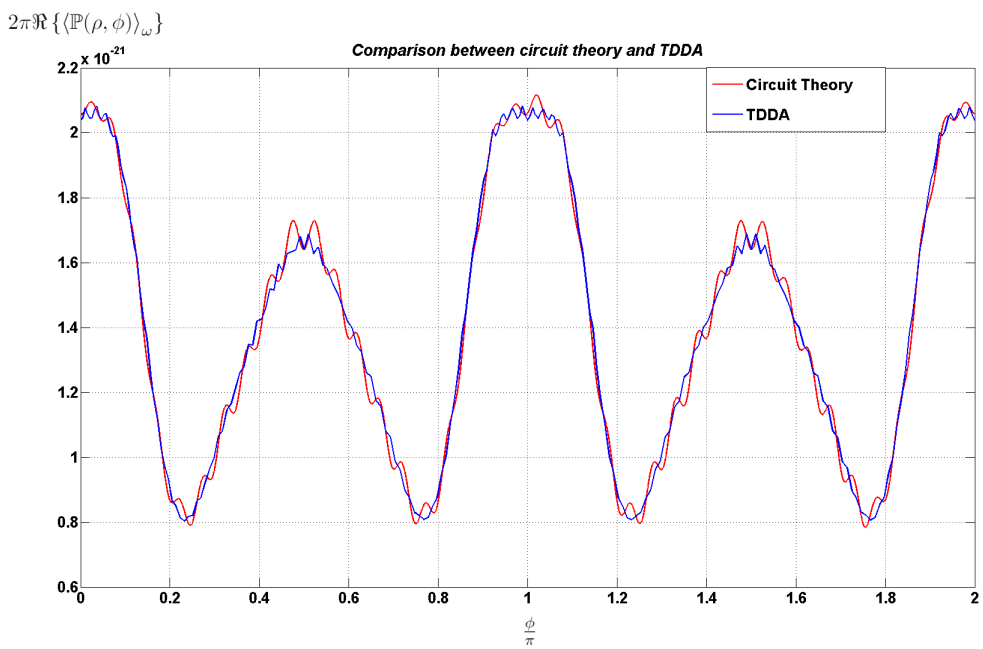

Figure 5.14: Plot of the real power radiated $2\pi\,\mathrm{Re}\{< \mathbb{P}(\rho_s, \phi) >_\omega\}$ computed at $\rho = \rho_s$. Blue line is for The thermal discrete dipole approximation (TDDA) of Fig.(5.13), while the red line is for the theoretical calculation of the poynting vector is calculated using Eq.(5.76).

.

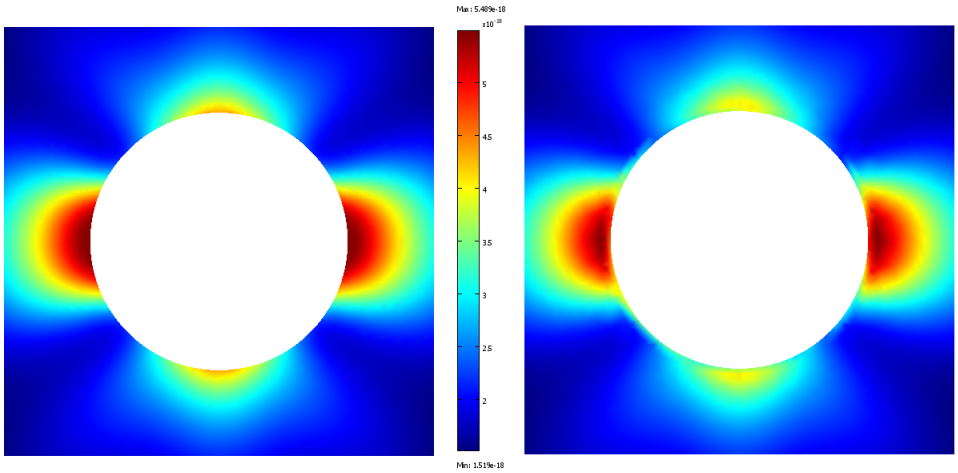

(a)
The thermal discrete
dipole approximation (TDDA)

(b)
Theoretical Calculation

Figure 5.15: Plot of the normalized thermal radiated Poynting vector to due to the following simulation setups: (a) The thermal discrete dipole approximation (TDDA) of Fig.(5.13). (b) Theoretical calculation. The poynting vector is calculated using Eq.(5.76).

.

5.8 Conclusions and Limitations

In this chapter, thermal radiation illusion using lossy mantle cloaks are addressed. It was shown that thermal radiation signature from an arbitrary shaped target thermal emitter can be replicated by a mantle cloak as long as both have the surface impedance or admittance at some reference surface. In order to relate the thermally radiated power to the surface impedance, a new circuit model for computing thermal radiation signature is proposed. The proposed model assumes that the surface impedance or admittance is known apiori and thermal radiation is computed accordingly. The circuit model is an extension to the the circuit model proposed by S. Maslovski et al in [78] which is based on fluctuation electrodynamics theorem. An equivalence between the thermal noise sources as used in the circuit model as the thermal surface currents fluctuating along the surface of the thermal emitter, was

done using the correspondence between the surface impedance and admittance with the susceptibility tensors quantifying the electromagnetic response of the surface. Numerical results due to the proposed theory and using thermal discrete dipole approximation were done compared for multiple emitters and the result show excellent agreement such that the numerical calculations confirm the proposed model.

Although the proposed model proved to be successful to compute thermal radiation, an inverse designing is required. The inverse problem can be defined as what is the surface impedance or admittance for a desired thermal radiation signature. It is obvious that there is no unique solution and an inverse scheme is required to developed. Also, the proposed model suffers from a further limitation that analytical solutions are not available for most cases and numerical calculations are required to compute the surface impedance of a thermal emitter. On the other hand, the circuit model cannot be used to compute the thermal emitted electromagnetic inside the thermal emitter but it can be only used to compute thermal radiation radiated outwards.

Although the theory proposed is illustrated for two dimensional space, it can be extended for three dimensional space and using spherical waves as basis as done in[80]. Finally, the circuit model proposed is most suited to the computation of thermal emission from an isolated thermal emitter, where it was assumed that there is no radiative heat transfer with other objects.

CHAPTER VI

Fluctuation Electrodynamics in Reciprocal Chiral Media using Field Transformation and Discontinuous Field Transformation based Mantle Cloaks

6.1 Introduction

In chapter III, we had investigated the applications of transformation optics (TO) theory upon thermal radiations in the frame work of Fluctuation Electrodynamics (FE). Also in chapter IV, we investigated discontinuous space transformation, and we showed the possibility of designing TO based mantle cloaks. In both cases, the parameters media of the objects to be cloaked and the target objects are constraint by the used space transformation. In this chapter we repeat the same steps done in chapters III and IV but with respect to field transformation instead of space transformations. The interdependence of shapes of the media of the object to be cloaked and the target object with in the context of heat conduction physics had been investigated in chapter II. In this chapter, we show that Field transformation (FT) in 2D space [71] can allow the decoupling of the shape from the media parameters for both the object to be cloaked and the target object. Duality transformation was summarized

in chapter I. In this chapter we consider FT and similar conclusions can be drawn using duality transformation.

Similar to TO where the physics is invariant under space transformation. Maxwell's equations are invariant under FT. FT is a transformation that is performed in the electromagnetic vector space where transformations as rotations and scaling are done in the space spanned by the components of the electric and magnetic fields. For instance, by applying FT upon electromagnetic field in empty 2D virtual space, E and H-polarizations are coupled and new polarizations are emerged in the physical space. Unlike TO, where anisotropic and inhomogeneous media emerge in the physical space due to the space transformation, FT leads to a physical space that includes chiral (also called bi-anisotropic) media. Based on the former point of view, we apply FT upon FE In in order to compute for thermal radiation from chiral media at local thermal equilibrium. We show that FE is invariant under FT transformation. This means that thermal radiation from a thermal emitter can be used to know the thermal radiation from another thermal emitter as long as their media are connected by FT. Actually starting by a virtual space including magneto-dielectric media, where the spectral correlations of the thermal electric and magnetic currents are found in terms of the imaginary parts of the complex permittivity and permeability, we can formulate FE for a chiral media using FT such that the spectral cross correlations between the the electric and magnetic currents are found in terms of the coupling coefficients (magneto-electric and electro-magnetic). Based on such invariance of FE under FT transformation, we will show that thermal illusion theme of chapter III can be extended to include chiral media using cloaks designed FT instead of TO as long as the media of cloaked object and the target object are related by FT transformation.

Also, similar to TO, FT produces cloaks that are bulky, homogeneous, chiral and

anisotropic. In this chapter we make use of the same theme of discontinuous transformation of chapter IV as a tool to design mantle cloaks that can replace such FT based cloaks. Unlike the cloaks derived in chapter IV, mantle cloaks derived in the chapter are local and homogeneous which make them competitive to other design techniques.

This chapter is organized as following: in section(6.2), the main theme of field transformation is summarized. In section(6.3), the covariance of FE under FT is investigated with the spectral correlations of the thermal sources before and after field transformation are studied and reported reported. Then thermal illusion based on continuous FT is reported. In section (6.4) mantle cloaks based on discontinuous field transformations are reported with the necessary susceptibility tensors of such meta-surfaces are computed in terms of the discontinuity jump of FT. Finally the circuit model for the mantle meta-surfaces is reported and it will be shown that they are a generalization of the electric transformer which is typically used as an impedance transformer component in electrical circuit. Numerical results are performed and they show consistency with the proposed models.

6.2 Field Transformation

Field transformation (FT) is another variant of the duality transformation which was summarized in chapter I. FT is different in the sense that in 2-D space, the transformation couples the out of plane field components of $TM_z/E-$ and $TE_z/H-$ polarizations differently from the coupling/transformation of the in-plane components. Also, unlike DT, FT can transform an arbitrary reciprocal dielectric anisotropic media into a reciprocal chiral bi-anisotropic media. In this section, first the main results of FT are summarized then we show that FE is covariant under transformation under real valued FT transformation. We consider the special case of transforming an

anisotropic dielectric where the electric and magnetic currents are uncorrelated, then by applying FT, the cross-correlation between electric and magnetic currents are derived in terms of the parameters of the chiral media located in the post transformation physical space.

6.2.1 Decomposition into longitudinal and transverse components

Here we considering a 2D space which is independent of the out-of-plane $z-$axis. Now, starting with Maxwell equations as following:

$$\nabla \times \bar{E} = i\omega\bar{B} - \bar{K} \tag{6.1}$$

$$\nabla \times i\bar{H} = \omega\bar{D} + i\bar{J} \tag{6.2}$$

Note the division by the imaginary number i in Ampere's law. The next step is to decompose all fields and the nabla operator in Maxwell's equations into out of plane and transverse components $\nabla = \nabla_T + \hat{\mathbf{z}}\partial_z$. Since the electromagnetic problem is independent of $z-$axis so $\partial_z = 0$, then

$$\begin{aligned}
&\nabla = \nabla_T \\
&\bar{E} = \bar{E}_T + \hat{\mathbf{z}}E_z \qquad \bar{H} = \bar{H}_T + \hat{\mathbf{z}}H_z \\
&\bar{D} = \bar{D}_T + \hat{\mathbf{z}}D_z \qquad B = \bar{B}_T + \hat{\mathbf{z}}B_z \\
&\bar{J} = \bar{J}_T + \hat{\mathbf{z}}J_z \qquad \bar{K} = \bar{K}_T + \hat{\mathbf{z}}K_z
\end{aligned} \tag{6.3}$$

where T indicates traverse component such that for a transverse vector, i.e $\bar{E}_T$, it can be expressed as $\bar{E}_T = \hat{x}E_x + \hat{y}E_y$. Now, assuming a general linear bi-an-isotropic where the constitutive parameters are defined as following:

$$
\begin{aligned}
\bar{D} &= \underline{\underline{\varepsilon}}\bar{E} + i\underline{\underline{\kappa}}\bar{H} \\
\bar{B} &= -i\underline{\underline{\eta}}\bar{E} + \underline{\underline{\mu}}\bar{H}
\end{aligned}
\tag{6.4}
$$

where the double underline indicates a square matrix, also $\underline{\underline{\varepsilon}}$, $\underline{\underline{\mu}}$, $\underline{\underline{\kappa}}$ and $\underline{\underline{\eta}}$ are electric permittivity, magnetic permeability, magneto-electric and electromagnetic coefficient tensors respectively. Decomposing Eq.(6.4) into longitudinal and transverse components as following:

$$
\begin{bmatrix} \bar{D}_T \\ D_z \\ i\bar{B}_T \\ iB_z \end{bmatrix} = \begin{bmatrix} \underline{\underline{\varepsilon}}_{TT} & \underline{\varepsilon}_{Tz} & \underline{\underline{\kappa}}_{TT} & \underline{\kappa}_{Tz} \\ \underline{\varepsilon}_{zT} & \varepsilon_{zz} & \underline{\kappa}_{zT} & \kappa_{zz} \\ \underline{\underline{\eta}}_{TT} & \underline{\eta}_{Tz} & \underline{\underline{\mu}}_{TT} & \underline{\mu}_{Tz} \\ \underline{\eta}_{zT} & \eta_{zz} & \underline{\mu}_{zT} & \mu_{zz} \end{bmatrix} \begin{bmatrix} \bar{E}_T \\ E_z \\ i\bar{H}_T \\ iH_z \end{bmatrix}
\tag{6.5}
$$

where single underline indicates a row or column vector (the distinction should be clear from the subscript). We can rewrite the constitutive relations in a matrix form as following:

$$
\begin{bmatrix} \bar{D}_T \\ i\bar{B}_T \end{bmatrix} = O_{4\times4} \begin{bmatrix} \bar{E}_T \\ i\bar{H}_T \end{bmatrix} + P_{4\times2} \begin{bmatrix} E_z \\ iH_z \end{bmatrix}
\tag{6.6}
$$

$$
\begin{bmatrix} D_z \\ iB_z \end{bmatrix} = M_{2\times4} \begin{bmatrix} \bar{E}_T \\ i\bar{H}_T \end{bmatrix} + N_{2\times2} \begin{bmatrix} E_z \\ iH_z \end{bmatrix}
\tag{6.7}
$$

with the matrices are defined as following:

$$O_{4\times4} = \begin{bmatrix} \underline{\underline{\epsilon}}_{TT} & \underline{\underline{\kappa}}_{TT} \\ \underline{\underline{\eta}}_{TT} & \underline{\underline{\mu}}_{TT} \end{bmatrix} \qquad P_{4\times2} = \begin{bmatrix} \underline{\epsilon}_{Tz} & \underline{\kappa}_{Tz} \\ \underline{\eta}_{Tz} & \underline{\mu}_{Tz} \end{bmatrix}$$
$$M_{2\times4} = \begin{bmatrix} \underline{\epsilon}_{zT} & \underline{\kappa}_{zT} \\ \underline{\eta}_{zT} & \underline{\mu}_{zT} \end{bmatrix} \qquad N_{2\times2} = \begin{bmatrix} \epsilon_{zz} & \kappa_{zz} \\ \eta_{zz} & \mu_{zz} \end{bmatrix} \tag{6.8}$$

where the subscripts are the dimensions of each matrix. Decomposing Maxwell's equations into longitudinal and transverse and keeping the problem independent of $\partial_z = 0$

$$\frac{1}{\omega}\nabla_{2\times4}\cdot\begin{bmatrix} \hat{\mathbf{z}}\times iH_T \\ \hat{\mathbf{z}}\times E_T \end{bmatrix} + M_{2\times4}\begin{bmatrix} E_T \\ iH_T \end{bmatrix} + N_{2\times2}\begin{bmatrix} E_z \\ iH_z \end{bmatrix} + \frac{1}{\omega}\begin{bmatrix} iJ_z \\ -K_z \end{bmatrix} = 0_{2\times1} \tag{6.9}$$

$$\frac{1}{\omega}\hat{\mathbf{z}}\times\nabla_{4\times2}\cdot\begin{bmatrix} iH_z \\ E_z \end{bmatrix} + O_{4\times4}\begin{bmatrix} E_T \\ iH_T \end{bmatrix} + P_{4\times2}\begin{bmatrix} E_z \\ iH_z \end{bmatrix} + \frac{1}{\omega}\begin{bmatrix} iJ_T \\ -K_T \end{bmatrix} = 0_{2\times1} \tag{6.10}$$

Where the introduced gradients are defined as following:

$$\nabla_{2\times4} = \begin{bmatrix} \partial_y & \partial_x & \partial_y & \partial_x \\ \partial_y & \partial_x & \partial_y & \partial_x \end{bmatrix} \tag{6.11}$$

$$\nabla_{4\times2} = \begin{bmatrix} \hat{\mathbf{x}}\partial_x & 0 \\ \hat{\mathbf{y}}\partial_y & 0 \\ 0 & \hat{\mathbf{x}}\partial_x \\ 0 & \hat{\mathbf{y}}\partial_y \end{bmatrix} \tag{6.12}$$

6.2.2 Transforming between virtual and physical spaces

Now, Consider transforming the longitudinal field components using an arbitrary transformation as following

$$\begin{bmatrix} E_z \\ iH_z \end{bmatrix} = \begin{bmatrix} A_{11} & A_{12} \\ A_{21} & A_{22} \end{bmatrix} \begin{bmatrix} E'_z \\ iH'_z \end{bmatrix} = A_{2\times 2} \begin{bmatrix} E'_z \\ iH'_z \end{bmatrix} \tag{6.13}$$

where the unprimed and primed indicates quantities in the virtual and physical spaces respectively. Assuming that Maxwell's Equations are invariant under transformation, then Maxwell's equations in the physical space are written as following:

$$\frac{1}{\omega}\nabla_{2\times 4}\cdot \begin{bmatrix} \hat{\mathbf{z}} \times i\bar{H}'_T \\ \hat{\mathbf{z}} \times \bar{E}'_T \end{bmatrix} + M'_{2\times 4} \begin{bmatrix} \bar{E}'_T \\ i\bar{H}'_T \end{bmatrix} + N'_{2\times 2} \begin{bmatrix} E'_z \\ iH'_z \end{bmatrix} + \frac{1}{\omega} \begin{bmatrix} iJ'_z \\ -K'_z \end{bmatrix} = 0_{2\times 1} \tag{6.14}$$

$$\frac{1}{\omega}\hat{\mathbf{z}} \times \nabla_{4\times 2}\cdot \begin{bmatrix} iH'_z \\ E'_z \end{bmatrix} + O'_{4\times 4} \begin{bmatrix} \bar{E}'_T \\ i\bar{H}'_T \end{bmatrix} + P'_{4\times 2} \begin{bmatrix} E_z \\ iH_z \end{bmatrix} + \frac{1}{k_0} \begin{bmatrix} i\bar{J}_T \\ -\bar{K}_T \end{bmatrix} = 0_{2\times 1} \tag{6.15}$$

Accordingly the transverse components are constrained to be transformed with a transformation as following:

$$\begin{bmatrix} E'_T \\ iH'_T \end{bmatrix} = F_{4\times 4} \begin{bmatrix} E_T \\ iH_T \end{bmatrix} \tag{6.16}$$

where $F_{4\times 4}$ is written as following:

$$F_{4\times 4} = \begin{bmatrix} A_{22}I_2 & A_{12}I_2 \\ A_{21}I_2 & A_{11}I_2 \end{bmatrix} \tag{6.17}$$

with I_2 is two by two identity matrix. Accordingly, the media in the physical space are transformed as following:

$$
\begin{aligned}
M'_{2\times4} &= A^{\tau}_{2\times2}\left[\frac{1}{\omega}G_{2\times4} + M_{2\times4}B_{4\times4}\right] \\
N'_{2\times2} &= A^{\tau}_{2\times2}N_{2\times2}A_{2\times2} \\
O'_{4\times4} &= B^{\tau}_{4\times4}O_{4\times4}B_{4\times4} \\
P'_{4\times2} &= B^{\tau}_{4\times4}\left[\hat{\mathbf{z}}\times\nabla_{4\times2}\begin{bmatrix} A_{21} & A_{22} \\ A_{11} & A_{12}\end{bmatrix} + P_{4\times2}A_{2\times2}\right]
\end{aligned}
\tag{6.18}
$$

where

$$
B_{4\times4} = \begin{bmatrix} A_{21}I_2 & A_{22}I_2 \\ A_{11}I_2 & A_{12}I_2 \end{bmatrix}^{-\tau} \tag{6.19}
$$

and

$$
G_{2\times4} = \begin{bmatrix} \partial_y c & -\partial_x c & \partial_y d & -\partial_x d \\ \partial_y a & -\partial_x a & \partial_y b & -\partial_x b \end{bmatrix} \tag{6.20}
$$

τ is matrix transpose operator. Also, the electric and magnetic current densities are transformed as following:for the transverse components of the current densities

$$
\begin{bmatrix} iJ'_T \\ -K'_T \end{bmatrix} = B^{\tau}_{4\times4}\begin{bmatrix} iJ_T \\ -K_T \end{bmatrix} \tag{6.21}
$$

while for the $z-$components of the current densities:

$$
\begin{bmatrix} iJ'_z \\ -K'_z \end{bmatrix} = A^{\tau}_{2\times2}\begin{bmatrix} iJ_z \\ -K_z \end{bmatrix} \tag{6.22}
$$

6.3 Transformation Fluctuation Electrodynamics

In this section we show how to calculate for the cross spectral correlations for thermal electric and magnetic currents in such bi-an-isotropic media by applying FT upon FE. Also, it will be shown that FE is covariant under FT transformation and the spectral correlations of the thermal current sources have the same form before and after transformation in the case when the FT is real. Finally we show the possibility of thermal radiation illusion using coats designed by FT. Numerical results show agreements with the theory. Numerical computations of thermal radiation from a chiral media are performed using thermal discrete dipole approximation (TDDA) summarized in D.

6.3.1 Covariance of FE under FT transformation

Now, consider a virtual space includes a reciprocal an-isotropic magneto-dielectric such that $\underline{\underline{\varepsilon}} = \underline{\underline{\varepsilon}}^{\tau}$ and $\underline{\underline{\mu}} = \underline{\underline{\mu}}^{\tau}$ and $\underline{\underline{\eta}} = \underline{\underline{\kappa}} = 0$. Then the spectral correlations of the electric thermal current sources are written as following:

$$\begin{aligned} \left\langle \bar{J}\bar{J}^{*} \right\rangle_{\omega} &= \frac{4\,\omega}{\pi}\theta(\omega,T)\; Im\{\underline{\underline{\varepsilon}}\} \\ \left\langle \bar{K}\bar{K}^{*} \right\rangle_{\omega} &= \frac{4\,\omega}{\pi}\theta(\omega,T)\; Im\{\underline{\underline{\mu}}\} \end{aligned} \tag{6.23}$$

by decomposing the currents into longitudinal and transverse then former correlations can be decomposed accordingly as following:

$$\begin{aligned} \left\langle \bar{J}_T\bar{J}_T^{*} \right\rangle_{\omega} &= \frac{4\,\omega}{\pi}\theta(\omega,T)\; Im\{\underline{\underline{\varepsilon}}_{TT}\} \\ \left\langle \bar{J}_T J_z^{*} \right\rangle_{\omega} &= \frac{4\,\omega}{\pi}\theta(\omega,T)\; Im\{\underline{\underline{\varepsilon}}_{Tz}\} = \left\langle J_z\bar{J}_T^{*} \right\rangle_{\omega} \\ \left\langle J_z J_z^{*} \right\rangle_{\omega} &= \frac{4\,\omega}{\pi}\theta(\omega,T)\; Im\{\varepsilon_{zz}\} \end{aligned} \tag{6.24}$$

Similar decomposition can be done for the thermal magnetic current densities. Note that $\underline{\underline{\varepsilon}}_{Tz} = \underline{\underline{\varepsilon}}_{zT}$ and $\underline{\underline{\mu}}_{Tz} = \underline{\underline{\mu}}_{zT}$. Similarly the spectral cross correlations of the transverse and z-components for the thermal electric magnetic currents densities in terms of the corresponding permitivities and permeabilities can be written as following:

$$\begin{aligned}
\begin{bmatrix} \langle J_T J_T^* \rangle_\omega & -i \langle J_T K_T^* \rangle_\omega \\ i \langle K_T J_T^* \rangle_\omega & \langle K_T K_T^* \rangle_\omega \end{bmatrix} &= \frac{4\,\omega}{\pi}\theta(\omega, T) \begin{bmatrix} Im\{\underline{\underline{\varepsilon}}_{TT}\} & 0 \\ 0 & Im\{\underline{\underline{\mu}}_{TT}\} \end{bmatrix} \\
\begin{bmatrix} \langle J_T J_z^* \rangle_\omega & -i \langle J_T K_z^* \rangle_\omega \\ i \langle K_T J_z^* \rangle_\omega & \langle K_T K_z^* \rangle_\omega \end{bmatrix} &= \frac{4\,\omega}{\pi}\theta(\omega, T) \begin{bmatrix} Im\{\underline{\varepsilon}_{Tz}\} & 0 \\ 0 & Im\{\underline{\mu}_{Tz}\} \end{bmatrix} \\
\begin{bmatrix} \langle J_z J_T^* \rangle_\omega & -i \langle J_z K_T^* \rangle_\omega \\ i \langle K_z J_T^* \rangle_\omega & \langle K_z K_T^* \rangle_\omega \end{bmatrix} &= \frac{4\,\omega}{\pi}\theta(\omega, T) \begin{bmatrix} Im\{\underline{\varepsilon}_{zT}\} & 0 \\ 0 & Im\{\underline{\mu}_{zT}\} \end{bmatrix} \\
\begin{bmatrix} \langle J_z J_z^* \rangle_\omega & -i \langle J_z K_z^* \rangle_\omega \\ i \langle K_z J_z^* \rangle_\omega & \langle K_z K_z^* \rangle_\omega \end{bmatrix} &= \frac{4\,\omega}{\pi}\theta(\omega, T) \begin{bmatrix} Im\{\varepsilon_{zz}\} & 0 \\ 0 & Im\{\mu_{zz}\} \end{bmatrix}
\end{aligned} \tag{6.25}$$

then according to the matrix notation defined in Eq.(6.8), the former cross correlations can be rewritten as following:

$$\left\langle \begin{bmatrix} iJ_T \\ -K_T \end{bmatrix} \otimes \begin{bmatrix} iJ_T & -K_T \end{bmatrix}^* \right\rangle_\omega = \frac{4\,\omega}{\pi}\theta(\omega, T) Im\left\{O_{4\times 4}\right\} \tag{6.26}$$

$$\left\langle \begin{bmatrix} iJ_T \\ -K_T \end{bmatrix} \otimes \begin{bmatrix} iJ_z & -K_z \end{bmatrix}^* \right\rangle_\omega = \frac{4\,\omega}{\pi}\theta(\omega, T) Im\left\{P_{4\times 2}\right\} \tag{6.27}$$

$$\left\langle \begin{bmatrix} iJ_z \\ -K_z \end{bmatrix} \otimes \begin{bmatrix} iJ_T & -K_T \end{bmatrix}^* \right\rangle_\omega = \frac{4\,\omega}{\pi}\theta(\omega, T) Im\left\{M_{2\times 4}\right\} \tag{6.28}$$

$$\left\langle \begin{bmatrix} iJ_z \\ -K_z \end{bmatrix} \otimes \begin{bmatrix} iJ_z & -K_z \end{bmatrix}^* \right\rangle_\omega = \frac{4\,\omega}{\pi}\theta(\omega,T) Im\left\{N_{2\times 2}\right\} \tag{6.29}$$

6.3.2 FE in the physical space

Using the transformation of the transverse thermal electric and magnetic currents of Eq.(6.21), then the cross spectral current correlation in the physical space is related to the the cross correlation in the virtual space as following:

$$\begin{aligned}\left\langle \begin{bmatrix} iJ'_T \\ -K'_T \end{bmatrix} \otimes \begin{bmatrix} iJ'_T & -K'_T \end{bmatrix}^* \right\rangle_\omega &= \left\langle B^T_{4\times 4} \begin{bmatrix} iJ_T \\ -K_T \end{bmatrix} \otimes \begin{bmatrix} iJ_T & -K_T \end{bmatrix}^* B_{4\times 4} \right\rangle_\omega \\ &= B^T_{4\times 4} \left\langle \begin{bmatrix} iJ_T \\ -K_T \end{bmatrix} \otimes \begin{bmatrix} iJ_T & -K_T \end{bmatrix}^* \right\rangle_\omega B_{4\times 4}\end{aligned} \tag{6.30}$$

since $B_{4\times 4}$ is a deterministic quantity, it is taken out of both sides of the cross correlation operator. Now substituting for the media losses (according to FE) of Eq.(6.26), then

$$\left\langle \begin{bmatrix} iJ'_T \\ -K'_T \end{bmatrix} \otimes \begin{bmatrix} iJ'_T & -K'_T \end{bmatrix}^* \right\rangle_\omega = \frac{4\,\omega}{\pi}\theta(\omega,T) B^T_{4\times 4} Im\{O_{4\times 4}\} B_{4\times 4} \tag{6.31}$$

Also since the matrix $O_{4\times 4}$ is transformed to the physical space according to Eq.(6.18), and **assuming that** $B_{4\times 4} \in \mathrm{Re}$**,** then

$$Im\{O'_{4\times 4}\} = B^T_{4\times 4} Im\{O_{4\times 4}\} B_{4\times 4} \tag{6.32}$$

then

$$\left\langle \begin{bmatrix} iJ'_T \\ -K'_T \end{bmatrix} \otimes \begin{bmatrix} iJ'_T & -K'_T \end{bmatrix}^* \right\rangle_\omega = \frac{4\,\omega}{\pi}\theta(\omega,T) Im\{O'_{4\times 4}\}$$

$$\begin{bmatrix} \langle J'_T J'^*_T\rangle_\omega & -i\,\langle J'_T K'^*_T\rangle_\omega \\ i\,\langle K'_T J'^*_T\rangle_\omega & \langle K'_T K'^*_T\rangle_\omega \end{bmatrix} = \frac{4\,\omega}{\pi}\theta(\omega,T) \begin{bmatrix} Im\{\underline{\underline{\epsilon}}'_{TT}\} & Im\{\underline{\underline{\kappa}}'_{TT}\} \\ \\ Im\{\underline{\underline{\eta}}'_{TT}\} & Im\{\underline{\underline{\mu}}'_{TT}\} \end{bmatrix} \tag{6.33}$$

since the media in virtual space was reciprocal then $\underline{\underline{\kappa}}'_{TT} = \underline{\underline{\eta}}'^{\tau}_{TT}$ so the

$$\langle K'_T J'^*_T\rangle_\omega = -\,\langle J'_T K'^*_T\rangle_\omega \tag{6.34}$$

but also,

$$\langle K'_T J'^*_T\rangle_\omega = \langle J'_T K'^*_T\rangle^\dagger_\omega \tag{6.35}$$

where † is the adjoint (complex and transpose) operator. Then

$$\langle J'_T K'^*_T\rangle_\omega = -\,\langle J'_T K'^*_T\rangle^\dagger_\omega \tag{6.36}$$

which means that $Re\{\langle J'_T K'^*_T\rangle_\omega\} = 0$ which is consistent with the properties of the reciprocal $\underline{\underline{\kappa}}'_{TT} = \underline{\underline{\eta}}'^{\tau}_{TT}$. Similar cross correlations relations between the $z-$components of thermal currents can be written as following:

$$\begin{aligned} \left\langle \begin{bmatrix} iJ'_z \\ -K'_z \end{bmatrix} \otimes \begin{bmatrix} iJ'_z & -K'_z \end{bmatrix}^* \right\rangle_\omega &= \left\langle A^\tau_{2\times 2} \begin{bmatrix} iJ_z \\ -K_z \end{bmatrix} \otimes \begin{bmatrix} iJ_z & -K_z \end{bmatrix}^* A_{2\times 2} \right\rangle_\omega \\ &= A^\tau_{2\times 2} \left\langle \begin{bmatrix} iJ_z \\ -K_z \end{bmatrix} \otimes \begin{bmatrix} iJ_z & -K_z \end{bmatrix}^* \right\rangle_\omega A_{2\times 2} \end{aligned} \tag{6.37}$$

Also since the matrix $N_{2\times4}$ is transformed to the physical space according to Eq.(6.18), and **Assuming that** $A_{2\times2} \in \text{Re}$ then the

$$Im\{N'_{2\times2}\} = A^{\tau}_{2\times2}\, Im\{N_{2\times2}\}\, A_{2\times2} \tag{6.38}$$

then

$$\left\langle \begin{bmatrix} iJ'_z \\ -K'_z \end{bmatrix} \otimes \begin{bmatrix} iJ'_z & -K'_z \end{bmatrix}^* \right\rangle_{\omega} = \frac{4\,\omega}{\pi}\theta(\omega,T) Im\{N'_{2\times2}\} \tag{6.39}$$

Similar cross correlations relations between the $z-$ and transverse components can be found in a simillar way to the previous subsections. The cross spectral correlation between the longitudinal and transverse components as following:

$$\begin{aligned} \left\langle \begin{bmatrix} iJ'_z \\ -K'_z \end{bmatrix} \otimes \begin{bmatrix} iJ'_T & -K'_T \end{bmatrix}^* \right\rangle_{\omega} &= \left\langle A^{\tau}_{2\times2} \begin{bmatrix} iJ_z \\ -K_z \end{bmatrix} \otimes \begin{bmatrix} iJ_T & -K_T \end{bmatrix}^* B_{4\times4} \right\rangle_{\omega} \\ &= A^{\tau}_{2\times2} \left\langle \begin{bmatrix} iJ_z \\ -K_z \end{bmatrix} \otimes \begin{bmatrix} iJ_T & -K_T \end{bmatrix}^* \right\rangle_{\omega} B_{4\times4} \end{aligned} \tag{6.40}$$

Also since the matrix $M_{2\times4}$ is transformed to the physical space according to Eq.(6.18), and **Assuming that both** $B_{4\times4} \in \text{Re}$ **and** $A_{2\times2} \in \text{Re}$ which imply that $A^{\tau}_{2\times2}\frac{1}{\omega}G_{2\times4}$ found in Eq.(6.18) is also real, then the

$$Im\{M'_{2\times4}\} = A^{\tau}_{4\times4} Im\{M_{2\times4}\} B_{4\times4} \tag{6.41}$$

then

$$\left\langle \begin{bmatrix} iJ'_z \\ -K'_z \end{bmatrix} \otimes \begin{bmatrix} iJ'_T & -K'_T \end{bmatrix}^* \right\rangle_\omega = \frac{4\,\omega}{\pi}\theta(\omega,T)Im\{M'_{2\times4}\} \tag{6.42}$$

but since the virtual space is vacuum $Im\{M_{2\times4}\} = 0$ then

$$\left\langle \begin{bmatrix} iJ'_z \\ -K'_z \end{bmatrix} \otimes \begin{bmatrix} iJ'_T & -K'_T \end{bmatrix}^* \right\rangle_\omega = 0 \tag{6.43}$$

Also a similar relation can be found using the same procedure for transverse-longitudinal correlations

$$\left\langle \begin{bmatrix} iJ'_T \\ -K'_T \end{bmatrix} \otimes \begin{bmatrix} iJ'_z & -K'_z \end{bmatrix}^* \right\rangle_\omega = \frac{4\,\omega}{\pi}\theta(\omega,T)Im\{P'_{4\times2}\} \tag{6.44}$$

since the media in the virtual space was reciprocal, then the

$$P'_{4\times2} = M'^{\tau}_{2\times4} \quad \text{and} \;\; Im\{P'_{4\times2}\} = Im\{M'^{\tau}_{2\times4}\} = 0 \tag{6.45}$$

then

$$\left\langle \begin{bmatrix} iJ'_z \\ -K'_z \end{bmatrix} \otimes \begin{bmatrix} iJ'_T & -K'_T \end{bmatrix}^* \right\rangle_\omega = \left\langle \begin{bmatrix} iJ'_T \\ -K'_T \end{bmatrix} \otimes \begin{bmatrix} iJ'_z & -K'_z \end{bmatrix}^* \right\rangle^\tau_\omega = 0 \tag{6.46}$$

then

$$\begin{gathered} \langle J'_z J'^*_T\rangle_\omega = \langle J'_T J'^*_z\rangle_\omega = \langle K'_z J'^*_T\rangle_\omega = \langle J'_T K'^*_z\rangle_\omega = 0 \\ \langle K'_z K'^*_T\rangle_\omega = \langle K'_T K'^*_z\rangle_\omega = \langle J'_z K'^*_T\rangle_\omega = \langle K'_T J'^*_z\rangle_\omega = 0 \end{gathered} \tag{6.47}$$

In summary, in a reciprocal chiral media, thermal electric and magnetic currents are uncorrelated.

6.3.3 Thermal illusion using FT based cloaks

In this section, we show how to achieve Thermal radiation illusion by FT transforming between two spaces making use of the FT transformation of FE discussed in previous subsection. We consider the following illustrative numerical example of transformation between $2D$ spaces. As shown in Fig. 6.1, the virtual space includes a thermal emitter α which has a circular shape of radius ρ_{ex}. It is desired that when thermally radiating, these cylinders mimic the TR signature of another circular thermal emitter α' with outer radius ρ_{ex} in vacuum object for E- and H-polarization.

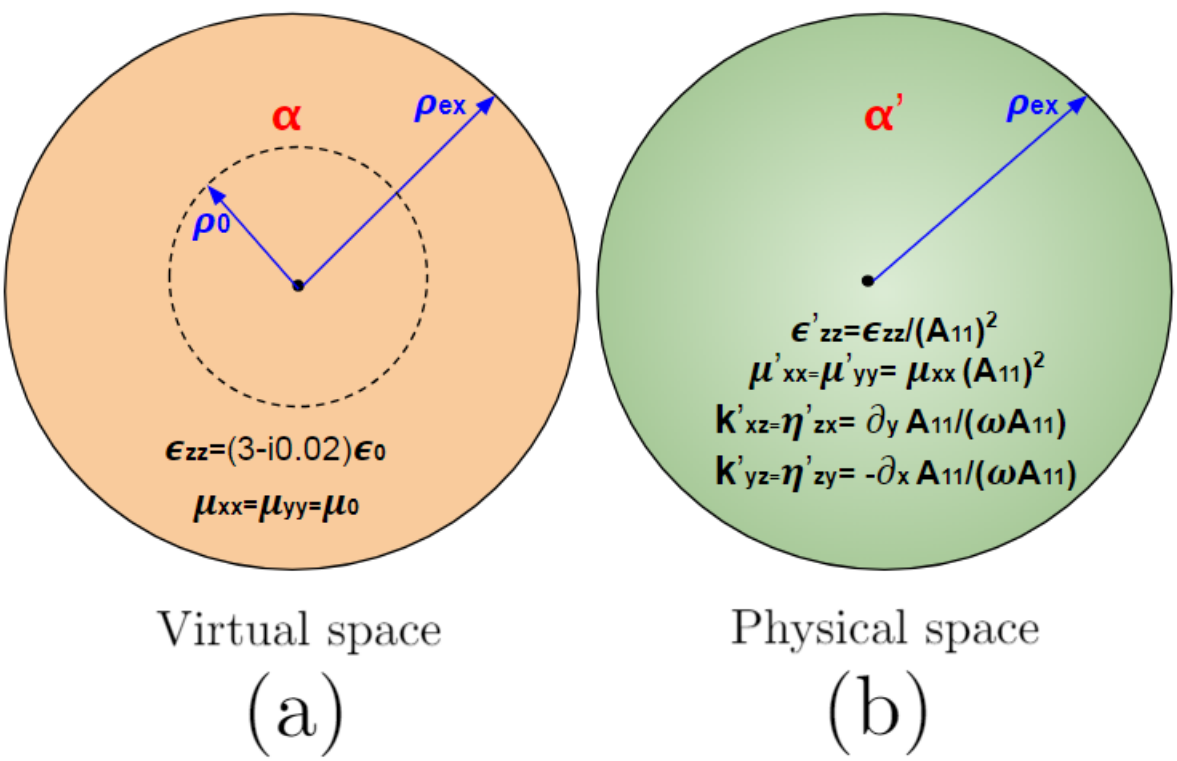

Figure 6.1: schematic of the TR illusion.

For simplicity We consider the case when $A_{12} = A_{21} = 0$, or E- and H- polar-

izations stay uncoupled in the physical space. Due to such decoupled, we consider only the E-polarized thermal radiation. Accordingly A_{11} is the only parameter that controls the transformation of E-polarization. The media of the thermal emitter α in the virtual space can considered to be as following:

$$\begin{aligned} \epsilon_{zz} &= (3 - i0.02)\epsilon_0 \\ \mu_{xx} &= \mu_{yy} = \mu_0 \end{aligned} \tag{6.48}$$

By applying a FT transformation the media of the thermal emitter α' in the physical space are written in terms of those of the virtual space as following:

$$\begin{aligned} \epsilon'_{zz} &= \frac{1}{A_{11}^2}\epsilon_{zz} \\ \mu'_{xx} &= \mu'_{yy} = A_{11}^2\mu_0 \\ k'_{zx} &= \eta'_{xz} = \frac{1}{\omega A_{11}}\frac{\partial A_{11}}{\partial y} \\ k'_{zy} &= \eta'_{yz} = -\frac{1}{\omega A_{11}}\frac{\partial A_{11}}{\partial x} \end{aligned} \tag{6.49}$$

Actually based on Eq.s(6.48) and (6.49), only the thermal electric current polarized along z axis contribute to the E-polarized thermal radiation. Appendix D summarizes the differential equations for both H- and E- polarizations in a general bi-anisotropic media spaces. For the example in hand, numerical simulation is performed using TDDA algorithm explained in appendix(D) with computations are done using COMSOL 3.5A. Thermally radiated poynting vector in both the virtual space and physical space is plotted in Fig.(6.2). As shown in Fig.(6.2) the thermally radiated poynting vector at $\rho > \rho_{ex}$ is the same for both spaces which reflects that $A_{11} = 1$ at $\rho > \rho_{ex}$. In summary, FT adds an extra degree of freedom to achieve thermal radiation and scattering illusion.

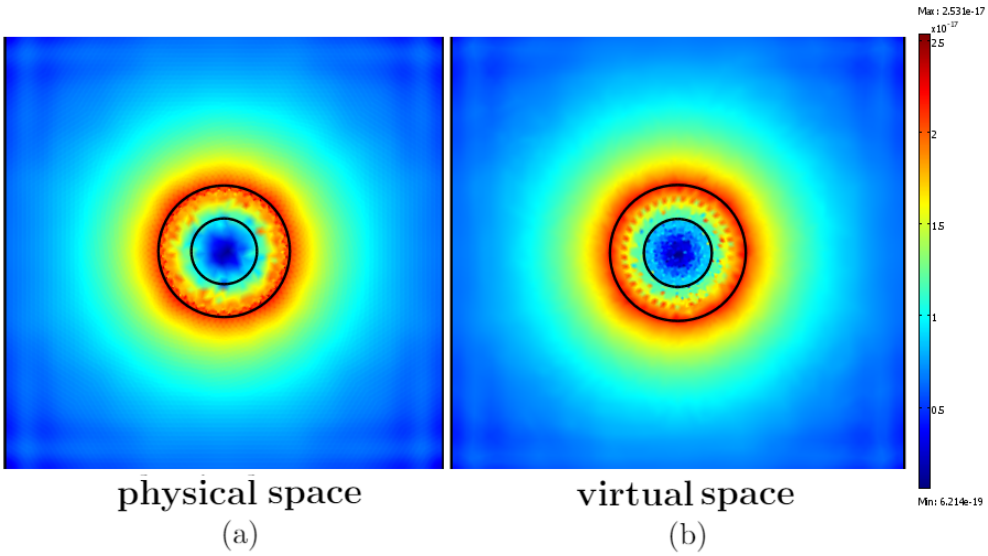

Figure 6.2: Thermally radiated poynting vector in both physical and virtual spaces. (a) Physical space. (b) virtual space. Simulation is done at $\lambda = 5\mu m$, $\rho_{ex} = 60\mu m$ and $\rho_0 = 30\mu m$

6.4 Discontinuous Field Transformation

As it was shown in previous section, one is free to tailor the FT transformation through manipulating the elements of $A_{2\times2}$ matrix in order to match between the properties of the object to be cloaked and the target object. The continuity of the elements of $A_{2\times2}$ forces designing cloaks that are bulky, inhomogeneous and bi-anisotropic. In a similar manner to chapter IV, we propose designing metasurfaces to replace the cloaks due to continuous FT transformations. First, we investigate discontinuous FT where two adjacent regions of space are field transformed differently and a chiral metasurface is computed according to the discontinuity. The susceptibility tensor of such metasurfaces are computed in terms of the Ft discontinuity using GSTC model and numerical simulation are performed to compare between both types of cloaks. Then, we will investigate the circuit model of such metasurface and we will show that it acts a step up (down) electric transformer that modulate the surface impedance of the coated object to match the same surface impedance of the target object. Finally, It will be shown that for a real FT, the metasurface is loss-less and

equivalent to an loss-less electric transformer and when considering thermal radiations, the lossless metasurface don't contribute to thermal radiation but it merely modulates the thermally radiated power from the cloaked object to match that of another target thermal emitter at the same absolute temperature.

6.4.1 GSTC model for a discontinuous FT based mantle cloak

In this subsection, we show the equivalence between a thin chiral meta-surface separating two regions and a discontinuous field transformation performed at these two regions. Starting with a virtual space, and for simplicity, consider a circular shaped boundary with radius $\rho = \rho_s$.

By applying the following discontinuous field transformation

$$\begin{aligned} A_{2\times 2} &= \begin{bmatrix} A_{11}(\rho,\phi) & A_{12}(\rho,\phi) \\ A_{21}(\rho,\phi) & A_{22}(\rho,\phi) \end{bmatrix} \quad \rho < \rho_s \\ &= \begin{bmatrix} 1 & 0 \\ 0 & 1 \end{bmatrix} \qquad \rho > \rho_s \end{aligned} \tag{6.50}$$

then the out of plane components are transformed as following:

$$\begin{bmatrix} E_z'^{+} \\ iH_z'^{+} \end{bmatrix} = A_{2\times 2}(\rho_s) \begin{bmatrix} E_z'^{-} \\ iH_z'^{-} \end{bmatrix} \tag{6.51}$$

where $+$ and $-$ indicate quantities at both sides of the boundary $\rho = \rho_s^+$ and $\rho = \rho_s^-$ respectively. Accordingly the transverse components are constrained to be transformed with a transformation as following:

$$\begin{bmatrix} E_\phi'^{-} \\ iH_\phi'^{-} \end{bmatrix} = B_{4\times 4}^{-1} \begin{bmatrix} E_\phi'^{+} \\ iH_\phi'^{+} \end{bmatrix} : \tag{6.52}$$

Now we derive the susceptibility tensor required for the metasurface that emerges due to the discontinuous FT. The discontinuity of the field transformation can be accommodated using a metasurface which susceptibility tensors which can derived using the GSTC model as following:

$$\begin{bmatrix} \Delta E_z \\ i\Delta H_z \end{bmatrix} = \omega \begin{bmatrix} \chi_{me}^{\phi z} & \chi_{mm}^{\phi z} \\ \chi_{ee}^{\phi z} & \chi_{em}^{\phi z} \end{bmatrix} \begin{bmatrix} E_{z,av} \\ iH_{z,av} \end{bmatrix} = \underline{\underline{\chi}}^{\phi z} \begin{bmatrix} E_{z,av} \\ iH_{z,av} \end{bmatrix} \tag{6.53}$$

where

$$\underline{\underline{\chi}}^{\phi z} = \frac{1}{2\omega} \left[\underline{\underline{A}}_{2\times 2} - \underline{\underline{I}} \right]^{-1} \left[\underline{\underline{I}} + \underline{\underline{A}}_{2\times 2} \right] \tag{6.54}$$

accordingly

$$\begin{aligned} \chi_{me}^{\phi z} &= \frac{1}{2\omega} \frac{A_{11}A_{22} - A_{12}A_{21} - A_{11} + A_{22} - 1}{A_{11}A_{22} - A_{12}A_{21} - A_{11} - A_{22} + 1} \\ \chi_{mm}^{\phi z} &= \frac{1}{2\omega} \frac{-2A_{12}}{A_{11}A_{22} - A_{12}A_{21} - A_{11} - A_{22} + 1} \\ \chi_{ee}^{\phi z} &= \frac{1}{2\omega} \frac{-2A_{21}}{A_{11}A_{22} - A_{12}A_{21} - A_{11} - A_{22} + 1} \\ \chi_{em}^{\phi z} &= \frac{1}{2\omega} \frac{A_{11}A_{22} - A_{12}A_{21} + A_{11} - A_{22} - 1}{A_{11}A_{22} - A_{12}A_{21} - A_{11} - A_{22} + 1} \end{aligned} \tag{6.55}$$

similarly, the susceptibility elements of the metasurface that relates the transverse components are derived as following:

$$\begin{bmatrix} \Delta E_\phi \\ i\Delta H_\phi \end{bmatrix} = -\omega \begin{bmatrix} \chi_{me}^{z\phi} & \chi_{mm}^{z\phi} \\ \chi_{ee}^{z\phi} & \chi_{em}^{z\phi} \end{bmatrix} \begin{bmatrix} E_{\phi,av} \\ iH_{\phi,av} \end{bmatrix} = -\underline{\underline{\chi}}^{z\phi} \begin{bmatrix} E_{\phi,av} \\ iH_{\phi,av} \end{bmatrix} \tag{6.56}$$

where

$$\underline{\underline{\chi}}^{z\phi} = \frac{1}{2\omega} \left[\underline{\underline{F}}_{2\times 2} - \underline{\underline{I}} \right]^{-1} \left[\underline{\underline{I}} + \underline{\underline{F}}_{2\times 2} \right] \tag{6.57}$$

accordingly

$$\chi_{me}^{z\phi} = \frac{1}{2\omega}\,\frac{A_{11}A_{22} - A_{12}A_{21} + A_{11} - A_{22} - 1}{A_{11}A_{22} - A_{12}A_{21} - A_{11} - A_{22} + 1}$$

$$\chi_{mm}^{z\phi} = \frac{1}{2\omega}\,\frac{-2A_{12}}{A_{11}A_{22} - A_{12}A_{21} - A_{11} - A_{22} + 1}$$

$$\chi_{ee}^{z\phi} = \frac{1}{2\omega}\,\frac{-2A_{21}}{A_{11}A_{22} - A_{12}A_{21} - A_{11} - A_{22} + 1} \tag{6.58}$$

$$\chi_{em}^{z\phi} = \frac{1}{2\omega}\,\frac{A_{11}A_{22} - A_{12}A_{21} - A_{11} + A_{22} - 1}{A_{11}A_{22} - A_{12}A_{21} - A_{11} - A_{22} + 1}$$

comparing Eq.s(6.55) and (6.58) we can see that

$$\underline{\underline{\chi}}^{z\phi} = \left(\underline{\underline{\chi}}^{z\phi}\right)^{\tau} \tag{6.59}$$

which is the necessary condition to ensure the reciprocity of the metasurface and also a natural consequence since the virtual space is reciprocal and FT one results in reciprocal media.

Now numerical simulations are performed using *COMSOL 3.5A* to validate the concept of the mantle metasurface based on discontinuous metasurface. Consider a virtual space with homogeneous magnetic dielectric media with constitutive parameters ϵ_d and μ_d, by applying the following field transformation

$$
\begin{aligned}
A_{2\times 2} &= \begin{bmatrix} A_{11} & 0 \\ 0 & A_{22} \end{bmatrix} \quad \rho < \rho_s \\
&= \begin{bmatrix} 1 & 0 \\ 0 & 1 \end{bmatrix} \qquad \rho > \rho_s
\end{aligned}
\tag{6.60}
$$

where A_{11} and A_{22} are constants and $A_{12} = A_{21} = 0$. In such case the E- and H-polarizations are uncoupled. The media is transformed as following:

$$
\begin{aligned}
\epsilon'_{zz} &= A_{11}^2 \epsilon_d \qquad \mu'_{\phi\phi} = \mu'_{\rho\rho} = A_{11}^{-2} \mu_d \\
\mu'_{zz} &= A_{22}^2 \mu_d \qquad \epsilon'_{\phi\phi} = \epsilon'_{\rho\rho} = A_{22}^{-2} \mu_d
\end{aligned}
\tag{6.61}
$$

considering the special case when $A_{11} = A_{22}^{-1} = A$, then the medium in the physical space is homogeneous and isotropic with the following constitutive parameters:

$$
\epsilon' = A^2 \epsilon_d \qquad \mu' = A^{-2} \mu_d \tag{6.62}
$$

with the fields are transformed as following

$$
E'_z = \frac{1}{A} E_z \;\; H'_T = A H_T \tag{6.63}
$$

Accordingly, the susceptibilities of the metasurface will be written as following:

$$
\begin{aligned}
\chi_{me}^{\phi z} = \chi_{em}^{\phi z} &= \frac{1}{2\omega} \frac{A+1}{A-1} \\
\chi_{mm}^{\phi z} = \chi_{ee}^{\phi z} &= 0
\end{aligned}
\tag{6.64}
$$

Numerical simulations are shown in Fig.s(6.3) and (6.4) where a plane wave is propagating in a PMC wave-guide including a cylindrical scatterer. In Fig.(6.3), the media parameters of the scatterer are chosen to be $\epsilon_d = \epsilon_0$, $\mu_d = \mu_0$, while Fig.(6.4), the media parameters of the scatterer are chosen to be $\epsilon_d = 10\epsilon_0$, $\mu_d = 2\mu_0$. For both simulations $A = 2$. The metasurface of susceptibilities in Eq.(6.64) is positioned at $\rho = \rho_s$ in the physical space. It is clear that the fields in the physical and virtual spaces are same for $\rho > \rho_s$

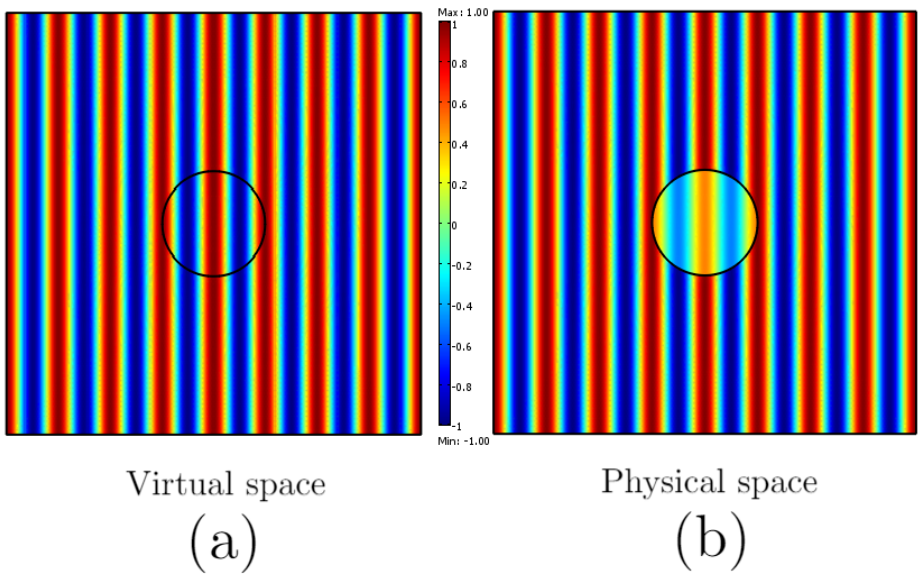

Figure 6.3: Schematic of invisibility cloaking using metasurface based on discontinuous FT. (a) Virtual space of vacuum. (b) Physical space including discontinuous FT based metasurfaces. Simulation is done with the following parameters: $\rho_s = 50\mu m$, wavelength is $100\mu m$, $\epsilon_d = \epsilon_0$, $\mu_d = \mu_0$ and $A = 2$

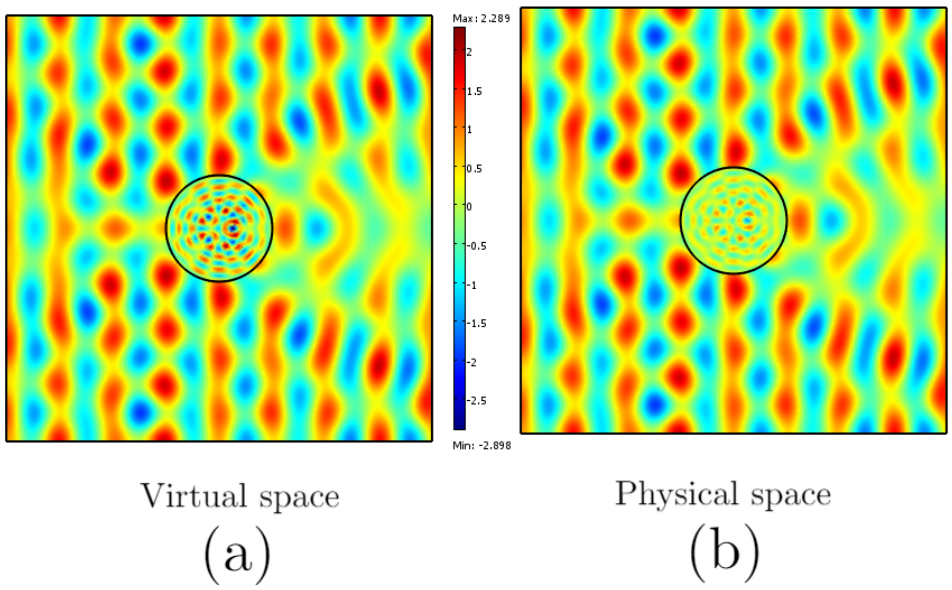

Figure 6.4: Schematic of scattering illusion cloaking using metasurface based on discontinuous FT. (a) Virtual space of vacuum. (b) Physical space including discontinuous FT based metasurfaces. Simulation is done with the following parameters: $\rho_s = 50\mu m$, wavelength is $100\mu m$,$\epsilon_d = 10\epsilon_0$, $\mu_d = 2\mu_0$, $A = 2$

Finally, a comparison is held between invisibility cloaking using continuous FT transformation and cloaking using metasurface based on discontinuous FT. In Fig.(6.5), a virtual space of vacuum is FT transformed into a physical space using the following transformation:

$$A_{11} = \begin{cases} 2 & \rho \geq \rho_0 \\ \frac{\rho_{ex}-\rho_0}{\rho_{ex}-\rho_0} + 1 & \rho_0 \leq \rho \leq \rho_{ex} \\ 1 & \rho \geq \rho_{ex} \end{cases} \tag{6.65}$$

the cloak is located in the region $\rho_0 < \rho < \rho_{ex}$. The bi-anisotropic term is plotted in Fig.(6.6). Also in Fig.(6.5,c) the cloak is replaced by the corresponding chiral metasurface and it is clear the fields in all space is the same at $\rho > \rho_{ex}$, also the fields in the physical spaces are the same for the region $\rho < \rho_0$.

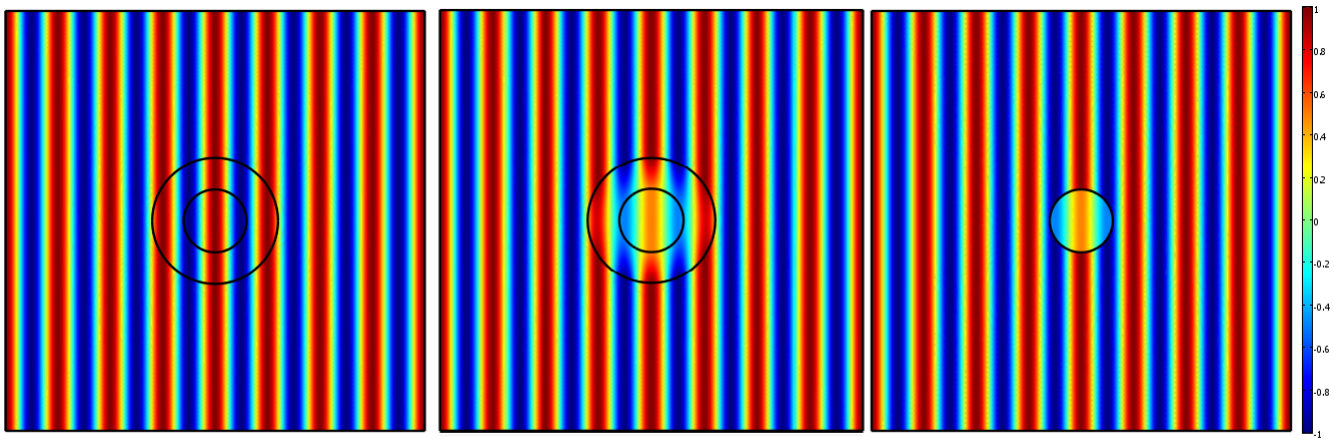

(a)Virtual space (vacuum) (b) FT cloak (c) Discontinuous FT metasurface

Figure 6.5: Comparison of invisibility cloaking using continuous FT based cloaks and discontinuous FT based metasurfaces. A plane wave is incident from the left side.(a) Virtual space of vacuum. (b) Physical space including continuous FT based cloak. (c) Physical space including discontinuous FT based metasurfaces. Simulation is done with the following parameters: $\rho_0 = 30\mu m$, $\rho_{ex} = 60\mu m$ and wavelength is $100\mu m$.

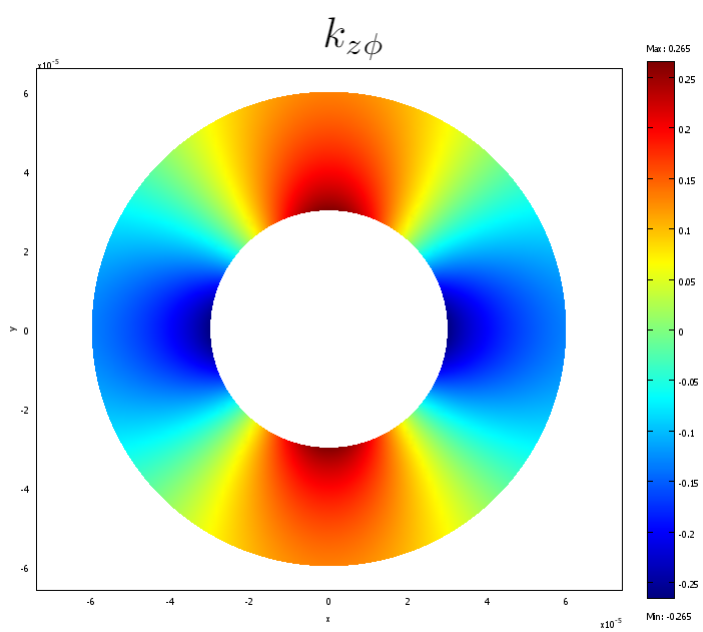

Figure 6.6: Plot of the magneto-electric coupling coefficient k_{zx} of the cloak due to continuous FT transformation.

6.4.2 Circuit model for the discontinuous FT mantle cloak

In chapter(V), It was shown theta thermal emitter can be compressed into a metasurface and both have the same thermal radiation signature as long as both have the same surface impedance. In section(6.3), it was shown that thermal radiation illusion is possible using continuous FT based cloaks and in the previous section it was shown that scattering and invisibility illusions are possible using such metasurface. Here we investigate the role of the discontinues FT based metasurface to achieve thermal radiation illusion. Now, consider a virtual space that includes a cylindrical shaped thermal emitter of homogeneous and isotropic media with permittivity ϵ_d and permeability μ_d and surrounded by vacuum. Considering E-polarization, such thermal emitter can be characterized by a non-local MS such that the surface impedance value vary with the cylindrical order as following:

$$Z_s[n] = j\eta_d \frac{J_n(k_d\rho)}{\dot{J}_n(k_d\rho)} \tag{6.66}$$

where $k_d = \omega\sqrt{\epsilon_d\mu_d}$ and $\eta_d = \sqrt{\frac{\mu_d}{\epsilon_d}}$ are the wave numbers and impedance of the thermal emitter in the virtual spaces. Now, by applying FT the thermal emitter is transformed into another thermal in the physical space with the shape and dimensions. Assuming the special case of discontinous FT, where $A_{11} = A_{22}^{-1} = A$ and $A_{12} = A_{21} = 0$ so that E- and H- polarizations are uncoupled. The $\rho > \rho_s$ region is unity transformed, so $A = 1$ then the fields in this region are the same for both the virtual and physical spaces. Now consider only E-polarization, the fields are transformed as following:

$$E'_z(\rho_s^-) = \frac{1}{A}E_z(\rho_s^-) = \frac{1}{A}E_z(\rho_s^+) \;\; H'_T(\rho_s^-) = AH_T(\rho_s^- AH_T(\rho_s^+) \tag{6.67}$$

then the medium in the physical space is homogeneous and isotropic with the

following constitutive parameters:

$$\epsilon' = A^2\epsilon_d \qquad \mu' = A^{-2}\mu_d \tag{6.68}$$

Now the surface impedance of the thermal emitter in the physical is written as following:

$$Z_s'[n] = j\eta' \frac{J_n(k'\rho)}{\dot{J}_n(k'\rho)} \tag{6.69}$$

where k' and η' are the wave number and impedance of the thermal emitter's medium in the physical space.

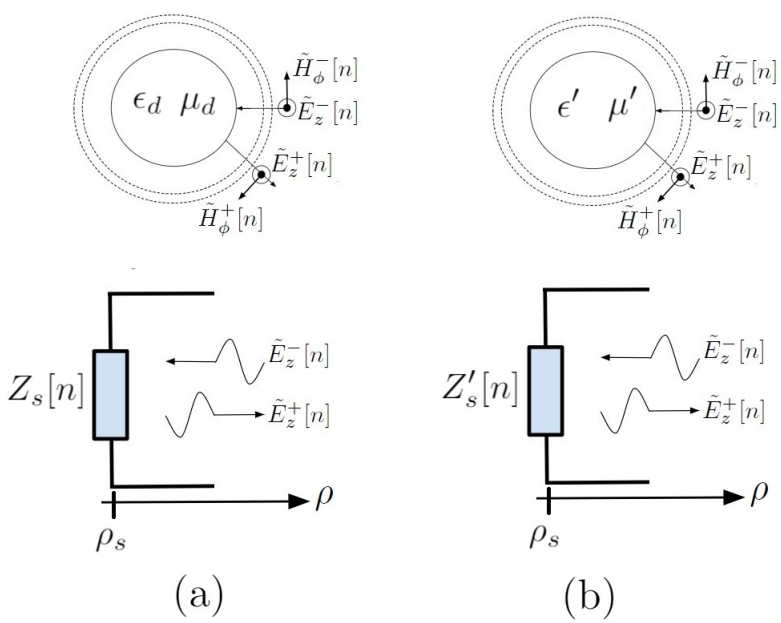

Figure 6.7: Schematic for thermal emitters in both spaces without metasurfaces and their equivalent surface impedance representation. (a)Virtual thermal emitter. (b) Physical space thermal emitter.

Actually, it is clear that

$$\begin{aligned} k_d &= k' \\ \eta_d &= A^{-2}\eta' \end{aligned} \tag{6.70}$$

then the relation between the surface impedances will be written as following:

$$Z'_s[n] = A^2 Z_s[n] \tag{6.71}$$

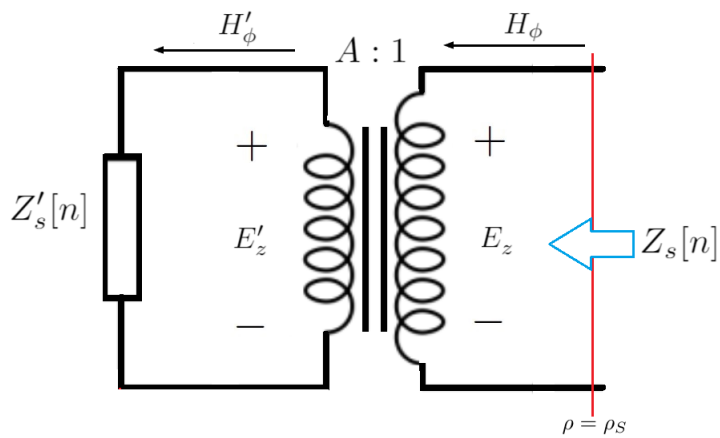

Figure 6.8: A Metasurface based on discontinuous FT can be modelled as a lossless electric transformer with turns ratio $A:1$. The imput impedance of the metasurface with the emitter in the physical space has the same surface impedance as the emitter in the virtual space.

The susceptibilities of the metasurface based on the former discontinuous FT are

$$\chi_{me}^{\phi z} = \chi_{em}^{\phi z} = \frac{1}{2\omega}\frac{A+1}{A-1}$$
$$\chi_{mm}^{\phi z} = \chi_{ee}^{\phi z} = 0 \tag{6.72}$$

Based on the former relation, the discontinuous metasurface can be modelled as an electric transformer which has turns ratio $A:1$ as shown in Fig.(6.8). The voltage ratio is $E'_z = \frac{1}{A}E_z$, while the current ratio is $H'_\phi = AH_\phi$ leading the step up (down) of the impedance $Z_s = A^2 Z'_s$ based on the turns ratio $A > 1$ ($A < 1$).

Based on this circuit model point of view, a discontinuous FT based metasurfaces don't contribute to thermal radiation but merely scales the surface impedance of the

coated thermal emitter. In what follows we prove that thermal radiation is not altered by proving that Nyquist's noise theorem is applied in both space. In what follows we make use of the circuit for thermal noise summarized in appendix(A). For the thermal emitter in the virtual space, its equivalent circuit is shown in Fig.(6.9), with the thermal sources are modelled as voltage source with spectral auto correlation written as following:

$$\left\langle \tilde{V}_s[n]\tilde{V}_s[n] \right\rangle_\omega = \frac{4}{\pi}\Theta(\omega, T)Z_s[n] \tag{6.73}$$

Now for the thermal emitter in the physical space, its equivalent circuit is shown in Fig.(6.9), with the thermal sources are modelled as voltage source with spectral auto correlation written as following:

$$\left\langle \tilde{V}'_s[n]\tilde{V}'_s[n] \right\rangle_\omega = \frac{4}{\pi}\Theta(\omega, T)Z'_s[n] \tag{6.74}$$

In order to prove that the metasurface don't alter the thermal radiation, both circuit models must be equivalent. Such equivalence is shown as following: since $Z'_s[n] = A^2 Z_s[n]$ and by using basic circuit analysis (applying Thevenin equivalence theorem), we find that:

$$V_s[n] = AV'_s[n] \tag{6.75}$$

then by substituting the former equation in Eq.(6.73), we retrieve Eq.(6.74), so we can conclude that thermal radiation illusion can be achieved using lossless metasurface based on real discontinuous FT transformation.

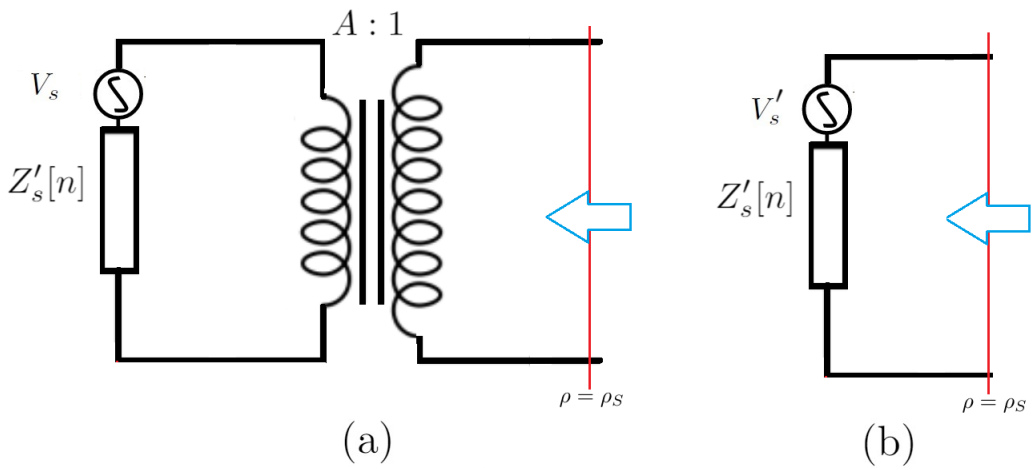

Figure 6.9: Circuit models of the thermal radiation the physical and virtual spaces. (a) Physical space circuitry where the thermal emitter is represented by surface impedance $Z'_s[n]$ and thermal noise is represented by voltage source $V'_s[n]$ connected with the transformer that represent the cloaking metasurface. (b)Virtual space circuitry where the thermal emitter is represented by surface impedance $Z_s[n]$ and thermal noise is represented by voltage source $V_s[n]$.

6.5 Conclusion

In this chapter, we have introduced and validated field transformation (FT) based technique to manipulate both the thermal radiation (TR) and the electromagnetic scattering signature for camouflage or illusion purposes. We showed that fluctuation electrodynamics (FE) is covariant under FT, so that by engineering the parameters of the materials in the physical space, one can get the same TR signature of another one emitted in the virtual space. The concept was illustrated by a numerical example employing a 2D field transformation. Then we propose a technique that combines both discontinuous FT and scattering cancellation techniques. The technique is used to design mantle metasurfaces such that two object related by FT have the same scattering signature. The metasurface is solely depends on the discontinuity of FT. The necessary susceptibility tensors of such metasurface are derived in terms of the FT discontinuity. Finally, a circuit model is derived to model for the mantle cloaks based on discontinuous FT. It was shown that such metasurface act as an electric

transformer which scale the surface impedance of the the coated object.

With respect to the proposed mantle cloaks, they have an advantages over those based on discontinuous transformation optics that they are local so they are much easier to fabricate and implement. A possible limitation is the chirality of such surfaces, however general methodologies to design chiral metasurfaces had been reported [25], [2], opening the door for their implantation in the desired near infra red range.

CHAPTER VII

Conclusions and Future Work

The main aim of the research work presented in this thesis is to present theoretically techniques to achieve thermal radiation and electromagnetic scattering illusions. Different techniques had been proposed based on transformation optics theory, scattering cancellation and duality transformations. The purpose of introducing these techniques is to provide a full theoretical framework so as to allow designing illusion cloaks. Notice that time-varying metasurfaces were considered during this PhD (although not described in this manuscript) and allowed us to emphasize solutions to mimic moving objects, as well as the possibility of linear frequency conversion. However the full theoretical framework is a goal which is still far beyond to be achieved in a single PhD thesis work. There are still more issues related to illusions which remain to be explored. Any future work must address the following the theoretical issues:

1. Is it possible to achieve thermal radiation illusion cloaking, when thermal emitters are out of local equilibrium?. A possible situation is when the temperature of the target and cloaked objects vary with time. In such case, fluctuation electrodynamics and fluctuation dissipation theorem are no more valid to be used to compute thermal fluctuations of the thermal sources. Also, cloaks due to transformation fluctuation electrodynamics of chapter (2) are no more valid. Also the space transformations had to vary in time to accommodate to the variation

of temperature distributions and accordingly, the thermal cloaks presented in chapter (1) are also no more valid to be used.

2. In chapter (5), homogeneous and non local metasurfaces had been proposed to mimic the scattering and the thermal radiation of a target object at constant temperature. Is it possible to apply the same methodology to achieve thermal illusion of a target object with non constant temperature. For instance a multi-layered cylindrical shaped thermal emitter with each layer has it own temperature. When compressing such emitter into a mantle metasurface of "zero thickness", the metasurface is required to have different temperatures simultaneously and this is physically impossible to achieve.

3. Both scattering cancellation and discontinuous transformation optics techniques assume circular and spherical shapes for the mantle cloaks in 2D and 3D spaces respectively. The main aim of such constraint is to have the metasurface shape conformal with the cylindrical and spherical bases, which simplifies the definition of the inner product and accordingly the calculation of the surface impedance. In other words, there is a lack in the literature for designing mantle metasurfaces with arbitrary shapes.

4. Although the theory presented in this work is exact, the dimensions of the objects considered in this thesis are in order of the thermal wavelength (around 10 μm). Typically the applications are concerned with objects with dimensions that are much larger than the thermal wave. The choice of small object is steamed from the limitation of the computational power of using fluctuation electrodynamics within the theoretical framework for calculating thermal radiation. For macroscopic objects, typically, it is the radiative transfer theory which is used. Except for the very simplistic cases, there is lack in the literature for the connection between the microscopic fluctuation electrodynamics theory

and the macroscopic radiative transfer theory.

5. As a step towards mimicking moving targets thermal emitter, time varying metasurface is needed to converting between different harmonic frequencies. However Doppler's effect is more elaborating than mere frequency shift. Actually, even in the simplest case when an object is moving with constant velocity in a fixed direction, special relativity theory must be applied. Then according to special relativity, in each specific direction, the thermal radiation spectrum will be shifted by a frequency shift which varies with the relative solid angle between such direction of observation and the direction of motion. Another relativistic effect is the coupling between transverse polarizations (polarizations directed in the plane normal the direction of motion) and such coupling is affects the apparent wave impedance of the emitted wave [117] and the apparent properties of the thermal emitter. Eventually the thermal radiated power radiated is further modified which shapes further the thermal radiation signature. In summary, Time varying bi-anisotropic (possibly non reciprocal) metasurface is required to achieve thermal radiation illusion of a moving thermal emitter. Of course if the target is accelerating or decelerating, general relativity theory must be considered and another metasurfaces with further complicated features is needed.

Other issues are related to physical realizations and should be addressed by any future work as following:

1. It is known based on the literature of frequency selective surfaces that mantle cloaks computed using scattering cancellation technique are typically modelled as shunt connected surface admittance. On the other had, mantle cloaks of chapter IV computed using discontinuous transformation optics technique is a network which contains series and shunt connected elements. It is noted

that little research had been done in order to design metasurface with series connected impedance.

2. There is no clear methodology to implement the tile varying varying metasurfaces.

   Actually experimental work is needed to verify the models proposed in this thesis, or simplistic cases are needed to chosen to be suitable for the available fabrication and experimental facilities. Notice also that homogenization techniques could provide great help to face such difficulties.

APPENDICES

APPENDIX A

Circuit Model for Thermal Radiation

A.1 Introduction

In this appendix we summarize the main tools to calculate for the thermal radiation (TR) from extended planar slabs and cylindrical shells as shown in Fig.(A.1). A thermal emitter media is always lossy and its constitutive parameters are in general complex valued. Without loss of generality, we consider the thermal emitter to be homogeneous isotropic local media with permittivity $\epsilon = \epsilon' - j\epsilon''$ and permeability $\mu = \mu' - j\mu''$, where ϵ', ϵ'', μ' and $\mu'' \in$ Re. We only consider electromagnetic propagation in 2D space. The $z-$ axis is chosen to be the axis of invariance so that $\frac{\partial}{\partial z} = 0$. This invariance allows to examine the radiation problem as a one dimensional problem with two independent polarization states E and H with respect to z axis. Also, the outer surface of the thermal emitter is assumed to be conformal with the basis (modes) used to describe the field. For instance, the outer surface of a planar emitter must be a perfect plane which is conformal with plane waves and the outer surface from a cylindrical emitter must be perfect cylinder which is conformal with cylindrical waves. The former requirement guarantee that there is no coupling or diffraction

between different modes. In what follows we show that TR can be calculated using two different but equivalent formulations that are:

1. Fluctuation electrodynamics (FE).

2. Nyquist's theorem for thermal noise in electrical resistors.

According to FE, thermal radiation is electromagnetic radiation from thermally fluctuating and in-coherent electric and magnetic current sources. Accordingly, TR is calculated by solving for the green's function of the in-homogeneous Helmholtz equation. As long as the TR radiation is in the direction normal to the planar slabs or in the radial direction of the cylindrical shells is the concern, then the TR calculation is reduced to be one dimensional problem. Such 1D problem can be formulated in terms of a wave propagation in 1D transmission line (TL). The advantage of such approach is that one can simply utilize the tools of the electrical network theory which simplifies the calculation of the thermally radiated field. In such transmission line (TL) model, planar slabs and cylindrical shells are represented by an equivalent circuit model, while the thermal sources are modeled as voltages and currents using Nyquist's theorem of electrical noise.

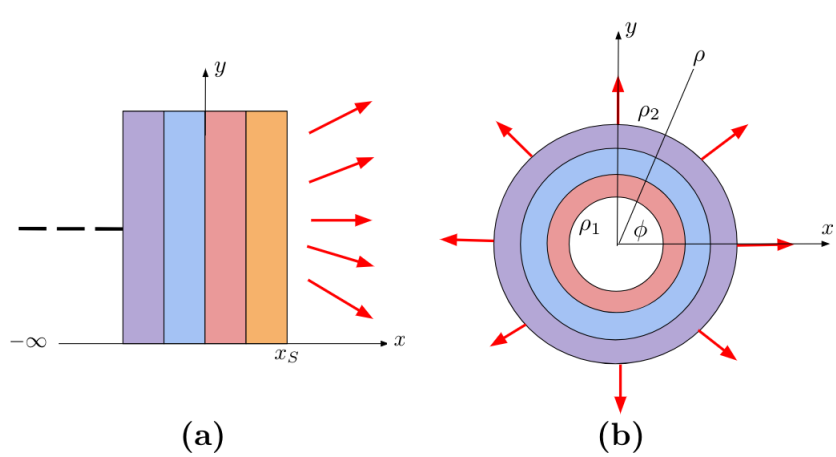

Figure A.1: In this appendix, thermal radiation from (a)stack of planar slabs aligned along x-axis and (b) cascaded cylindrical shells.

This appendix is arranged as following: in section(A.2), Helmholtz equation is derived for a homogeneous, isotropic media including electric and magnetic current sources. The governing equations for both E and H-polarizations are derived. In section(A.3), TR radiation from extended planar slabs is investigated. Also, modal transmission line model is derived and shown to be equivalent to the 1D Helmholtz equation. TR radiation is calculated by both ways where thermal noise is introduced to the modal transmission line through Nyquist theorem while FE is used to introduce the statistics of the thermally fluctuating electric and magnetic currents. Finally TR calculation will be shown to be more simplified using the impedance Z-matrix of the planar slab. The Z-matrix models the slab as a lumped element and thermal noise is introduced using Nyquist's theorem. In section(A.4), the same procedures for calculating TR from cylindrical slabs are shown, with a focus on the Z-matrix representation of the cylindrical slabs. Finally in section(A.5), TR from semi-infinite planar emitter and from cylindrical emitter (that includes the origin) is studied as a limiting case for the planar slabs and cylindrical shell. It will be shown that the surface impedance in both cases includes all the necessary information required to calculate for the TR.

A.2 Helmholtz Equation in Isotropic and Homogeneous Media

Starting with Maxwell's equation

$$\begin{aligned} \nabla \times \bar{E} &= -i\omega\bar{B} - \bar{K} \qquad & \nabla \cdot \bar{D} &= 0 \\ \nabla \times \bar{H} &= i\omega\bar{D} + \bar{J} \qquad & \nabla \cdot \bar{B} &= 0 \end{aligned} \tag{A.1}$$

Note that the medium is assumed to have no free electric or magnetic charge density. Such assumption implies that $\nabla \cdot \bar{J} = \nabla \cdot \bar{K} = 0$. Such assumption is imposed as the time average of thermal electric and magnetic currents vanish $< \bar{J} >_\omega = < \bar{K} >_\omega = 0$. The constitutive relation of the media is written as following:

$$\begin{bmatrix} \bar{D} \\ \bar{B} \end{bmatrix} = \begin{bmatrix} \epsilon & 0 \\ 0 & \mu \end{bmatrix} \begin{bmatrix} \bar{E} \\ \bar{H} \end{bmatrix} \tag{A.2}$$

substituting the former relation in Maxwell's equations, then applying a curl operator upon faraday's law as following:

$$\begin{aligned} \nabla \times \nabla \times \bar{E} &= -i\omega\mu \nabla \times \bar{H} - \nabla \times \bar{K} \\ &= \omega^2 \mu\epsilon \bar{E} - i\omega\mu \bar{J} - \nabla \times \bar{K} \end{aligned} \tag{A.3}$$

then in-homogeneous Helmholtz equation is written as following:

$$\nabla^2 \bar{E} + k^2 \bar{E} = -i\omega\mu \bar{J} - \nabla \times \bar{K} \tag{A.4}$$

where $k = \frac{\omega}{c}$ is the propagation wave number in the media. We had used the following identity relation

$$\nabla \times \nabla \times \bar{E} = \nabla(\nabla \cdot \bar{E}) - \nabla^2 \bar{E} = -\nabla^2 \bar{E} \tag{A.5}$$

similarly the Helmholtz's equation for the magnetic field

$$\nabla^2 \bar{H} + k^2 \bar{H} = -i\omega\epsilon \bar{K} - \nabla \times \bar{J} \tag{A.6}$$

It is assumed that the space is invariant along $z-$axis such that $\frac{\partial}{\partial z} = 0$. Such invariance allow decomposing the electromagnetic problem to be decomposed into two independent problems for two different polarizations; E-polarization where $\bar{E} = \hat{z} E_z$ and H-polarization where $\bar{H} = \hat{z} H_z$. In what follows we derive the governing equations

for each polarization. starting with decomposing the electromagnetic vector field quantities into along and transverse to $z-$axis, as following:

$$\begin{aligned} \bar{E} &= \bar{E}_T + \hat{z}E_z & \bar{H} &= \bar{H}_T + \hat{z}H_z \\ \bar{J} &= \bar{J}_T + \hat{z}J_z & \bar{K} &= \bar{K}_T + \hat{z}K_z \end{aligned} \tag{A.7}$$

substituting the fields in Maxwell's equations as following:

$$\begin{aligned} \nabla \times \hat{z}E_z &= -i\omega\mu\bar{H}_T - \bar{K}_T & \nabla \times \bar{H}_T &= i\omega\epsilon\hat{z}\bar{E}_z + \hat{z}\bar{J}_z \\ \nabla \times \hat{z}H_z &= i\omega\epsilon\bar{E}_T + \bar{J}_T & \nabla \times \bar{E}_T &= -i\omega\mu\hat{z}\bar{H}_z - \hat{z}\bar{K}_z \end{aligned} \tag{A.8}$$

It is clear that the sets $\{E_z,\ \bar{H_T}\ ,\bar{K_T}$ and $J_z\ \}$ and $\{H_z,\ \bar{E_T}\ ,\bar{J_T}$ and $K_z\ \}$ are independent from each other. Both sets are named as $E-$ and $H-$ polarizations respectively. For E-polarization, the governing Helmholtz equation is expressed in terms of E_z as following:

$$\nabla^2(E_z\hat{z}) + k^2(E_z\hat{z}) = -\nabla \times \underline{K}_T - i\omega\mu(J_z\hat{z}) \tag{A.9}$$

where the transverse component $\bar{H}_T$ is computed through Eq.(A.8). While for H-polarization, the governing Helmholtz equation is expressed in terms of H_z as following:

$$\nabla^2(H_z\hat{z}) + k^2(H_z\hat{z}) = -\nabla \times \underline{J}_T - i\omega\varepsilon(K_z\hat{z}) \tag{A.10}$$

where the transverse component $\bar{E}_T$ is computed through Eq.(A.8).

A.3 Thermal Radiation from Planar Slabs

Consider stack of planar slab aligned parallel to the plane $y-z$ such that $x-$axis is the normal to the faces of all the slabs. The planar slabs are assumed to be invariant in $y-z$ plane. In general, The planar layers are of different media or

different temperature distributions, however each layer is assumed to be isotropic, homogeneous and its temperature is uniform. Due to the planar nature of the thermal emitter, the modes are taken to be plane waves.

We are interested to examine the TR in $x-$direction. The thermally radiated electromagnetic field is the sum of E- and H- polarized plane waves. Considering the E-polarization E_z, we are searching for solutions having the following form:

$$\begin{aligned} \bar{E}_z(x,y) &= \tilde{E}_z(x)e^{ik_y y} & \bar{H}_T(x,y) &= \tilde{\bar{H}}_T(x)e^{ik_y y} \\ \bar{J}_T(x,y) &= \tilde{\bar{J}}_z(x)e^{ik_y y} & K_z(x,y) &= \tilde{K}_z(x)e^{ik_y y} \end{aligned} \tag{A.11}$$

substituting the fields in the Helmholtz's equation of Eq.(A.9) as following:

$$\frac{\partial^2}{\partial x^2}\tilde{E}_z(x) + k_x^2\tilde{E}_z(x) = -\frac{\partial}{\partial x}\tilde{K}_y(x) + ik_y\tilde{K}_x(x) - i\omega\mu\tilde{J}_z(x) \tag{A.12}$$

where $k_x = \sqrt{k^2 - k_y^2}$. Solving the former ordinary differential equation involves the solution of the homogeneous form of same equation or in other words the Helmholtz equation in a free source homogeneous media $\tilde{K}_y = \tilde{K}_x(x) = \tilde{J}_z(x) = 0$

$$\frac{\partial^2}{\partial x^2}\tilde{E}_z(x) + k_x^2 E_z(x) = 0 \tag{A.13}$$

then the electric field has the following

$$\bar{E}_z(x,y) = \tilde{E}_z(x) = \tilde{\bar{E}}_z^{+}e^{-i(k_x x + k_y y)} + \tilde{\bar{E}}_z^{-}e^{(ik_x x - ik_y y)} \tag{A.14}$$

which is superposition of forward and backward propagating plane waves with spatial frequencies $(\pm k_x, k_y)$ and amplitudes $\tilde{\bar{E}}_z^{+}$ and $\tilde{\bar{E}}_z^{-}$ respectively. Similarly for H-polarization:

$$\frac{\partial^2}{\partial x^2}\tilde{H}_z(x) + k_x^2 H_z(x) = -\frac{\partial}{\partial x}\tilde{J}_y(x) + ik_y\tilde{J}_x(x) - i\omega\epsilon\tilde{K}_z(x) \tag{A.15}$$

In general, an arbitrary propagating field can be decomposed into plane waves using Fourier transform with respect to time and transverse coordinate y as following

$$\bar{E}(x,y) = \frac{1}{2\pi}\int \tilde{\bar{E}}(k_y)e^{-j(k_y y + k_x x)}dk_y\, d\omega \tag{A.16}$$

where the tilde indicates a Fourier transformed quantity. k_x and k_y are the Cartesian components of the wave vector, such that $k_x^2 + k_y^2 = k^2 = \omega^2\epsilon\mu$. For each plane wave specified by k_y, its wave impedance is defined as following:

$$\eta = \{ \begin{array}{ll} \omega\mu \,/\, k_x & \text{E-polarization} \\ k_x \,/\, \omega\epsilon & \text{H-polarization} \end{array} \tag{A.17}$$

Fluctuation Electrodynamics According to FE theory, Thermal sources associate the media losses. The losses quantified by the imaginary part of the permittivity induce thermally fluctuating thermal electric current density, while the imaginary part of the permeability induce fluctuating magnetic current densities. The spectral correlations of the thermal electric and magnetic currents are written as following:

$$\begin{aligned} \langle K_x(x)K_x^*(x)\rangle_\omega = \left\langle K_y(x)K_y^*(x)\right\rangle_\omega = \langle K_z(x)K_z^*(x)\rangle_\omega = -\frac{4\omega}{\pi}\theta(\omega,T)\,\mathrm{Im}\{\mu(x)\} \\ \langle J_x(x)J_x^*(x)\rangle_\omega = \left\langle J_y(x)J_y^*(x)\right\rangle_\omega = \langle J_z(x)J_z^*(x)\rangle_\omega = -\frac{4\omega}{\pi}\theta(\omega,T)\,\mathrm{Im}\{\epsilon(x)\} \end{aligned} \tag{A.18}$$

where Im is the imaginary operator. Since the media is assumed to be non-chiral, then the cross spectral correlation between thermal magnetic and electric currents vanishes, and the cross spectral correlation between different Cartesian components of the thermal electric or magnetic currents vanish as following:

$$\left\langle K_\alpha(x)J_\beta^*(x)\right\rangle_\omega = \left\langle K_\alpha(x)K_{\beta\neq\alpha}^*(x)\right\rangle_\omega = \left\langle J_\alpha(x)J_{\beta\neq\alpha}^*(x)\right\rangle_\omega = 0 \tag{A.19}$$

where α and $\beta = \{x, y\}$

A.3.1 Telegraphic equation

A modal transmission line is typically used to represent the propagation of plane waves [114] and each mode is specified by the quantities which are conserved along the propagation direction as the polarization state (E/H), angular frequency ω and transverse wave vector k_y. The telegraphic equation models the propagation of electromagnetic signals along a wave-guide. The telegraphic equation models a 1-D propagation of a voltage $V(x,t)$ and current $I(x,t)$ waves along $x-$axis. In this subsection the telegraphic equation is derived and the correspondence between its quantities and the 1D Helmholtz equation is highlighted. The starting point for deriving Telegraphic equation is to consider an infinitesimal section of length Δx of a transmission line as shown in Fig.(A.2). Assuming time harmonic dependence $e^{j\omega t}$ and by applying Kirchoff's voltage and current laws along the circuit as following:

$$\begin{aligned} V(x+\Delta x) - V(x) &= -\frac{1}{2}[R(x) + j\omega L(x)]\Delta x\,(I(x) + I(x+\Delta x)) - V_s(x)\Delta x \\ I(x+\Delta x) - I(x) &= -[G(x) + j\omega C(x)]\Delta x \frac{V(x) + V(x+\Delta x)}{2} - I_p(x)\Delta x \end{aligned} \tag{A.20}$$

where V_s and I_s are series connected voltage source per unit length and parallel connected current source per unit length. By dividing by Δx and taking the limit $\Delta x \longrightarrow 0$, so that the equation becomes:

$$\begin{aligned} \frac{dV}{dx}(x) &= -[R(x) + j\omega L(x)]I(x) - V_s(x) = -Z_s(x)I(x) - V_s(x) \\ \frac{dI}{dx}(x) &= -[G(x) + j\omega C(x)]V(x) - I_s(x) = -Y_s(x)V(x) - I_p(x) \end{aligned} \tag{A.21}$$

where $Z_s = R + j\omega L$, $Y_p = G + j\omega C$. Note the the subscripts s and p indicate series and parallel. The wave equation is derived by applying $\frac{d}{dx}$ on both equations

as following:

$$\begin{aligned}\frac{d^2V}{dx^2}(x) &= -\frac{dZ_s}{dx}I(x) + Z_sY_pV(x) + Z_sI_p - \frac{dV_s}{dx}\\ \frac{d^2I}{dx^2}(x) &= -\frac{dY_s}{dx}V(x) + Y_sZ_sI(x) + Y_sV_s - \frac{dI_s}{dx}\end{aligned} \tag{A.22}$$

The former two Equations equations are coupled. In the case where the transmission line is divided into sections of uniform parameters such that $\frac{dZ_s}{dx} = \frac{dY_s}{dx} = 0$, the wave equations will be uncoupled as following:

$$\begin{aligned}\frac{d^2V}{dx^2}(x) - Z_sY_pV(x) &= \frac{d^2V}{dx^2}(x) + k_x^2V(x) = Z_sI_p\\ \frac{d^2I}{dx^2}(x) - Y_pZ_sI(x) &= \frac{d^2I}{dx^2}(x) + k_x^2I(x) = Y_pV_s\end{aligned} \tag{A.23}$$

In the case when the transmission line is uniform and source-free $V_s = I_s = 0$ the

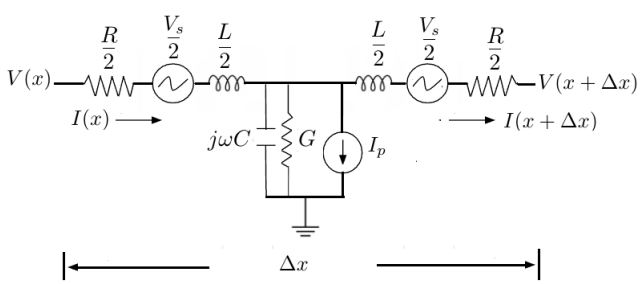

Figure A.2: Distributed parameter model of a transmission line.

solution of the former differential equations will be

$$\begin{aligned}V(x) &= V^+e^{jk_xx} + V^-e^{-jk_xx}\\ I(x) &= \frac{1}{\eta}\left[V^+e^{jk_xx} - V^-e^{-jk_xx}\right]\end{aligned} \tag{A.24}$$

where

$$
\begin{aligned}
k_x &= -j\sqrt{Z_s Y_p} = -j\sqrt{(R+j\omega L)(G+j\omega C)} \\
\eta &= \sqrt{\frac{Z_s}{Y_p}} = \sqrt{\frac{R+j\omega L}{G+j\omega C}}
\end{aligned}
\tag{A.25}
$$

where k_x is the propagation wave number and η is the characteristic impedance of the transmission line.

Correspondance between Telegraphic and 1D Helmholtz's equations Each plane wave specified by (k_y), can be modeled by a modal transmission line which is defined by two quantities, the wave impedance $\eta(k_y)$ and the wave number $\kappa_x = \sqrt{k^2 - k_y^2}$ along the propagation direction x. In each homogeneous slab the transverse components (with respect to direction of propagation x) of electric and magnetic fields of an incident plane wave are represented as voltage and current waves respectively along the transmission line. The correspondence between the different quantities can be shown by comparing Eq.s (A.12) and (A.23), such that for E-polarization

$$
\begin{aligned}
&V^E = \tilde{E}_z \quad I^E = -\tilde{H}_y \quad Z_s^E = j\omega\mu \quad Y_s^E = j\frac{k_x^2}{\omega\mu} \\
&L^E = \mathrm{Re}\{\mu\} \quad C^E = \mathrm{Re}\{\frac{k_x^2}{\omega^2\mu}\} \quad R = -\omega\,\mathrm{Im}\{\mu\} \quad G = -\,\mathrm{Im}\{\frac{k_x^2}{\omega^2\mu}\} \\
&V_s^E = \tilde{K}_y \quad I_s^E = -\tilde{J}_z + \frac{k_y}{\omega\mu}\tilde{K}_x
\end{aligned}
\tag{A.26}
$$

Accordingly the correspondence between the thermal sources can be deduced. The spectral correlation of the voltage and current sources can be derived from the spectral correlations of the corresponding electric and magnetic thermal current densities in

Eq.(A.18) and using the former equations as following:

$$\begin{aligned}
\left\langle V_s^E V_s^E \right\rangle_\omega &= \left\langle K_y(x) K_y^*(x) \right\rangle_\omega = -\frac{4\omega}{\pi}\theta(\omega,T)\,\mathrm{Im}\{\mu(x)\} \\
\left\langle I_s^E I_s^E \right\rangle_\omega &= \left\langle J_z(x) J_z^*(x) \right\rangle_\omega + \frac{k_y^2}{\omega|\mu|^2}\left\langle K_x(x) K_x^*(x) \right\rangle_\omega \\
&= -\frac{4\omega}{\pi}\theta(\omega,T)\left[\mathrm{Im}\{\epsilon\} + \frac{k_y^2}{\omega^2|\mu|^2}\,\mathrm{Im}\{\mu\}\right] \\
&= -\frac{4\omega}{\pi}\theta(\omega,T)\,\mathrm{Im}\left\{\epsilon - \frac{k^2 - k_x^2}{\omega^2\mu\mu^*}\mu^*\right\} \\
&= -\frac{4\omega}{\pi}\theta(\omega,T)\,\mathrm{Im}\left\{\frac{k_x^2}{\omega^2\mu}\right\}
\end{aligned} \tag{A.27}$$

where we had used $\mathrm{Im}\{\mu\} = -\,\mathrm{Im}\{\mu^*\}$, $k_x^2 = k^2 - k_y^2$ and $k^2 = \omega^2\mu\epsilon$. Note that $k_y \in \mathrm{Re}$. But the spectral correlations of the current and voltage sources can be deduced directly from Nyquist theorem as following:

$$\begin{aligned}
\left\langle V_s^E V_s^{E*} \right\rangle_\omega &= \frac{4}{\pi}\theta(\omega,T)R = -\frac{4\omega}{\pi}\theta(\omega,T)\,\mathrm{Im}\{\mu\} \\
\left\langle I_s^E I_s^{E*} \right\rangle_\omega &= \frac{4}{\pi}\theta(\omega,T)G = -\frac{4\omega}{\pi}\theta(\omega,T)\,\mathrm{Im}\{\frac{k_x^2}{\omega^2\mu}\}
\end{aligned} \tag{A.28}$$

Similarly, for H-polarization, the correspondence between the telegraph's and Helmholtz equation quantities is as following:

$$\begin{aligned}
&V^H = \tilde{E}_y \quad I^H = \tilde{H}_z \quad Y_p = j\omega\epsilon \quad Z_s^H = j\frac{k_x^2}{\omega\epsilon} \\
&C^H = \mathrm{Re}\{\epsilon\} \quad L^H = \mathrm{Re}\{\frac{k_x}{\omega\epsilon}\} \quad G^H = -\omega\,\mathrm{Im}\{\epsilon\} \quad R^H = -\omega\,\mathrm{Im}\{\frac{k_x}{\omega\epsilon}\} \\
&I_s^H = \tilde{J}_y \quad V_s^H = -\tilde{K}_z + \frac{k_y}{\omega\epsilon}\tilde{J}_x
\end{aligned} \tag{A.29}$$

Similarly, we can find that the spectral correlations of the current and voltage

sources can be found from the spectral correlations of Eq.(A.18) as following:

$$\begin{aligned}
\left\langle I_p^H I_p^{H*} \right\rangle_\omega &= \left\langle J_y(x) J_y^*(x) \right\rangle_\omega = -\frac{4\omega}{\pi}\theta(\omega,T)\,\mathrm{Im}\{\epsilon\} \\
\left\langle V_s^H V_s^{H*} \right\rangle_\omega &= \left\langle K_z(x) K_z^*(x) \right\rangle_\omega + \frac{k_y^2}{\omega|\epsilon|^2}\left\langle J_x J_x^* \right\rangle_\omega \\
&= -\frac{4\omega}{\pi}\theta(\omega,T)\,\mathrm{Im}\left\{\frac{k_x^2}{\omega^2\epsilon}\right\}
\end{aligned} \tag{A.30}$$

which is consistent with the spectral correlations of the current and voltage sources deduced from Nyquist theorem as following:

$$\begin{aligned}
\left\langle V_s^H V_s^H \right\rangle_\omega &= \frac{4}{\pi}\theta(\omega,T)R^H = -\frac{4\omega}{\pi}\theta(\omega,T)\,\mathrm{Im}\{\frac{k_x^2}{\omega^2\epsilon}\} \\
\left\langle I_s^E I_s^E \right\rangle_\omega &= \frac{4}{\pi}\theta(\omega,T)G^H = -\frac{4\omega}{\pi}\theta(\omega,T)\,\mathrm{Im}\{\epsilon\}
\end{aligned} \tag{A.31}$$

A.3.2 TR using Z-matrix

Another approach to calculate for TR is to use the equivalent lumped circuit model for such slab. The equivalent circuit can be derived using the Z-matrix of such slab as it will be shown in what follows. Starting with a homogeneous planar slab, each E- or H- polarized plane wave with tangential components of the propagation wave-number (also equivalently tangential momentum) k_y, the planar slab is represented with a two port linear circuit model as was shown in Fig.(A.4). The two port network is quantified with an impedance matrix which relates the voltages (electric field) and currents (magnetic fields) connected to the terminals 1 and 2 respectively as following:

$$\begin{aligned}
\tilde{V}_1(k_y) &= \tilde{\tilde{Z}}_{11}(k_y)\tilde{I}_1(k_y) + \tilde{\tilde{Z}}_{12}(k_y)\tilde{I}_2(k_y) \\
\tilde{V}_2(k_y) &= \tilde{\tilde{Z}}_{21}(k_y)\tilde{I}_1(k_y) + \tilde{\tilde{Z}}_{22}(k_y)\tilde{I}_2(k_y)
\end{aligned} \tag{A.32}$$

where $\tilde{V}_1 = \tilde{E}_{z,1}$,$\tilde{V}_2 = \tilde{E}_{z,2}$, $\tilde{I}_1 = -\tilde{H}_{y,1}$and $\tilde{I}_2 = \tilde{H}_{y,2}$. The voltages and currents at the two terminals of a section of the transmission line of length d can be expressed in terms of a $Z-$ matrix

$$\tilde{\tilde{Z}}_{11} = -j\eta\, cot(k_x \frac{\Delta x}{2}) \quad \tilde{\tilde{Z}}_{12} = -j\eta\, csc(k_x \Delta x)$$
$$\tilde{\tilde{Z}}_{21} = -j\eta\, csc(k_x \Delta x) \quad \tilde{\tilde{Z}}_{22} = -j\eta\, cot(k_x \frac{\Delta x}{2}) \tag{A.33}$$

where $k_x = \sqrt{k^2 - k_y^2}$. Now let's consider the T-Network representation of the impedance $Z-$matrix as shown in Fig.(A.3). In such T-network, the terminals 1 and 2 are connected by the series impedances $\tilde{\tilde{Z}}_{s,1}$ and $\tilde{\tilde{Z}}_{s,2}$ and parallel impedance $\tilde{\tilde{Z}}_p$ which are related to the $Z-$ parameters as following:

$$\tilde{\tilde{Z}}_{s,1} = \tilde{\tilde{Z}}_{11} - \tilde{\tilde{Z}}_{12} = j\eta\, tan(k_x \frac{\Delta x}{2})$$
$$\tilde{\tilde{Z}}_p = \tilde{\tilde{Z}}_{21} = -j\eta\, csc(k_x \Delta x) \tag{A.34}$$
$$\tilde{\tilde{Z}}_{s,1} = \tilde{\tilde{Z}}_{22} - \tilde{\tilde{Z}}_{12} = j\eta\, tan(k_x \frac{\Delta x}{2})$$

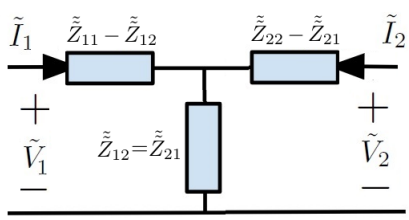

Figure A.3: T-Network representation for the $Z-$matrix of a planar slab.

The losses associated with these impedances will be accompained by thermal electric voltage or current sources according to Nyquist theorem. There are equivalent arrangements of the T-network with the accompanied thermal sources as shown in Fig.(A.4). The auto-correlation of the associated thermal voltage and current sources are according Nyquist's theorem of electrical noise as following:

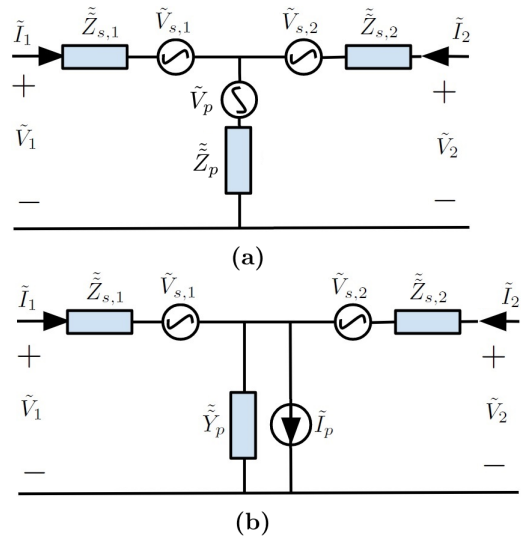

Figure A.4: Two equivalent T-networks with the impedances are associated with Nyquist noise sources represented as voltage (current) sources connected in series (parallel) to the losses represented as series impedance (parallel admittance) respectively. (a) The parallel branch is associated with $\tilde{V}_p$ (b) The parallel branch is associated with $\tilde{I}_p$.

$$\begin{aligned}
\left\langle \tilde{V}_{s,1}(k_y)\tilde{V}^*_{s,1}(k'_y)\right\rangle_\omega &= 4\frac{\epsilon_0}{\pi}\Theta(\omega,T)\,\mathrm{Re}\{\tilde{\tilde{Z}}_{s,1}(k_y\}\delta(k'_y-k_y)\\
\left\langle \tilde{V}_{s,2}(k_y)\tilde{V}^*_{s,2}(k'_y)\right\rangle_\omega &= 4\frac{\epsilon_0}{\pi}\Theta(\omega,T)\,\mathrm{Re}\{\tilde{\tilde{Z}}_{s,2}(k_y)\}\delta(k'_y-k_y)\\
\left\langle \tilde{V}_{p}(k_y)\tilde{V}^*_{p}(k'_y)\right\rangle_\omega &= 4\frac{\epsilon_0}{\pi}\Theta(\omega,T)\,\mathrm{Re}\{\tilde{\tilde{Z}}_{p}(k_y)\}\delta(k'_y-k_y)\\
\left\langle \tilde{I}_{p}(k_y)\tilde{I}^*_{p}(k'_y)\right\rangle_\omega &= 4\frac{\epsilon_0}{\pi}\Theta(\omega,T)\,\mathrm{Re}\{\tilde{\tilde{Y}}_{p}(k_y)\}\delta(k'_y-k_y)
\end{aligned} \tag{A.35}$$

Note that since the thermal voltage sources are associated with different impedances then these sources are uncorrelated or in other words their cross spectral correlations vanish as following:

$$\left\langle \tilde{V}_{s,1}(k_y)\tilde{V}^*_{s,2}(k'_y)\right\rangle_\omega = \left\langle \tilde{V}_{s,2}(k_y)\tilde{V}^*_{p}(k'_y)\right\rangle_\omega = \left\langle \tilde{V}_{p}(k_y)\tilde{V}^*_{s,1}(k'_y)\right\rangle_\omega = 0 \tag{A.36}$$

Similar relation for the T-network (b), replacing $\tilde{V}_p$ with $\tilde{I}_p$. Finally, thermally radiated poynting vector to the surrounded media can be simply calculated by representing the surrounding as loads connected on both sides of the circuit model shown in Fig.(A.4).

The relation between the Z-matrix and the differential length model In the case when the length of the slab is greater than the wavelength of the propagating plane wave, the T-network of a finite length slab shown in Fig.(A.4.b) is reduced to the circuit model of a differential length of the transmission line that represents the plane slab shown in Fig.(A.2) . In this case the phase $k_x\Delta x$ is a small quantity, so that one apply the paraxial approximation upon the values of the elements of the $Z-$matrix such that

$$\begin{aligned}
\tilde{\tilde{Z}}_{s,1} &= +j\eta\, tan(k_x\frac{\Delta x}{2}) \simeq \frac{1}{2}(R+j\omega L)\Delta x \\
\tilde{\tilde{Z}}_{p} &= -j\eta\, csc(k_x\Delta x) \simeq (G+j\omega C)\Delta x \\
\tilde{\tilde{Z}}_{s,2} &= +j\eta\, tan(k_x\frac{\Delta x}{2}) \simeq \frac{1}{2}(R+j\omega L)\Delta x
\end{aligned} \tag{A.37}$$

where we have used Eq.(A.25) and the paraxial approximation $tan(\theta) \simeq \theta$ and $csc(\theta) \simeq \frac{1}{\theta}$ when $\theta \to 0$.

A.3.3 Masloviski's model

Although the circuit model introduced by Masloviski [[78]] was formally derived using reciprocity theorem, here we provide a simpler circuit approach. In Masloviki's work, as shown in Fig.(A.5), the planar slab at temperature T is represented as a network which is quantified by Z-matrix. The sources of the thermal noise are represented by the voltage sources $\tilde{e}_1$ and $\tilde{e}_2$ connected to the terminals 1 and 2. The relation between the voltages and currents at the terminal ends are related as following:

$$
\begin{aligned}
\tilde{V}_1(k_y) + \tilde{e}_1(k_y) &= \tilde{\tilde{Z}}_{11}(k_y)\tilde{I}_1(k_y) + \tilde{\tilde{Z}}_{12}(k_y)\tilde{I}_2(k_y) \\
\tilde{V}_2(k_y) + \tilde{e}_2(k_y) &= \tilde{\tilde{Z}}_{21}(k_y)\tilde{I}_1(k_y) + \tilde{\tilde{Z}}_{22}(k_y)\tilde{I}_2(k_y)
\end{aligned}
\tag{A.38}
$$

The spectral correlations of the thermal voltage sources are closely related to the arguments of the $Z-$ matrix as following:

$$
\begin{aligned}
\left\langle \tilde{e}_1(k_y)\tilde{e}_1^*(k_y') \right\rangle_\omega &= 4\frac{\Theta(\omega,T)}{\pi}\,\mathrm{Re}\{\tilde{\tilde{Z}}_{11}(k_y)\}\delta(k_y'-k_y) \\
\left\langle \tilde{e}_2(k_y)\tilde{e}_2^*(k_y') \right\rangle_\omega &= 4\frac{\Theta(\omega,T)}{\pi}\,\mathrm{Re}\{\tilde{\tilde{Z}}_{22}(k_y)\}\delta(k_y'-k_y) \\
\left\langle \tilde{e}_1(k_y)\tilde{e}_2^*(k_y') \right\rangle_\omega &= 4\frac{\Theta(\omega,T)}{\pi}\,\mathrm{Re}\{\tilde{\tilde{Z}}_{12}(k_y)\}\delta(k_y'-k_y))
\end{aligned}
\tag{A.39}
$$

Actually this correlation can be simply found using the T-network shown in Fig.(A.4). Since by definition, the voltage sources $\tilde{e}_1$ and $\tilde{e}_2$ are the Thevinin sources, then by applying Thevenin's theorem of electrical circuits as shown in Fig.(A.6), we find that

$$
\begin{aligned}
\tilde{e}_1(k_y) &= \tilde{V}_{s,1}(k_y) + \tilde{V}_p(k_y) \\
\tilde{e}_2(k_y) &= \tilde{V}_{s,2}(k_y) + \tilde{V}_p(k_y)
\end{aligned}
\tag{A.40}
$$

then using the latter equation, the spectral correlation of $\tilde{e}_1$ and $\tilde{e}_2$ can be found as following:

$$
\begin{aligned}
\left\langle \tilde{e}_1(k_y)\tilde{e}_1^*(k_y') \right\rangle_\omega &= \left\langle \tilde{V}_{s,1}(k_y)\tilde{V}_{s,1}^*(k_y') \right\rangle_\omega + \left\langle \tilde{V}_p(k_y)\tilde{V}_p^*(k_y') \right\rangle_\omega + \left\langle \tilde{V}_{s,1}(k_y)\tilde{V}_p^*(k_y') \right\rangle_\omega + \left\langle \tilde{V}_p(k_y)\tilde{V}_{s,1}^*(k_y') \right\rangle_\omega \\
&= \left\langle \tilde{V}_{s,1}(k_y)\tilde{V}_{s,1}^*(k_y') \right\rangle_\omega + \left\langle \tilde{V}_p(k_y)\tilde{V}_p^*(k_y') \right\rangle_\omega \\
&= 4\frac{\Theta(\omega,T)}{\pi}\left[\mathrm{Re}\{\tilde{\tilde{Z}}_{11}(k_y) - \tilde{\tilde{Z}}_{12}(k_y)\} + \mathrm{Re}\{\tilde{\tilde{Z}}_{12}(k_y)\}\right]\delta(k_y'-k_y)) \\
&= 4\frac{\Theta(\omega,T)}{\pi}\left[\mathrm{Re}\{\tilde{\tilde{Z}}_{11}(k_y)\}\right]\delta(k_y'-k_y))
\end{aligned}
\tag{A.41}
$$

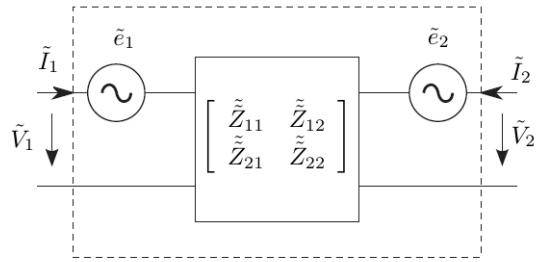

Figure A.5: The equivalent circuit model as proposed by Masloviski et al. A planar slab is represented as a network which is quantified by Z-matrix. The sources of the thermal noise are represented by the voltage sources $\tilde{e}_1$ and $\tilde{e}_2$ which spectral correlations are depicted in Eq.s (A.43).

where we have used the correlation of Eq.(A.36). Similarly

$$\begin{aligned}
\left\langle \tilde{e}_2(k_y)\tilde{e}_2^*(k_y') \right\rangle_\omega &= \left\langle \tilde{V}_{s,2}(k_y)\tilde{V}_{s,2}^*(k_y') \right\rangle_\omega + \left\langle \tilde{V}_p(k_y)\tilde{V}_p^*(k_y') \right\rangle_\omega + \left\langle \tilde{V}_{s,2}(k_y)\tilde{V}_p^*(k_y') \right\rangle_\omega + \left\langle \tilde{V}_p(k_y)\tilde{V}_{s,2}^*(k_y') \right\rangle_\omega \\
&= \left\langle \tilde{V}_{s,2}(k_y)\tilde{V}_{s,2}^*(k_y') \right\rangle_\omega + \left\langle \tilde{V}_p(k_y)\tilde{V}_p^*(k_y') \right\rangle_\omega \\
&= 4\frac{\Theta(\omega,T)}{\pi}\left[\mathrm{Re}\{\tilde{\tilde{Z}}_{22}(k_y) - \tilde{\tilde{Z}}_{12}(k_y)\} + \mathrm{Re}\{\tilde{\tilde{Z}}_{12}(k_y)\}\right]\delta(k_y' - k_y) \\
&= 4\frac{\Theta(\omega,T)}{\pi}\left[\mathrm{Re}\{\tilde{\tilde{Z}}_{22}(k_y)\}\right]\delta(k_y' - k_y))
\end{aligned} \tag{A.42}$$

and finally the cross correlation between $\tilde{e}_1(k_y)$ and $\tilde{e}_2(k_y)$ is derived as following:

$$\begin{aligned}
\left\langle \tilde{e}_1(k_y)\tilde{e}_2^*(k_y') \right\rangle_\omega &= \left\langle \tilde{V}_{s,1}(k_y)\tilde{V}_{s,2}^*(k_y') \right\rangle_\omega + \left\langle \tilde{V}_p(k_y)\tilde{V}_p^*(k_y') \right\rangle_\omega + \left\langle \tilde{V}_{s,1}(k_y)\tilde{V}_p^*(k_y') \right\rangle_\omega + \left\langle \tilde{V}_p(k_y)\tilde{V}_{s,2}^*(k_y') \right\rangle_\omega \\
&= \left\langle \tilde{V}_p(k_y)\tilde{V}_p^*(k_y') \right\rangle_\omega \\
&= 4\frac{\Theta(\omega,T)}{\pi}\left[\mathrm{Re}\{\tilde{\tilde{Z}}_{12}(k_y)\}\right]\delta(k_y' - k_y)
\end{aligned} \tag{A.43}$$

The derivation provided here is much simpler than the derivation of Masloviski et al but the reader is still referred to their work for a formal derivation of the circuit models used in this appendix.

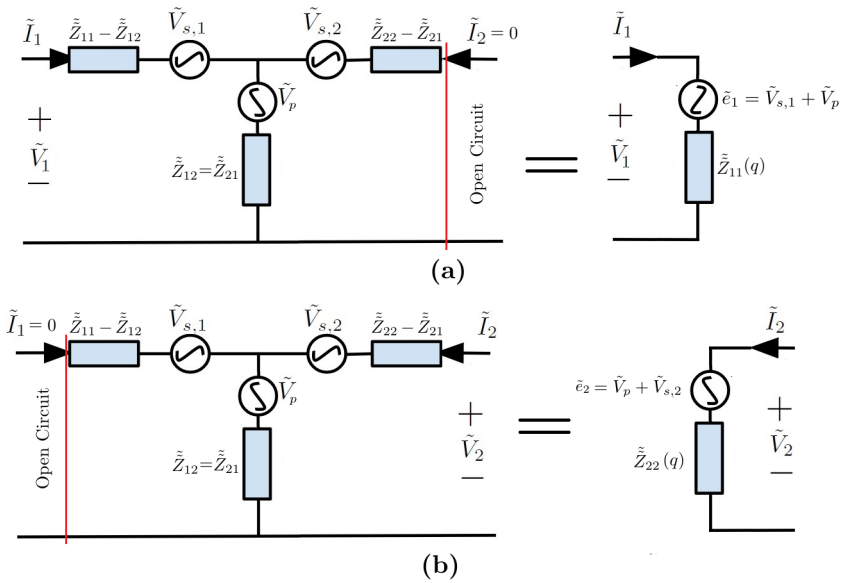

Figure A.6: Schematic shows the steps for deriving the spectral correlations of Eq.s (A.43) from the T-Network shown in Fig.(A.4)

A.4 Thermal Radiation from Cylindrical Shells

In a similar manner for planar slabs, we are also interested to examine TR in the radial direction from stack of infinite extended cylindrical shells. The axis of such cylinders is chosen to be the $z-$axis which is taken as the invariance axis. The cylinders are stacked in the radial directions and also, they are assumed to be invariant along the azimuthal $\phi-$ direction. In such geometry, the polar coordinates (ρ, ϕ) are the most appropriate to be used. Considering E-polarization and re-writing the Maxwell's equations of Eq.(A.8) in terms the polar coordinates as following:

$$\begin{aligned}
&\frac{\partial E_z}{\partial \rho} = j\omega\mu H_\phi + K_\phi \\
&\frac{1}{\rho}\frac{\partial E_z}{\partial \phi} = -j\omega\mu H_\rho - K_\rho \\
&\frac{H_\phi}{\rho} + \frac{\partial H_\phi}{\partial \rho} - \frac{1}{\rho}\frac{\partial H_\rho}{\partial \phi} = j\omega\epsilon E_z + J_z
\end{aligned} \tag{A.44}$$

We are interested to compute TR along the radial ρ direction. In such case, the thermally radiated field is expressed in terms of the cylindrical wave basis. Accordingly,

we are searching for solutions which have the following form:

$$\begin{aligned} E_z(\rho,\phi) &= \tilde{E}_z[\rho,n]e^{in\phi} & \bar{H}_T(\rho,\phi) &= \tilde{\bar{H}}_T[\rho,n]e^{in\phi} \\ \bar{J}_T(\rho,\phi) &= \tilde{\bar{J}}_T[\rho,n]e^{in\phi} & K_z(\rho,\phi) &= \tilde{K}_z[\rho,n]e^{in\phi} \end{aligned} \tag{A.45}$$

Note that the former field forms are eigenfunctions of the operator $\frac{\partial}{\partial\phi}$ such that $\frac{\partial}{\partial\phi} \Leftrightarrow jn$. Substituting the former field forms in the Maxwell's equations of Eq.(A.44), then

$$\begin{aligned} \tilde{H}_\rho &= -\frac{n}{\omega\mu\rho}\tilde{E}_z + \frac{1}{\omega\mu}\tilde{K}_\rho \\ \frac{H_\phi}{\rho} + \frac{\partial\tilde{H}_\phi}{\partial\rho} - \frac{jn}{\rho}\tilde{H}_\rho &= j\omega\epsilon\tilde{E}_z + \tilde{J}_z \end{aligned} \tag{A.46}$$

The Helmholtz Equation will have the following form:

$$\frac{1}{\rho}\frac{\partial}{\partial\rho}\left(\rho\frac{\partial}{\partial\rho}\tilde{E}_z\right) - \frac{n^2}{\rho^2}\tilde{E}_z + k^2\tilde{E}_z = -\frac{1}{\rho}\frac{\partial}{\partial\rho}\left(\rho\tilde{K}_\phi\right) + j\frac{n}{\rho}\tilde{K}_\rho - i\omega\mu\tilde{J}_z \tag{A.47}$$

Solving the former ordinary differential equation involves the solution of the homogeneous form of same equation or in other words the Helmholtz equation in a free source homogeneous media $\tilde{K}_\phi[\rho,n] = \tilde{K}_\rho[\rho,n] = \tilde{J}_z[\rho,n] = 0$.

$$\frac{1}{\rho}\frac{\partial}{\partial\rho}\left(\rho\frac{\partial}{\partial\rho}\tilde{E}_z\right) - \frac{n^2}{\rho^2}\tilde{E}_z + k^2\tilde{E}_z = 0 \tag{A.48}$$

The former Equation is Bessel's Equation of order n and the solution will have the following form:

$$\tilde{E}_z(\rho,n) = \tilde{\tilde{E}}_z^+ H_n^{(2)}(k\rho) + \tilde{\tilde{E}}_z^- H_n^{(1)}(k\rho) \tag{A.49}$$

where $H_n^{(1)}(k\rho)$ and $H_n^{(2)}(k\rho)$ are Hankel functions of 1st and 2nd types representing in and out going cylindrical waves respectively. $\tilde{\tilde{E}}_z^+$ and $\tilde{\tilde{E}}_z^-$ are the amplitudes of

such cylindrical waves. A general electric field solution will have the following form:

$$E_z(\rho,\phi) = \sum_n \left[\tilde{\tilde{E}}_z^+[n]H_n^{(2)}(k\rho) + \tilde{\tilde{E}}_z^-[n]H_n^{(1)}(k\rho)\right] e^{in\phi} \tag{A.50}$$

A.4.1 Radial transmission line

Although the derivation was done assuming a transmission line to be aligned along x-axis, however the same model can be extended to other coordinate systems for example the radial transmission line which is aligned radially along the ρ [39], [3]. The voltage and current waves are related to the electric and magnetic fields as following: for $E - polarization$

$$V = \sqrt{\rho}E_z \qquad I = -\sqrt{\rho}H_\phi \tag{A.51}$$

while for $H - polarization$

$$V = \sqrt{\rho}E_\phi \qquad I = \sqrt{\rho}H_z \tag{A.52}$$

Now, the modal voltage and current cylindrical waves are written as following:

$$\begin{aligned} V(\rho,\phi) &= \sum_n \tilde{V}[n,\rho]e^{jn\phi} \\ I(\rho,\phi) &= \sum_n \tilde{I}[n,\rho]e^{jn\phi} \end{aligned} \tag{A.53}$$

such that

$$\begin{aligned} \tilde{V}[n,\rho] &= \sqrt{\rho}\tilde{E}_z[n] = \sqrt{\rho}\left(E_n^+H_n^{(2)}(k\rho) + E_n^-H_n^{(1)}(k\rho)\right)e^{jn\phi} \\ \tilde{I}[n,\rho] &= -\sqrt{\rho}\tilde{H}_\phi[n] = j\frac{\sqrt{\rho}}{\eta}\left(E_n^+\dot{H}_n^{(2)}(k\rho) + E_n^-\dot{H}_n^{(1)}(k\rho)\right)e^{jn\phi} \end{aligned} \tag{A.54}$$

where E_n^- and E_n^+ are the amplitudes of the out-going and the in-going cylindrical waves respectively. The complex power carried by a cylindrical wave of order n is calculated as following:

$$\begin{aligned}\frac{1}{2}\tilde{V}[n,\rho]\tilde{I}^*[n,\rho] &= -j\frac{\rho}{2\eta}\left[|E_n^+|^2 H_n^{(2)}(k\rho)\dot{H}_n^{(2)*}(k\rho) + |E_n^-|^2 H_n^{(1)}(k\rho)\dot{H}_n^{(1)*}(k\rho)\right] \\ &\quad - j\frac{\rho}{2\eta}\left[E_n^+ E_n^{-*} H_n^{(2)}(k\rho)\dot{H}_n^{(1)*}(k\rho) + E_n^- E_n^{+*} H_n^{(1)}(k\rho)\dot{H}_n^{(2)*}(k\rho)\right] \\ &= -j\frac{\rho}{2\eta} \times j\frac{2}{\pi k\rho}\left[|E_n^+|^2 - |E_n^-|^2\right] - j\frac{\rho}{2\eta} \times \mathrm{Re}\left\{E_n^- E_n^{+*} H_n^{(1)}(k\rho)\dot{H}_n^{(2)*}(k\rho)\right\}\end{aligned} \tag{A.55}$$

Note that $H_n^{(1)}(k\rho) = H_n^{(2)*}(k\rho)$ also $H_n^{(2)}(k\rho)\dot{H}_n^{(2)*}(k\rho) = J_n(k\rho)\dot{J}_n(k\rho) + Y_n(k\rho)\dot{Y}_n(k\rho) + j\frac{2}{\pi k\rho}$ and $H_n^{(1)}(k\rho)\dot{H}_n^{(1)*}(k\rho) = J_n(k\rho)\dot{J}_n(k\rho) + Y_n(k\rho)\dot{Y}_n(k\rho) - j\frac{2}{\pi k\rho}$.

For the special case of lossless transmission line (k and $\eta \in \mathrm{Re}$), the radiated real power per unit angle ϕ carried by the cylindrical wave of order n will be written as following:

$$\mathrm{Re}\{\frac{1}{2}\tilde{V}[n,\rho]\tilde{I}^*[n,\rho]\} = \frac{1}{\pi k\eta}\left[|E_n^+|^2 - |E_n^-|^2\right] \tag{A.56}$$

then the total power carried will be

$$\int_0^{2\pi} \mathrm{Re}\{\frac{1}{2}\tilde{V}[n,\rho]\tilde{I}^*[n,\rho]\}d\phi = \frac{2}{k\eta}\left[|E_n^+|^2 - |E_n^-|^2\right] \tag{A.57}$$

similar calculation can be done for H-polarization.

A.4.2 TR from cylindrical shell using circuit model

In a similar fashion for thermal radiation from planar slab, thermal radiation from cylindrical shells can be calculated by the the Z-matrix of such shell. Considering an E-polarized cylindrical wave propagating along a cylindrical shell bounded between

two cylinders $\rho_1 < \rho < \rho_2$. Considering the medium to be homogeneous and isotropic media with permittivity ϵ and permeability μ then $k = \omega\sqrt{\epsilon\mu}$ is the propagation wave number. Defining voltage and currents at the inner $\rho = \rho_1$ and outer $\rho = \rho_2$ sides of the annulus ring as following:

$$\begin{aligned}
\tilde{V}_1[n] &= \sqrt{\rho_1}\tilde{E}_{z,1}[n] = \sqrt{\rho_1}\left(E_n^+ H_n^{(2)}(k\rho_1) + E_n^- H_n^{(1)}(k\rho_1)\right) e^{jn\phi} \\
\tilde{I}_1[n] &= -\sqrt{\rho_1}\tilde{H}_{\phi,1}[n] = j\frac{\sqrt{\rho_1}}{\eta}\left(E_n^+ \dot{H}_n^{(2)}(k\rho_1) + E_n^- \dot{H}_n^{(1)}(k\rho_1)\right) e^{jn\phi} \\
\tilde{V}_2[n] &= \sqrt{\rho_2}\tilde{E}_{z,2}[n] = \sqrt{\rho_2}\left(E_n^+ H_n^{(2)}(k\rho_2) + E_n^- H_n^{(1)}(k\rho_2)\right) e^{jn\phi} \\
\tilde{I}_2[n] &= -\sqrt{\rho_2}\tilde{H}_{\phi,2}[n] = j\frac{\sqrt{\rho_2}}{\eta}\left(E_n^+ \dot{H}_n^{(2)}(k\rho_2) + E_n^- \dot{H}_n^{(1)}(k\rho_2)\right) e^{jn\phi}
\end{aligned} \tag{A.58}$$

where $H_n^{(1)}$ and $H_n^{(2)}$ are Hankel functions of order n of 1st and 2nd types, E_n^+ and E_n^- are the amplitude of outgoing ($+\rho$ direction) and in-going ($-\rho$ direction) of cylindrical waves of order n. In order to construct Z-Matrix representation, Eq.(A.58) is arranged as following:

$$\begin{aligned}
\begin{bmatrix} \tilde{V}_1[n] \\ \tilde{V}_2[n] \end{bmatrix} &= \begin{bmatrix} \sqrt{\rho_1}H_n^{(2)}(k\rho_1) & \sqrt{\rho_1}H_n^{(1)}(k\rho_1) \\ \sqrt{\rho_2}H_n^{(2)}(k\rho_2) & \sqrt{\rho_2}H_n^{(1)}(k\rho_2) \end{bmatrix} \begin{bmatrix} E_n^+ \\ E_n^- \end{bmatrix} \\
&= \begin{bmatrix} \sqrt{\rho_1}H_n^{(2)}(k\rho_1) & \sqrt{\rho_1}H_n^{(1)}(k\rho_1) \\ \sqrt{\rho_2}H_n^{(2)}(k\rho_2) & \sqrt{\rho_2}H_n^{(1)}(k\rho_2) \end{bmatrix} \begin{bmatrix} j\frac{\sqrt{\rho_1}}{\eta}\dot{H}_n^{(2)}(k\rho_1) & j\frac{\sqrt{\rho_1}}{\eta}\dot{H}_n^{(1)}(k\rho_1) \\ j\frac{\sqrt{\rho_2}}{\eta}\dot{H}_n^{(2)}(k\rho_2) & j\frac{\sqrt{\rho_2}}{\eta}\dot{H}_n^{(1)}(k\rho_2) \end{bmatrix}^{-1} \begin{bmatrix} \tilde{I}_1[n] \\ \tilde{I}_2[n] \end{bmatrix} \\
&= \begin{bmatrix} \tilde{\tilde{Z}}_{11}^{shell}[n] & -\tilde{\tilde{Z}}_{12}^{shell}[n] \\ \tilde{\tilde{Z}}_{21}^{shell}[n] & -\tilde{\tilde{Z}}_{22}^{shell}[n] \end{bmatrix} \begin{bmatrix} \tilde{I}_1[n] \\ \tilde{I}_2[n] \end{bmatrix}
\end{aligned} \tag{A.59}$$

where the Z-Matrix elements are evaluated as following:

$$\tilde{\tilde{Z}}_{11}^{shell}[n] = -j\eta \frac{H_n^{(2)}(k\rho_1)\dot{H}_n^{(1)}(k\rho_2) - H_n^{(1)}(k\rho_1)\dot{H}_n^{(2)}(k\rho_2)}{\dot{H}_n^{(2)}(k\rho_1)\dot{H}_n^{(1)}(k\rho_2) - \dot{H}_n^{(1)}(k\rho_1)\dot{H}_n^{(2)}(k\rho_2)}$$

$$\begin{aligned}\tilde{\tilde{Z}}_{12}^{shell}[n] &= -j\eta\sqrt{\frac{\rho_1}{\rho_2}}\frac{H_n^{(2)}(k\rho_1)\dot{H}_n^{(1)}(k\rho_1) - H_n^{(1)}(k\rho_1)\dot{H}_n^{(2)}(k\rho_1)}{\dot{H}_n^{(2)}(k\rho_1)\dot{H}_n^{(1)}(k\rho_2) - \dot{H}_n^{(1)}(k\rho_1)\dot{H}_n^{(2)}(k\rho_2)} \\ &= \frac{\eta}{\sqrt{\rho_1\rho_2}}\frac{4\,/\,(\pi k)}{\dot{H}_n^{(2)}(k\rho_1)\dot{H}_n^{(1)}(k\rho_2) - \dot{H}_n^{(1)}(k\rho_1)\dot{H}_n^{(2)}(k\rho_2)}\end{aligned} \tag{A.60}$$

$$\begin{aligned}\tilde{\tilde{Z}}_{21}^{shell}[n] &= -j\eta\sqrt{\frac{\rho_2}{\rho_1}}\frac{H_n^{(2)}(k\rho_2)\dot{H}_n^{(1)}(k\rho_2) - H_n^{(1)}(k\rho_2)\dot{H}_n^{(2)}(k\rho_2)}{\dot{H}_n^{(2)}(k\rho_1)\dot{H}_n^{(1)}(k\rho_2) - \dot{H}_n^{(1)}(k\rho_1)\dot{H}_n^{(2)}(k\rho_2)} \\ &= \frac{\eta}{\sqrt{\rho_1\rho_2}}\frac{4\,/\,(\pi k)}{\dot{H}_n^{(2)}(k\rho_1)\dot{H}_n^{(1)}(k\rho_2) - \dot{H}_n^{(1)}(k\rho_1)\dot{H}_n^{(2)}(k\rho_2)}\end{aligned}$$

$$\tilde{\tilde{Z}}_{22}^{shell}[n] = +j\eta \frac{H_n^{(1)}(k\rho_2)\dot{H}_n^{(2)}(k\rho_1) - H_n^{(2)}(k\rho_2)\dot{H}_n^{(1)}(k\rho_1)}{\dot{H}_n^{(2)}(k\rho_1)\dot{H}_n^{(1)}(k\rho_2) - \dot{H}_n^{(1)}(k\rho_1)\dot{H}_n^{(2)}(k\rho_2)}$$

Note that $H_n^{(2)}(k\rho)\dot{H}_n^{(2)*}(k\rho) = J_n(k\rho)\dot{J}_n(k\rho) + Y_n(k\rho)\dot{Y}_n(k\rho) - j\frac{2}{\pi k\rho}$. Similar calculations can be done for H-polarization.

A.5 Thermal Radiation from Semi-Infinite Planar or Cylindrical Emitters with Constant Temperature

Now, we examine the thermal radiation from both a semi-infinite planar emitter and cylindrical shaped emitter. Both cases are limiting cases of the planar slab and the cylindrical shell under the condition that the temperature is constant all over the emitter. As it was shown previously, the thermal radiation from stack of planar or cylindrical layers can be calculated based on the impedance matrices of these layers. In the special case where the temperature T is uniform all over the planar thermal

emitter residing in the $x \leq x_S$ or a cylindrical emitter resides at $\rho \leq \rho_s$, the emitter's reflectively, absorptivity and emissivity are quantified by the surface impedance of the emitter computed at the emitter's outer surface. The surface impedance is the input (local) impedance computed at the interface with vacuum towards the emitter. In this case, the knowledge of the input impedance is sufficient to compute for the thermal radiation towards the surroundings (here it is assumed to be vacuum) and there is no further need for knowledge of interior nature of the emitter [9]. Accordingly in such case, the equivalent circuit of the thermal emitter is simplified such that the thermal radiating source is represented by a Nyquist noise voltage source [90] in series with the resistive part of the input impedance [13] (see appendix D). As shown in Fig.(A.8), the surface impedance $\tilde{Z}_S(q)$ of the mode (q) - to the emitter's side - is defined as following:

$$\tilde{Z}_S(q) = \tilde{R}(q) + j\tilde{X}(q) \tag{A.61}$$

such that $\tilde{R}$ $(\tilde{X})$ is the real (imaginary) part which quantifies the losses (stored energy) in the thermal emitter. Note that mode can be either a plane wave in case of planar emitter or cylindrical wave in case of cylindrical emitter with $q = k_y$ or $q = n$ respectively. This surface impedance encapsulates all the information about the detailed nature of the thermal emitter at $z < 0$. The z-matrix of a semi-infinite planar or a cylindrical emitter is shown in Fig.(A.7), where the terminal 1 is located at $x = -\infty$ or $\rho = 0$. In either cases the terminal 2 is modeled to be open circuit so $\tilde{I}_1(q) = 0$. Accordingly from terminal 1, the $Z-$matrix is reduced to be

$$\tilde{V}_2(q) = \tilde{Z}_{22}(q)\tilde{I}_2(q) \tag{A.62}$$

so that $\tilde{Z}_S(q) = \tilde{Z}_{22}(q)$. As shown in Fig.(A.8), the thermal radiation from the planar emitter into vacuum is represented as a voltage source $V_S(q)$ in series with the equivalent impedance $\tilde{Z}_S(q)$ of the mode (q) towards the emitter side, both in series

with the input impedance of the same mode in vacuum $\tilde{Z}_0(q)$. The Nyquist voltage correlation [13] (see appendix D) is as following:

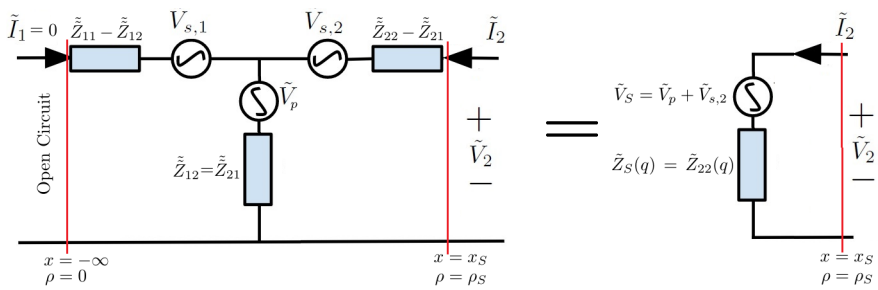

Figure A.7: Schematic of the T-circuit model for a thermally radiated mode(q) from a semi-infinite planar emitter located at $x \leq x_S$ or a cylindrical emitter located at $0 \leq \rho \leq \rho_S$. Terminal 1 is an open circuit. Then the equivalent circuit model is reduced to a surface impedance $\tilde{Z}_S(q) = \tilde{Z}_{22}$ with the Nyquist voltage connected in series.

$$\begin{aligned} \left\langle \tilde{V}_S(q)\tilde{V}_S^*(q) \right\rangle &= \frac{4\Theta(\omega,T)}{\pi} Re\{\tilde{Z}_S(q)\} \\ &= \frac{4\Theta(\omega,T)}{\pi} \tilde{Z}_S(q) \end{aligned} \tag{A.63}$$

where $\Theta(\omega, T)$ is the Planck's function. Computing for the time average radiated power per unit frequency per unit area of spatial frequency q flowing into the meta surface will give

$$\begin{aligned} \mathbf{P}(\bar{q}) = \quad & 4 \times \frac{1}{2} Re\{\tilde{V}\tilde{I}^*\} \\ = \quad & 4 \times \frac{1}{2} \frac{Re\{\tilde{Z}_0\}}{|\tilde{Z}_0 + \tilde{Z}|^2} < |\tilde{V}_s(q)|^2 > \\ = \quad & 4 \times \frac{1}{2} \frac{Re\{\tilde{Z}_0\}}{|\tilde{Z}_0 + \tilde{Z}_S|^2} \frac{4\Theta(\omega,T)}{\pi} \tilde{R} \end{aligned}$$

Due to the Fourier transform defined in Eq.(A.16), $\mathbf{P}(q)$ is the thermally radiated E- (H-) polarized power spectral density carried by the mode (q). Notice that the factor 4 is because ω is strictly positive quantity $\omega > 0$ [52], so all electromagnetic

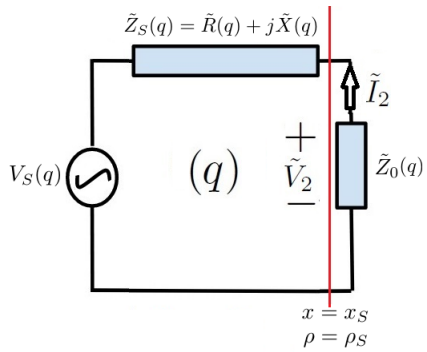

Figure A.8: Schematic of the circuit model for thermal radiation of the mode $(\bar{q})$ into vacuum from either a semi-infinite planar emitter located at $x < 0$ or from a cylindrical emitter located at $\rho < \rho_s$. The equivalent impedance of the mode from emitter side is $\tilde{Z}(q) = \tilde{R}(q) + j\tilde{X}(q)$ and the input impedance from the vacuum side is $\tilde{Z}_0(q)$. This circuit model is applied to both E and H polarizations using the appropriate corresponding impedance

field quantities are analytical functions with positive time harmonic frequencies only.

Finally, the radiated poynting vector per unit frequency is written as following for the semi-infinite planar emitter

$$\frac{dP}{d\omega} = 2 \times \frac{1}{(2\pi)^2} \int \int \mathbf{P}(\omega, \bar{q})\, d^2\bar{q} \tag{A.64}$$

where the factor 2 takes into account the contributions of both E- and H- polarizations.

APPENDIX B

Transformation Optics Theory

Transformation optics is a mathematical tools based on both differential geometry and tensor calculus such that Maxwell's equations are coordinate transformed. The main idea is that constitutive parameters of a given media (namely the permittivity and permeability) is equivalent to the metric of an empty space. In this appendix we summarize the main results of transformation Optics theory. The purpose of this appendix is to provide sufficient explanation of the formulas of TO theory sued in this thesis, the mathematical treatment provided here is not rigorous, however it provides the necessary background to do the space transformation with sufficient mathematical maturity. The reader is referred to [63] for more formal treatment and detailed explanation. The appendix is organized as following: first, informal explanation of contravariant and covariant components of a vector is explained adapted from [81], then informal explanation of the basic geometric algebra objects a true vectors, bi-vectors (axial vectors) adapted from [67]. Then a more formal treatment of transformation optics is provided adapted from [63]. First, the basic notation used in tensor calculus, then space transformation of Maxwell and Heat diffusion Eq.s are summarized. In this thesis, we typically deal with two-dimensional spaces, this is why in this appendix we only focus on two dimensional spaces.

B.1 Informal introduction

In this section, a simplified introduction to the notion of covariant and contravariant components of a vector in a curvilinear coordinate system then a simplified explanation for geometric objects as used in geometric algebra.

B.1.1 Covariant vs contravariant components of a vector

Consider an Euclidean two dimensional space spanned by Cartesian coordinates (x, y) and consider a position vector $\bar{r} = a\hat{x} + b\hat{y}$ as shown in Fig.(B.1). The length of the vector can be written in terms of its Cartesian components as following:

$$\sqrt{\bar{r} \cdot \bar{r}} = \sqrt{a^2 + b^2} \tag{B.1}$$

Now, consider a different oblique coordinate system (u, v) as shown in Fig.(B.1.b,c). (u, v) can be written in terms of (x, y) as following:

$$\begin{aligned} u &= x \\ v &= x\, cos(\alpha) + y\, sin(\alpha) \end{aligned} \tag{B.2}$$

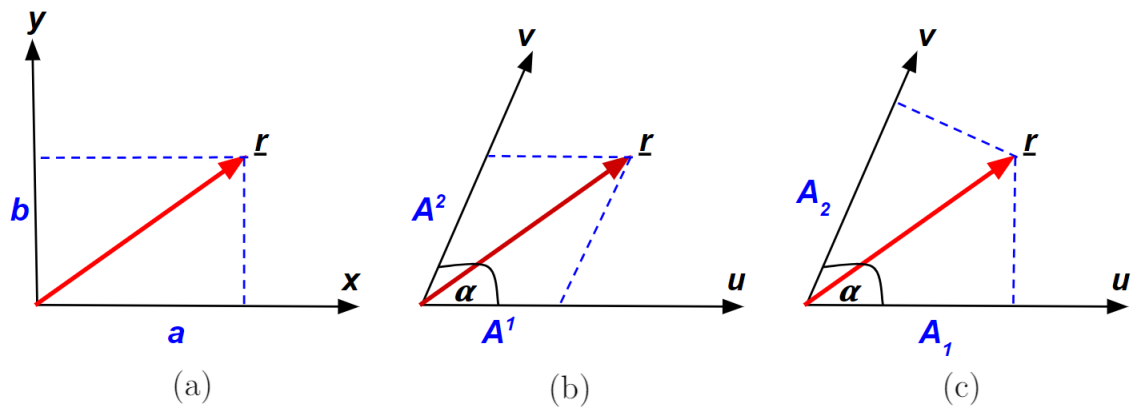

Figure B.1: A position vector $\bar{r}$ has its components described in: (a) Cartesian coordinates. (b)(u, v) coordinate system using contravariant components. (c) (u, v) coordinate system using covariant components.

The contravariant components of the same vector $\bar{r}$ are the length of the parallel vectors to the coordinates (u, v), these components can be written as following:

$$\begin{aligned} \bar{r} &= \begin{bmatrix} A^1 \\ A^2 \end{bmatrix} \\ A^1 &= a - \frac{b}{tan(\alpha)} \\ A^2 &= \frac{b}{sin(\alpha)} \end{aligned} \tag{B.3}$$

On the other hand the covariant components of the vector $\bar{r}$ are the length of the normal projections of the vector upon the coordinates (u, v) and these components can be written as following:

$$\begin{aligned} \bar{r} &= \begin{bmatrix} A_1 & A_2 \end{bmatrix} \\ A_1 &= a \\ A_2 &= a\, cos(\alpha) + b\, sin(\alpha) \end{aligned} \tag{B.4}$$

Now, it is required to compute for the length of the vector in terms of the oblique coordinate. This can be done by computing the inner product between the contravariant and covariant components as following:

$$\begin{bmatrix} A^1 \\ A^2 \end{bmatrix} \begin{bmatrix} A^1 & A^2 \end{bmatrix} = A^1 A_1 + A^2 A_2 = a^2 + b^2 \tag{B.5}$$

which is the same as Eq.(B.1).

Actually covariant and contravariant representations are dual geometric representations of vectors having the same role (bra)s and (ket)s in quantum mechanics. Also it is worth to mention that Cartesian coordinate system has the unique property that its covariant and contravariant components coincide.

B.1.2 Geometric algebra objects

It is known that one major disadvantage of vector calculus is the notion of the curl (rot) operator which is not intuitive and can be only computed over a two dimensional manifold cannot be used generalized to higher order ones. For similar reasons, the standard treatment in tensor calculus and accordingly transformation optics do not differentiate between the different types of vectors which count to physical quantities with different natures.

Scalars Scalars are known to be tensors of zero order. Their most important property is that they are invariant under space transformation. They have the same value using any coordinate system to describe the space.

True vectors True vectors are the typical vectors as defined in vector calculus. They are directed quantities with length. They are often represented by an arrow. Consider the following example from electrostatics, where the potential difference V

is computed a line integral of the electric field $\bar{E}$ along the path l

$$V = \int \bar{E} \cdot d\bar{l} \tag{B.6}$$

Since V is scalar quantity, then $\bar{l}$ is a vector and $\bar{E}$ is a dual vector. In interestingly

$$\bar{E} = -\nabla V \tag{B.7}$$

Actually in differential forms language the previous equation can be written

$$\bar{E} = -d \wedge V = -dV \tag{B.8}$$

when applied upon a tenosr, the d operator raises the order of the tensor by 1. Also d can be thought to be a vector by it self. More details about differential forms can be found in [67].

Bi-vectors or axial vectors Axial vectors represent directed flux density quantities, for instance electric and magnetic current and field densities j, K, D and B are axial vectors. Geometric algebra make clear distinction between true vectors and axial vectors. Axial vectors are the dual bi-vectors to the differential area which is by it self a bi-vector.

Consider a differential area dA placed on a flat space spanned by Cartesian coordinates, then

$$dA = (dx\ \hat{x}) \wedge (dy\ \hat{y}) = dxdy\ \hat{x} \wedge \hat{y} \tag{B.9}$$

dA is a directed area in which the normal unit vector to the area. The former equation says that dA is a bi-vector and the wedge stress the anti-symmetric property of dA. In order to define an inner product a dual bivector is need to be defined.

Consider the integral form of Gauss's law: a charge Q enclosed by a surface equates the electric flux density D flowing normal to surface area as following

$$Q = \iint \bar{D} \cdot dA \tag{B.10}$$

Q is a scalar quantity and dA is a bivector then $\bar{D}$ must be a dual bivector. In the same 2D space, a bivector can be always written as following:

$$\bar{D} = (a\hat{x}) \wedge (b\hat{y}) \tag{B.11}$$

so the former inner product can be written as following:

$$Q = \int adx + bdy \tag{B.12}$$

In vector and tensor calculus the bivector $\hat{x} \wedge \hat{y}$ is replaced by $\hat{z}$. By such notation a bivector is written as an axial vector. Another important property of bivectors is that can be emerged due to applying the operator d upon a true vector. For instance, consider Faraday's law:

$$d \wedge \bar{E} = \frac{\partial}{\partial t}\bar{B} \tag{B.13}$$

where $\bar{B}$ is a dual bivector and $\bar{E}$ is a dual vector. Finally in transformation optics distinction between vectors and bi-vectors are not required, however by keeping such distinction in mind, the mathematical complexity of the space transformation can reduce significantly.

B.2 Tensor calculus convention

It is important to understand the notation that is typically used in the literature of transformation optics theory which is by itself adopted from Tensor calculus. Here we summarize the main notations as following:

Index notation for space components: Tensor calculus is mainly used to describe the physics in coordinate system free notation, Unlike the commonly known vector calculus notation where vector components are labeled by the corresponding coordinate system used to describe the vector. For instance, in vector calculus framework, the Cartesian components of the vector $\bar{a}$ is written as

$$\bar{a} = \hat{x}a_x + \hat{y}a_y + \hat{z}a_z \tag{B.14}$$

while in tensor calculus the vector $\bar{a}$ will be written as following

$$\bar{a} = \sum_i e_i a^i = e_1 a^1 + e_2 a^2 + e_3 a^3 \tag{B.15}$$

where the indices $1, 2$ and 3 correspond to the x, y and z components. In general, for any coordinate system the indices of vector or tensors will indicate to coordinate system used.

Einstein convention is a notational convention that achieves notational simplicity. According to the convention, a term includes repeated indices indicate a summation of that term over all possible values of the index. For instance considering the inner product $a^i b_i$ between the vector a^i and a dual vector b_i in $N-$dimensional space, so that:

$$a^i b_i = \sum_{i=1}^{N} a^i b_i = a^1 b_1 + a^2 b_2 + a^3 b_3 + ... + a^N b_N \tag{B.16}$$

As it is clear from the previous example, the summation sign can be omitted as it is understood from the repeated index i that it corresponds to a summation. Repeated indices can occur within mixed tensors as following

$$g_i^i = \sum_{i=1}^{N} g_i^i = g_1^1 + g_2^2 + g_3^3 + ... + g_N^N \tag{B.17}$$

Matrix Notation It is known that second rank tensors can be represented using the linear algebra notation of matrices. For instance the following mixed tensor

$$J_i^{i'} = \frac{dx^{i'}}{dx^i} \tag{B.18}$$

where i, i', j' and $j = \{1, 2, ..., N\}$. Such second order mixed tensor can written as a matrix $\mathbf{J}$. We adopt the convention that the upper index is the row while the lower is the column.

Contavariant versus covariant A vector in an arbitrary coordinate systen $\{x^i\}$ can either be written in a covariant or a contravariant form. The contravariant components of a vector $\bar{V}$ is written as following:

$$\bar{V} = \{V^i\} \tag{B.19}$$

while the covariant compoenents of a vector $\bar{V}$ is written as following:

$$\bar{V} = \{V_i\} \tag{B.20}$$

B.3 Space Transformation

We consider two coordinate systems x^i and $x^{i'}$ where i and i' are indices. The differentials of the two sets of coordinates, $\{x^{i'}\}$ and $\{x^i\}$ are related by the chain

rule as following:

$$dx^i = J^i_{i'} dx^{i'} \qquad dx^{i'} = J^{i'}_i dx^i \tag{B.21}$$

where

$$J^{i'}_i = \frac{\partial x^{i'}}{\partial x^i} \qquad J^i_{i'} = \frac{\partial x^i}{\partial x^{i'}} \tag{B.22}$$

$J^i_{i'}$ is the Jacobian matrix for the transformation from $x^{i'}$ to x^i coordinates, while $J^{i'}_i$ is the Jacobian matrix for the transformation from x^i to $x^{i'}$ coordinates. Similar relations relate the differential operators in both coordinate systems as following:

$$\frac{\partial}{\partial x^i} = J^{i'}_i \frac{\partial}{\partial x^{i'}} \qquad \frac{\partial}{\partial x^{i'}} = J^i_{i'} \frac{\partial}{\partial x^i} \tag{B.23}$$

It is important to note that $J^i_{i'}$ are $J^{i'}_i$ are inverse matrices such that their matrix product unity as following:

$$J^i_{i'} J^{i'}_j = J^{i'}_j J^i_{i'} = \delta^i_j \tag{B.24}$$

Note that the $\delta^i_j = 1$ iff $i = j$. Also, the Jacobian matrices can be written in matrix notation so that

$$\mathbf{J} = J^{i'}_i \qquad \mathbf{J}^{-1} = J^i_{i'} \tag{B.25}$$

The real power of Einstein's convention can be seen when space transforming tensor of higher orders using the Jacobians of the transformation as following:

$$A^{i'j'}_{k'l'} = A^{ij}_{kl} J^{i'}_i J^{j'}_j J^k_{k'} J^l_{l'} \tag{B.26}$$

B.3.1 Tensors of first order

Length The distance between two points residing in a space is inherent property of that space and the distance is independent of the coordinate system that describes the space. This means that a differential length ds is invariant under coordinate transformation, in other words, the length ds is a property which is in dependent of the coordinates used to compute it. The differential distance ds in a 2D flat space described by Cartesian coordinates will be written as following:

$$ds^2 = dx^2 + dy^2 = \delta_{ij} dx^i dx^j \tag{B.27}$$

where δ_{ij} is Kronecker delta function. Now by using different coordinate system $x^{i'}$, the distance ds is rewritten as

$$ds^2 = \delta_{ij} J^i_{i'} dx^{i'} J^j_{j'} dx^{j'} = g_{i'j'} dx^{i'} dx^{j'} \tag{B.28}$$

where we substituted the chain rule of Eq.(B.21). The new matrix $g_{i'j'}$ is the metric tensor of the space with coordinate system $x^{i'}$ and it is related to the Jacobian matrix of the coordinate transformation as following:

$$g_{i'j'} = \delta_{ij} J^{i'}_i J^{j'}_j \tag{B.29}$$

By applying further coordinate transformation from $x^{i'}$ to $x^{i''}$, the length ds in an arbitrary space is written as following

$$ds^2 = g_{i'j'} J^{i'}_{i''} J^{j'}_{j''} dx^{i''} dx^{j''} \tag{B.30}$$

In general, the metric tensor is transformed as following

$$g_{i'j'} = g_{ij} J^i_{i'} J^j_{j'} \tag{B.31}$$

The former equation can be re-expressed in matrix form as following:

$$\mathbf{G'} = \mathbf{J}^{\tau}\mathbf{G}\mathbf{J} \tag{B.32}$$

where $G = g_{ij}$ and $G' = g_{i'j'}$ An important property of the metric tensor that it is always symmetric

$$g_{ji} = g_{ij} \qquad \mathbf{G} = \mathbf{G}^{\tau} \tag{B.33}$$

An Euclidean space is a special case where it is the only orthonormal space so that its metric tensor is $g_{ij} = \delta_{ij}$.

Vectors The Vector field is an entity independent of the coordinate system to describe it, however its components change according the coordinate system. Considering a vector field as a dual vector then considering the previous example of Eq.(B.6), then

$$\phi = E_i dx^i = E_{i'} dx^{i'} \tag{B.34}$$

since a differential length is transformed according to Eq.(**??**), the covariant components of a vector field is transformed as following:

$$E_{i'} = J^i_{i'} E_i \tag{B.35}$$

similarly its contravariant components are transformed as following:

$$E^{i'} = J^{i'}_i E^i \tag{B.36}$$

Both the covariant and contravariant components of the vector are related by the

metric tensor g_{ij}as following $V_i = g_{ij}V^j$. It is important to note that

$$g^{ij}g_{ik} = \delta^j_k \tag{B.37}$$

B.3.2 Tensors of second order

Area Since we mainly deal with 2D spaces, the notion of differential area expressed in terms of arbitrary coordinates has to revised. A z directed differential area dA_z in a flat space with Cartesian coordinate system is written as following:

$$dA_z = dx^1 \wedge dx^2 = -dx^2 \wedge dx^1 \tag{B.38}$$

where the $\wedge$ is wedge product. Upon coordinate transformation, the latter differential Area dA_z is transformed to the corresponding area dA'_z element in terms of the coordinate system $\{x^i\}$ as following

$$dA_z^{'} = J_1^{i^{'}} J_2^{j^{'}} dA_z = det(\mathbf{J})dA_z \tag{B.39}$$

where the determinant of the matrix $det(\mathbf{J}) = J_1^{i^{'}} J_2^{j^{'}}$ and

$$dA_z^{'} = dx^{1^{'}} \wedge dx^{2^{'}} = det(\mathbf{J})dx^1 \wedge dx^2 \tag{B.40}$$

The other components of the bi-vector should be considered

$$dA_j = dz \wedge dx^i \tag{B.41}$$

these components are transformed as following

$$dA_{j'} = dz \wedge dx^{i'} = J_i^{i'} dz \wedge dx^i \tag{B.42}$$

where $j \neq i$. But $J_i^{i'} = det(\mathbf{J}) J_{j'}^j$ the

$$dA_{j'} = dz \wedge dx^{i'} = det(\mathbf{J}) J_{j'}^j dA_j \tag{B.43}$$

Axial Vectors In 2D space problem , it is z axis is the axis of invariance so differential area and dual bivectors have one component which is "directed" to z and other two components directed in the transverse plane. Let q^z be an axial vector, then by space transformation from $\{x^i\}$ to $\{x^{i'}\}$, the axial vector is transformed into $q^{'}_z =$ as following:

$$q^{'z} = \frac{1}{det(\mathbf{J})} q^z \tag{B.44}$$

note that the inner product between a bi-vector and dual bi vector is invariant under space transformation, as following

$$q'z \cdot dA'_z = q^z \cdot dA_z \tag{B.45}$$

where made use of Eq.(B.39). Similarly, the transverse components are transformed as following:

$$q_T^{j'} = det(\mathbf{J}) J_j^{j'} q_T^j \tag{B.46}$$

where T is for transverse. Note that the inner product between the transverse directed bi-vector and dual bi vector is invariant under space transformation, as following:

$$q_T^{j'} dA'_j = q_T^j dA \tag{B.47}$$

where we made use of B.43.

B.4 Coordinate Transformation of Maxwell's and Fourier's law of Heat Conduction

Here we investigate the space transformation of both electromagnetic propagation and heat diffusion by applying the coordinate transformation upon both Maxwell's equations and Fourier's law of heat conduction. It will be show that both set of equations are covariant under transformation, or in other words, they have the same form.

B.4.1 Maxwell's Equations

Using Gibbsian's vector calculus notation Maxwell's Eq.s are written as following:

$$\begin{aligned} \nabla \times \bar{E} &= -\mu \frac{\partial \bar{H}}{\partial t} - \bar{K} \qquad & \nabla \cdot \bar{D} &= \rho_e \\ \nabla \times \bar{H} &= \epsilon \frac{\partial \bar{E}}{\partial t} + \bar{j} \qquad & \nabla \cdot \bar{B} &= \rho_m \end{aligned} \tag{B.48}$$

where $\bar{E}$, $\bar{D}$, $\bar{H}$ and$\bar{B}$ are electric and magnetic field intensities and densities respectively, $\bar{J}$ and $\bar{K}$ are the electric and magnetic current densities and ρ_e and ρ_m are the free electric and magnetic charge densities.

In two dimensional space the electromagnetic problem in hand is invariant along the normal to the space axis, electromagnetic field is decomposed into two independent polarizations $E-$ and $H-$ polarizations. Considering $E-$ polarization case where $\bar{E} = \hat{z}E_z$ and $\bar{H} = \bar{H}_T$, where T to denote transverse. In the virtual the constitutive parameters are written

$$\begin{aligned} B^i &= \mu^{il} \frac{\partial}{\partial t} H_l \\ D_z &= \epsilon^{zz} \frac{\partial}{\partial t} E_z \end{aligned} \tag{B.49}$$

by space transformation with the Jacobin is $A_i^{i'} = \frac{\partial x^{i'}}{\partial x^i}$ and since D,B are axial vectors, while E is scalar and H is true vector, then the media is transformed as following

$$\begin{aligned} B_T^{i'} &= \frac{1}{det(A)} A_i^{i'} B_T^i = \frac{1}{det(A)} A_i^{i'} \mu^{il} A_l^{l'} H_{l'} = \mu^{i'l'} H_{l'} \\ D_z' &= \frac{1}{det(\mathbf{A})} \epsilon^{zz} E_z = \epsilon^{'zz} E_z' \end{aligned} \tag{B.50}$$

where $E_z' = E_z$ and $H_{i'} = A_{i'}^i H_i$ then

$$\begin{aligned} \epsilon^{'zz} &= \frac{1}{det(\mathbf{A})} \epsilon^{zz} \\ \mu^{i'l'} &= \frac{1}{det(\mathbf{A})} A_i^{i'} \mu^{il} A_l^{l'} \end{aligned} \tag{B.51}$$

In summary,Following the transformations depicted in the previous section, then the quantities of E-polarization are transformed as follows:

$$\begin{aligned} \varepsilon_{zz}^{'} &= \frac{\varepsilon_{zz}}{det(\mathbf{A})} \\ j_z^{'} &= \frac{j_z}{det(\mathbf{A})} \\ \mu_T^{m'n'} &= \frac{1}{det(\mathbf{A})} A_m^{m'} A_n^{n'} \mu_T^{mn} \\ K_T^{'m} &= \frac{1}{det(\mathbf{A})} K_T^m \\ H_T^{'m} &= A_{m'}^m H_T^m \\ E_z^{'} &= E_z \end{aligned} \tag{B.52}$$

and similarly for H-polarization

$$
\begin{aligned}
\mu_{zz}^{'} &= \frac{\mu_{zz}}{det(\mathbf{A})} \\
K_z^{'} &= \frac{K_z}{det(\mathbf{A})} \\
\epsilon_T^{m'n'} &= \frac{1}{det(\mathbf{A})} A_m^{m'} A_n^{n'} \epsilon_T^{mn} \\
J_T^{'m} &= \frac{1}{det(\mathbf{A})} A_m^{m'} J_T^m \\
E_T^{'m} &= A_{m'}^m E_T^m \\
H_z^{'} &= H_z
\end{aligned}
\tag{B.53}
$$

B.4.2 Space Transformation of Fourier's law of heat conduction

Transformation optics can be applied to Fourier's law of heat conduction

$$
\begin{aligned}
q^i &= \kappa^{ij} (\nabla T)_j \\
\nabla \cdot \bar{q} &= \frac{1}{\sqrt{g}} \left(\sqrt{g} q^i \right)_{,i} = C \frac{\partial}{\partial t} T + Q
\end{aligned}
\tag{B.54}
$$

where $\bar{q}$ is the heat flux, κ is the thermal conductivity and T is the temperature field. Q is thermal flux source($Q > 0$) or sinks ($Q < 0$) and C is the heat capacity. Space transformation is applied such that the laws of physics have the same form as following:

$$
\begin{aligned}
q^i &= \kappa^{ij} (\nabla T)_j \\
\nabla \cdot \bar{q} &= C \frac{\partial}{\partial t} T + Q
\end{aligned}
\tag{B.55}
$$

since q is an axial vector directed in the transverse plane then it is transformed as following:

$$
q^{i'} = \frac{1}{det(J)} J_i^{i'} q^i \tag{B.56}
$$

where ∇T is a true vector then it is transformed as following:

$$(\nabla T)_{j'} = J^{j}_{j'}(\nabla T)_{j} \tag{B.57}$$

substituting in Eq.(B.56) and Eq. (B.57) in Eq.(B.55), then

$$det(J)J^{i}_{i'}q^{i'} = \kappa^{ij}J^{j'}_{j}(\nabla T)_{j'} \tag{B.58}$$

then accordingly,

$$\kappa^{i'j'} = \frac{1}{det(J)}J^{i'}_{i}\kappa^{ij}J^{j'}_{j}(\nabla T)_{j'} \tag{B.59}$$

since heat capacitance C is stored energy per unit area then it transformed as following:

$$C' = \frac{1}{det(J)}C \tag{B.60}$$

Also since Q is power generated or absorbed per unit area then it transformed as following:

$$Q' = \frac{1}{det(J)}Q \tag{B.61}$$

APPENDIX C

Kirchoff's Reciprocity and Circuit Model's Proof

C.1 Generalized Kirchoff's laws for arbitrary Thermal Emitters

As shown in chapter V, scattering of an incident field from a scatterer is represented as a linear network connected to multiple waves guides with each wave-guide carries an incident mode and its reflection. Since we assume only linear meta-surfaces then it can be described with a scattering matrices that relate the incident and scattered power waves on both sides of the metasurface. In chapterV, we only deal with cylindrical shaped metasurfaces. As it was shown in Eq.(5.1), that cylindrical waves constitute an orthogonal basis with the inner product is defined by the Fourier transform computed on the cylindrical Metasurface for $\phi = \{-\pi, \pi\}$. It is important to note that such basis is defined solely in vacuum. It is important to note that such basis is defined solely in vacuum. Considering an incident and scatterd fields described using cylindrical wave basis, then the scattering of the incident power wave amplitude $a$from a target object into the scattered power wave amplitude b is quantified using the Scattering matrix $\underline{\underline{S}}$ which relates the incident and scattered power waves from

object of different modes (orders). The scattering matrix can be defined as following:

$$\underline{b} = \underline{\underline{S}}\,\underline{a} \tag{C.1}$$

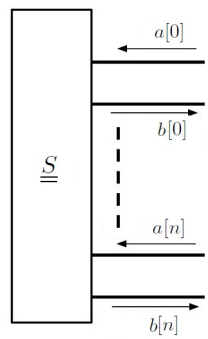

Figure C.1: schematic of the scattering matrix matrix $\underline{\underline{S}}$

The scattering matrix $\underline{\underline{S}}$ can singular value decomposed as following

$$\underline{\underline{S}} = \underline{\underline{V}}\,\underline{\underline{D}}\,\underline{\underline{V}}^{\dagger} \tag{C.2}$$

where $\underline{\underline{V}}$ is unitray matrix (so $\underline{\underline{VV}}^{\dagger} = \underline{\underline{U}}$ where $\underline{\underline{U}}$ is the identity matrix) and $\underline{\underline{D}}$ is a diagonal matrix. Kirchoff's law is closely related to the former SVD equation. The matrix $\underline{\underline{D}}$ is by itself a diagonal scattering matrix so that an incident and scattered modes are of the same basis (which are the set of eigenvectors of $\underline{\underline{D}}$). $\underline{\underline{V}}$ can be undestood as lossles network and serve as mode converter between the eigenvector modes of $\underline{\underline{D}}$ and the cylindrical wave basis that propagates in vacuum. Accordingly Kirchoff's law says that the emissivity $\alpha_i$and absorbitivity $\varepsilon_i$of an eigenvector mode $|i\rangle$ of $\underline{\underline{D}}$ are equal. Such statement can be read as following

$$\alpha_i = (\underline{\underline{U}} - \underline{\underline{DD}}^{\dagger})_{ii} = (\underline{\underline{U}} - \underline{\underline{D}}^{\dagger}\underline{\underline{D}})_{ii} = \varepsilon_i \tag{C.3}$$

where ii is the indeices of the row and coloums of the matrices $\underline{\underline{DD}}^{\dagger}$ and $\underline{\underline{D}}^{\dagger}\underline{\underline{D}}$.

Consequently the total absorbtion and the total emissivity equates as following

$$\sum_i \alpha_i = trace\{\underline{\underline{U}} - \underline{\underline{DD^\dagger}}\} = trace\{\underline{\underline{U}} - \underline{\underline{D}}^\dagger \underline{\underline{D}}\} = \sum_i \varepsilon_i \tag{C.4}$$

In [83], Kirchoff's law was generalized to scatterers with non-diagonal scattering matrices. first by defining an absorptivity matrix $\underline{\underline{A}}$ as following:

$$\underline{\underline{A}} = \underline{\underline{U}} - \underline{\underline{S}}^\dagger \underline{\underline{S}} \tag{C.5}$$

and defining an emissivity matrix $\underline{\underline{E}}$ as following:

$$\underline{\underline{E}} = \underline{\underline{U}} - \underline{\underline{SS^\dagger}} \tag{C.6}$$

In such case, Kirchoff's law can be re-written

$$\underline{\underline{E}} = \underline{\underline{A}}^\dagger \tag{C.7}$$

and the total absorbitivity equates the total emissivity

$$trace\{\underline{\underline{A}}\} = trace\{\underline{\underline{E}}^\dagger\} = trace\{\underline{\underline{E}}\}^* \tag{C.8}$$

where $*$ is complex conjugation operator. however the trace is similarity-invariant, which means that

$$trace\{\underline{\underline{E}}\} = trace\{\underline{\underline{U}} - \underline{\underline{DD^\dagger}}\} = trace\{\underline{\underline{U}} - \underline{\underline{D}}^\dagger \underline{\underline{D}}\} = trace\{\underline{\underline{A}}\} = trace\{\underline{\underline{A}}\}^* \in \mathbf{R} \tag{C.9}$$

The former equation says that the trace of the emissivity and absorbitivity matrices equates and they have to be real quantities.

C.2 Proof for the circuit model using Landauer Formalism

In this section we prove the circuit model proposed in chapter V. The following proof makes use of Kirchhoff's reciprocity, where at thermal equilibrium at temperature T, according to the theory of fluctuation electrodynamics, the ensemble time averaged thermally radiated poynting vector from a thermal emitter characterized by scattering matrix $\underline{\underline{S}}$ expressed in Landauer Formalism [7] as following:

$$\begin{aligned}\left\langle \underline{\underline{\tilde{\mathbb{P}}}} \right\rangle_{\omega} &= 4 \times \frac{1}{2}\frac{\theta(\omega,T)}{\pi}\,\mathrm{Re}\{\left[\underline{\underline{U}} - \underline{\underline{S}}^{\dagger}\underline{\underline{S}}\right]\} \\ &= 4 \times \frac{1}{2}\frac{\theta(\omega,T)}{\pi}\,\mathrm{Re}\{\left[\underline{\underline{U}} - \underline{\underline{S}}\underline{\underline{S}}^{\dagger}\right]^{\dagger}\}\end{aligned} \tag{C.10}$$

where $\underline{\underline{U}}$ is a unit matrix and $\underline{\underline{U}} - \underline{\underline{S}}^{\dagger}\underline{\underline{S}}$ is the emissivity matrix of the thermal emitter, while $\underline{\underline{U}} - \underline{\underline{S}}\underline{\underline{S}}^{\dagger}$ is its absorbitivity matrix. Here, we analytically derive Eq.(5.76) from Eq.(C.10).

The derivation starts by relating the scattering matrix $\underline{\underline{S}}$ and the impedance matrix $\underline{\underline{Y}}_s$, where both are expressed interms of cylindrical wave basis. In vacuum, cylindrical waves constitute an orthogonal basis that can describe any field evaluated along a circular boundary with a constant radius. Such basis is the same as a Fourier series of the field with the periodic variable is the azimuthal angle ϕ. Considering only E polarized thermal radiation in 2D space with invariant along z axis ($\frac{\partial}{\partial z} = 0$), the electric and magnetic fields are described as forward and backward cylindrical propagating waves. The fields are described in terms of propagating power waves' amplitudes so they can be related to the scattering matrices. Assuming $e^{i\omega t}$ time

harmonic dependence, the fields of $E-$ polarization are as following :

$$
\begin{aligned}
V(\phi) &= \sqrt{\rho} E_z \\
&= \sum_{n=-\infty}^{n=\infty} \left(\tilde{V}_n^- H_n^{(1)}(k_0\rho) + \tilde{V}_n^+ H_n^{(2)}(k_0\rho) \right) e^{jn\phi} = \left(\tilde{Z}_n^+ \tilde{I}_n^+ H_n^{(2)}(k_0\rho) + \tilde{Z}_n^- \tilde{I}_n^- H_n^{(1)}(k_0\rho)) \right) e^{jn\phi} \\
&= \sum_{n=-\infty}^{n=\infty} \frac{1}{\sqrt{\tilde{G}_n}} (a_n + b_n) \\
I(\phi) &= -\sqrt{\rho} H_\phi \\
&= \sum_{n=-\infty}^{n=\infty} \frac{1}{\eta_0} (j\tilde{V}_n^- H_n'^{(1)}(k_0\rho) + j\tilde{V}_n^+ H_n'^{(2)}(k_0\rho)) e^{jn\phi} = \sum_n \left(\tilde{I}_n^- H_n'^{(1)}(k_0\rho) - \tilde{I}_n^+ H_n'^{(2)}(k_0\rho) \right) e^{jn\phi} \\
&= \sum_{n=-\infty}^{n=\infty} \frac{1}{\sqrt{\tilde{G}_n}} (-\tilde{Y}_n^- a_n + \tilde{Y}_n^+ b_n) \\
\tilde{G}_n &= \mathrm{Re}\{\tilde{Y}_n^-\} = \mathrm{Re}\{\tilde{Y}_n^+\} \\
\tilde{Y}_n^+ &= j \frac{H_n^{(2)'}(k_0\rho)}{\eta_0 H_n^{(2)}(k_0\rho)} \qquad \tilde{Y}_n^- = -j \frac{H_n^{(1)'}(k_0\rho)}{\eta_0 H_n^{(1)}(k_0\rho)} = \tilde{Y}_n^{+*}
\end{aligned}
\tag{C.11}
$$

where $k_0 = \omega\sqrt{\epsilon_0\mu_0}$, $H_n^{(1)}$ and $H_n^{(2)}$ are nth order Hankel functions of 1st and 2nd types that represent in- and out-going cylindrical waves respectively. The coefficients a and b are defined such that they directly quantify for the propagating in and out-going poynting vectors. The total real power flowing in the radial direction is expressed in terms of the power waves as following:

$$
\begin{aligned}
\frac{1}{2}\,\mathrm{Re}\{\int_0^{2\pi} -E_{z,l}(\phi) H_{\phi,l}^*(\phi)\rho d\phi\} &= \frac{1}{2}\,\mathrm{Re}\{\int_0^{2\pi} V(\phi) I^*(\phi) d\phi\} \\
&= \frac{1}{2}\,\mathrm{Re}\left[\sum_n \frac{1}{G_n} \left(-Y_n^{-*}|a_n|^2 + Y_n^{+*}|b_n|^2 - Y_n^{-*} a_n b_n^* + Y_n^{+*} a_n^* b_n \right) \right]
\end{aligned}
\tag{C.12}
$$

since $(-Y_n^{-*} b_n a_n^* + Y_n^{+*} b_n^* a_n) = -2jIm\{Y_n^{-*} a_n b_n^*\}$ then

$$\frac{1}{2}\,\mathrm{Re}\{\int_0^{2\pi} -E_{z,l}(\phi) H_{\phi,l}^*(\phi)\rho d\phi\} = \frac{1}{2}\sum_n -|a_n|^2 + |b_n|^2 \tag{C.13}$$

The in and outgoing "power waves" amplitudes are related by the scattering operator $\underline{\underline{S}}$ as following as following

$$\underline{b} = \underline{\underline{S}}\,\underline{a} \tag{C.14}$$

since

$$\begin{aligned} \underline{a} &= \underline{\underline{F}}\left[\underline{\underline{\tilde{Y}}}^{+}\underline{\tilde{V}} - \underline{\tilde{I}}\right] \\ \underline{b} &= \underline{\underline{F}}\left[\underline{\underline{\tilde{Y}}}^{-}\underline{\tilde{V}} + \underline{\tilde{I}}\right] \end{aligned} \tag{C.15}$$

where $\underline{\underline{F}} = diag\{1\,/\,2\sqrt{G_n}\,\} \in \mathrm{Re}$ is a diagonal matrix with elements $1\,/\,2\sqrt{G_n}$ and and $\underline{\underline{\tilde{Y}}}^{+}$ is a diagonal matrix with elements $\tilde{Y}_n^{+}$, and similarly $\underline{\underline{\tilde{Y}}}^{+} = \left(\underline{\underline{\tilde{Y}}}^{-}\right)^{\dagger}$. The surface impedance $\underline{\underline{\tilde{\tilde{Y}}}}_s$ relates the voltage and current waves as in Eq.(5.16) (Noting that the current $\underline{\tilde{I}}$ is flowing in $+\rho$ direction) then:

$$\underline{\tilde{I}} = -\underline{\underline{\tilde{\tilde{Y}}}}_s\,\underline{\tilde{V}} \tag{C.16}$$

and by substituting Eq.s(C.15-C.16)in Eq.(C.14), the scattering matrix is related to the impedance representation as following:

$$\underline{\underline{S}} = \underline{\underline{F}}\left(\underline{\underline{\tilde{\tilde{Y}}}}^{-} - \underline{\underline{\tilde{Y}}}_s\right)\left(\underline{\underline{\tilde{\tilde{Y}}}}^{+} + \underline{\underline{\tilde{Y}}}_s\right)^{-1}\underline{\underline{F}}^{-1} \tag{C.17}$$

,

then

$$\underline{\underline{S}}^{\dagger}\underline{\underline{S}} = \underline{\underline{F}}^{-\dagger}\left(\underline{\underline{\tilde{\tilde{Y}}}}^{+} + \underline{\underline{\tilde{Y}}}_{s}\right)^{-\dagger}\left(\underline{\underline{\tilde{\tilde{Y}}}}^{-} - \underline{\underline{\tilde{Y}}}_{s}\right)^{\dagger}\underline{\underline{F}}^{\dagger}\underline{\underline{F}}\left(\underline{\underline{\tilde{\tilde{Y}}}}^{-} - \underline{\underline{\tilde{Y}}}_{s}\right)\left(\underline{\underline{\tilde{\tilde{Y}}}}^{+} + \underline{\underline{\tilde{Y}}}_{s}\right)^{-1}\underline{\underline{F}}^{-1}$$
$$= \underline{\underline{F}}^{-\dagger}\left(\underline{\underline{\tilde{\tilde{Y}}}}^{+} + \underline{\underline{\tilde{Y}}}_{s}\right)^{-\dagger}\left(\underline{\underline{\tilde{\tilde{Y}}}}^{+}\underline{\underline{F}}^{\dagger}\underline{\underline{F}}\,\underline{\underline{\tilde{\tilde{Y}}}}^{-} - \underline{\underline{\tilde{Y}}}_{s}^{\dagger}\underline{\underline{F}}^{\dagger}\underline{\underline{F}}\,\underline{\underline{\tilde{\tilde{Y}}}}^{-} - \underline{\underline{\tilde{\tilde{Y}}}}^{+}\underline{\underline{F}}^{\dagger}\underline{\underline{F}}\,\underline{\underline{\tilde{\tilde{Y}}}}_{s} + \underline{\underline{\tilde{Y}}}_{s}^{\dagger}\underline{\underline{F}}^{\dagger}\underline{\underline{F}}\,\underline{\underline{\tilde{\tilde{Y}}}}_{s}\right)\left(\underline{\underline{\tilde{\tilde{Y}}}}^{+} + \underline{\underline{\tilde{Y}}}_{s}\right)^{-1}\underline{\underline{F}}^{-1} \tag{C.18}$$

and since the unit matrix $\underline{\underline{U}}$ can be written as following:

$$\underline{\underline{U}} = \underline{\underline{F}}^{-\dagger}\left(\underline{\underline{\tilde{\tilde{Y}}}}^{+} + \underline{\underline{\tilde{Y}}}_{s}\right)^{-\dagger}\left(\underline{\underline{\tilde{\tilde{Y}}}}^{+} + \underline{\underline{\tilde{Y}}}_{s}\right)^{\dagger}\underline{\underline{F}}^{\dagger}\underline{\underline{F}}\left(\underline{\underline{\tilde{\tilde{Y}}}}^{+} + \underline{\underline{\tilde{Y}}}_{s}\right)\left(\underline{\underline{\tilde{\tilde{Y}}}}^{+} + \underline{\underline{\tilde{Y}}}_{s}\right)^{-1}\underline{\underline{F}}^{-1}$$
$$= \underline{\underline{F}}^{-\dagger}\left(\underline{\underline{\tilde{\tilde{Y}}}}^{+} + \underline{\underline{\tilde{Y}}}_{s}\right)^{-\dagger}\left(\underline{\underline{\tilde{\tilde{Y}}}}^{-}\underline{\underline{F}}^{\dagger}\underline{\underline{F}\underline{\tilde{\tilde{Y}}}}^{+} + \underline{\underline{\tilde{Y}}}_{s}^{\dagger}\underline{\underline{F}}^{\dagger}\underline{\underline{F}\underline{\tilde{\tilde{Y}}}}^{+} + \underline{\underline{\tilde{\tilde{Y}}}}^{-}\underline{\underline{F}}^{\dagger}\underline{\underline{F}\underline{\tilde{\tilde{Y}}}}_{s} + \underline{\underline{\tilde{Y}}}_{s}^{\dagger}\underline{\underline{F}}^{\dagger}\underline{\underline{F}\underline{\tilde{\tilde{Y}}}}_{s}\right)\left(\underline{\underline{\tilde{\tilde{Y}}}}^{+} + \underline{\underline{\tilde{Y}}}_{s}\right)^{-1}\underline{\underline{F}}^{-1} \tag{C.19}$$

since $\underline{\underline{\tilde{\tilde{Y}}}}^{-}$, $\underline{\underline{F}}^{\dagger}$, $\underline{\underline{F}}$ and $\underline{\underline{\tilde{\tilde{Y}}}}^{+}$ are diagonal matrices then $\underline{\underline{\tilde{\tilde{Y}}}}^{+}\underline{\underline{F}}^{\dagger}\underline{\underline{F}}\,\underline{\underline{\tilde{\tilde{Y}}}}^{-} = \underline{\underline{\tilde{\tilde{Y}}}}^{-}\underline{\underline{F}}^{\dagger}\underline{\underline{F}}\,\underline{\underline{\tilde{\tilde{Y}}}}^{+}$ then

$$\underline{\underline{U}} - \underline{\underline{S}}^{\dagger}\underline{\underline{S}} = \underline{\underline{F}}^{-\dagger}\left(\underline{\underline{\tilde{\tilde{Y}}}}^{+} + \underline{\underline{\tilde{Y}}}_{s}\right)^{-\dagger} 2\left(\underline{\underline{\tilde{Y}}}_{s}^{\dagger}\underline{\underline{F}}^{\dagger}\underline{\underline{F}}Re\{\underline{\underline{\tilde{\tilde{Y}}}}^{+}\} + Re\{\underline{\underline{\tilde{\tilde{Y}}}}^{+}\}\underline{\underline{F}}^{\dagger}\underline{\underline{F}\underline{\tilde{\tilde{Y}}}}_{s}\right)\left(\underline{\underline{\tilde{\tilde{Y}}}}^{+} + \underline{\underline{\tilde{Y}}}_{s}\right)^{-1}\underline{\underline{F}}^{-1} \tag{C.20}$$

but since $Re\{\underline{\underline{\tilde{\tilde{Y}}}}^{+}\}\underline{\underline{F}}^{\dagger}\underline{\underline{F}} = \frac{1}{2}\underline{\underline{U}}$ or $Re\{\underline{\underline{\tilde{\tilde{Y}}}}^{+}\} = \frac{1}{2}\underline{\underline{F}}^{-2}$ and substituting in Eq.(C.10)

$$\begin{aligned}\underline{\underline{U}} - \underline{\underline{S}}^{\dagger}\underline{\underline{S}} &= \underline{\underline{F}}^{-\dagger}\left(\underline{\underline{\tilde{\tilde{Y}}}}^{+} + \underline{\underline{\tilde{Y}}}_{s}\right)^{-\dagger}\left(\underline{\underline{\tilde{Y}}}_{s}^{\dagger} + \underline{\underline{\tilde{\tilde{Y}}}}_{s}\right)\left(\underline{\underline{\tilde{\tilde{Y}}}}^{+} + \underline{\underline{\tilde{Y}}}_{s}\right)^{-1}\underline{\underline{F}}^{-1} \\ &= \underline{\underline{F}}^{-\dagger}\left(\underline{\underline{\tilde{\tilde{Y}}}}^{+} + \underline{\underline{\tilde{Y}}}_{s}\right)^{-\dagger}\underline{\underline{\tilde{L}}}\left(\underline{\underline{\tilde{\tilde{Y}}}}^{+} + \underline{\underline{\tilde{Y}}}_{s}\right)^{-1}\underline{\underline{F}}^{-1}\end{aligned} \tag{C.21}$$

since $\underline{\underline{U}} - \underline{\underline{S}}^{\dagger}\underline{\underline{S}}$ is symmetric matrices then

$$\underline{\underline{F}}^{\dagger}\left[\underline{\underline{U}} - \underline{\underline{S}}^{\dagger}\underline{\underline{S}}\right]\underline{\underline{F}} = \left[\underline{\underline{U}} - \underline{\underline{S}}^{\dagger}\underline{\underline{S}}\right]\underline{\underline{F}}^{2} \tag{C.22}$$

since $\underline{\underline{F}}^{-2} = 2Re\{\underline{\underline{\tilde{\tilde{Y}}}}^{+}\}$, then

$$\underline{\underline{U}} - \underline{\underline{S}}^{\dagger}\underline{\underline{S}} = \left(\underline{\underline{\tilde{\tilde{Y}}}}^{+} + \underline{\underline{\tilde{Y}}}_{s}\right)^{-\dagger} \underline{\underline{\tilde{L}}} \left(\underline{\underline{\tilde{\tilde{Y}}}}^{+} + \underline{\underline{\tilde{Y}}}_{s}\right)^{-1} 2Re\{\underline{\underline{\tilde{\tilde{Y}}}}^{+}\} \tag{C.23}$$

since $\underline{\underline{\tilde{L}}} \in \mathbb{R}$, then by substituting in Eq.(C.10)

$$\begin{aligned} \left\langle \underline{\underline{\tilde{\mathbb{P}}}} \right\rangle_{\omega} &= 4 \times \frac{1}{2}\frac{\theta(\omega,T)}{\pi} \times 2\,\mathrm{Re}\left\{ \left(\underline{\underline{\tilde{\tilde{Y}}}}^{+} + \underline{\underline{\tilde{Y}}}_{s}\right)^{-1} \underline{\underline{\tilde{L}}} \left(\underline{\underline{\tilde{\tilde{Y}}}}^{+} + \underline{\underline{\tilde{Y}}}_{s}\right)^{-\dagger} Re\{\underline{\underline{\tilde{\tilde{Y}}}}^{+\dagger}\} \right\} \\ &= \frac{4\theta(\omega,T)}{\pi}\,\mathrm{Re}\left\{ \left(\underline{\underline{\tilde{\tilde{Y}}}}^{+} + \underline{\underline{\tilde{Y}}}_{s}\right)^{-1} \underline{\underline{\tilde{L}}} \left(\underline{\underline{\tilde{\tilde{Y}}}}^{+} + \underline{\underline{\tilde{Y}}}_{s}\right)^{-\dagger} \underline{\underline{\tilde{\tilde{Y}}}}^{+\dagger} \right\} \end{aligned} \tag{C.24}$$

which is the same as the real part of the expression as of Eq.(5.76) that was derived by the circuit model proposed.

APPENDIX D

Thermal Radiation Calculation using TDDA

In order to compute thermal radiation from an arbitrary media which can be in general bi-anisotropic and inhomogeneous chiral media, we make use of thermal discrete dipole approximation(TDDA). In what follows we summarize analytical procedure for the numerical simulations that will done to calculate for the thermal radiated poynting vector and that was used to solve Maxwell Equations. We first start with the definition of the ensemble averaged time average Poynting vector given as following:

$$\langle S \rangle_{\omega} = 4 \times \frac{1}{2} Re\{\langle \underline{E} \times \underline{H}^{*} \rangle\} \tag{D.1}$$

The scalar product of this vector with the local normal of a surface gives the flux carried through this surface. The nth magnetic field component H_n can be calculated using the Green functions of the operator as follows:

$$H_n(\underline{r}) = \sum_m G_{nm}^{HH} \circ K_m + G_{nm}^{HE} \circ J_m \tag{D.2}$$

Similarly, the components of the electric field are calculated using the Green functions of the operator as follows:

$$E_q(\underline{r}) = \sum_m G_{qm}^{EH} \circ K_m + G_{qm}^{EE} \circ J_m \tag{D.3}$$

where $*$ indicates convolution process and G_{nm}^{HH} ,G_{nm}^{HE} are the nth component of the magnetic green's function due to m^{th} component of the electric J_m and magnetic $K_m$current densities respectively and similarly, G_{qm}^{EH} and G_{qm}^{EE} are the qth component of the electric green's function due to the same sources, where $n, q = \{\phi, z\}$ and $m = \{x, y, z\}$. r is the position vector of the observation point and $\{r_m\}$ are position vectors inside the thermal emitter volume.

Since we are concerned only with the radial component of the time average poynting vector the ensemble averaged Poynting vector will be as follows:

$$\langle \underline{S} \rangle_\rho = \hat{\rho} \left[2Re\{\left\langle E_\phi \, H_z^* - E_z \, H_\phi^* \right\rangle_\omega\} \right] \tag{D.4}$$

with the first term in the previous equation is written as following;

$$\begin{aligned} \langle E_\phi \, H_z^* \rangle_\omega &= \sum_m \sum_n \left\langle (G_{\phi m}^{EH} \circ K_m + G_{\phi m}^{EE} \circ J_m)(G_{zn}^{HH} \circ K_m + G_{zn}^{HE} \circ J_m)^* \right\rangle_\omega \\ &= \sum_m \sum_n G_{\phi m}^{EH} \circ \langle K_m K_n^* \rangle_\omega \circ G_{nz}^{HE} + G_{\phi m}^{EH} \circ \langle K_m J_n^* \rangle_\omega \circ G_{nz}^{EE} \\ &+ \sum_m \sum_n G_{\phi m}^{EE} \circ \langle J_m K_n^* \rangle_\omega \circ G_{nz}^{HE} + G_{\phi m}^{EE} \circ \langle J_m J_n^* \rangle_\omega \circ G_{nz}^{EE} \end{aligned} \tag{D.5}$$

similarly for the second term,

$$\begin{aligned} \left\langle E_z \, H_\phi^* \right\rangle_\omega &= \sum_m \sum_n G_{zm}^{EH} \circ \langle K_m \, K_n^* \rangle \circ G_{\phi n}^{HE*} + \, G_{\phi m}^{EH} \circ \langle K_m \, J_n^* \rangle \circ G_{nz}^{EE*} \\ &+ \sum_m \sum_n G_{\phi m}^{EE} \circ \langle J_m \, K_n^* \rangle \circ G_{nz}^{HE*} + G_{\phi m}^{EE} \circ \langle J_m \, J_n^* \rangle \circ G_{nz}^{EE*} \end{aligned} \tag{D.6}$$

substituting the cross correlation of electric and magnetic thermal currents derived

in chap VI, then

$$\begin{aligned}\left\langle E_z\, H_\phi^* \right\rangle_\omega = & \frac{4\omega}{\pi}\theta(\omega,T)\iint \sum_m \sum_n G_{zm}^{EH}(\bar{r}-\bar{r}')Im\{\mu_{mn}\}\delta(r'-r'')G_{n\phi}^{HE*}(r-r'')dr'dr'' \\ & + j\frac{4\omega}{\pi}\theta(\omega,T)\iint \sum_m \sum_n G_{zm}^{EH}(\bar{r}-\bar{r}')Im\{\kappa_{mn}\}\delta(r'-r'')G_{n\phi}^{HE*}(r-r'')dr'dr'' \\ & - j\frac{4\omega}{\pi}\theta(\omega,T)\iint \sum_m \sum_n G_{zm}^{EH}(\bar{r}-\bar{r}')Im\{\eta_{mn}\}\delta(r'-r'')G_{n\phi}^{HE*}(r-r'')dr'dr'' \\ & + \frac{4\omega}{\pi}\theta(\omega,T)\iint \sum_m \sum_n G_{zm}^{EH}(\bar{r}-\bar{r}')Im\{\mu_{mn}\}\delta(r'-r'')G_{n\phi}^{HE*}(r-r'')dr'dr''\end{aligned} \tag{D.7}$$

since all the media is assumed to be local

$$\begin{aligned}\left\langle E_z\, H_\phi^* \right\rangle_\omega = & \frac{4\omega}{\pi}\theta(\omega,T)\int \sum_m \sum_n G_{zm}^{EH}(\bar{r}-\bar{r}')Im\{\mu_{mn}(\bar{r}')\}G_{n\phi}^{HE*}(\bar{r}-\bar{r}')dr' \\ & + j\frac{4\omega}{\pi}\theta(\omega,T)\int \sum_m \sum_n G_{zm}^{EH}(\bar{r}-\bar{r}')Im\{\kappa_{mn}(\bar{r}')\}G_{n\phi}^{HE*}(\bar{r}-\bar{r}')dr' \\ & - j\frac{4\omega}{\pi}\theta(\omega,T)\int \sum_m \sum_n G_{zm}^{EH}(\bar{r}-\bar{r}')Im\{\eta_{mn}(\bar{r}')\}G_{n\phi}^{HE*}(\bar{r}-\bar{r}')dr' \\ & + \frac{4\omega}{\pi}\theta(\omega,T)\int \sum_m \sum_n G_{zm}^{EH}(\bar{r}-\bar{r}')Im\{\eta_{mn}(\bar{r}')\}G_{n\phi}^{HE*}(\bar{r}-\bar{r}')dr'\end{aligned} \tag{D.8}$$

a similar expression can be derived for $\langle E_\phi\, H_z^* \rangle_\omega$.

COMSOL Simulation In order to numerically compute the former expressions, we follow the same procedure of chapter(2). In the current case, we have used COMSOL Multiphysics with general PDE modules for full wave simulations as follows:

$$\nabla_{2\times4}\cdot(-c_{4\times4}\cdot\nabla_{4\times2}u+\alpha_{4\times4}u+\gamma_{4\times1})+\beta_{2\times4}\cdot\nabla_{4\times2}u+a_{2\times2}u=f_{2\times1} \tag{D.9}$$

where $u = \begin{bmatrix} E_z \\ iH_z \end{bmatrix}$, and the coefficients of the PDE differential equation are

written as following:

$$
\begin{aligned}
c_{4\times4} &= -W_{4\times4}O_{4\times4}^{-1}W_{4\times4} \\
\alpha_{4\times2} &= \omega W_{4\times4}O_{4\times4}^{-1}P_{4\times2} \\
\beta_{2\times4} &= \omega M_{2\times4}O_{4\times4}^{-1}W_{4\times4} \\
\gamma_{4\times1} &= W_{4\times4}O_{4\times4}^{-1}\begin{bmatrix} iJ_T \\ -K_T \end{bmatrix} \\
a_{2\times2} &= \omega^2\left[M_{2\times4}O_{4\times4}^{-1}P_{4\times2} - N_{2\times2}\right]
\end{aligned}
\tag{D.10}
$$

$$
f_{2\times1} = \omega\begin{bmatrix} iJ_z \\ -K_z \end{bmatrix} - \omega M_{2\times4}O_{4\times4}^{-1}\begin{bmatrix} iJ_T \\ -K_T \end{bmatrix}
$$

where

$$
W_{4\times4} = \begin{bmatrix} \underline{\underline{0}} & \underline{\underline{R}} \\ \underline{\underline{R}} & \underline{\underline{0}} \end{bmatrix} = \begin{bmatrix} 0 & 0 & 0 & -1 \\ 0 & 0 & 1 & 0 \\ 0 & -1 & 0 & 0 \\ 1 & 0 & 0 & 0 \end{bmatrix}
\tag{D.11}
$$

and other media matrices are defined in Eq.(6.8) in chapter VI.

Special case E and H polarizations In the special case of non-chiral media, where E and H- polarizations are uncoupled so $P_{4\times2} = 0_{4\times2}$ and $M_{2\times4} = 0_{2\times4}$, the differential Eq.(D.9) will be reduced to be

$$
\nabla\cdot(-c_{4\times4}\cdot\nabla u + \gamma_{4\times1}) + a_{2\times2}u = f_{2\times1}
\tag{D.12}
$$

in such case, the coefficients of the PDE differential equation are rewritten as following:

$$c_{4\times4} = \begin{bmatrix} \frac{\underline{\underline{\mu}}_{TT}}{det(\underline{\underline{\mu}}_T T)} & \underline{\underline{0}} \\ \underline{\underline{0}} & \frac{\underline{\underline{\epsilon}}_{TT}}{det(\underline{\underline{\epsilon}}_T T)} \end{bmatrix}$$

$$\alpha_{4\times4} = 0_{4\times4} \quad \beta_{2\times2} = 0_{2\times2}$$

$$\gamma_{4\times1} = W_{4\times4} O_{4\times4}^{-1} \begin{bmatrix} iJ_T \\ -K_T \end{bmatrix} = \begin{bmatrix} \frac{1}{det(\underline{\underline{\mu}}_{TT})}(-\mu_{xy}K_T^x + \mu_{xx}K_T^y) \\ \frac{1}{det(\underline{\underline{\mu}}_{TT})}(-\mu_{yy}K_T^x + \mu_{xy}K_T^y) \\ \frac{i}{det(\underline{\underline{\epsilon}}_{TT})}(\epsilon_{xy}J_T^x - \epsilon_{xx}J_T^y) \\ \frac{i}{det(\underline{\underline{\epsilon}}_{TT})}(\epsilon_{yy}J_T^x - \epsilon_{xy}J_T^y) \end{bmatrix} \tag{D.13}$$

$$a_{2\times2} = -\omega^2 N_{2\times2}$$

$$f_{2\times1} = \begin{bmatrix} i\omega J_z \\ -\omega K_z \end{bmatrix}$$

Numerical Implementation Here, we briefly summarize the numerical procedures that we used to perform the final calculation. Due to the stochastic nature of thermal radiation, we took account only for the radial component time averaged Poynting vector of the emitted field $< S >$. In all calculations a triangular mesh was created such that it spans the thermally radiating object; then we calculated the location of each unit cell and its area Δa_i indexed with $i = 1, 2, , L$, where L is the total number of cells. then sweeping over the centroids of the cells such that for each loop, a point current source is located at each centroid. In order to evaluate the Green functions defined previously in this appendix, we have used COMSOL Multiphysics with general PDE modules for full wave simulations utilizing the differential

Eq.s mentioned above. Finally, the total thermally radially radiated poynting vector is computed by summing over the power radiated from the point sources.

APPENDIX E

Fluctuation dissipation theorem

In this appendix, we state Nyquist thermal noise theorem as it was formulated by fluctuation electrodynamics theorem. Then a simplistic derivation for Eq.(1.21), which states the spectral correlations of the thermal electric current fluctuating in a thermal emitter. This derivation is adapted from [8]. No claim of novelty is imposed about the derivations stated in this appendix.

E.1 Fluctuation Dissipation Theorem

Nyquits noise is not an exclusive property of electrical resistors, however thermal fluctuations of a generic linear system is related to its thermodynamic impedance. For a lossy system that can absorb energy from an external applied force, a generalized impedance can be defined and thermal noise or spontaneous fluctuations are related to the resistive part of the impedance in the same manner thermal noise of electrical resistors are treated by Nyquist's theorem. Callen and welton [13] generalized the concept of a thermodynamic impedance. A classical system is actually a quantum system but densely distributed energy levels. Quantum mechanically, thermal fluctuations and spontaneous emissions are modelled as time dependent external

perturbations. Callen and Welton treated such problem using perturbation method of quantum mechanics and they compute the thermodynamic impedance (and more importantly the resistance) in terms of the transition between different energy level of such system. Their theory is named fluctuation dissipation theorem (DFT). In what follows we just state the relevant results of FDT in terms of electrical impedance and admittance. Nyquist's theorem of thermal noise in electrical resistors can be sttsted as following: given a n electrical ristor with resistance R. When being isolated (not connected to other circuit elemnets) the thermal noise can be modeled as voltage source connected in seies with a oisless resistor with the sale value R. The auto correlation of the thermal voltage sources is written as following:

$$\left\langle \tilde{V}_s \tilde{V}_s \right\rangle_\omega = \frac{4}{\pi}\Theta(\omega, T)R \tag{E.1}$$

Another corollary: the thermal noise can be represented by a current source connected in parallel (shunt) with the resistor with conductance $G = \frac{1}{R}$. The auto correlation of the thermal current sources is written as following:

$$\left\langle \tilde{I}_s \tilde{I}_s \right\rangle_\omega = \frac{4}{\pi}\Theta(\omega, T)G \tag{E.2}$$

Finally if the resistor has a parasitic capacitance and/or inductance, so that the resistor has an impedance Z or admittance Y, then the theorem is re written as following:

$$\begin{aligned} \left\langle \tilde{V}_s \tilde{V}_s \right\rangle_\omega &= \frac{4}{\pi}\Theta(\omega, T)Re\{Z\} \\ \left\langle \tilde{I}_s \tilde{I}_s \right\rangle_\omega &= \frac{4}{\pi}\Theta(\omega, T)Re\{Y\} \end{aligned} \tag{E.3}$$

E.2 Fluctuation Electrodynamics correlations: Simplified derivation

Consider the media of a thermal emitter is to be made of a homogeneous and isotropic dielectric which consists of uncoupled weakly damped isotropic harmonic oscillators. Each oscillator models the electric dipole moment aroused due to the motion of a bound charges in the presence of an applied electric field. Averaging this dipole moment over the volume of the material gives rise to a macroscopic dipole moment per unit volume.

Consider a harmonic oscillator under applied electric field E with the following differential equation that model its displacement x:

$$\frac{d^2}{dt^2}x + \gamma\frac{d}{dt}x + \omega_0^2 x = \frac{e}{m}E \tag{E.4}$$

where e, m , ω_0 and γ respectively denote the charges, masses, natural frequencies and damping constants of the oscillators. Assuming the time harmonic dependence $E(t) = \tilde{E}e^{i\omega t}$ and $x(t) = \tilde{x}e^{i\omega t}$

$$-\omega^2\tilde{x} + j\gamma\omega\tilde{x} + \omega_0^2\tilde{x} = \frac{e}{m}E \tag{E.5}$$

then the $\tilde{x}$ will have the following form:

$$\tilde{x} = \frac{\frac{e}{m}\tilde{E}}{-\omega^2 + j\gamma\omega + \omega_0^2} \tag{E.6}$$

the polarization vector due to the charge motion can be written as following:

$$\tilde{P} = e\tilde{x}\delta(\bar{r} - \bar{r}_1) = j\omega\tilde{x} = \frac{\frac{e^2}{m}\tilde{E}}{-\omega^2 + j\gamma\omega + \omega_0^2}\delta(\bar{r} - \bar{r}_1) \tag{E.7}$$

since for a linear media, the electric field density is related to the electric field

intensity as following

$$\tilde{D} = \epsilon_0 \tilde{E} + \tilde{P} = \epsilon(\omega)\tilde{E} \tag{E.8}$$

where ϵ is the media's permittivity with is written as following:

$$\epsilon(\omega) = \epsilon_0 + \frac{\frac{e^2}{m}}{-\omega^2 + j\gamma\omega + \omega_0^2}\delta(\bar{r} - \bar{r}_1) \tag{E.9}$$

Now since current density at $\bar{r}_1$ can be written as $J(\bar{r}_1, t) = I(t)\delta(\bar{r} - \bar{r}_1)$ where I is the electric current and δ is delta Dirac function. The auto-correlation of the current density is related to the auto-correlation of the currents as following:

$$\langle J(\bar{r}_1, t)J(\bar{r}_2, t')\rangle = \langle I(t)I(t')\rangle \delta(\bar{r} - \bar{r}_1)\delta(\bar{r} - \bar{r}_2) = \langle I(t)I(t')\rangle \delta(\bar{r}_1 - \bar{r}_2) \tag{E.10}$$

On the other hand, the electric current induced due the charge oscillations of the one bounded oscillator is $I(t) = -ev(t)$ where $v(t) = v_0 cos(\omega' t)e^{-i\frac{\gamma}{2}t}$ is the velocity of the oscillator's mass and $\omega' = \sqrt{\omega_0^2 - (\frac{\gamma}{2})^2}$. Then the auto-correlation correlation of the electric current $I(t)$ can be written following:

$$\langle I(t)I(t')\rangle = e^2 \langle v(t)v(t')\rangle = e^2 \left\langle v_0^2 \right\rangle cos(\omega'(t - t'))e^{-i\frac{\gamma}{2}(t-t')} \tag{E.11}$$

considering the double Fourier transform with respect to t and t'

$$\langle I(\omega)I^*(\omega')\rangle_\omega = 4\pi e^2 \left\langle v_0^2 \right\rangle \omega Im \left\{ \frac{1}{-\omega^2 + j\gamma\omega + \omega_0^2} \right\} \delta(\omega - \omega') \tag{E.12}$$

since $\langle v_0^2 \rangle = \frac{1}{m}\theta(\omega, T)$ where $\theta(\omega, T)$ is the free energy of a (one-dimensional) quantum harmonic oscillator of frequency at temperature T, then substituting in Eq.(E.12), we get

$$\langle I(\omega)I^*(\omega')\rangle_\omega = 4\pi \frac{e^2}{m}\theta(\omega, T)\omega Im \left\{ \frac{1}{-\omega^2 + j\gamma\omega + \omega_0^2} \right\} \delta(\omega - \omega') \tag{E.13}$$

then the spectral correlation of the current densities

$$\langle J(\bar{r}_1,\omega)J^*(\bar{r}_1,\omega')\rangle_\omega = 4\pi\theta(\omega,T)\omega Im\left\{\epsilon(\omega)\right\}\delta(\omega-\omega')\delta(\bar{r}_1-\bar{r}_2) \tag{E.14}$$

BIBLIOGRAPHY

BIBLIOGRAPHY

[1] J. T. Aberle and R. Loepsinger-Romak. Antennas with non-foster matching networks. *Synthesis Lectures on Antennas*, 2(1):1–53, 2007.

[2] K. Achouri, M. A. Salem, and C. Caloz. General metasurface synthesis based on susceptibility tensors. *IEEE Transactions on Antennas and Propagation*, 63(7):2977–2991, 2015.

[3] G. Addamo. *Electromagnetic waves in loaded cylindrical structures: a radial transmission line approach*. Technische Universiteit Eindhoven, 2008.

[4] A. Alù. Mantle cloak: Invisibility induced by a surface. *Physical review B*, 80(24):245115, 2009.

[5] A. Alù, D. Rainwater, and A. Kerkhoff. Plasmonic cloaking of cylinders: finite length, oblique illumination and cross-polarization coupling. *New Journal of Physics*, 12(10):103028, 2010.

[6] P. Bamfield. *Chromic phenomena: technological applications of colour chemistry*. Royal Society of Chemistry, 2010.

[7] S.-A. Biehs and P. Ben-Abdallah. Revisiting super-planckian thermal emission in the far-field regime. *Physical Review B*, 93(16):165405, 2016.

[8] G. Bimonte, T. Emig, M. Kardar, and M. Krüger. Nonequilibrium fluctuational quantum electrodynamics: Heat radiation, heat transfer, and force. *Annual Review of Condensed Matter Physics*, 8:119–143, 2017.

[9] G. Bimonte and E. Santamato. General theory of electromagnetic fluctuations near a homogeneous surface in terms of its reflection amplitudes. *Physical Review A*, 76(1):013810, 2007.

[10] J. G. V. Bladel. *Electromagnetic Fields*. John Wiley & Sons.

[11] S. Y. Buhmann, D. T. Butcher, and S. Scheel. Macroscopic quantum electrodynamics in nonlocal and nonreciprocal media. *New Journal of Physics*, 14(8):083034, 2012.

[12] D. Butcher. Quantum theory of light and dispersion forces in non-reciprocal and bianisotropic media. 2014.

[13] H. B. Callen and T. A. Welton. Irreversibility and generalized noise. 83(1):34–40.

[14] F. Capolino. *Theory and phenomena of metamaterials*. CRC press, 2009.

[15] H. Chen, X. Luo, H. Ma, and C. Chan. The anti-cloak. *Optics express*, 16(19):14603–14608, 2008.

[16] K. Chen and S. Fan. Nonequilibrium casimir force with a nonzero chemical potential for photons. *Physical review letters*, 117(26):267401, 2016.

[17] P. Y. Chen and A. Alu. Patterned metallic surfaces to realize 1-d, 2-d and 3-d ultrathin invisibility cloaks. In *Antennas and Propagation Society International Symposium (APSURSI), 2010 IEEE*, pages 1–4. IEEE, 2010.

[18] P.-Y. Chen and A. Alù. Atomically thin surface cloak using graphene monolayers. *ACS nano*, 5(7):5855–5863, 2011.

[19] P.-Y. Chen and A. Alu. Mantle cloaking using thin patterned metasurfaces. *Physical review B*, 84(20):205110, 2011.

[20] P.-Y. Chen, C. Argyropoulos, and A. Alù. Broadening the cloaking bandwidth with non-foster metasurfaces. *Physical review letters*, 111(23):233001, 2013.

[21] P.-Y. Chen, F. Monticone, and A. Alu. Suppressing the electromagnetic scattering with an helical mantle cloak. *IEEE Antennas and Wireless Propagation Letters*, 10:1598–1601, 2011.

[22] P.-Y. Chen, J. Soric, and A. Alù. Invisibility and cloaking based on scattering cancellation. *Advanced Materials*, 24(44), 2012.

[23] P.-Y. Chen, J. Soric, Y. R. Padooru, H. M. Bernety, A. B. Yakovlev, and A. Alù. Nanostructured graphene metasurface for tunable terahertz cloaking. *New Journal of Physics*, 15(12):123029, 2013.

[24] C. M. Cornelius and J. P. Dowling. Modification of planck blackbody radiation by photonic band-gap structures. *Physical Review A*, 59(6):4736, 1999.

[25] A. I. Dimitriadis, D. L. Sounas, N. V. Kantartzis, C. Caloz, and T. D. Tsiboukis. Surface susceptibility bianisotropic matrix model for periodic metasurfaces of uniaxially mono-anisotropic scatterers under oblique te-wave incidence. *IEEE Transactions on Antennas and Propagation*, 60(12):5753–5767, 2012.

[26] G. Dupont, S. Guenneau, S. Enoch, G. Demesy, A. Nicolet, F. Zolla, and A. Diatta. Revolution analysis of three-dimensional arbitrary cloaks. 17(25):22603–22608.

[27] W. Eckhardt. First and second fluctuation-dissipation-theorem in electromagnetic fluctuation theory. 41(5):305–309.

[28] S. Enoch, J.-J. Simon, L. Escoubas, Z. Elalmy, F. Lemarquis, P. Torchio, and G. Albrand. Simple layer-by-layer photonic crystal for the control of thermal emission. *Applied Physics Letters*, 86(26):261101, 2005.

[29] N. M. Estakhri and A. Alù. Ultra-thin unidirectional carpet cloak and wavefront reconstruction with graded metasurfaces. *IEEE Antennas and Wireless Propagation Letters*, 13:1775–1778, 2014.

[30] M. Farhat, S. Mühlig, C. Rockstuhl, and F. Lederer. Scattering cancellation of the magnetic dipole field from macroscopic spheres. *Optics express*, 20(13):13896–13906, 2012.

[31] R. P. Feynman, R. B. Leighton, and M. Sands. *The Feynman lectures on physics, Vol. I: The new millennium edition: mainly mechanics, radiation, and heat*, volume 1. Basic books, 2011.

[32] R. Fleury and A. Alu. Cloaking and invisibility: A review. In *Forum for Electromagnetic Research Methods and Application Technologies (FERMAT)*, volume 1, 2014.

[33] R. Graham and H. Haken. Quantum theory of light propagation in a fluctuating laser-active medium. *Zeitschrift für Physik A Hadrons and nuclei*, 213(5):420–450, 1968.

[34] J.-J. Greffet, P. Bouchon, G. Brucoli, E. Sakat, and F. Marquier. Generalized kirchhoff law.

[35] J. Guan, W. Li, W. Wang, and Z. Fu. General boundary mapping method and its application in designing an arbitrarily shaped perfect electric conductor reshaper. 19(20):19740–19751.

[36] S. Guenneau, C. Amra, and D. Veynante. Transformation thermodynamics: cloaking and concentrating heat flux. *Optics Express*, 20(7):8207–8218, 2012.

[37] S. Guenneau, D. Petiteau, M. Zerrad, and C. Amra. Bicephalous transformed media: concentrator versus rotator and cloak versus superscatterer. 22(19):23614–23619.

[38] K. Gupta, A. Nishkam, and N. Kasturiya. Camouflage in the non-visible region. *Journal of Industrial Textiles*, 31(1):27–42, 2001.

[39] R. F. Harrington. Time-harmonic electromagnetic fields. 2001.

[40] H. A. Haus and R. B. Adler. *Circuit theory of linear noisy networks*. Technology Press of Massachusetts Institute of Technology, 1959.

[41] R. Heid. Chapter 12, "density functional perturbation theory and electron phonon coupling". *Emergent Phenomena in Correlated Matter: Autumn School Organized by the Forschungszentrum Jülich and the German Research School*

for Simulation Sciences at Forschungszentrum Jülich 23-27 September 2013; Lecture Notes of the Autumn School Correlated Electrons 2013, 3, 2013.

[42] C. Henkel. Nanoscale thermal transfer an invitation to fluctuation electrodynamics. 72(2):99–108.

[43] Y. H. HOE. *Near-Field Radiative Heat Transfer in Presence of Surface Charge*. PhD thesis, 2016.

[44] J. R. Howel, R. Siegel, and M. Meng c. Thermal radiation heat transfer 5th edition, 460-466, 2011.

[45] L. Hsu, T. Lepetit, and B. Kanté. Extremely thin dielectric metasurface for carpet cloaking. *arXiv preprint arXiv:1503.08486*, 2015.

[46] C. Huang, J. Yang, X. Wu, J. Song, M. Pu, C. Wang, and X. Luo. Reconfigurable metasurface cloak for dynamical electromagnetic illusions. *ACS Photonics*, 2017.

[47] M. M. Idemen. *Discontinuities in the electromagnetic field*, volume 40. John Wiley & Sons, 2011.

[48] P. A. Jacobs. Thermal infrared characterization of ground targets and backgrounds. 2006.

[49] W. X. Jiang, J. Y. Chin, Z. Li, Q. Cheng, R. Liu, and T. J. Cui. Analytical design of conformally invisible cloaks for arbitrarily shaped objects. 77(6):066607.

[50] Z. H. Jiang and D. H. Werner. Exploiting metasurface anisotropy for achieving near-perfect low-profile cloaks beyond the quasi-static limit. *Journal of Physics D: Applied Physics*, 46(50):505306, 2013.

[51] J. D. Joannopoulos, S. G. Johnson, J. N. Winn, and R. D. Meade. *Photonic crystals: molding the flow of light*. Princeton university press, 2011.

[52] K. Joulain, R. Carminati, J.-P. Mulet, and J.-J. Greffet. Definition and measurement of the local density of electromagnetic states close to an interface. *Physical Review B*, 68(24):245405, 2003.

[53] K. Joulain, J.-P. Mulet, F. Marquier, R. Carminati, and J.-J. Greffet. Surface electromagnetic waves thermally excited: Radiative heat transfer, coherence properties and casimir forces revisited in the near field. 57(3):59–112.

[54] M. A. Kats, R. Blanchard, S. Zhang, P. Genevet, C. Ko, S. Ramanathan, and F. Capasso. Vanadium dioxide as a natural disordered metamaterial: perfect thermal emission and large broadband negative differential thermal emittance. *Physical Review X*, 3(4):041004, 2013.

[55] C. Khandekar, W. Jin, O. D. Miller, A. Pick, and A. W. Rodriguez. Giant frequency-selective near-field energy transfer in active–passive structures. *Physical Review B*, 94(11):115402, 2016.

[56] A. V. Kildishev and V. M. Shalaev. Transformation optics and metamaterials. *Physics-Uspekhi*, 54(1):53, 2011.

[57] E. F. Kuester, M. A. Mohamed, M. Piket-May, and C. L. Holloway. Averaged transition conditions for electromagnetic fields at a metafilm. *IEEE Transactions on Antennas and Propagation*, 51(10):2641–2651, 2003.

[58] N. Kundtz, D. A. Roberts, J. Allen, S. Cummer, and D. R. Smith. Optical source transformations. 16(26):21215–21222.

[59] G. Labate, S. Podilchak, and L. Matekovits. Analytical synthesis of dispersive mantle cloaks for metallic cylinders: a zero contrast methodology. *arXiv preprint arXiv:1704.03323*, 2017.

[60] G. Labate, S. K. Podilchak, and L. Matekovits. Closed-form harmonic contrast control with surface impedance coatings for conductive objects. *Applied Optics*, 56(36):10055–10059, 2017.

[61] Y. Lai, H. Chen, Z.-Q. Zhang, and C. Chan. Complementary media invisibility cloak that cloaks objects at a distance outside the cloaking shell. *Physical review letters*, 102(9):093901, 2009.

[62] U. Leonhardt. U. leonhardt, science 312, 1777 (2006). *Science*, 312:1777, 2006.

[63] U. Leonhardt and T. Philbin. *Geometry and light: the science of invisibility*. Courier Corporation, 2012.

[64] U. Leonhardt and T. G. Philbin. General relativity in electrical engineering. *New Journal of Physics*, 8(10):247, 2006.

[65] C. Li and F. Li. Two-dimensional electromagnetic cloaks with arbitrary geometries. 16(17):13414–13420.

[66] Y. Li, X. Bai, T. Yang, H. Luo, and C.-W. Qiu. Structured thermal surface for radiative camouflage. *Nature communications*, 9(1):273, 2018.

[67] I. V. Lindell. *Differential forms in electromagnetics*, volume 22. John Wiley & Sons, 2004.

[68] I. V. Lindell. *Multiforms, Dyadics and Electromagnetic Media*. John Wiley & Sons, 2015.

[69] I. V. Lindell and A. H. Sihvola. Duality transformation for nonreciprocal and nonsymmetric transmission lines. *IEEE transactions on microwave theory and techniques*, 45(1):129–131, 1997.

[70] I. V. Lindell and A. Vitanen. Duality transformations for general bi-isotropic (nonreciprocal chiral) media. *IEEE transactions on antennas and propagation*, 40(1):91–95, 1992.

[71] F. Liu, Z. Liang, and J. Li. Manipulating polarization and impedance signature: A reciprocal field transformation approach. *Physical review letters*, 111(3):033901, 2013.

[72] S. Liu, H.-X. Xu, H. C. Zhang, and T. J. Cui. Tunable ultrathin mantle cloak via varactor-diode-loaded metasurface. *Optics express*, 22(11):13403–13417, 2014.

[73] S. Liu, H. C. Zhang, H.-X. Xu, and T. J. Cui. Nonideal ultrathin mantle cloak for electrically large conducting cylinders. *JOSA A*, 31(9):2075–2082, 2014.

[74] Y. Liu and X. Zhang. Recent advances in transformation optics. *Nanoscale*, 4(17):5277–5292, 2012.

[75] C. Luo, A. Narayanaswamy, G. Chen, and J. Joannopoulos. Thermal radiation from photonic crystals: a direct calculation. *Physical Review Letters*, 93(21):213905, 2004.

[76] B. R. Mahafza. *Radar Systems Analysis and Design Using MATLAB Second Edition*. Chapman and Hall/CRC, 2005.

[77] M. Maldovan. Sound and heat revolutions in phononics. *Nature*, 503(7475):209, 2013.

[78] S. I. Maslovski, C. R. Simovski, and S. A. Tretyakov. Equivalent circuit model of radiative heat transfer. *Physical Review B*, 87(15):155124, 2013.

[79] S. I. Maslovski, C. R. Simovski, and S. A. Tretyakov. Conjugate-impedance matched metamaterials for super-planckian radiative heat transfer. In *Metamaterials X*, volume 9883, page 98830O. International Society for Optics and Photonics, 2016.

[80] S. I. Maslovski, C. R. Simovski, and S. A. Tretyakov. Overcoming black body radiation limit in free space: metamaterial superemitter. *New Journal of Physics*, 18(1):013034, 2016.

[81] Mathview. Differential geometry part 3 transformations and the metric tensor.

[82] M. McCall. Transformation optics and cloaking. *Contemporary Physics*, 54(6):273–286, 2013.

[83] D. A. Miller, L. Zhu, and S. Fan. Universal modal radiation laws for all thermal emitters. *Proceedings of the National Academy of Sciences*, 114(17):4336–4341, 2017.

[84] A. Monti, J. C. Soric, A. Alù, A. Toscano, and F. Bilotti. Anisotropic mantle cloaks for tm and te scattering reduction. *IEEE Transactions on Antennas and Propagation*, 63(4):1775–1788, 2015.

[85] B. A. Munk. *Frequency selective surfaces: theory and design*, volume 29. Wiley Online Library.

[86] A. Narayanaswamy and G. Chen. Thermal emission control with one-dimensional metallodielectric photonic crystals. *Physical Review B*, 70(12):125101, 2004.

[87] A. Narayanaswamy and G. Chen. Thermal near-field radiative transfer between two spheres. *Physical Review B*, 77(7):075125, 2008.

[88] X. Ni, Z. J. Wong, M. Mrejen, Y. Wang, and X. Zhang. An ultrathin invisibility skin cloak for visible light. *Science*, 349(6254):1310–1314, 2015.

[89] A. Nicolet, F. Zolla, and S. Guenneau. Electromagnetic analysis of cylindrical cloaks of an arbitrary cross section. 33(14):1584–1586.

[90] H. Nyquist. Thermal agitation of electric charge in conductors. *Physical review*, 32(1):110, 1928.

[91] J. Ordonez-Miranda, L. Tranchant, B. Kim, Y. Chalopin, T. Antoni, and S. Volz. Effects of anisotropy and size of polar nano thin films on their thermal conductivity due to surface phonon-polaritons. *Applied Physics Express*, 7(3):035201, 2014.

[92] C. R. Otey, L. Zhu, S. Sandhu, and S. Fan. Fluctuational electrodynamics calculations of near-field heat transfer in non-planar geometries: A brief overview. *Journal of Quantitative Spectroscopy and Radiative Transfer*, 132:3–11, 2014.

[93] M. N. Ozisik. *Boundary value problems of heat conduction*. Courier Corporation, 2013.

[94] Y. R. Padooru, A. B. Yakovlev, P.-Y. Chen, and A. Alù. Analytical modeling of conformal mantle cloaks for cylindrical objects using sub-wavelength printed and slotted arrays. *Journal of Applied Physics*, 112(3):034907, 2012.

[95] Y. R. Padooru, A. B. Yakovlev, P.-Y. Chen, and A. Alù. Line-source excitation of realistic conformal metasurface cloaks. *Journal of Applied Physics*, 112(10):104902, 2012.

[96] I. Palocz and A. Oliner. Equivalent network of a multimode planar grating. *IEEE Transactions on Microwave Theory and Techniques*, 18(5):244–252, 1970.

[97] J. B. Pendry, D. Schurig, and D. R. Smith. Controlling electromagnetic fields. *science*, 312(5781):1780–1782, 2006.

[98] D. Polder and M. Van Hove. Theory of radiative heat transfer between closely spaced bodies. *Physical Review B*, 4(10):3303, 1971.

[99] B.-I. Popa and S. A. Cummer. Complex coordinates in transformation optics. 84(6):063837.

[100] R. F. Reynolds and M. J. Kinsella. Thermal and visual camouflage system, Jan. 15 2002. US Patent 6,338,292.

[101] A. W. Rodriguez, M. H. Reid, and S. G. Johnson. Fluctuating-surface-current formulation of radiative heat transfer: theory and applications. *Physical Review B*, 88(5):054305, 2013.

[102] S. M. Rytov. *Theory of electric fluctuations and thermal radiation.* Electronics Research Directorate, Air Force Cambridge Research Center, Air Research and Development Command, U.S. Air Force.

[103] S. M. Rytov. Theory of electric fluctuations and thermal radiation. Technical report, AIR FORCE CAMBRIDGE RESEARCH LABS HANSCOM AFB MA, 1959.

[104] R. Schittny, M. Kadic, S. Guenneau, and M. Wegener. Experiments on transformation thermodynamics: molding the flow of heat. *Physical review letters*, 110(19):195901, 2013.

[105] D. Schurig, J. Mock, B. Justice, S. A. Cummer, J. B. Pendry, A. Starr, and D. Smith. Metamaterial electromagnetic cloak at microwave frequencies. *Science*, 314(5801):977–980, 2006.

[106] A. N. Serdyukov, A. H. Sihvola, S. A. Tretyakov, and I. V. Semchenko. Duality in electromagnetics: application to tellegen media. *Electromagnetics*, 16(1):51–61, 1996.

[107] D. P. Sheehan. Infrared cloaking, stealth, and the second law of thermodynamics. *Entropy*, 14(10):1915–1938, 2012.

[108] L. Shen, B. Zheng, Z. Liu, Z. Wang, S. Lin, S. Dehdashti, E. Li, and H. Chen. Large-scale far-infrared invisibility cloak hiding object from thermal detection. *Advanced Optical Materials*, 3(12):1738–1742, 2015.

[109] C. Simovski, S. Maslovski, I. Nefedov, and S. Tretyakov. Optimization of radiative heat transfer in hyperbolic metamaterials for thermophotovoltaic applications. *Optics express*, 21(12):14988–15013, 2013.

[110] D. R. Smith, W. J. Padilla, D. Vier, S. C. Nemat-Nasser, and S. Schultz. Composite medium with simultaneously negative permeability and permittivity. *Physical review letters*, 84(18):4184, 2000.

[111] J. Soric, P. Chen, A. Kerkhoff, D. Rainwater, K. Melin, and A. Alù. Demonstration of an ultralow profile cloak for scattering suppression of a finite-length rod in free space. *New journal of Physics*, 15(3):033037, 2013.

[112] J. C. Soric, A. Alù, A. Kerkhoff, and D. Rainwater. Experimental demonstration of a conformal mantle cloak for radio-waves. In *Antennas and Propagation Society International Symposium (APSURSI), 2012 IEEE*, pages 1–2. IEEE, 2012.

[113] R. R. Syms, O. Sydoruk, and L. Solymar. Transmission-line model of noisy electromagnetic media. *IEEE Transactions on Microwave Theory and Techniques*, 61(1):14–22, 2013.

[114] T. Tamir and S. Zhang. Modal transmission-line theory of multilayered grating structures. *Journal of lightwave technology*, 14(5):914–927, 1996.

[115] R. Twiss. Nyquist's and thevenin's theorems generalized for nonreciprocal linear networks. *Journal of Applied Physics*, 26(5):599–602, 1955.

[116] R. Ulrich. Far-infrared properties of metallic mesh and its complementary structure. *Infrared Physics*, 7(1):37–55, 1967.

[117] J. Vehmas, S. Hrabar, and S. Tretyakov. Transmission lines emulating moving media. *New Journal of Physics*, 16(9):093065, 2014.

[118] S. Vellucci, A. Monti, A. Toscano, and F. Bilotti. Scattering manipulation and camouflage of electrically small objects through metasurfaces. *Physical Review Applied*, 7(3):034032, 2017.

[119] J. Wang and J. Du. Plasmonic and dielectric metasurfaces: Design, fabrication and applications. *Applied Sciences*, 6(9):239, 2016.

[120] M. Wegener and S. Linden. Shaping optical space with metamaterials. *Phys. Today*, 63(10):32–36, 2010.

[121] M. Wei, Q. Yang, X. Zhang, Y. Li, J. Gu, J. Han, and W. Zhang. Ultrathin metasurface-based carpet cloak for terahertz wave. *Optics Express*, 25(14):15635–15642, 2017.

[122] S. Wijewardane and D. Goswami. A review on surface control of thermal radiation by paints and coatings for new energy applications. *Renewable and Sustainable Energy Reviews*, 16(4):1863–1873, 2012.

[123] www.baesystems.com.

[124] T. Yang, H. Chen, X. Luo, and H. Ma. Superscatterer: enhancement of scattering with complementary media. *Optics express*, 16(22):18545–18550, 2008.

[125] Y. Yang, L. Jing, B. Zheng, R. Hao, W. Yin, E. Li, C. M. Soukoulis, and H. Chen. Full-polarization 3d metasurface cloak with preserved amplitude and phase. *Advanced Materials*, 28(32):6866–6871, 2016.

[126] L. A. Zadeh. The determination of the impulsive response of variable networks. 21(7):642–645.

[127] L. A. Zadeh. Frequency analysis of variable networks. 38(3):291–299.

[128] X. Zang and C. Jiang. Overlapped optics, illusion optics, and an external cloak based on shifting media. *JOSA B*, 28(8):1994–2000, 2011.